TESIS DE LA UNIVERSIDAD
DE ZARAGOZA

2021

103

Ennio Giovanni Luciano

Flame Transfer Function: description, interpretation and use for prediction and control of thermoacoustic instabilities in premixed methane and biogas flames

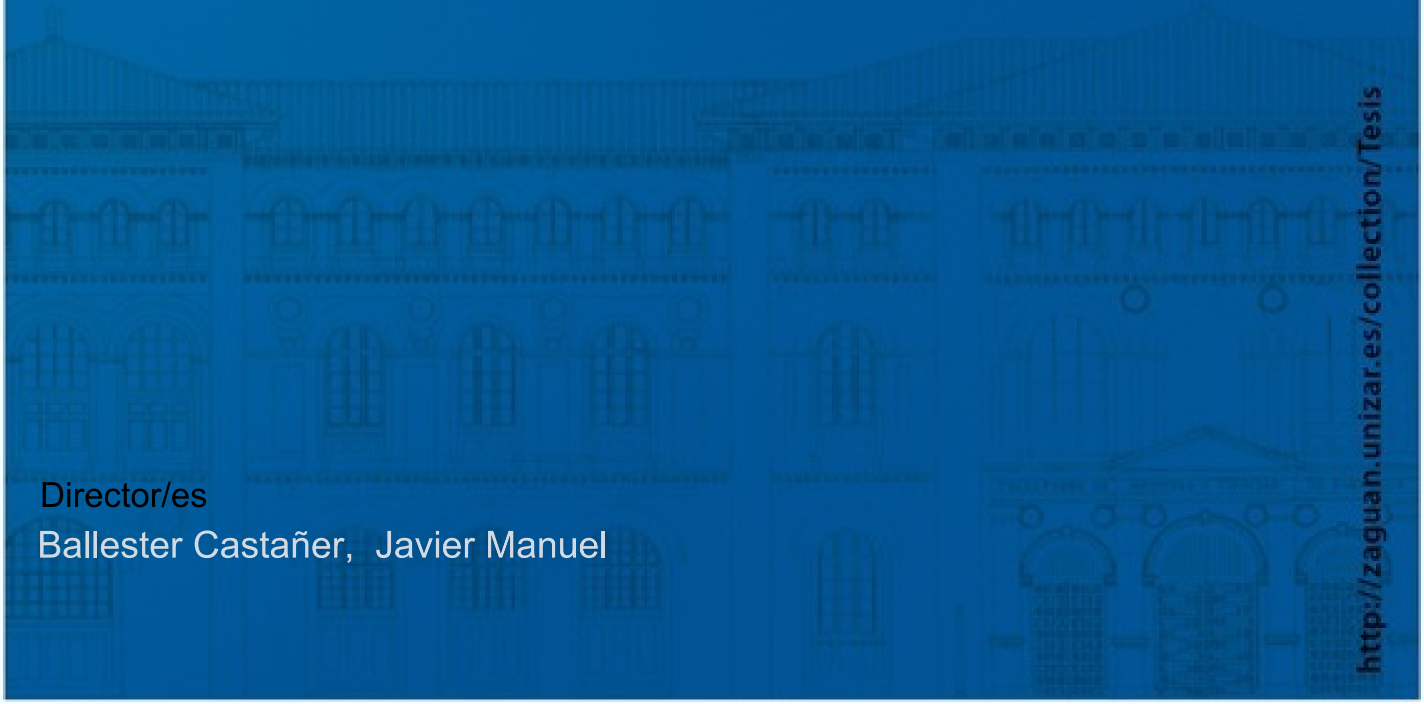

Director/es
Ballester Castañer, Javier Manuel

ISSN 2254-7606

Prensas de la Universidad
Universidad Zaragoza

Servicio de Publicaciones

ISSN 2254-7606

Tesis Doctoral

FLAME TRANSFER FUNCTION: DESCRIPTION, INTERPRETATION AND USE FOR PREDICTION AND CONTROL OF THERMOACOUSTIC INSTABILITIES IN PREMIXED METHANE AND BIOGAS FLAMES

Autor

Ennio Giovanni Luciano

Director/es

Ballester Castañer, Javier Manuel

UNIVERSIDAD DE ZARAGOZA
Escuela de Doctorado

Programa de Doctorado en Mecánica de Fluidos

2021

Flame Transfer Function: description, interpretation and use for prediction and control of thermoacoustic instabilities in premixed methane and biogas flames

Ennio Giovanni Luciano

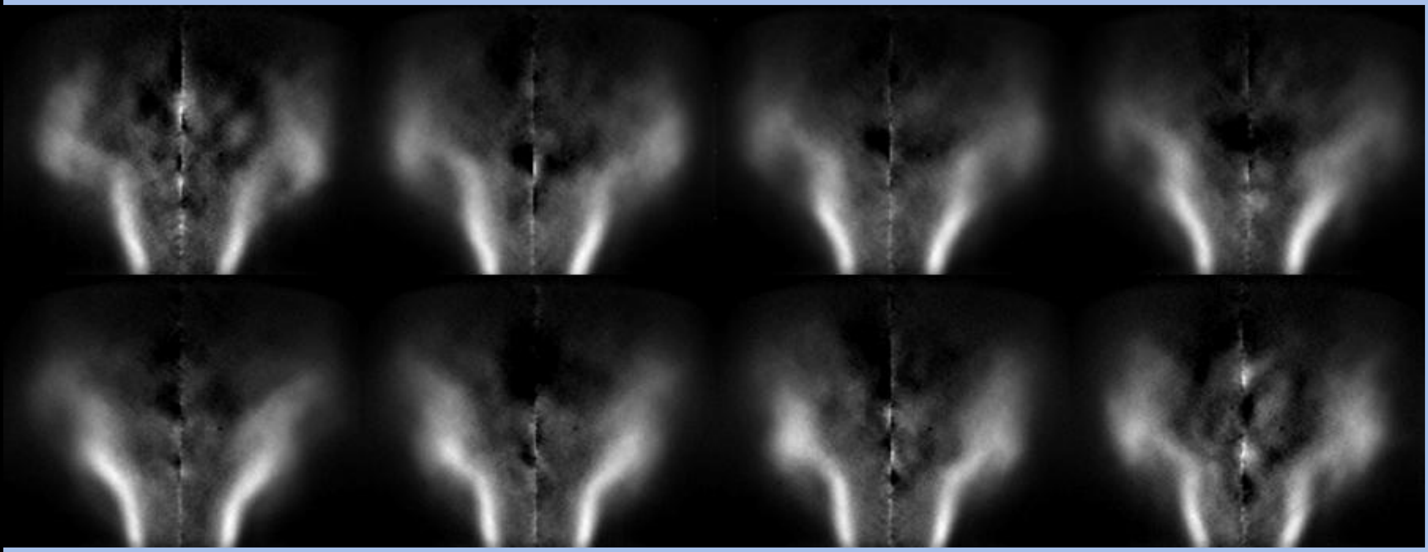

Supervisor:

Prof. Javier Ballester Castañer

CSIC
CONSEJO SUPERIOR DE INVESTIGACIONES CIENTÍFICAS

LIFTEC

Universidad Zaragoza
1542

Flame Transfer Function: description, interpretation and use for prediction and control of thermoacoustic instabilities in premixed methane and biogas flames

by

Ennio Giovanni Luciano

Thesis submitted for the Degree of Doctor of Philosophy

Supervisor: Prof. Javier Ballester Castañer

LIFTEC (CSIC/Universidad de Zaragoza)

October 2020

CSIC
Consejo Superior de Investigaciones Científicas

LIFTEC

Universidad Zaragoza
1542

Non al denaro,
non all'amore
né al cielo

Agradecimientos

Especialmente al principio, hacer un doctorado es como ir a ciegas en un mundo laberíntico: es muy sencillo perderse, caer, dar mil vueltas para volver siempre al mismo punto y no encontrar nunca una salida. Por lo tanto, en primer lugar quiero dar las gracias a mi director, Javier Ballester, por haberme guiado en cada paso a lo largo de este laberinto, hasta su salida.

Este estudio tiene detrás un enorme esfuerzo experimental, hecho de días pasados en laboratorio para plantear o hacer ensayos, y cuyos resultados son sin duda lo que más valor otorga a esta tesis. Todo esto no hubiera sido posible sin el gran trabajo de Luis, Alberto y Antonio, mil gracias.

Gracias a todos mis compañeros del LIFTEC por su acogida y por los buenos momentos juntos, tanto dentro como fuera del trabajo. Quiero agradecer en especial a Álvaro S., por toda la ayuda que me dio en el trabajo y por su envidiable organización de los eventos fuera de ello...de hecho, espero volver pronto para disfrutar de otro juepincho u otra cena-pelotazo (si la COVID nos deja).

Gracias a Eduardo Á., Álvaro M., Eduardo T., Jesús O., que me tuvieron como codirector de su TFG/TFM; espero haberles podido enseñar algo, aunque sea un mínimo; desde luego ellos a mí me enseñaron mucho.

Gracias a todos los que cruzaron su camino con el mío a lo largo de mi estancia en Zaragoza, si a la gente de allí se les llama maños es porque son grandes personas (tanto los nativos como los de adopción). Siempre me acordaré con profundo cariño de las experiencias que viví y de la gente que crucé por esa magnifica ciudad y por España entera.

Gracias de corazón a mi familia, al igual que Zaragoza tiene su pilar especial, yo tengo el mío en ellos. A pesar de la distancia que nos separaba y de las dificultades en comunicar por medios telemáticos, siempre me han estado, y los he sentido, muy cerca, y esto tiene un mérito no cuantificable con una simple nota.

Finalmente, gracias a ti, querido lector que, llegando a este punto, no te sientes identificado con ninguno de los grupos mencionados, o creías merecer un lugar más relevante dentro de estas pocas líneas. Si, leyendo esta página, has llegado a esta conclusión, es muy probable tú tengas razón.

Abstract

Thermoacoustic instabilities have gained particular importance in the gas turbine field since lean premixed combustion became the leading technology for this type of power plants. Lean flames allow producing very low pollutants emissions, but they result more prone to thermoacoustic phenomena, which are produced by the constructive coupling of the heat released by the flame and of the acoustic field of the burner.

The Flame Transfer Function (FTF) represents the linear response of the flame to acoustic inputs, and constitutes a fundamental element for the analysis of thermoacoustic phenomena. This work investigates various aspects regarding FTF, from its description and interpretation to its use for the prediction and control of thermoacoustic instabilities.

The first part presents a novel method to process bandfiltered flame images, called "Cross-Correlation Mapping Method" (CCM), which describes the local contribution of each flame parcel to the formation of the global FTF. The method has been developed analytically and validated experimentally, revealing a high potential in the interpretation, both qualitative and quantitative, of the phenomena behind the dynamics of the flames studied.

In the second part, FTF has been used as an input to a simple thermoacoustic model of a burner, the so-called dispersion equation. The objective was to assess the validity of the linear response of the flame to predict the natural, unstable modes of the system, so conditions in which the flame response is extremely non-linear. A comprehensive experimental campaign has been carried out, varying various operational parameters, reaching conditions of strong, self-induced instability (limit cycle conditions) in the experimental rig. The modes predicted match quite well with the experimental frequencies registered, so concluding that the FTF may be used to predict potential unstable modes. Since the FTF can be described by just one curve, instead of the family of curves needed to describe the non-linear response (flame describing function, FDF), this fact represents a notable simplification in terms both of computational cost to simulate and of experimental effort to collect data for FDF.

The third and last part focuses on a novel system to control thermoacoustic instabilities, called pseudo-active instability control (PAIC) system. PAIC operation is based on the principles of active systems (a secondary injection of fuel controlled by an active element), but the control proposed is composed of purely passive elements, so it gathers the advantages of both systems. In this work a first proof of concept of PAIC has been proposed, where the main difficulty found has been a suitable definition of the FTF for the pilot flame

used to control the instabilities. Nevertheless, the analysis performed revealed great potentialities of PAIC in damping instabilities, even though the pilot flame response resulted pivotal for the control proposed.

A further added value of this work is that it analyzes the dynamic response of both methane and biogas flames. If the former have been widely studied in the literature, the research about the latter is much more limited; in particular, not a study has been found where the FTF of a biogas flame is shown and analyzed. In this work, an in-depth analysis of the dynamic response of biogas flames has been performed, and compared with methane and for a broad range of operational conditions.

This work originates from the collection of five papers published by the author (with various co-authors) either in journals or in international congresses relevant to the field.

Resumen

Las inestabilidades termoacústicas han cobrado gran importancia en el campo de las turbinas de gas desde que la combustión de premezcla pobre se convirtió en la tecnología de combustión predominante en este tipo de plantas. Esta estrategia de combustión permite reducir considerablemente las emisiones de gases contaminantes; sin embargo, el empobrecimiento de las llamas aumenta la probabilidad de generar inestabilidades dinámicas provocadas por el acoplamiento constructivo entre la fluctuación de calor desprendido por la llama y el campo acústico del quemador.

La función de transferencia de la llama (*Flame Transfer Function*, FTF) representa la respuesta de la llama, en el rango lineal, a excitaciones acústicas, y constituye un elemento fundamental para analizar los fenómenos termoacústicos. Este trabajo investiga diversas facetas de la FTF, desde su descripción e interpretación hasta su uso para la predicción y el control de inestabilidades de llama.

La primera parte presenta un método novedoso para procesar imágenes de llama filtradas en bandas de quimioluminiscencia, que se ha denominado "*Cross-Correlation Mapping Method*" (CCM). Este método permite describir la contribución local de cada parte de la llama a la formación de la FTF global. Este procesado de imágenes ha sido desarrollado teóricamente y posteriormente validado mediante ensayos específicos. La investigación ha revelado un alto potencial del CCM para la interpretación, tanto cuantitativa como cualitativa, de los fenómenos que generan la dinámica de las llamas analizadas.

En la segunda parte, la FTF ha sido utilizada como datos de entrada para un modelo termoacústico simplificado de un quemador, también conocido con el nombre de "*ecuación de dispersión*". El objetivo era analizar la validez de la respuesta lineal de la llama para la predicción de los modos inestables del sistema, condiciones en las cuales la respuesta de la llama resulta extremadamente no lineal. Para este análisis se ha llevado a cabo un amplio estudio experimental, variando sistemáticamente ciertos parámetros de operación, con el objetivo de estudiar condiciones de fuerte inestabilidad auto-inducida (ciclo límite). Los modos identificados por el modelo presentan una buena correspondencia con los registrados experimentalmente, demostrando que la FTF puede utilizarse para predecir los modos inestables de un quemador. Dado que la FTF está descrita por una única curva, esto representa una notable simplificación en términos de coste computacional y experimental

respecto al uso de la FDF (*Flame Describing Function*), que requiere la generación y utilización de una familia de curvas.

La tercera y última parte de este estudio se centra en el desarrollo de un novedoso sistema de control, llamado *pseudo-active instability control* (PAIC). Su funcionamiento se basa en los principios de sistemas de control activos (inyección fluctuante de combustible secundario modulada por un elemento activo), con la diferencia de que el PAIC está formado únicamente por elementos puramente pasivos; de esta manera, este nuevo concepto podría combinar las ventajas de ambos sistemas de control. En este trabajo se ha desarrollado una primera evaluación del funcionamiento del PAIC, siendo la mayor dificultad encontrada en el estudio la definición de la FTF de la llama piloto utilizada para controlar las inestabilidades. Aunque la definición de la FTF de la llama piloto resulte de fundamental importancia para el diseño de un sistema PAIC, el análisis muestra un alto potencial del concepto propuesto para amortiguar las inestabilidades generadas en quemadores de premezcla pobre.

Un valor añadido de este trabajo reside en el análisis de la respuesta dinámica de llamas de metano y biogás. Mientras que las primeras han sido analizadas en un gran número de estudios, la información disponible sobre llamas de biogás es muy escasa. En particular, no se ha encontrado en literatura ningún estudio que analice la FTF asociada a la respuesta dinámica de una llama de biogás. Este trabajo recoge un análisis detallado de la dinámica de llamas de biogás, comparándola con la de llamas de metano para una amplia variedad de condiciones de operación.

La mayor parte de la información presentada en esta tesis se ha publicado en cinco artículos científicos firmados por el autor (y por varios coautores) en revistas y congresos internacionales.

Contents

List of figures

List of tables

1

Thesis as a compendium

This document collects the work made in order to obtain the degree of Doctor of Philosophy in Fluid Mechanics, degree confirmed by the University of Zaragoza.

The study carried out focuses on various aspects of the phenomenon of thermoacoustic instability, which have been studied both at theoretical and at experimental level. The results obtained have been published in either scientific journals or international congresses. Some of these works constitute the main body of this dissertation, intended as a compendium of the contents of these papers, which references are listed here below:

- Paper 1: *E. Luciano, J. Ballester, Analysis of the Dynamic Response of Premixed Flames through Chemiluminescence Cross-Correlation Maps, Combust. Flame 194 (2018) 296-308*
- Paper 2: *E. Luciano, J. Ballester, Analysis of the Dynamics of Premixed Methane and Biogas Flames Based on Cross-correlation Maps, Combust. Sci. Technol. 191 (2019) 1-26*
- Paper 3: *E. Luciano, E. Tizné, J. Ballester, Use of Flame Transfer Function to Predict Combustor Unstable Modes, 24th International Congress on Sound and Vibration (2017), paper 905*
- Paper 4: *J. Oliva, E. Luciano, J. Ballester, Damping of Combustion Instabilities Through Pseudo-Active Control, ASME Turbo Expo 2018: Turbomachinery Technical Conference and Exposition (2018), paper 51067*
- Paper 5: *E. Luciano, J. Oliva, Á. Sobrino, J. Ballester, Analysis of a Pseudo-active Approach for the Control of Thermoacoustic Instabilities, Combust. Sci. Technol. 192 (2020) 1-28*

The possibility of presenting a doctoral thesis as a collection of published papers is established by the regulation of the doctoral degree of the University of Zaragoza, which also defines the minimum requirements and the structure this typology of doctoral thesis must be compliant with.

Therefore, this document has been elaborated, both in its form and in its contents, in accordance with the regulation established by the University of Zaragoza for doctoral thesis presented as a compendium of publications.

2

Introduction

2.1 Motivation

Gas turbines play, nowadays, a fundamental role in the energy system, since they guarantee high flexibility in their operation [1], which can cope with the intermittent production of renewable sources, such as solar or wind.

Due to the more and more restrictive regulation about pollutants emissions established in Europe during the last decades, lean premixed combustion has become the leading technology for gas turbines [2, 3]. In fact, it allows reaching lower temperature values in the primary combustion zone, which in turn causes a strong reduction of pollutants emissions (e.g. CO, NO_x) keeping a good efficiency of the cycle [4].

Nevertheless, this technology can present also disadvantages, especially if the operational point moves close to the technical minimum, which is becoming a standard situation for gas turbines and thermal power plants in general. The higher amount of air in the primary zone could cause, on the one hand, a steep increase in the CO emissions [5]. On the other hand, lean flames have shown more proneness to reach unstable regimes [3], mainly related to thermoacoustic instabilities or to blow-out.

Thermoacoustic instabilities are produced by a constructive coupling of the heat released by the flame with the acoustic field in the combustion chamber. Firstly described by Lord Rayleigh [6], thermoacoustic phenomena may lead to a sudden and huge increase of the pressure fluctuation inside the combustor, which, in turn, can cause minor or major damages to the turbine hardware, as well as a sudden switching off of the device, all of them with detrimental economic consequences for the power plant.

In the last years, scientists and companies have been committed to investigate in depth the field of flame dynamics, due to the major importance this phenomenon has acquired for both manufacturers and operators of gas turbines. In this context, an extensive body of literature has been produced, in which the problem has been addressed following theoretical, computational and/or experimental approaches.

Although those efforts have led to a number of advances in both the knowledge and the control of thermoacoustic instability, the phenomenon still presents grey areas and researchers are called to break new ground in this field. In particular, most of the published studies are focused on flames produced by either natural gas or its main component, pure methane. Despite the great majority of the gas turbines are nowadays fed by natural gas, climate change concern is pushing the energy production towards greener and more sustainable fuels.

In this respect, both syngases and biogases are expected to play a central role in the future energy scenarios. Syngas is the acronym for synthetic gas; it is the product of the gasification of solid fuels, which gives a mixture of gaseous fuels (H_2, CO and CH_4) and, in minor extent, inert gases (N_2, H_2O, CO_2) [5, 7]. Biogas derives from the anaerobic digestion of biological products (generally byproducts of food industry or organic residuals), which produces, as a result, a blend of mainly methane and CO_2 [8, 9].

The use of either syngas or biogas to produce energy allows lowering considerably the related carbon dioxide emissions [5, 9]; therefore, the use of these fuels to replace natural gas is strongly encouraged by the public and the authorities [8]. However, the switching in the fuel used in a gas turbine may bring a series of technical problems [10-12], some of them related to the dynamics of the flames produced by these fuels. In fact, the alteration of the chemical composition of the fuel compounds results in a drastic change of the stability range and of the dynamic response of the flame to acoustic inputs, with respect to methane or natural gas.

Since the amount of CO_2 contained in biogases can reach a considerable percentage (up to 40% [13]), the studies about biogas flames dynamics have focused mostly on the blow-out instability, since it represents a prominent problem for this fuel (see, e.g., [11, 14-16]). On the contrary, very few works concerning other combustion dynamics, such as thermoacoustic instabilities, can be found in the literature about biogas flames ([17, 18] represent the few examples of works dealing with this issue).

In this context, this work is intended to investigate more in depth what can be considered the main parameter involved in a thermoacoustic coupling, that is, the dynamic response of the flame to acoustic inputs. Different aspects of the flame dynamic response will be addressed, from the nature of the involved phenomena to the use of the 'flame transfer function' (FTF) to predict and control thermoacoustic instabilities. Even though the FTF has been already widely investigated for methane flames, the present study is considered to bring new perspectives on the interpretation of flame images to characterize its dynamics, as well as alternative approaches for the control of the related instabilities. Moreover, a comprehensive investigation has been also carried out on biogas flames, comparing their response with that generated by methane ones. This adds further value to this work, since, as mentioned above, very few studies have dealt with the dynamic response of biogas flames.

2.2 Flame response as a key element in thermoacoustics

The main physical parameters involved in thermoacoustics are the fluctuations of combustor pressure (p'), of the air-fuel mixture velocity at the inlet of the burner (u') and of the heat released by the flame (Q'). Each variable affects the other through a feedback loop, leading to either constructing or destructive coupling among the variables involved.

Pressure oscillations propagate both upwards, towards the combustion chamber outlet, and downwards, towards the injection of the air-fuel mixture. These variations alter the mass flow rate of the air-fuel blend entering into the combustion chamber in a measure dictated by the acoustic response of the injection channels (expressed by the acoustic impedance, Z) which can be directly related to the velocity fluctuations at the inlet of the combustor, u'. Moreover, p' travels also along the injection channels, reaching the point at which air and fuel are premixed, affecting also the quantity of fuel injected into the main air stream, and so causing oscillations in the equivalence ratio of the mixture, Φ' [19-21]. Fluctuations in these two variables may alter the heat released by the flame, Q', due to oscillations in the quantity of fuel entering into the chamber and/or in the instantaneous reaction rate. In turn, a fluctuation of the heat instantaneously released inside the combustion chamber causes a variation in the pressure of the burner, closing the thermoacoustic loop.

The response of a flame to acoustic inputs is generally described, in the linear regime, by the so-called Flame Transfer Function (FTF). The FTF describes the global response of the flame, in terms of heat release rate fluctuation (Q'), to perturbations in the equivalence ratio, Φ', or in the velocity of the fuel-air mixture at the inlet of the combustion chamber, u', as a function of frequency, f. When the amplitude of the forcing oscillations increases, the heat release rate fluctuation saturates, so the linearity between the parameters involved is lost [22, 23]. In this case the FTF becomes a family of curves, for different excitation amplitudes, known as Flame Describing Function (FDF) [24, 25]. A more detailed description of the flame response to acoustic inputs will be given in the next chapter.

The FTF (or FDF) represents the pivotal magnitude which connects the acoustics of the system with the heat released. Due to its central role in the thermoacoustic coupling, many theoretical [26-28], computational [29, 30] and experimental [31-33] studies have been aimed at characterizing the FTF, as a means to better understand the nature of the flame response to acoustics.

However, these works have been mostly focused on traditional fossil fuels (natural gas, pure methane), whereas the dynamic response of flames produced by other possible turbine propellants have received much less attention in the literature. In particular, not a study has been found, either theoretical or experimental, reporting an FTF for a biogas flame, which, as mentioned before, can be considered a suitable alternative to natural gas for the energy transition towards a greener production. Moreover, even for traditional fuels, further work is still needed to reach a comprehensive understanding of the relationship between the FTF and the underlying physical phenomena, since some aspects still remain unclear.

As mentioned above, the flame response is one of the key components in the feedback loop leading to thermoacoustic instabilities; in fact, almost each theoretical modeling (apart from the simplest ones) aimed at describing the thermoacoustics of combustion systems requires the FTF as an indispensable input. A common objective is the study of stability ranges of a thermoacoustic system, that is, the natural modes at which a system oscillates, and also whether the oscillation is stable or unstable (i.e. p' amplitude goes to zero or diverges). Rankine-Hugoniot relations [21] represent the basis for each of these models, which can then be simplified or particularized according to the level of detail required. Many studies report stability analyses of thermoacoustic systems, from the simple quarter-wave models [34, 35] to the ones which describe in detail the acoustics of every single part of a complex burner [2, 21, 34-38]. Due to the absence of works related to biogas flame response, stability studies for biogas are limited to purely experimental results [11] or highly simplified descriptions such as quarter-wave models [17], whereas, to the author's knowledge, thermoacoustic models which take into account the flame response, as described by its FTF/FDF, have not been applied for biogas flames.

The prediction of instability modes is particularly important to calibrate control systems designed to damp combustion instabilities. These devices can be divided in two categories: active and passive [39, 40]. The former actuate by means of a dynamic element (usually a valve) which operates in closed-loop according to a reference signal (generally p'), whereas the latter consist of purely passive elements, such as quarter-wave tubes, Helmoltz resonators [41], perforated plates [42] etc. The two systems present pros and cons, which will be summarized in the next chapter, and are somewhat complementary: the drawbacks of one could be compensated by the presence of the other and vice-versa. So, a possibility could be combining the two systems in one which presents the advantages of both; few attempts have been made in this direction [43, 44], but the application of such systems is not still mature for large-scale applications and further investigation is needed in this direction.

In this context, this compendium of works is intended for breaking new ground in the field of thermoacoustic instabilities. In particular, the topics mentioned above have been the object of a careful investigation, which pivots around the FTF as a central piece in the thermoacoustic feedback loop. The relationship between the FTF and flame behaviors has been studied through a novel methodology, called *cross-correlation mapping* (CCM), which involves the processing of bandfiltered flame images. A 1D acoustic model has been developed and employed to assess the unstable modes of a lab-scale burner operating both with methane and biogas, confirming that good results can be obtained using FTF to predict non-linear conditions. A novel system to damp instabilities has been designed, named as *pseudo-active control*, which is intended to combine the advantages of both active and passive systems.

The whole investigation has been carried out by combining theoretical and experimental approaches. Also, most of the topics have been assessed for both pure methane and biogas flames. This represents an added value of this study, since the analysis of biogas flame response, as remarked before, has not been studied in detail in previous works.

The results of the studies carried out have been disseminated in a number of publications, both in international congresses and in recognized journals. Five of them (cited in Chapter 0) have been chosen to constitute the main body of this work, and they can be grouped according to the topics mentioned above:

- Papers 1 and 2 [45, 46] are related to the development of the cross-correlation mapping and its use for the study of the relationship between local and global flame dynamics.
- Paper 3 [47] deals with the use of a 1D thermoacoustic model for the prediction of the natural, unstable modes, based on the description of different flames in terms of their FTF
- Papers 4 and 5 [48, 49] describe the pseudo-active control system developed

The content of each topic will be summarized in the next chapter, whereas the published papers which compose this compendium constitute the Chapter 4

3

Report

3.1 Background

The concern, both public and scientific, about the climate change has led the world, and in particular Europe, to a radical evolution of the energy panorama during the last decades. In fact, European policy reacted to the need of a climatic breakthrough by setting ambitious targets in terms of growth rate of renewable technologies production and energy efficiency, as well as of the reduction of greenhouse gases and pollutants emissions (e.g. EU 20-20-20 [50], COP 21 [51], Climate Action Plan 30 [52]).

These goals led the European Countries to both incentivize the installation of new capacity fed by renewable energy sources (RES), and to regulate the emissions of traditional thermal plants (CO_2 in particular). Due to these measures, the connection of more and more solar and wind capacity has been witnessed throughout Europe (+380% in the last 18 years [53]).

Nevertheless, this huge amount of intermittent energy introduced into the electric system, which nowadays has replaced in a huge extent that produced by traditional thermal plants [53], has led to new issues for the electric grid, such as the lack of inertia and upward reserve margin, as well as the need of more flexible plants which can ramp-up in order to compensate the steep variations of the residual load (i.e. the demand not supplied by RES).

Therefore, thermal plants have lost their original role of base load suppliers, whereas they are more and more often asked for guaranteeing flexibility to the system and act like “peakers”. In this context, gas turbines play a fundamental role for the power system, since they represent one of the most flexible technology fed by traditional fuels [1].

In order to reduce the emissions of pollutants (in particular NO_x), in the last decades most of gas turbine facilities have adopted the lean premixed combustion technology [2, 4, 21]; it consists of mixing fuel and air upstream of the combustion chamber in a way that the blend can result almost homogeneous and reaching an amount of air far above the stoichiometric one (Fig. 3.1).

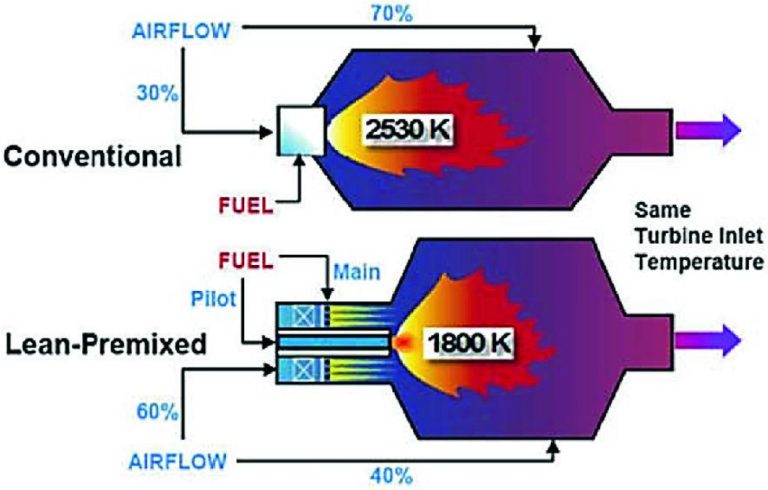

Fig. 3.1. Conventional vs. lean premixed combustion [54]

This is an effective method to guarantee that the temperature, in the primary combustion zone, is almost constant and low with respect to the one the flame would have reached with a stoichiometric blend. These conditions inhibit the formation of thermal NO_x to levels far below the thresholds imposed nowadays in regulations [55], keeping the efficiency of the cycle at the same level reached with other combustion techniques.

Despite all the advantages described, lean premixed combustion presents also some drawbacks, one of them being that the combustor is more prone to incur in combustion dynamics [2, 5, 19, 21, 56]. Among them, thermoacoustic instabilities represent a major problem for both manufacturers and operators of gas turbines. In fact, this combustion dynamics, if not controlled, leads to a sudden and huge increase of the pressure fluctuation (p') inside the combustion chamber which, in turn, can cause both minor and major damages to the facility. Also, an eventual forced switching off of the plant due to an uncontrolled growth of p' has technical and economic consequences for the operator.

The massive application of lean premixed combustion has raised the interest of the scientific community towards the study of thermoacoustic instabilities, even though the related basic phenomenology was already observed and described at the end of 19th century by Rayleigh [6]. The efforts spent in the last decades to investigate thermoacoustic instabilities led to a better understanding of the phenomenon and how to control it; in the next section the main mechanisms and physical parameters involved in thermoacoustic coupling will be briefly described.

3.1.1 Thermoacoustic instability

The coupling between the acoustic field of a system and the heat released by a source contained in this system was firstly described by Lord Rayleigh [6]. He observed that, over a period, the pressure fluctuation (p') produced in a control volume where a heat source was located could increase hugely if the oscillation of the heat released (Q') was in phase with the acoustic oscillation of the system, whereas a damping of the pressure oscillation occurred if the two oscillations were out-of-phase.

These considerations led to the so-called Rayleigh criterion, which states that the acoustic energy released over a period, E, is greater than zero if p' and Q' oscillate in phase and smaller than zero if the two oscillations are out-of-phase. However, an in-phase oscillation of p' and Q' is a condition necessary but not sufficient to observe the instability, since the energy produced must also exceed the losses (L) caused by various effects (viscosity, sound radiation, heat transfer, etc. [21]). The formulation for the variation in time of acoustic energy is summarized in Eq. (3.1), where γ indicates the specific heat ratio and $\bar{p}$ the mean pressure inside the control volume considered

$$E(T) = \frac{\gamma - 1}{\gamma \bar{p}} \int_0^T p'(t) \cdot Q'(t) dt - L(T) \tag{3.1}$$

If the coupling between p' and Q' is constructive and exceeds the losses, a net positive amount of energy is added to the system for each period, which results in an increment of p' amplitude.

However, the Q' fluctuation cannot grow indefinitely, but at a certain point the amplitude of the fluctuations in the flame reaches saturation [2, 20, 23]. Moreover, also the losses increase with p' magnitude, often in a non-linear way [1, 21]. Hence, if the combustor resists the mechanical stress induced, eventually a state of equilibrium is reached in a condition called limit cycle [1, 23, 31]. This equilibrium is characterized by high-amplitude pressure fluctuations which can cause both minor and major damages to the turbine hardware; an example is shown in Fig. 3.2 [4].

Fig. 3.2. Burner assembly: new one (left) and after limit cycle (right) [4]

The relationship described by the Rayleigh's criterion is, however, just one part of the phenomenon of thermoacoustic instability, as sketched in Fig. 3.3. For an open system like a turbine burner, the driving mechanisms that lead to the instability involve also fluctuations in the velocity of the flow at the inlet of the burner (designated as u') and/or in the equivalence ratio of the mixture entering into the burner (indicated as Φ'). Heat release fluctuations, Q', are a source of noise, generated by unsteady volumetric expansions. In general, p' does not have a direct effect on the flame, but the acoustic field and combustion are coupled through fluctuations in fuel and air flows.

In particular, p' induces oscillations in the flow injected into the burner, which can be described by the fluctuation of the inlet velocity, u' (the cross sectional area can be considered constant). Also, the propagation of the pressure wave along the injection duct can reach the point at which the fuel is injected and premixed with air, and so it can alter the amount of fuel that is premixed with air, causing an oscillation of the equivalence ratio of the blend, Φ'. Both variations concur to vary the instantaneous heat released by the flame, closing the thermoacoustic loop. A detailed description of these mechanisms can be found in [57] and [21].

Unsteady burning can also produce periodic temperature fluctuations, which are advected downstream and may generate acoustic waves upon acceleration at the combustor exit. This phenomenon is identified in the literature as entropy waves (s') [21] and constitutes an additional, although less studied, mechanism leading to thermoacoustic instabilities.

The relationship between p' and u' can be described by the acoustic impedance (Z) of the injection duct which, for simple geometries, is not difficult to model if the boundary conditions are known. Similarly, also the interaction between p' and Φ' can be modeled in a straightforward way if the geometry is not complex. In case of an elaborated geometrical configuration of the injection, the problem can be anyway reduced to a series of simple geometrical configurations (see [21, 37]).

The flame response, Q', to acoustic inputs (u',Φ') is generally quantified in terms of the flame transfer function (FTF) in case the flame response is linear, or flame describing function (FDF) if Q' saturates. It represents, together with the interaction of the pure acoustic variables, the second fundamental piece of the thermoacoustic coupling. Nevertheless, the description of the flame response normally is much less straightforward to describe and model than the acoustic impedance, and, due to its paramount importance in thermoacoustics, the determination and interpretation of the FTF (or FDF) is still the object of careful investigation.

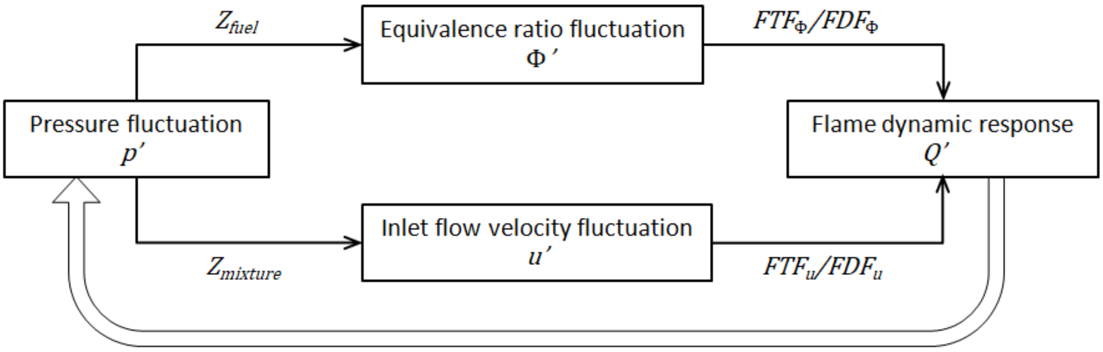

Fig. 3.3. Feedback loop characterizing thermoacoustics of a gas turbine burner

3.1.2 *Description of the flame response*

As described before, the two magnitudes which affect the heat released by the flame and are, in turn, affected by the pressure oscillation produced into the combustion chamber are the fluctuation of the inlet velocity of the air-fuel mixture entering in the combustor, u', and of its equivalence ratio, Φ'. Even though the mechanism that creates these oscillations is similar (both of them are due to an acoustic interaction between pressure oscillations and gas flows), both effects must be considered separately, and the global fluctuation of the heat release rate, Q', is the combined result of the two mechanisms.

The flames studied in this work can be considered perfectly premixed, that is, the equivalence ratio is constant and not affected by the pressure oscillation produced in the burner (in the next chapter, the experimental facility used will be described, including these details). Therefore, fluctuations in equivalence ratio can be considered negligible for the experiments performed and, so, this section will be mainly focused on the response of the flame to fluctuations in the inlet flow velocity, u'. Moreover, the flames studied present the classic "V-shape" configuration [58] (see Fig. 3.4); so, for the sake of conciseness, the following description of the characteristics of the flame response is referred to V-shaped flames, whereas other flame configurations do not necessarily share the same features.

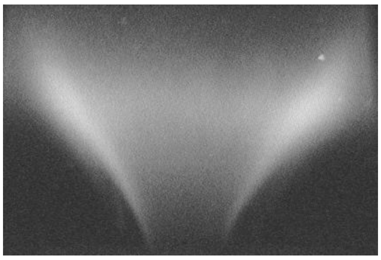

Fig. 3.4. Example of a V-shaped methane flame (Φ=0.86)

As mentioned before, if a flame is subjected to an acoustic forcing, u', at a certain frequency, f, it exhibits an oscillation, at the same frequency, of the heat released with an amplitude determined by the dynamic response of the flame. In the low range of amplitudes, the relationship between Q' and u' is linear; however, as the amplitude of u' increases, the flame response saturates and the linearity between the two magnitudes is lost [2, 20, 23]. The acoustic response of the flame is commonly described in terms of the *flame transfer function* (FTF) if the response is linear, and of the *flame describing function* (FDF) if the amplitudes reach the non-linear range. Their definitions are given in Eq. (3.2), where ω_f represents the angular forcing frequency ($\omega_f = 2\pi f$), while the overscripts "^" and "¯" indicate, respectively, the fast Fourier transform and the mean value of the magnitude.

$$FTF(\omega_f) = \frac{\hat{Q}(\omega_f)/\bar{Q}}{\hat{u}(\omega_f)/\bar{u}} \qquad FDF(\omega_f, |u'|) = \frac{\hat{Q}(\omega_f, |u'|)/\bar{Q}}{\hat{u}(\omega_f)/\bar{u}} \tag{3.2}$$

The definition of both FTF and FDF is practically the same, but, due to the independence from the u' amplitude, the representation of the former in the Bode domain results in just one curve, as a function of the forcing frequency f. The latter, instead, consists of a family of curves, one for each value of $|u'|$. An example of FTF and FDF is given in Fig. 3.5.

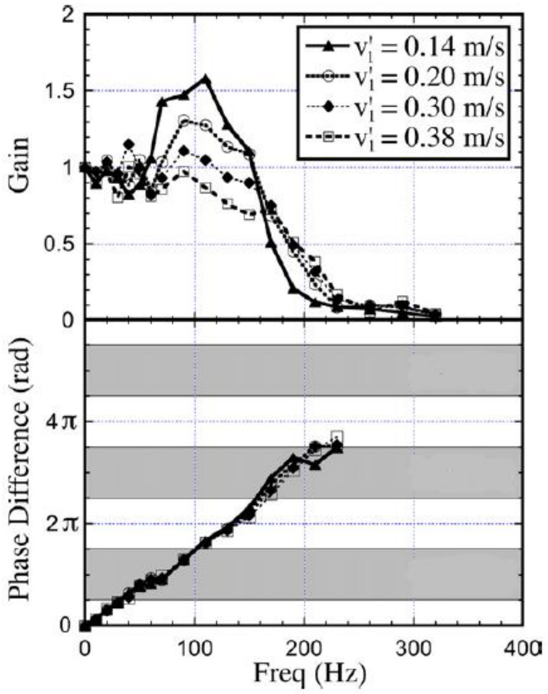

Fig. 3.5. Flame describing function varying the amplitude of u' [24]

The gain (G) curves represented in Fig. 3.5 indicate that the flame analyzed presents a low-pass filter behavior, both for FTF and for FDF. This feature is not something peculiar of the case analyzed, but it is a well-known characteristic for the type of flames considered (as reported in, e.g., [27, 32, 59]). The FDF gain decreases with $|u'|$, due to the gradual saturation of the Q' amplitude [20, 31, 37, 60].

As for the phase, φ, a linear trend is obtained with frequency, both for FTF and for FDF. This behavior is another characteristic commonly found for V flames [27, 31, 32, 61]. It is mathematically consistent with the existence of a characteristic constant time lag, τ ($\varphi = 2\pi f \tau$), which can be interpreted as the average time a fuel particle takes to travel from the combustor injection until it is burnt [19, 20]. Another feature that Fig. 3.5 shows is that the FDF phase barely varies with $|u'|$ and is very similar to that of the FTF. Considering the interpretation proposed for τ, it makes sense that the travel time for a fuel particle in a burner is determined by the mean flow and does not depend on the fluctuation of the flow velocity at the injection; moreover, this general behavior is well documented in a number of works (e.g. [24, 31, 37, 60]).

Many authors have investigated the flame dynamics theoretically [26-28], experimentally [31-33] and computationally [29, 30]. This huge interest is motivated by the importance of FTF/FDF for the modeling of a thermoacoustic system, being the key piece which connects the thermal and the acoustic parts of a thermoacoustic system. However, both the complexity of modeling the dynamics of realistic flames and the incomplete understanding of the mechanisms which finally give rise to the global response observed in Fig. 3.5 still make the description of the flame response a challenging scientific objective.

Moreover, as mentioned before in this document, the experiments have been mainly performed on traditional fuels, whereas the research about the response of flames produced by other types of fuel blends is much more limited. In particular, to the author's knowledge, the FTF/FDF of biogas flames or the differences with respect to methane have not been documented in the literature. Due to the growing importance of biogas and biofuels in general to meet the targets established by the European Union about greenhouse gases emissions [8], the dynamic response of flames produced by these alternative fuels needs to be characterized, since they are called to substitute natural gas, in a not negligible extent, in the next future.

The flame response represents the fundamental piece on which this work is built. The first part of the document describes an in-depth analysis performed about the mechanisms involved in the formation of the FTF. To do so, a novel method, which highlights the contribution of each flame region to the global flame response, has been developed. It has been called *cross-correlation method* (CCM) and involves a simple processing of bandfiltered flame images. Despite its simplicity, the method proposed gives useful insights on the formation of the FTF, as well as on the underlying phenomena. Moreover, it revealed itself useful to define characteristic magnitudes of the flames analyzed, related with the characteristic time lag of the FTF, τ.

The second part of this dissertation focuses on the use of FTF to predict the natural oscillation frequencies characteristic of a lab-scale combustor, in particular the unstable ones, using a quite simple model called "dispersion equation" [32, 34, 35]. One of the main points of this part will be the evaluation of predictive capabilities of simple thermoacoustic models to assess limit cycle frequency using FTF as an input, despite the flame response should be better characterized by the FDF (since the conditions tested are far from the linear regime). Moreover, the changes due to variations in operational conditions and fuel composition will be assessed and contrasted with predictions obtained with the "dispersion equation".

The prediction of the natural unstable modes of a facility is particularly important for the correct design of the control systems to be installed in the burner, in particular for passive ones [39]. The third and last part of this work deals with a novel system proposed to damp thermoacoustic instabilities. The system acts in a purely passive way, but exploiting principles typical of active systems; therefore, it has been called *pseudo-active instability control* (PAIC). It is intended to gather the pros of active and passive systems, avoiding, at the same time, the cons they present. The experiments performed have demonstrated the applicability of this kind of system, but the complexity of the flame configuration studied in this case (a pilot, diffusion flame burning in the core of a main, premixed one) makes a proper design of the PAIC still a matter to be investigated in depth. In particular, its design and optimization heavily relies on a correct description of the dynamics of the pilot diffusion flame, but it is very difficult to isolate its response from that of the main premixed one. Further work is needed to assess properly this aspect, crucial for a PAIC system.

The cross-correlation method and the prediction of natural modes has been applied not only for flames produced by traditional fuels, but also for two blends of methane and CO_2 (85%-15% and 60%-40% in volume for CH_4 and CO_2, respectively) representing two possible compositions of biogas [13]. Thus, the biogas flame response has been obtained, studied and compared with that produced by pure methane. To the author's knowledge, this is the first time a biogas flame response is presented and analyzed in the literature. Furthermore, the study does not limit its scope to the simple description of the data obtained, but it analyzes in depth the dynamic response of biogas flames, comparing them with pure methane ones. Also, the impact of changes in fuel composition on the thermoacoustic behavior of a combustor is expected to be suitably accounted for by using the FTF specifically measured for the fuels considered. The predictions obtained by combining a thermoacoustic model with the FTF obtained for biogas flames gives information about the modifications in the natural modes and stability with respect to those obtained with methane, representative of the traditional fuel used in stationary gas turbines. In summary, the analysis performed is thought to offer valuable insights into the biogas flames dynamics and their similarities and differences with respect to methane ones, a topic which few authors have treated and needs further investigation.

All the work carried out and compiled in this thesis is mainly based on a large experimental campaign. The experimental combustor and the equipment available allowed a broad variety of configurations, such as the variation of the geometry or the acoustic boundary conditions, changes in the fuel flow and in the equivalence ratio of the mixture injected, testing with various fuels (in this case, methane and two different biogas compositions) and the possibility of an external acoustic forcing of the system. The instrumentation available has been used to determine different combustion and acoustic variables. Apart from the data directly provided by the instruments, further post processing was applied to maximize the information that could be used to describe and understand the underlying physics (e.g., multi-microphone method, CCM, phase-locked imaging). Therefore, the core of this study is composed of hundreds of tests and repetitions for each topic analyzed, which, eventually, have led to the results published and summarized in this dissertation. The characteristics of the facility used to perform the tests, as well as the instrumentation used to collect the experimental data and the experimental methods applied will be described in the next section.

3.2 **Experimental methods**

3.2.1 Experimental rig

The experimental rig used to perform the tests compiled in this work is sketched in Fig. 3.6. It is an atmospheric, swirl-stabilized, premixed burner composed of a plenum, an annular injector duct and a cylindrical combustion chamber.

The air necessary for the combustion is conveyed by a compressor to a premixer in which the fuel, supplied from tanks, is injected. Both air and fuel mass flows are regulated in closed-loop with thermal mass flow controllers. The air-fuel blend is then split in two branches and injected into the plenum through two orifices. The diameter of the orifices (2.5 mm) was selected in order to achieve choked flow conditions for all the operational conditions tested; this guarantees that the flow entering the rig is constant, and so is the value of the equivalence ratio, no matter what the pressure value in the plenum is. Therefore, the flames studied can be considered perfectly premixed, that is, without fluctuations or spatial variations in the equivalence ratio.

The plenum is connected to the combustion chamber by means of an annular duct (outer and inner diameters are 40 and 25 mm, respectively) of 600 mm in length. An axial swirler with six 30° vanes (geometrical swirl number S=0.48) is located 380 mm upstream of the injection plane. The acoustic boundary conditions at the entrance of the annular duct can be adjusted by means of a restriction shaped as a crenelated plug (see Fig. 3.6) with eight teeth of 25 mm in length. The relative position of the restriction with respect to the injection entrance can be adjusted to modify the open section through which the air-fuel mixture enters the annular duct, so varying the acoustic boundary conditions at the inlet of the annular duct.

The combustion chamber is a cylinder (120 mm in diameter and up to 1,250 mm in length) composed of 3 sections of different lengths. The first section (400 mm in length) is fixed and its first part (220 mm) is a quartz cylinder, guaranteeing optical access to the flame, whereas the second part is made of stainless-steel. The other two segments (350 and 500 mm, both made of stainless-steel) can be mounted on top of the fixed section, so giving 4 possible lengths of the combustion chamber: 400, 750, 900 and 1,250 mm. The variation of the length of combustion chamber modifies its acoustic properties, allowing to change the natural modes of the facility and also to cover a wide range of instability amplitudes, from stable conditions to strong limit cycles. The exit of the chamber can be open to the atmosphere or closed with a refrigerated lid, changing in this way the acoustic boundary condition at the outlet; for this study only the open end will be considered.

A mid-pressure fan conveys the combustion products to a chimney, extracting them through an axisymmetric lateral slot at the chamber outlet, in order to keep the open-end condition. The whole combustion chamber wall is cooled by air which flows in an external, annular shield in co-current with the combustion products. This air stream flows between the walls of the combustion chamber and an outer cylindrical steel enclosure, whose first section (400 mm) is further refrigerated by a water jacket.

A secondary fuel injector (plain orifice of 2.5 mm in diameter) is located at the center of the bluff body. The pilot fuel flow is fed from a methane tank and regulated by a dedicated thermal mass flow controller. An orifice of 0.2 mm in diameter is located between the mass flow controller and the rig. This orifice has two purposes: it chokes the pilot fuel flow, so it guarantees acoustic isolation of the facility from the rest of the pilot feeding line, and it represents a well-known acoustic boundary condition for the secondary line. Downstream of this orifice, the line consists of two different sections: a polyamide tube (8 mm i.d.), whose length can be adjusted, followed by a stainless steel pipe (length 1.133 m, 8 mm i.d.), ending in the secondary injector.

3.2.2 *Instrumentation*

The facility is equipped with 6 pressure transducers (PT thereafter, PCB 103B02); five of them are located along the annular duct, between the swirler and the dump plane, at different distances. They allow, using the multi-microphone method [21], estimating the value of u' along the injection tube from the data collected. Also, one PT is located at the injection plane, in order to measure p' inside the combustion chamber.

Two photomultiplier tubes (PMT thereafter, Hamamatsu H5784-03) are mounted perpendicular to the quartz section of the combustion chamber. One of them (from now on PMT1) is fixed and its view angle includes the whole flame. The second PMT (PMT2) is mounted on a system which allows its 2-D translation in a controlled way, and its end is fitted with a tube (i.d. 4 mm, length 90 mm) which reduces the portion of the flame seen by the PMT2 to a circle of 8.5 mm in diameter at the central axis of the flame. This measuring volume is small enough to characterize the spatial variations in local radiation intensity while providing a sufficiently strong signal to guarantee a high signal-to-noise ratio. The configuration of the two PMT is sketched in Fig. 3.7. Both PMTs can be fitted with optical filters covering either the OH* emission peak (310±5 nm) or the CH* one (430±5 nm). Both chemiluminescent radicals can be directly related to the instantaneous heat released by the flame [33, 62-64], so both measurements can be considered suitable to estimate Q. In this work, OH* is mainly used, since it is normally considered more apt to describe the heat released by a premixed flame [65].

The signals recorded by both the PTs and the PMTs are conditioned by a signal amplifier (PCB 482C05) and, then, acquired through an acquisition board (NI PCI-6229), which allows recording at a sampling frequency up to 10,000 Hz.

An intensified CCD camera (ICCD, Hamamatsu C8484-05), fitted with a UV lens, is employed to record the spatial distribution of the heat released by the flame. Two loudspeakers (Eminence DELTA 10-A, 10″) are installed into the plenum where the air-fuel mixture is injected. They are powered in phase by the same amplifier and can acoustically excite the flame externally at the selected frequency.

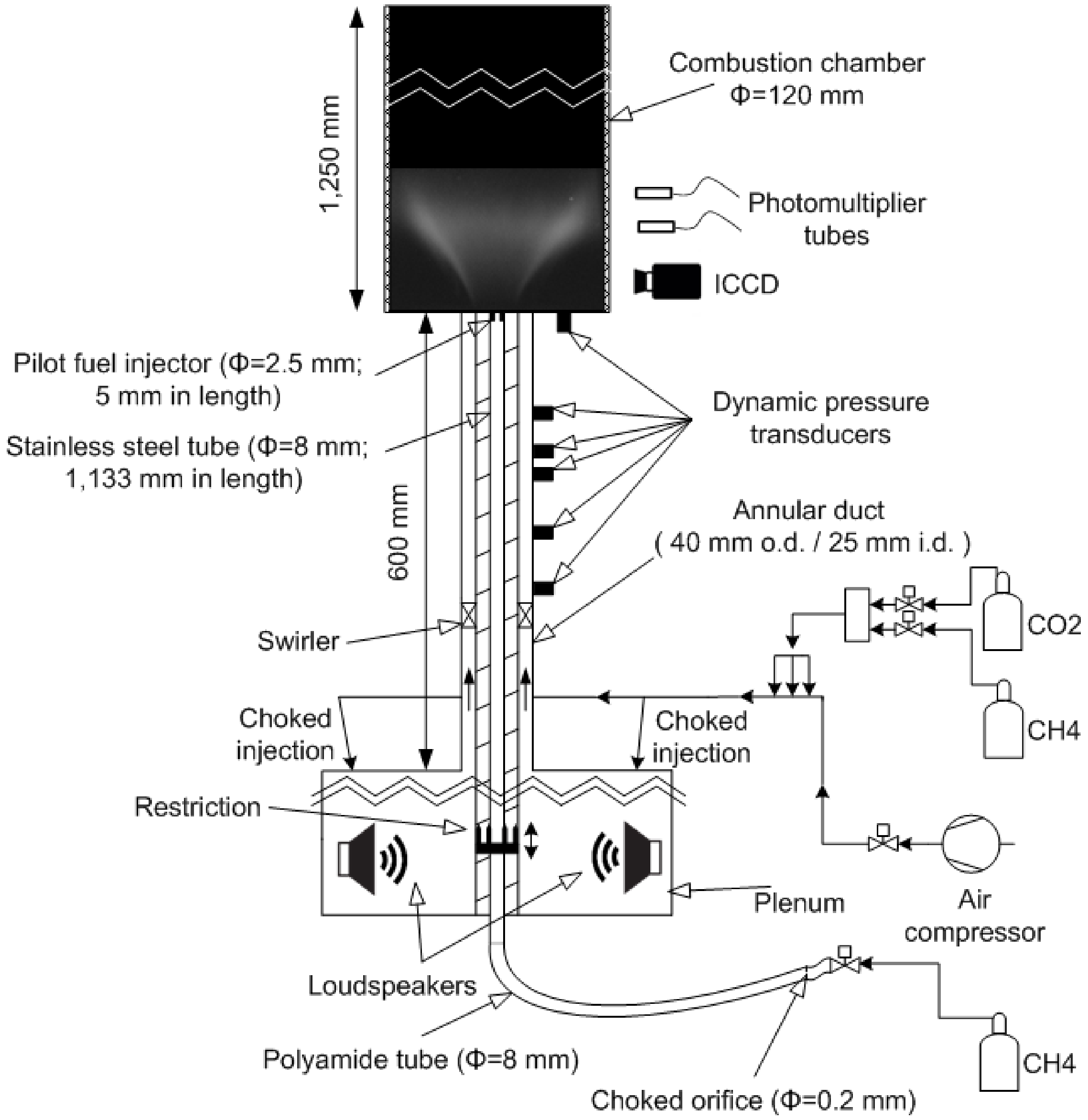

Fig. 3.6. Experimental rig and instrumentation used

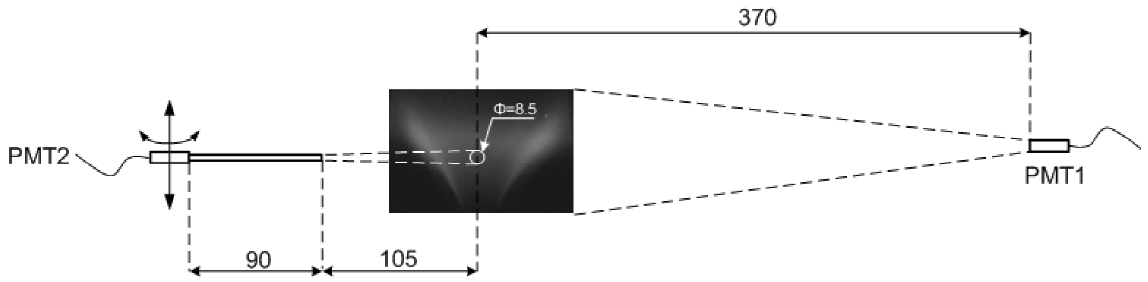

Fig. 3.7. Location of the two PMTs relative to the flame. All dimensions in mm

3.2.3 *Test methodology*

Fuels and operational conditions

As mentioned before, this work deals with 3 different fuels: pure methane and two mixtures of CH_4 and CO_2 (85-15% and 60-40% by volume for CH_4 and CO_2, respectively), which represent two possible blends of biogas [13]. From now on, they will be designated as biogas (85-15) and biogas (60-40), respectively.

The standard applied for this work is setting a constant mass flow for methane flames of 3 Nm^3/h (almost corresponding to a power of 30 kW), whereas the air flow is regulated in order to obtain the desired value of Φ.

The range of Φ values tested varied between 0.66 and 0.98, spanning from a point close to the lower stability limit of the burner to nearly stoichiometric conditions. It has been observed that the flame anchoring is not stable for Φ values lower than 0.66 and flame blowout could happen; this is the reason why no test have been performed for flames leaner than $\Phi=0.66$. Considering the cross sectional area of the annular duct and the flows defined, the mean injection velocity, $\bar{u}$, of the mixture into the combustion chamber is shown in Table 3.1.

Table 3.1. Φ values tested, and related values of $\bar{u}$, for pure methane flames (3 Nm^3/h)

Φ	0.98	0.92	0.86	0.80	0.72	0.66
$\bar{u}$ [m/s]	12.7	13.4	14.3	15.2	16.8	18.2

Since the analyses performed focus mostly on FTF, for biogas flames (both blends) it was decided to test the same Φ values as for pure methane and to keep constant, for each Φ, the $\bar{u}$ value obtained for CH_4. This guarantees that, in case of external forcing, the magnitude of u' induced is the same independently of the fuel studied.

Due to these two constraints, the amount of methane injected into the facility cannot be the same for the three fuels, and it also varies with Φ for biogas mixtures. Therefore, the power released by the flame differs from methane to biogas and this difference depends on the equivalence ratio; nevertheless, this variation results very slight, 7% in the worst case.

Measurement of FTF

The flame transfer function was measured, for a given operational condition, with the combustion chamber of 400 mm (shortest length). Since this combustion chamber produces stable conditions for every fuel and Φ tested, a possible natural instability does not overlap with external forcing and so the strong disturbances due to instabilities (or even limit cycles) reached with longer chamber lengths could be avoided.

The facility is acoustically forced through the loudspeakers, with frequency varying from 50 to 600 Hz with 10 Hz steps (above 600 Hz the flame does not show any response to external excitation, due to the low-pass filter behavior described before). For each frequency the forcing lasts 6 seconds, of which the central 4 are recorded, in order to discard possible transient effects due to changes in frequency. During this 4-second period, both the dynamic pressure and OH* chemiluminescence (proportional to heat release rate) are recorded by PTs and PMT1, respectively, sampling at 4 kHz, for a total of 16,000 data per frequency tested.

The input voltage to the amplifier is kept constant at 2.5 V for each frequency. However, the resulting forcing amplitude varies according to the frequency, due to the acoustic response of the facility. Nevertheless, it has been verified that the flame response is always within the linear regime.

For each frequency, the value of u' at the dump plane is estimated by applying the multi-microphone method [21] to the p' values collected from the five PTs installed along the injection duct. Both Q' and $\bar{Q}$ are obtained from the data recorded by PMT1; performing the fast Fourier transform of each dynamic variable for each frequency sampled (see Eq. (3.2)), the value of FTF is estimated. This procedure has been carried out for each operational condition mentioned before, and repeated tests were systematically performed to verify and consolidate the results obtained.

Acoustic stable/unstable condition

The procedure to record the natural stability condition of the facility is quite similar to the one adopted for FTF, except that in this case the facility is not externally excited. Four seconds are registered with both PTs and PMT1, acquiring at 4 kHz, in order to characterize the acoustic and flame fluctuations naturally occurring in the test rig.

These tests are more relevant in case of a natural instability, which occurred for combustion chambers longer than 400 mm, all of them inducing a more or less strong limit cycle (in general the magnitude registered increases with the combustion chamber length). For these tests, the PT located at the dump plane results particularly important, since it directly yields the magnitude and the frequency of the p' peak inside the combustion chamber. So, the variations of these magnitudes can be assessed by changing the operational conditions (e.g. fuel, Φ, restriction at the entrance, etc.) within the ranges attainable with the facility and the test matrix described above.

Acquisition of bandfiltered flame images

The ICCD camera is located at a suitable distance to include in its view angle the whole flame for each operational condition considered. The exposure time is set to 80 µs, much shorter than the period of the highest frequency of interest for this study (600 Hz, that is 1.67 ms); therefore the images acquired can be considered as instantaneous. OH* chemiluminescence images can be recorded either for natural conditions or externally exciting the facility through the loudspeakers at a certain frequency. The signal of the PT located at the dump plane is acquired simultaneously to the images acquisition, and the p' signal is synchronized with each frame acquired, in order to assign, during the post processing, each image to a certain interval within the pressure cycle (the p' cycle has been divided in 34 equal parts, ≈10.6°, and each image assigned to a slot; a minimum of 12 images per portion were recorded). A total of 500 images are acquired per operational condition, sufficient to obtain a dataset representative of the dynamics of the flame, even for the description of the flame evolution along the p' cycle.

3.3 Cross-correlation mapping method (CCM)

3.3.1 Introduction

Combustion plays a determinant role in the onset of a thermoacoustic instability by converting fluctuations in the feed flows into fluctuations in heat release rate, which finally act as a source of acoustic energy. Depending on the amplitude and delay in the flame response, and on the acoustic losses induced, the system may remain stable or the disturbance may grow to reach a limit cycle. In linear regime, this dynamic behavior is quantified in terms of the flame transfer function, FTF, which expresses the global response of a flame to a given perturbation (injection and/or equivalence ratio, depending on the particular case). Since this work deals with perfectly premixed flames, the following analysis will be focused on the flame response to u'.

Due to its major importance in thermoacoustic analyses, a number of studies have been dedicated to better understand the flame response, which, for the most common case of a premixed, V-shaped flame, coincide in that it presents a low-pass filter behavior in gain (G) and a linear trend in phase (φ) [24, 26, 29-33]. However, besides these two general and well established trends, the information regarding the FTF formation is still a matter under careful investigation.

The global response of a flame is the combined result of the dynamic response of all flame regions, each one presenting a different magnitude and phase. Therefore, the bulk value of Q' could include widely different contributions: from some flame portions which oscillate in phase with Q', supporting the final global oscillation, to other ones which could act in an opposite way, damping the response to an acoustic input. A proper assessment and interpretation of the local response at the different flame regions will contribute to better understand the phenomena ruling the flame dynamics and to gain insights into the FTF characteristics.

Local details are lost in global flame signals, so some kind of spatially-resolved information is needed to analyze the contribution of each flame area to the global dynamics; for that purpose, flame images appear to be a most valuable tool. Furthermore, the proportionality between the instantaneous heat release rate and the radiation emission at certain wavelengths (e.g. CH* or OH* peaks) [33, 62-64] allows investigating locally the heat fluctuation generated by acoustic inputs. However, the process to extract from chemiluminescence images reliable information on the effective contribution of each flame area to the global response is not so obvious.

Various methods for the post processing of bandfiltered flame images can be found in the literature to assess the flame dynamics. The most simple (and common) approaches consist in the use of time-averaged images, either line-of-sight or Abel-deconvoluted (see, e.g., [32, 33, 56, 66, 67]), or the standard deviation of the intensity recorded [68-71]. Also, more sophisticated methods have been employed, such as the phase-locking of the chemiluminescent images, in order to analyze the flame dynamics along a cycle (p' is normally taken as a reference signal) [32, 37, 56, 61, 71-73], Rayleigh index maps [74-77], to assess the contribution to the acoustic energy release of each flame zone, or flame maps resulting from the fast Fourier transform (FFT) of each pixel signal acquired along the images recording [66, 78]. All these techniques have been used to gain insight into the flame dynamics, but in the author's opinion, they do not properly assess the actual contribution of each flame zone to the global flame response and, hence, to the FTF. A more in-depth discussion can be found in [45].

In this work, a novel processing of chemiluminescence images, so called *cross-correlation mapping method* (CCM), has been proposed and applied to a broad range of fuels and combustion conditions in the experimental facility described above. A preliminary version of the method was described in [79, 80], but none of those two works provide a detailed analysis and physical interpretations of the meaning of cross-correlation maps. Paper 1 [45] of this compendium performs a comprehensive analysis of the information contained in CC maps and how useful they are to assess the global flame dynamics. The cross-correlation maps were demonstrated to be directly related to meaningful FTF parameters and to the actual contribution of different flame regions to the final flame response. When applied to a broad range of flames, the experimental results showed very good match with the patterns expected from theoretical considerations. The final maps obtained clearly reveal the dynamic phenomena generated by the acoustic excitation, highlighting the usefulness of CCM for thermoacoustic analyses.

Paper 2 [46] consolidates some interpretations postulated from the CCM analysis performed in Paper 1. To do so, local FTF have been measured and compared with the indirect conclusions obtained in [45]. Also, further insight into flame dynamics can be gained from some variables which can be deduced from CC maps; in particular, the characteristic convective length of the flames,

L (which will be defined later in this chapter) was estimated, as an example of a practical application of CCM to relate local and global characteristics of the flame dynamic response.

Both studies focus not only on pure methane flame, but also on biogas ones. On the one hand, this analysis proves that CCM is applicable to different fuels; on the other hand, these two papers are, to the author's knowledge, the first example in which the FTF of biogas flames is shown and analyzed, in comparison with pure methane ones.

The objective of this section is to summarize the CCM methodology and the main findings of Paper 1 and Paper 2; for further details, both works can be consulted in Section 4.

3.3.2 Theoretical formulation of CCM

FTF has been already defined in Eq. (3.2) as a function of the angular forcing frequency ω_f. In the frequency domain, it can also be defined in terms of a gain, G, and a phase, φ.

$$FTF(\omega_f) = \frac{\hat{Q}(\omega_f)/\bar{Q}}{\hat{u}(\omega_f)/\bar{u}} = G(\omega_f) \cdot \exp\left[-i\varphi(\omega_f)\right] \tag{3.3}$$

In the temporal domain and considering a harmonic oscillation in time for the injection velocity u', as in Eq. (3.4), the flame response, Q', can be obtained by applying the gain and the phase for the value of ω_f considered (Eq. (3.5))

$$u'(t) = u'_0 \cdot \cos(\omega_f t) \tag{3.4}$$

$$Q'(t) = \frac{u'_0}{\bar{u}} \cdot \bar{Q} \cdot G(\omega_f) \cdot \cos\left[\omega_f t - \varphi(\omega_f)\right] \tag{3.5}$$

Real turbulent flames can exhibit, locally, heat fluctuations not related to the forcing frequency, ω_f, but to other local phenomena (e.g. turbulence, wobbling, etc.). So, heat release rate fluctuation at a generic position x, Q'_x, can be split in two contributions (Eq. (3.6)), one oscillating with the forcing frequency ω_f (designated as Q'_{x,ω_f}) and the other one associated with other phenomena occurring at different frequencies (generically ω_j), indicated as Q'_{x,ω_j}.

$$Q'_x(t) = Q'_{x,\omega_f}(t) + Q'_{x,\omega_j}(t) \tag{3.6}$$

The dynamic response at point x due to the forcing frequency can be expressed in terms of a local flame transfer function, $\mathrm{FTF_x}$ (characterized by gain G_x and phase φ_x: $FTF_x(\omega_f) = G_x(\omega_f) \cdot \exp\left[-i\varphi_x(\omega_f)\right]$)

$$Q'_{x,\omega_f}(t) = \frac{u'_0}{\bar{u}} \cdot \bar{Q}_x \cdot G_x(\omega_f) \cdot \cos\left[\omega_f t - \varphi_x(\omega_f)\right] \tag{3.7}$$

The final, global heat release fluctuation, Q', is the combined result of the contributions from each single flame zone, Q'_x. In these local contributions, the magnitude of each local oscillation is not the only characteristic to be taken into account; the level of synchrony of each flame zone with respect to the bulk fluctuation must also be considered to extract the part of Q'_x actually contributing to Q'. The cross-correlation method, which is based on Eq. (3.8), represents a simple yet suitable method to assess this contribution. It is calculated as the cross-correlation of the variables $Q'(t)$ and $Q'_x(t)$ for zero time lag, averaged over a length of time, T, much longer than the period of the forcing signal. In Eq. (3.8), Q'_x has been split in the two terms defined in Eq. (3.6).

$$Q' * Q'_x = \frac{1}{T}\int_0^T Q'(t) \cdot Q'_x(t)dt = \frac{1}{T}\int_0^T Q'(t) \cdot Q'_{x,\omega_f}(t)dt + \frac{1}{T}\int_0^T Q'(t) \cdot Q'_{x,\omega_j}(t)dt \tag{3.8}$$

The last integral is the average product of a signal at a defined frequency, $\boldsymbol{\omega_f}$, with other ones which oscillate at different frequencies. If averaged over a sufficiently long period of time, this integral goes to zero. This is a first, important feature of CCM: it filters out the spurious contributions that could appear in the local heat release oscillation.

On the other hand, the first term is the averaged integral of two signals oscillating at the same frequency, so the final result will not be null. Rewriting the global and local heat release fluctuations in terms of the global and local FTF, the following expression is obtained:

$$\begin{aligned} Q' * Q'_x = \frac{1}{T}\int_0^T \left(\frac{u'_0}{\bar{u}}\right)^2 &\cdot \bar{Q} \cdot \bar{Q}_x \cdot G(\omega_f) \cdot G_x(\omega_f) \\ &\cdot \cos\left[\omega_f t - \varphi(\omega_f)\right] \cdot \cos\left[\omega_f t - \varphi_x(\omega_f)\right] dt \end{aligned} \tag{3.9}$$

The trigonometric identity $2 \cdot \cos(a) \cdot \cos(b) = \cos(a-b) + \cos(a+b)$ can be used to reformulate Eq. (3.9). Considering that the second term of this identity also vanishes in the integration for a sufficient period of time, the final result is expressed in Eq. (3.10).

$$Q' * Q'_x = \frac{1}{2}\left(\frac{u'_0}{\bar{u}}\right)^2 \bar{Q} \cdot \bar{Q}_x \cdot G(\omega_f) \cdot G_x(\omega_f) \cdot \cos\left[\varphi_x(\omega_f) - \varphi(\omega_f)\right] \tag{3.10}$$

The function $Q' * Q'_x$ can then be normalized by the average heat release rates with all space-independent parameters grouped in a lumped constant, $K(\omega_f)$, to give:

$$q' * q'_x = \frac{Q' * Q'_x}{\bar{Q}_x \cdot \bar{Q}} = K(\omega_f) \cdot G_x(\omega_f) \cdot \cos[\varphi_x(\omega_f) - \varphi(\omega_f)] \tag{3.11}$$

$$K(\omega_f) = \frac{1}{2}\left(\frac{u'_0}{\bar{u}}\right)^2 \cdot G(\omega_f) \tag{3.12}$$

The function $q' * q'_x$ is, then, proportional to the local gain, G_x, but it also depends on the synchronism between the global and the local fluctuations, that is, on the difference between the local and global phases. In particular, an in-phase oscillation between Q' and Q'_x, so $\varphi_x(\omega_f) = \varphi(\omega_f)$, means that the heat release fluctuation in this area contributes entirely to the global response of the flame, whereas the flame parcels in which $\varphi_x(\omega_f) - \varphi(\omega_f) = \pi$ have a damping effect on the global fluctuation, and the flame zones in which $\varphi_x(\omega_f) - \varphi(\omega_f) = \pi/2$ do not contribute at all to the global FTF. So, $q' * q'_x$ describes exactly what was searched for, that is, the effective contribution of each region of the flame to its global dynamic response.

In order to apply the method to a series of chemiluminescence frames, Eq. (3.8) should be transposed to the finite domain of the pixels composing the bandfiltered images of the flame. Assuming that the intensity at pixel x, I_x, is proportional to local heat release rate, Q_x (both are depth-integrated values), Eq. (3.13) can be applied to obtain cross-correlation (CC) maps from experimental data, where $i' * i'_x$ denotes the value of $q' * q'_x$ as estimated from chemiluminescence images.

$$i' * i'_x = \frac{\sum_{j=1}^{N_{im}} \left(I'_x \cdot \sum_{k=1}^{N_{px}} (I'_x)_k \right)_j}{N_{im} \cdot \bar{I}_x \cdot \bar{I}} \tag{3.13}$$

$\bar{I}_x$ and I'_x represent, respectively, the mean and fluctuating component of the intensity collected at pixel x, while $\bar{I}$ is the mean OH* intensity for the whole flame, calculated by summing up all pixels of the mean, line-of-sight integrated map. The calculations are performed over N_{im} instantaneous images, each one consisting of N_{px} pixels.

In case the FTF studied presents some particular functional form, further details may be gained. For the cases studied, the n-τ model [21] can suitably fit the FTF obtained, in particular due to the linear trend observed in the measured FTF phase. In fact, this linear evolution of the phase with respect to frequency can be expressed as $\varphi(\omega_f) = \omega_f \cdot \tau$, being τ a characteristic time delay between the input (u') and the output (Q') of the FTF.

Therefore, both global and local FTF can be defined in terms of local (n_x-τ_x) and global (n-τ) parameters of the model, being $n(\omega_f) \equiv G(\omega_f)$, $n_x(\omega_f) \equiv G_x(\omega_f)$, $\varphi(\omega_f) = \omega_f \cdot \tau$ and $\varphi_x(\omega_f) = \omega_f \cdot \tau_x$. Thus, Eq. (3.11) can be rewritten as follows:

$$q' * q'_x = K(\omega_f) \cdot n_x(\omega_f) \cdot \cos[\omega_f \cdot (\tau_x - \tau)] \tag{3.14}$$

Sensitive time lags can be related to characteristic velocities and lengths. Suitable values for characteristic velocities can be proposed based on the coupling mechanisms involved in the flame dynamics (some examples could be the speed of sound, the velocity in the injection duct or some relevant velocity of the gases along the flame, depending on the particular case).

On the contrary, the identification of a length which suitably defines the time lag associated to FTF is not so obvious. As a matter of fact, in general at least three different dimensions are needed to describe an FTF of a turbulent, perfectly premixed, swirling flame (two concerning the flame and one representative of the swirl effect [27, 71, 81]). The analysis of phase-locked images of the flames studied in Paper 1 excluded the influence of the swirler in the dynamics shown (see [45]), so the attention of the study could focus just on the flame. However, even focusing just on the flame characteristic length L, its definition not always coincides among the works that have dealt with this theme. In fact, L has been defined by some authors as the total flame length [21] or as different fractions of it [20, 24, 31, 56]; some works identify L as the distance at which the maximum heat release occurs [67, 78, 82-84] while others relate it to the center of mass of the flame [61, 81, 85].

In this context, CC maps could represent a suitable alternative to define a characteristic length of the flame related to the FTF time lag τ, being this latter explicitly included in CC formulation (Eq. (3.14)). τ can be estimated as L/V, and the same can be applied for the local time delay ($\tau_x \sim L_x/V_x$); assuming that the convective velocity does not sensibly vary along the jet path ($V \sim V_x$), it holds that $\tau_x/\tau \sim L_x/L$. So, the cosine argument of Eq. (3.14) can be reformulated as follows:

$$\cos[(\omega_f \cdot (\tau_x - \tau)] = \cos\left[\omega_f \cdot \tau \cdot \left(\frac{L_x}{L} - 1\right)\right] \tag{3.15}$$

This last equation leads to conclude that the CC maps should exhibit oscillations, at least along the jet path, with a wavelength inversely proportional to ω_f. The results section will show that this conclusion is completely supported by the experimental results; moreover, CC maps will be used to estimate the characteristic flame length L, and this estimation will be further validated by local measurements. Also, characteristic magnitudes for pure methane and biogas flames (such as FTF time delay or convective lengths) will be analyzed and compared.

3.3.3 Test matrix

Paper 1 and Paper 2 analyze perfectly premixed, V-shaped flames of pure methane, biogas (85-15) and biogas (60-40) (see Section 3.2.3); the equivalence ratios tested for each blend are Φ=0.98, 0.86 and 0.72.

For each operational condition, the following experiments have been conducted:

- Measurement of FTF;
- Recording of OH* filtered images of flames with external excitation.

The general details of the experimental methods used can be found in Section 3.2.3. In Paper 2, also local FTFs have been reported for specific flame areas. The method used is exactly the same applied for global FTF, but using the PMT2 (see Fig. 3.7) to record local heat release fluctuations. This analysis has been carried out for a pure methane flame at Φ=0.86. The location of the areas analyzed is marked in Fig. 3.8, superimposed both on the Abel-inverted map of the flame (left) and on the normalized CC map (right). The axial and radial coordinates of each point (respectively indicated as H and R) are reported in Table 3.2.

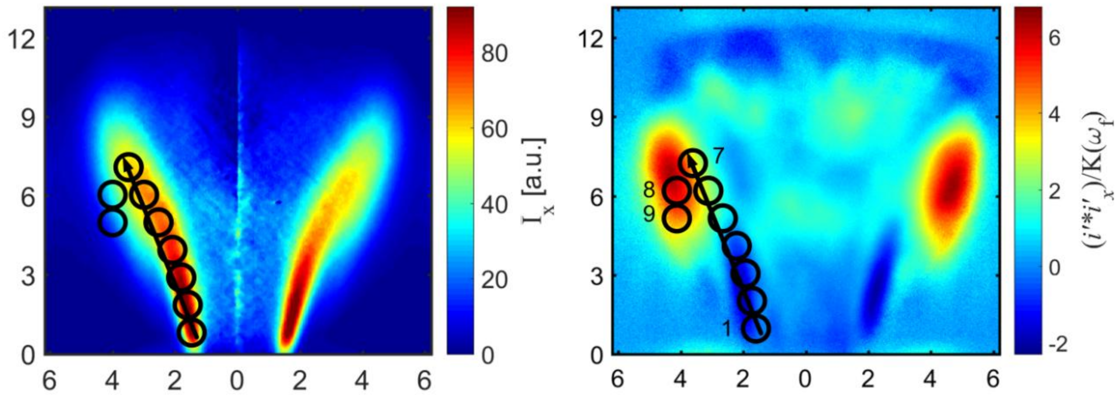

Fig. 3.8. Flame areas selected to measure local FTF, superimposed on an Abel-transformed map (left) and on a cross-correlation map (right). Coordinates in cm

Table 3.2. Axial and radial coordinates of the flame areas probed with PMT2

Point code	1	2	3	4	5	6	7	8	9
H [cm]	1.0	2.0	3.0	4.0	5.0	6.0	7.0	6.0	5.0
R [cm]	1.7	1.8	1.9	2.2	2.7	3.1	3.7	4.1	4.1

The flame parcels analyzed lay either on the flame sheet or on the peak areas highlighted in CC maps. The reasons behind the choice of the flame regions will be explained in Section 3.3.4; nevertheless it can be observed how the areas selected include all the flame regions highlighted by the CC method.

The analysis of both studies focus on the CCM post-processing of bandfiltered images of flames externally excited through the loudspeakers. The selected forcing frequencies are f_{ex}=90, 150, 230, 400 Hz (the last one has been analyzed only in Paper 1). For all the excitation frequencies, the forcing amplitude has been kept within the linear range of flame response [45].

3.3.4 *Results and discussion*

Analysis of the dynamics of methane and biogas flames

The FTF obtained for the three blends studied (from left to right, respectively, methane, biogas (85-15) and biogas (60-40)) are shown in Fig. 3.9. For each blend, three curves are represented, each one corresponding to one value of Φ.

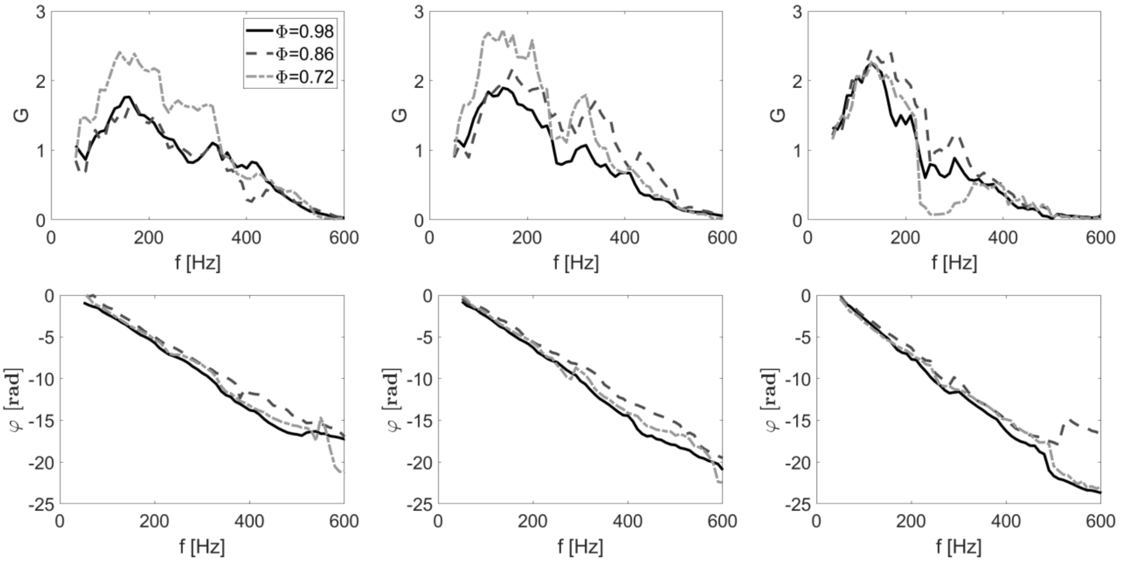

Fig. 3.9. FTF gain (top row) and phase (bottom row) for each blend and Φ tested. Methane: left; biogas (85-15): center; biogas (60-40): right

The main features identified in the literature (see Section 3.1.2) for the FTF of perfectly-premixed, V-shaped methane flames are confirmed for the tests performed. In fact, all the gains obtained present low-pass filter behaviors and the phases are nearly linear with respect to the forcing frequency.

A reduction in Φ leads, generally, to an increase in the FTF magnitudes, at least in the frequency range where the flames result more responsive (between 50 and 400 Hz).

The general features identified for methane flames are confirmed when CO_2 is added to the air-fuel mixture. In fact, the low-pass filter behavior can be clearly observed for the biogas flames tested; also, gain values are in general higher, at the same frequency, for biogas than for pure methane, which means that the effects of CO_2 addition are similar to the ones observed by increasing the air dilution.

The same happens for the phase slope, which presents an almost linear trend for both pure methane and biogas flames, and so the response can be well described by a constant time delay, τ. The values of τ calculated for each operational condition tested are represented in Fig. 3.10. The variation of the time delay with Φ is quite similar for the blends tested, displaying a minimum at Φ=0.86; blending with CO_2 leads to an increase of the time delay, especially for biogas (60-40).

The sudden drop in the gain at 250-300 Hz observed for biogas (60-40) at Φ=0.72 is due to a change in the flame configuration for this operational condition; in fact, the acoustic excitation in this case induces a change in the flame shape, passing from a typical V-shape to a "trumpet" configuration [58]. This shape change only affects the gain values, whereas no major effects can be appreciated in the phase.

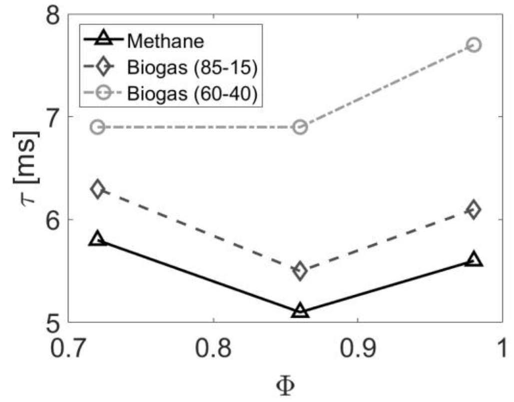

Fig. 3.10. Evolution of the time delay, τ, for the operational conditions tested

In order to better understand the FTF results obtained, and in general the effects induced on the flame by both the air flow variation and the introduction of CO_2 into the blend, some examples of average, line-of-sight maps are reported in Fig. 3.11 for some selected tests.

Along the top row, the change in flame structure due to air addition is displayed; as the flame becomes leaner, it expands along both the radial and the vertical dimensions. Similar variations can be appreciated in the bottom row, where the equivalence ratio is kept constant and CO_2 is added. This observation is consistent with the observation pointed out above for the FTF: CO_2 effects are primarily related to diluting the air-fuel mixture, as it happens in cases with a higher air excess. However, dilution with CO_2 seems to be more effective, since higher air quantities are needed to induce the same effects on the flames. For instance, the leanest methane flame, Φ=0.72, exhibits a flame pattern similar to the case with 40% CO_2 and Φ=0.86; this corresponds to an addition of almost 7 Nm^3/h of air in the first case versus less than 2 Nm^3/h of CO_2 in the second one. This can be also appreciated in the variation of time lags shown in Fig. 3.10 (this analysis will be developed in detail later).

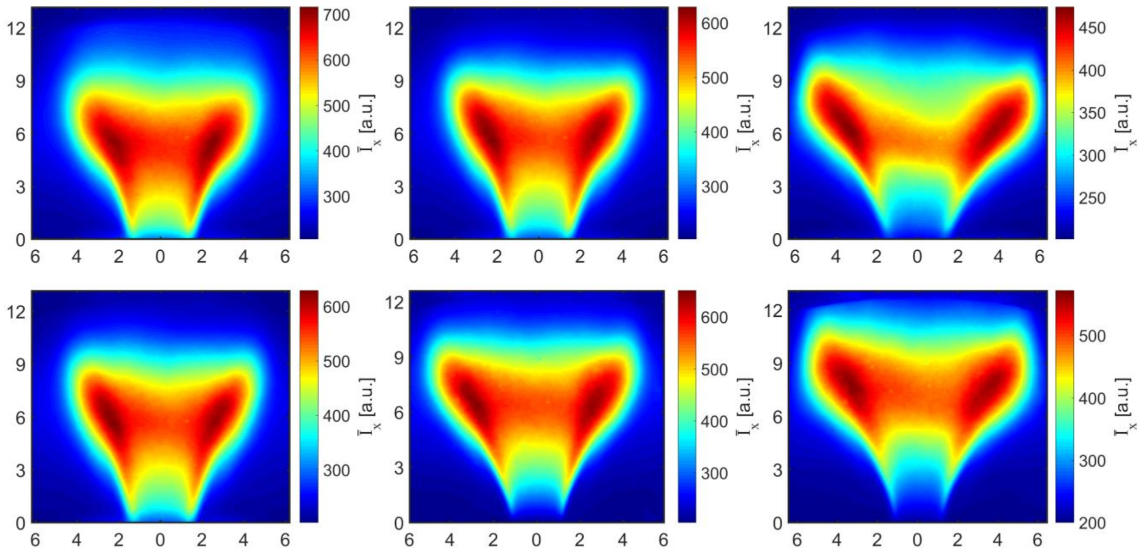

Fig. 3.11. Average images of depth-integrated OH chemiluminescence. Top row: pure methane flames at Φ=0.98 (left), Φ=0.86 (middle), Φ=0.72 (right). Bottom row: flames at Φ=0.86 of pure CH_4 (left), CH_4-CO_2=85%-15% (middle), CH_4-CO_2=60%-40% (right)*

When externally excited, the dynamic behavior of the flames studied is dominated by the vortex shedding phenomenon. This mechanism has been described in many previous works (e.g., [19, 23, 24, 31, 33, 56, 69]) as one of the main causes of instability in lean premixed flames.

As an example, Fig. 3.12 shows Abel-deconvoluted, phase-locked maps (p' used as a reference signal, 45° steps are represented) of a pure methane flame at Φ=0.98, externally forced at 230 Hz. The maps highlight that the heat fluctuation is produced in the upper region of the flame, which starts at 135°, where the downstream part of the flame wraps itself towards the outer zone. This rolled zone increases its intensity and dimensions and moves downstream along the cycle, until 315°. Here the wrapped structure gradually disappears and the flame tip recovers the original V shape and, after 90°, the cycle starts again.

This motion is due to the shedding of coherent macrostructures at the dump plane, which move downstream along the flame. These vortices impinge on the outer part of the flame, dragging gas parcels from the reaction layer along their rotating direction. At the flame basis, the vortices dimension is still modest, and the effect is not so apparent. When moving downstream, vortices grow in size and strength, but neighbor vortices obstruct the dragging of gases, due to their equal rotating direction. The obstruction disappears when the coherent macrostructures reach the flame tip, which, then, winds around the vortex kernel when it reaches the downstream part of the flame, creating the flapping movement observed, also called vortex roll-up (more details about this dynamics can be found in [24]). The discussed dynamics is well captured and represented by the CC method, as it will be shown in the following analysis.

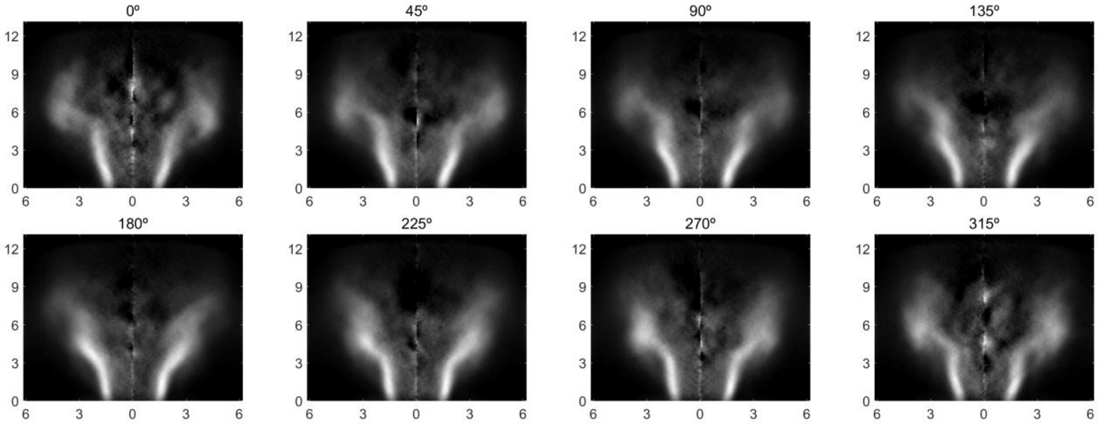

Fig. 3.12. Abel-deconvoluted maps of the heat released (averaged within 10.6^o intervals) along the pressure cycle at Φ=0.98, f_{ex}=230 Hz. Axes scale in cm

Cross-correlation maps

In Fig. 3.13-a, an example of CC map is shown for a pure methane flame at Φ=0.98 and forced at 230 Hz. It was calculated by applying Eq. (3.13) to a set of 500 bandfiltered images recorded for this operational condition. This map displays a sequence of spots, which alternate positive and negative values and grow in intensity from the dump plane to the flame tip. They are disposed along the flame sheet and, to better assess their position, in Fig. 3.13-b the flame region has been superposed (shadowed area) on the CC map. The combustion area has been identified by the Abel-transformed map of the operational condition analyzed, considering just the pixels with intensities greater than 45% of the peak value; the white, solid line indicates the center of the shadowed area.

The zones highlighted by the CC map are located on the outer edge of the flame sheet, and they gradually move outwards, with the peak laying almost completely outside the flame area. The relative position of the spots highlighted in CC map is considered perfectly consistent with the dominant dynamics of the flame, that is, the vortex shedding phenomenon. Moreover, it indicates that the heat release fluctuations occur mostly outside the average flame area, hence mean flame maps are not an appropriate means to assess dynamic variables associated with the flame.

A distinctive feature of the CC maps with respect to other flame representations is the presence of negative areas, which indicates zones fluctuating out-of-phase with respect to the bulk oscillation. So, these regions tend to damp the oscillation and to diminish the generation of acoustic energy from other flame parcels oscillating in phase with the global heat release rate (positive zones of the CC map). The combination of all, positive and negative, contributions builds up the global Q' signal and, hence, the FTF. Fig. 3.13-a shows positive and negative spots alternating along the outer part of the flame sheet. This oscillation can be better observed in Fig. 3.13-c, where the solid line represent the evolution along the axial distance (L_x) of CC values integrated along the width of the shadowed area represented in Fig. 3.13-b. Both X and Y axes have been normalized, the former with respect to the position of the fluctuation peak and the latter considering the maximum of the fluctuation obtained. Once this normalization has been performed, the similarity between the experimental pattern and the one obtained through Eq. (3.15), represented by a gray, dashed line, results remarkable, supporting the validity of the theoretical formulation proposed above and, hence, the physical interpretation of the cross-correlation maps.

The continuous increment of the amplitude of the experimental oscillation can be ascribed, according to Eq. (3.11), to an almost monotonic increment of the local gain, G_x, since $K(\omega_f)$ is a constant for a given operational condition. Moreover, the location of the "characteristic flame length" L can be easily determined, according to these results, by the location where the $i' * i'_x$ peak occurs. The observed match between the experimental results and the theoretical formulation and the intuitive interpretation of the CC method are thought to make it a valid option to scrutinize the actual role of the different flame regions in the global flame response and, hence, in shaping the global FTF. As it was mentioned, similar information cannot be obtained from the maps derived from chemiluminescence images normally used.

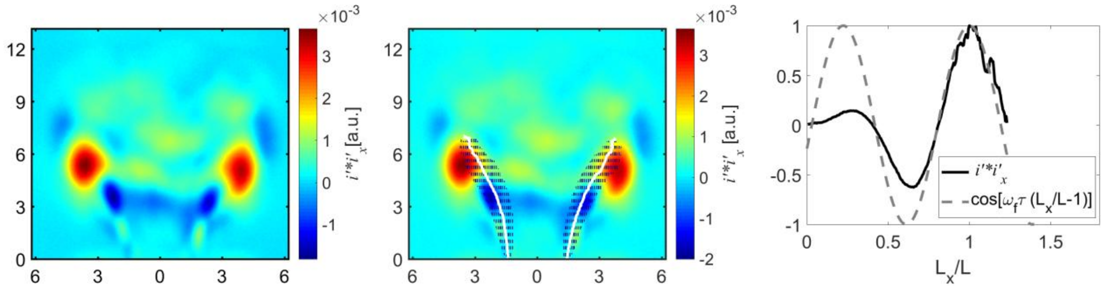

Fig. 3.13. a) CC map for a methane flame at Φ=0.98 and forced at 230 Hz; b) Superposition of the relative combustion zone (shadowed area), as identified from the respective Abel map, on the CCM map (the white, solid line indicates the center of this area); c) comparison between $i' * i'_x$ values along the shadowed area in (b) and the theoretical curve (dashed line) predicted from Eq. (3.15) for 230 Hz and τ=5.6 ms

The images recorded for the methane flames studied have been post-processed according to the cross-correlation method and the results are shown in Fig. 3.14. The $i' * i'_x$ values displayed in the maps have been normalized by $K(\omega_f)$, as defined in Eq. (3.12), calculated for each map of Fig. 3.14 as a function of the global FTF gain and of the normalized velocity fluctuation for the forcing frequency considered. This is an alternative way to analyze CC maps which requires additional data (FTF, $u'_0/\bar{u}$) with respect to a simple sequence of bandfiltered images, but it also provides additional information as discussed below.

In fact, considering Eq. (3.11), this normalization yields:

$$\frac{i' * i'_x}{K(\omega_f)} \approx \frac{q' * q'_x}{K(\omega_f)} = G_x(\omega_f) \cdot \cos[\varphi_x(\omega_f) - \varphi(\omega_f)] \tag{3.16}$$

The right-hand side of Eq. (3.16) indicates that the normalized values obtained in CC maps represent the local FTF gain modulated according to the relative phase between the global and local heat fluctuation. Therefore, the normalized CC map can be interpreted as the actual contribution a flame parcel gives to Q', so that local values of $(i' * i'_x)/K(\omega_f)$ are the "effective local gain".

The patterns displayed in Fig. 3.14 for the tests carried out at 90, 150 and 230 Hz are similar to the one observed in Fig. 3.13, with positive and negative spots alternating along the flame sheet which grow in magnitude from the dump plane to the flame tip. The cycles described grow in number with the forcing frequency, in accordance with what was predicted when developing the theoretical formulation for $n - \tau$ model (see Eq. (3.15)).

Peak values in the range between 5 and 13 have been obtained, always surrounding the flame tip, which indicate a very high local contribution of these flame portions to the global FTF. For all cases these values are greater than the global gain obtained (G between 1 and 3 for the frequencies tested, see Fig. 3.9). This difference is easily explainable by considering that FTF is an average, weighed with $\bar{Q}_x$, of the local responses from all flame parcels, including those presenting values close to zero or even out-of-phase with the global one. Kim et al. [32] obtained analogous results, with local gains significantly higher than the global one, for CH_4-H_2 M-shaped flames.

As described before for the particular case shown in Fig. 3.13, the patterns obtained for all the cases tested are thought to be perfectly in line with the mechanism ruling the dynamics of the flame analyzed, that is, the vortex shedding phenomenon. The peak values identify the vortex roll-up area, which represents the zone mainly contributing to the global FTF formation.

The maps obtained by exciting the fames at 400 Hz do not show the oscillating pattern observed in the rest of the cases. This could be ascribed to the less responsive behavior of the flame to high frequencies (as demonstrated by the low values of G; see Fig. 3.9) and to the low u' reached for high frequencies, as explained in [45]. Since both G and u'_0 are included in the denominator of Eq. (3.16) (that is, $K(\omega_f)$), this magnifies the effect of the noise in CC maps, leading to noisy patterns with peak values > 15, probably unrealistic.

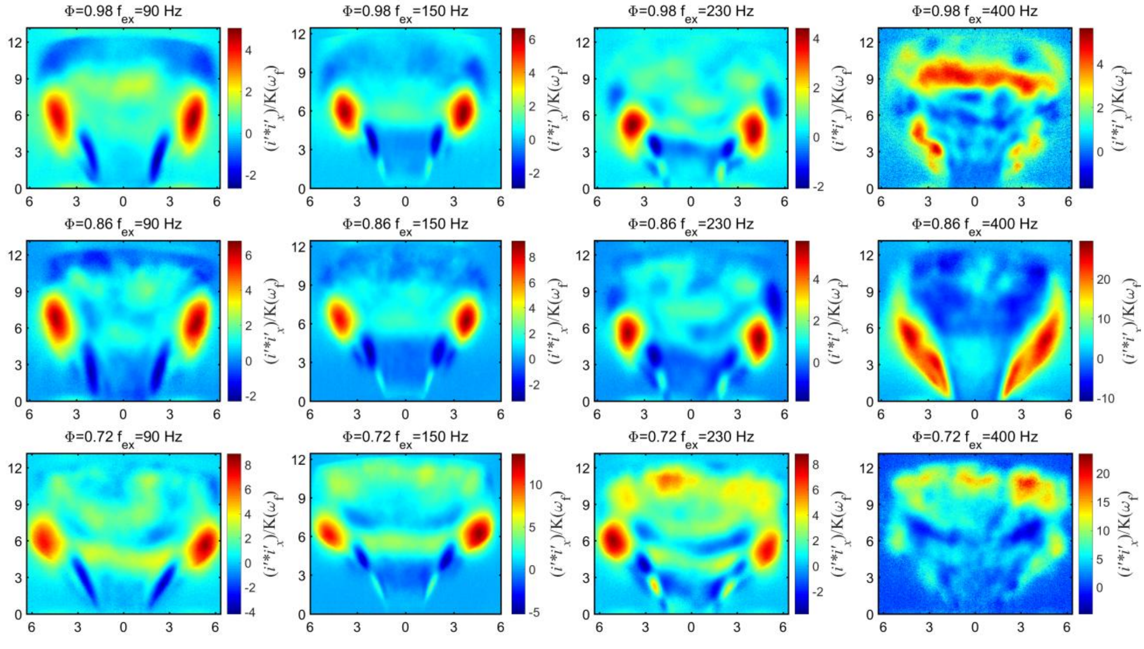

Fig. 3.14. Normalized CC maps, $(i' * i'_x)/K(\omega_f)$, for different equivalence ratios and forcing frequencies.

As mentioned before, the $(i' * i'_x)/K(\omega_f)$ values can be interpreted as the "local effective gain" of each flame parcel. However, this value does not inform about the absolute contribution of each zone to the global FTF, which should be calculated as a summation of each local FTF weighed with the mean value of the local heat release rate, $\bar{I}_x$ [32] (see Eq. (3.17)). This leads to an additional alternative formulation of the CCM method in terms of $(i' * I'_x)/K(\omega_f)$, obtained by multiplying $(i' * i'_x)/K(\omega_f)$ by the average local intensity, $\bar{I}_x$. Both magnitudes have different physical interpretations: $(i' * I'_x)/K(\omega_f)$ is a measure of the absolute contribution of a flame portion to the global FTF, whereas $(i' * i'_x)/K(\omega_f)$ is the "effective local gain", as defined in Eq. (3.16).

Some examples of $(i' * I'_x)/K(\omega_f)$ maps are represented in Fig. 3.15. Apart from a little contraction of the peak zones with respect to $(i' * i'_x)/K(\omega_f)$ maps, the general pattern is almost equal to the one observed in Fig. 3.14, since, for the cases analyzed, $\bar{I}_x$ is almost constant along the shear layer. So, the difference between the two representations, at least for the particular cases tested, is considered important for a quantitative analysis, but not relevant in terms of a qualitative assessment. However, this similarity is not thought to apply to the general case.

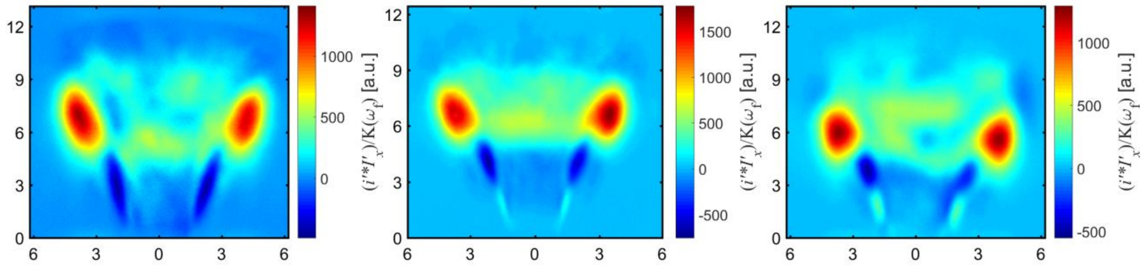

Fig. 3.15. $(i' * I'_x)/K(\omega_f)$ maps for methane flames at Φ=0.86 forced at 90 (left), 150 (middle) and 230 Hz (right)

The sinusoidal evolution of the CC values along the flame sheet (calculated as in Fig. 3.13-c) has been represented in Fig. 3.16 for all the tests performed. The curves show that the number of cycles increases with f_{ex}, as predicted if the CCM formulation is particularized for the $n-\tau$ model (Eq. (3.15)). Also, the oscillation amplitude increases along the flame length, until reaching a maximum near the tip of the flame, which is located at almost the same distance from the dump plane for all values of Φ.

These curves, and in particular their local maxima/minima, can be further analyzed in order to gain insight about the gain of local FTF, G_x or, better, n_x, since Eq. (3.15) is valid considering a description of both local and global FTF by an $n-\tau$ model. Local extrema satisfy the condition $\varphi_x(\omega_f) - \varphi(\omega_f) = k\pi$ (where k is an integer), and, hence, the cosine of Eq. (3.16) is equal to ±1. The maxima/minima of the curves represented in Fig. 3.16 are shown in Fig. 3.17

versus L_x; it can be seen how the values always increase with L_x, until they reach a maximum at L_x near the flame tip. This parameter was also determined from local FTF measurements in [32] for CH_4-H_2, M-shaped flames, with results very similar to those obtained here, only based on OH* chemiluminescence images.

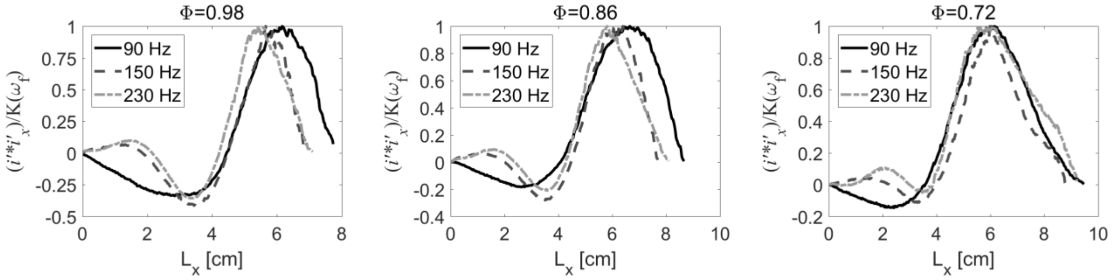

Fig. 3.16 Oscillations along the jet path for CC maps of Fig. 3.14

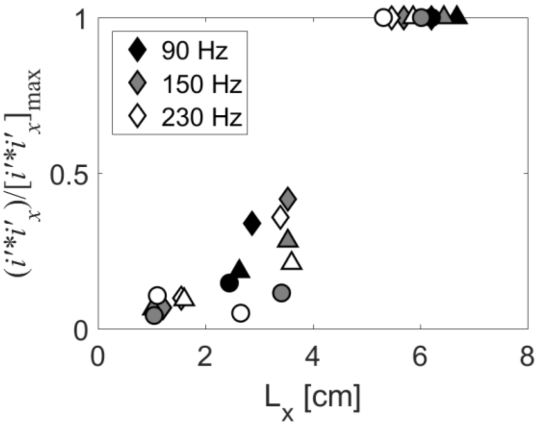

Fig. 3.17. Evolution of local maxima/minima of $(i' * i'_x)$ values (normalized with the respective peak value) along the flame axial distance. Symbols: (◊) Φ=0.98; (Δ) Φ=0.86; (o) Φ=0.72 – grey levels vary with f_{ex}, as indicated in the legend

CC processing has also been applied to biogas flames, obtaining very similar results to those shown up to now for pure methane flames; therefore, for the sake of conciseness, the analysis has focused on the results for pure methane. Some examples of biogas maps will be shown later on in this section.

The comparison performed between the experimental data collected and the theoretical formulation proposed about CC method leads to two main conclusions:

- Local FTF gain monotonically increases from the dump plane to the flame tip, at least in the low-medium frequency range;

- The characteristic flame length associated with the convective time lag normally found in the FTF can be determined from the location of the peak value in CC maps.

Also, it should be noted that the assessment of the "characteristic flame length" L (i.e. Eq. (3.15)) is based on two main hypotheses:

- The local FTF can be suitably described by an $n - \tau$ model;
- The "characteristic convective velocity" V of the flames studied can be considered constant along the flame sheet.

Local FTF measurement

In order to better assess the two conclusions mentioned above, and the related hypotheses behind them, local FTF measurements have been collected for specific flame regions. In Fig. 3.8 the points location on the flame maps is shown, while their absolute position is given in Table 3.2 in terms of axial, H, and radial, R, distances with respect to the dump plane and to the center line, respectively. These locations have been chosen, on the one hand, because they represent the zone highlighted by the CC method and, on the other hand, since they could provide experimental evidences directly related to the two conclusions inferred from the analysis of CC maps presented in the previous paragraphs.

In particular, points from 1 to 7 sweep the whole flame shear layer, from the dump plane to the flame tip. The local FTF obtained for these points are shown in Fig. 3.18, superposed to the global FTF (black, solid line) for the operational condition tested (pure methane flame, Φ=0.86).

Local gains, G_x, at the points located near the injection plane (1-3) display an almost flat evolution with frequency. Instead, points located farther downstream along the flame (5-7) present a low-pass filter behavior with gain peaking in the range 100-200 Hz, whereas point 4 represents the transition between those two distinct behaviors.

Consistently with what has been concluded from the analysis of CC maps, the local FTF gain gradually increases with the distance from the dump plane, at least in the frequency range in which the CC experiments have been performed (90 – 230 Hz). For higher frequencies, the local gain obtained at the downstream part of the flame decreases, presenting values comparable to those obtained at the base of the flame.

The observed increase in local FTF gain with H is considered consistent with the vortex shedding dynamics, which, as discussed above, is the governing phenomenon for the flames studied. Near the dump plane, the vortices are still small and their effects are rather modest; as they move downstream, they grow in dimension and strength, but also neighbor vortices mutually obstruct their dragging of burning gases, due to their equal rotating direction. This creates cusps and hollows on the flame edge, while at the flame tip there is no obstacle to the ingestion of gases by the vortex and the roll-up phenomenon happens (see [24] for a more detailed explanation). The higher the excitation frequency is, the smaller the macrostructures formed will be, so also their dragging force will diminish; this might be the reason why the local FTF develop low pass filter behaviors as the probed points approach the flame tip.

The phase of both the local and the global FTFs exhibits a linear trend with respect to the forcing frequency. The slope and, hence, the time delay increase with H, consistently with the observed flame dynamics, considering the convective displacement of the macrostructures from the injection to the flame tip. Also relevant, as discussed below, is the fact that the phase curve for the global FTF practically coincides with that of the local response at H=6 cm.

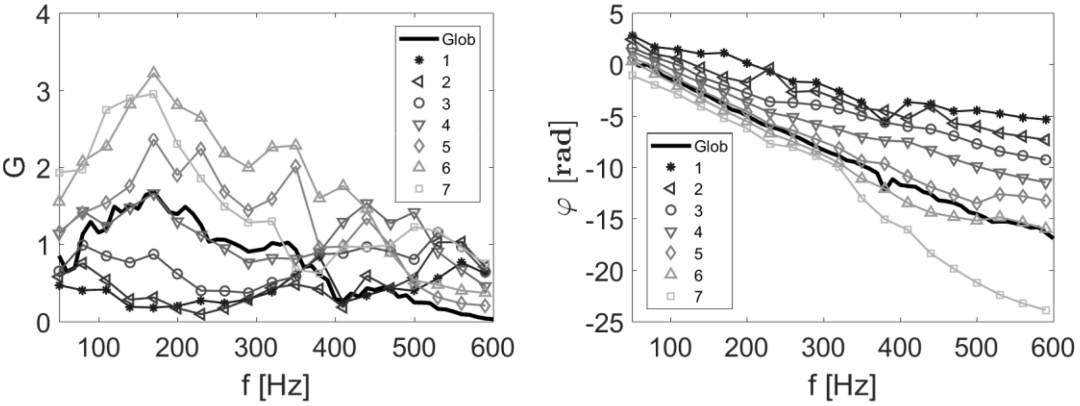

Fig. 3.18. Gain (left) and phase (right) of the global and local FTF measured at points 1-7 of Fig. 3.8 (pure methane flame, Φ=0.86)

The linear trends observed in all the local FTF's phases further support the analysis performed above on CC maps, since the application of $n-\tau$ model can be considered a suitable approach to describe the local flame transfer function obtained for the cases tested.

The evolution of the local time delays obtained for points 1-7 is depicted as a function of H in Fig. 3.19-left. The values obtained are grouped along a straight line, with τ_x at H=6 cm being almost equal to the global time lag measured. The linear trend obtained for τ_x indicates that considering a constant convective velocity along the flame sheet is a plausible assumption for the cases studied; in other terms, the equivalence $\tau_x/\tau \sim L_x/L$, applied to obtain Eq. (3.15), holds for the cases analyzed. Also, point 6 is located very near to the peak value in the CC map (see Fig. 3.8-right). Since the two main hypotheses formulated to carry out the CC analysis can be considered valid, the location of point 6 (H=6 cm) may be considered representative of the average convective length traveled by a perturbation until it generates a fluctuation in heat release rate; that is, $L \approx L_x$ at point 6.

The evolution of local gain with H is represented in Fig. 3.19-right for the three frequencies tested throughout this work: 90, 150 and 230 Hz. The three cases show a peak at point 6, with a shape very similar to the one presented in Fig. 3.17, confirming the good match between the evolutions extracted from the CC maps analysis and the ones obtained from direct measurements of local FTF.

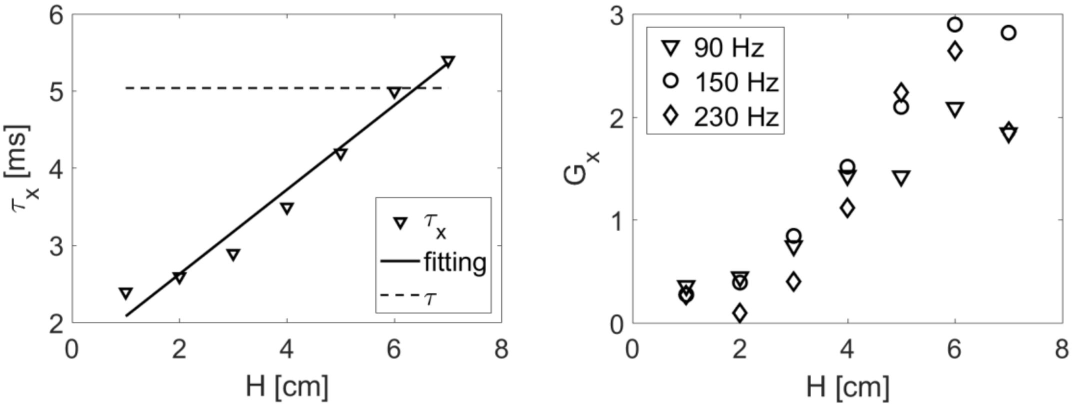

Fig. 3.19. Left: Variation of local time lag, τ_x,with the axial coordinate, H; right: evolution of local gain, G_x,as a function of H at f_{ex}=90, 150 and 230 Hz

The local FTF has been also measured at points 8 and 9, that is, in the core of the region of peak CC values where the dynamic activity is expected to be particularly strong. The gain and phase values are reported in Fig. 3.20, along with those obtained at points 5 and 6 (same height but located in the region of the flame shear layer) and the global FTF.

The slopes of the phases are very similar among these points and to those of the global FTF; this fact indicates that the area highlighted by the CC maps (vortex roll-up zone) can be considered representative of the global time lag obtained by an integral measure of the flame fluctuation. Still, some minor yet consistent differences can be seen between the two pairs of points located at the same height (6-8 and 5-9), with slopes that coherently evolve with H (steeper decay for points 6 and 8), while they result very similar between the pairs of points at the same heights.

The local FTF gains for points 8-9 present low-pass filter behavior, as the ones obtained for the downstream part of the flame along the shear layer (see Fig. 3.18), in line with the analysis presented above about the dynamics inferred at the upstream and downstream parts of the flame by the vortices impingement. Moreover, their magnitude is far above the values displayed in Fig. 3.18, with peaks around 7, clearly indicating the high sensitivity of this flame area to the dynamics induced by the vortices shed at the dump plane.

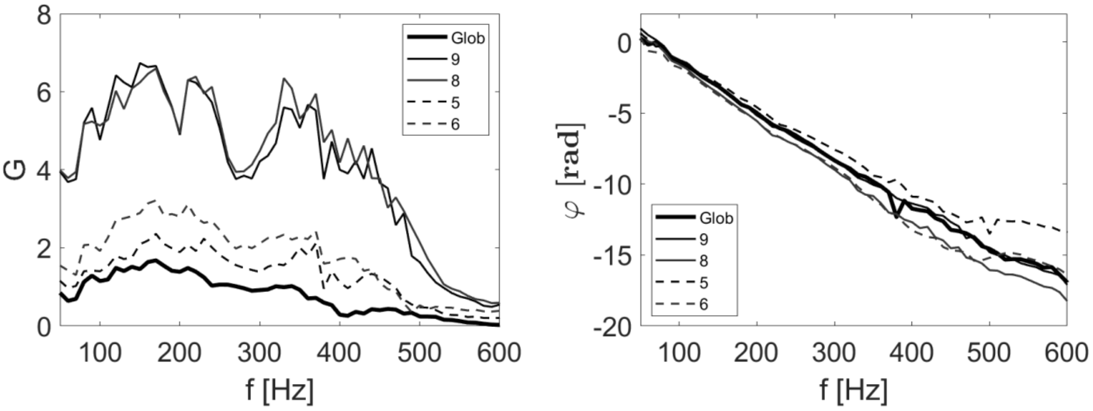

Fig. 3.20. Gain (left) and phase (right) of the global FTF (black line) and of the local ones measured both at points 9-10 (solid lines) and at 5-6 (dashed line)

At this point it is worth stressing that the high values of local gains do not necessarily mean that the vortex roll-up areas are actually the ones that contribute the most to the global FTF formation. In fact, as it has been highlighted above, the FTF is the weighed summation of local FTFs with the mean local heat release rate, $\bar{Q}_x$ [38, 45, 86].

$$FTF = \sum FTF_x \frac{\bar{Q}_x}{\bar{Q}} \tag{3.17}$$

Applying Eq. (3.3) to both local and global FTF and re-arranging Eq. (3.17), the following expression for G holds:

$$G = \sum G_x e^{i(\varphi_x - \varphi)} \frac{\bar{Q}_x}{\bar{Q}} \tag{3.18}$$

Since G is a real number, Eq. (3.18) can be simplified to

$$G = \sum G_x \cos\left(\varphi_x - \varphi\right) \frac{\bar{Q}_x}{\bar{Q}} \tag{3.19}$$

Equation (3.19) has been applied to the values obtained for points 1-9 and compared with the global FTF; the result is shown in Fig. 3.21. The similarity is remarkable despite the small area considered with respect to the whole flame, confirming that the flame areas considered (automatically highlighted in CC maps) are actually the ones which most actively contribute (either supporting or damping the oscillation) to the formation of the global FTF, whereas the participation of other flame zones to the global dynamics is negligible (values close to zero in CC representations).

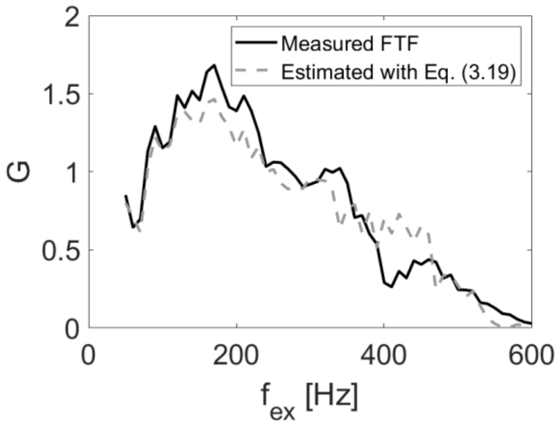

Fig. 3.21. Global FTF and its estimate by applying Eq. (3.19) to the FTF$_x$ measured at points 1-9

The expression $G_x \cdot \cos(\varphi_x - \varphi)$ is also coincident with the definition of "effective local gain" given to the normalized CCM values $(i' * i'_x)/K(\omega_f)$ (see Eq. (3.16)). Therefore, Eq. (3.19) can be reformulated as follows:

$$G = \sum_x \frac{i' * i'_x}{K(\omega_f)} \frac{\bar{Q}_x}{\bar{Q}} \tag{3.20}$$

The last expression only needs a series of bandfiltered images to be applied, since all the parameters involved can be easily extracted from chemiluminescence maps (in particular, average, line-of-sight map and CC map). G has been estimated with Eq. (3.20) for all the operational conditions tested, that is, three fuel blends (methane, biogas (85-15) and biogas (60-40)) at three different equivalence ratios (0.72, 0.86, 0.98) forced at three different frequencies (90, 150, 230 Hz). The results are compared with the global FTF measurements (see Fig. 3.9) in Fig. 3.22. The relative difference only exceeds 15% in one case (out of 27 tests), which again confirms the consistence of the procedure and the methodology proposed.

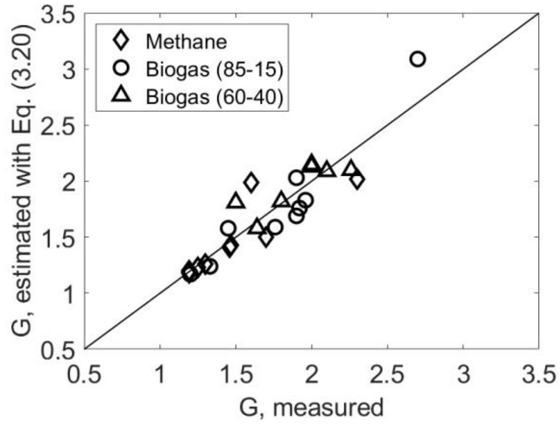

Fig. 3.22. Comparison between measured values of G and the corresponding estimates from cross-correlation maps through Eq. (3.20)

As mentioned above, the data shown in Fig. 3.22 derive from calculations performed on both average, line-of-sight integrated and CC maps for all the operational conditions tested. Therefore, it is worthwhile at this point comparing CC representations for methane and biogas (the same analysis for average maps has been already performed, see Fig. 3.11); for the sake of brevity, just the operational condition at f_{ex}=90 Hz, Φ=0.86 will be analyzed (Fig. 3.23). The peak spots gradually move downstream and outwards as the amount of CO_2 increases, an evolution that could be expected considering the increase in the flame dimensions caused by the injection of CO_2 into the air-fuel mixture. Moreover, it can be observed how biogas maps show almost half cycle more with respect to pure methane ones. This variation can be ascribed to the different time lags obtained for the different blends (see Fig. 3.10), which affects the oscillation patterns according to Eq. (3.15). The same effect does not happen when Φ increases, since the time lag value is less sensitive to a given increment in air mass flow than to the same amount of CO_2, as Fig. 3.10 clearly shows.

Apart from these distinctive features, CC maps for biogas flames show the same characteristics already analyzed for methane ones (so, they are not shown, for brevity): the number of cycles depicted along the flame sheet increases with the forcing frequency, whereas no major variations appear when changing the equivalence ratio. This is perfectly in line with the theoretical analysis performed and with the experimental data collected.

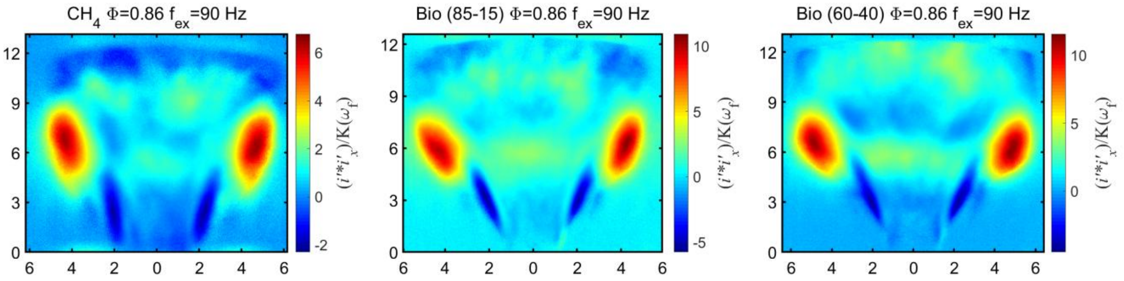

Fig. 3.23. CC maps for f_{ex}=90 Hz, Φ=0.86. From left to right pure methane, biogas (85-15) and biogas (60-40) flames

Characteristic convective length, L

As a final exercise, a quantitative analysis has been attempted to determine the "characteristic flame length" L, defined as the average distance travelled by the perturbation until it produces a heat fluctuation. It has been both derived theoretically and proved experimentally throughout this section that this length may be suitably identified by the position of the peaks highlighted in CC maps. At the same time, it has been shown how these peak pockets represent the flame areas where vortex roll-up phenomenon happens. Durox et al. [24] performed a similar analysis for laminar flames governed by vortex shedding and identified as the characteristic flame length the distance between injection and the vortex roll-up region; the same approach was used in [31] for non-linear regime, confirming that this distance can be considered representative of a flame dynamic response governed by vortex shedding phenomenon.

Therefore, the distance between the edge of the bluff body at the injection plane (Fig. 3.6) and the center of the peak in the CC maps, designated as D, has been calculated for each operational condition tested (the test with biogas (60-40) at Φ=0.72 and f_{ex}=230 Hz has not been considered, due to the shape change the flame suffers, as it has been discussed before). The values of D are represented in Fig. 3.24 as a function of Φ; each data point is calculated as the average of the lengths obtained for all the forcing frequencies considered.

The behaviors depicted in Fig. 3.24 are in line with the trends expected from the analysis of CC maps: D increases with Φ and CO_2 quantity; the only exception is biogas (85-15) at Φ=0.98, which presents a value of D greater than the ones measured for the same blend in leaner conditions.

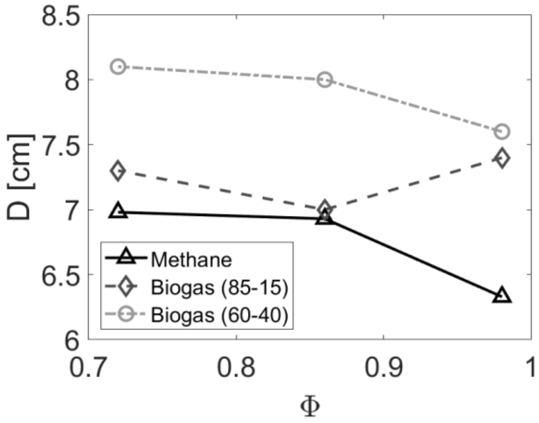

Fig. 3.24. Distance between injector and CC peak, D, as a function of the equivalence ratio, Φ, and fuel composition

The convective lengths extracted can be related to the time lags derived from the FTF phase through an estimated average propagation velocity of the perturbations from the injection plane to the place in which the heat fluctuation is produced (V). However, a proper estimation of V is not so obvious, since various definitions have been proposed in the literature: some authors defined it as the injection velocity of the mixture into the combustion chamber ($\bar{u}$) [82, 85], others as the bulk velocity of the flow along the flame jet path [20, 59] or as a fraction of the latter [24]. Nevertheless, it is reasonable to consider that a proper value of the characteristic velocity V should be assessed according to the phenomena dominating the dynamics of the flames tested (vortex shedding for the cases analyzed), that is the reason why various definitions can be found in the literature for the same parameter.

Alemela [21] measured the velocity field for flames in a configuration very similar to the one used for this work (swirl-stabilized, V-shaped flames) and proposed the following relationship between some operational parameters and the value of the maximum velocity along the jet path, designated here as u^*:

$$u^* = \bar{u}\left[1 + C\left(\frac{T_h}{T_c} - 1\right)\right] \tag{3.21}$$

According to Eq. (3.21), u^* is proportional to the mean injection velocity, $\bar{u}$, and it also depends on the ratio between the adiabatic flame temperature, T_h, and the temperature of the mixture at the inlet of combustion chamber, T_c, where C is a coefficient characteristic of the burner used. The C value measured by Alemela was 0.08; due to both the impossibility of performing the same assessment and the similarity between the facility used for this study and the one used by Alemela, it has been assumed C=0.1 for the present study (very close to the value obtained in [21]).

The u^* velocities, calculated with Eq. (3.21), can be compared with the values of V, estimated by dividing the convective lengths obtained from CC maps, D, by the sensitive time lag derived from the FTF, τ. Table 3.3 summarizes the parameters involved in the calculations and the results obtained (T_c is supposed constant at 293 K, whereas T_h has been estimated as the adiabatic flame temperature, calculated with the CEA2 code [87], for each fuel and Φ tested). The values obtained for u^* reveal an important difference from the ones obtained as $V = D/\tau$, with the former always being greater.

Considering that some relation between both magnitudes should exist, a proportionality factor k can be defined between the two velocities ($k = V/u^*$). This factor has been calculated for each condition tested and reported in Table 3.3; the values obtained oscillate in a rather narrow range, between 0.4 and 0.6, with an average value around 0.5. These results, obtained for a wide variety of operational conditions, clearly indicate that the perturbations measured travel at a velocity of about one half of the maximum speed registered along the flame sheet.

The ratio obtained is fully consistent with vortex shedding being the phenomena ruling the flame dynamics for the cases considered. In fact, Guiberti [88] found the same relationship between the displacing velocity of the vortices and the maximum velocity of the flame; this result is also confirmed by Durox and co-workers [24, 31] for laminar V-flames.

These last results further confirm the suitability of CC method to gain insight into flame dynamics and, in particular, to define some key FTF characteristics, such as the “characteristic convective length”.

Table 3.3. Estimated convective velocity for the cases analyzed

Methane							
Φ	$\bar{u}$ [m/s]	T_h [K]	D [cm]	τ [ms]	u^*[m/s]	V=D/τ [m/s]	$k\left(\frac{D}{\tau u^*}\right)$
0.98	12.7	2210	6.33	5.6	19.34	11.30	0.53
0.86	14.3	2078	6.93	5.0	21.26	13.75	0.59
0.72	16.8	1866	6.98	5.8	24.05	12.04	0.46
Biogas (85-15)							
Φ	$\bar{u}$ [m/s]	T_h [K]	D [cm]	τ [ms]	u^*[m/s]	V=D/τ [m/s]	$k\left(\frac{D}{\tau u^*}\right)$
0.98	12.7	2177	6,81	6.3	19.22	11.55	0.55
0.86	14.3	2048	6,41	6.0	21.14	11.65	0.50
0.72	16.8	1842	6,67	7.1	23.94	10.45	0.40
Biogas (60-40)							
Φ	$\bar{u}$ [m/s]	T_h [K]	D [cm]	τ [ms]	u^*[m/s]	V=D/τ [m/s]	$k\left(\frac{D}{\tau u^*}\right)$
0.98	12.7	2091	6.88	7.7	18.93	9.87	0.48
0.86	14.3	1967	7.38	6.9	20.83	11.65	0.51
0.72	16.8	1777	7.46	6.9	23.64	11.76	0.46

3.3.5 *Conclusions*

The two studies summarized in this section focus on a novel approach for the processing and interpretation of chemiluminescent flame images, called cross-correlation method (CCM). The objective of this study was to investigate in depth the physical meaning of the results obtained by applying CCM, showing the potentialities of this method in the analysis of flame dynamics.

Cross-correlation mapping has revealed itself as a simple yet suitable method to assess the actual contribution of each flame zone to the global heat fluctuation (and, so, to the global FTF). In its simplest formulation, CCM just needs a sequence of bandfiltered flame images; the results obtained allow a good qualitative analysis of the contribution of each flame area to the global FTF. If other parameters of the flame dynamics are known, also quantitative assessments can be performed, including the "local effective gain", $(i' * i'_x)/K(\omega_f)$, as well as the net contribution a flame zone gives to the global FTF (designated as $(i' * I'_x)/K(\omega_f)$).

Experimental results for both pure methane and biogas flames show patterns that clearly match with the theoretical formulation proposed and, so, with the physical rationale behind the method. In particular, oscillatory patterns have been obtained along the flame shear layer, evolving exactly as predicted in the theoretical development of the process (under certain reasonable hypotheses). These oscillatory patterns have led to two main conclusions:

- The local FTF gain monotonically increases along the flame length;
- The peaks highlighted by the CC maps can be considered as a suitable option to estimate the characteristic flame length.

These two deductions, obtained by contrasting the CCM theoretical formulation and the experimental results, have been also experimentally verified by measuring the local FTF in appropriate flame areas. The results obtained from local FTF fully confirmed the deductions inferred by the CCM analysis, and they also prove the suitability of the hypotheses made to simplify theoretical formulation and to infer the abovementioned tentative conclusions (namely, describing local FTFs through $n-\tau$ model and considering the characteristic convective velocity constant along the flame shear layer).

Also, the results have further confirmed the good match between experimental data and theoretical development, leading to a quantitative estimation of the "characteristic flame length" obtained by the CC maps. A close connection between the flame dynamics observed (dominated by the vortex shedding phenomenon) and the geometrical values obtained by CC maps is evident.

The assessment has been performed for a wide range of cases; in particular, two different CH_4-CO_2 mixtures (emulating biogas compositions) have been tested. The availability of these data made it possible comparing the characteristics of the flames for the three fuels studied. The CO_2 addition produces longer and wider flames with respect to pure methane, at equal injection velocity and equivalence ratio. This size increasing is apparent in FTF phases, showing a significant increment of the time delay. This fact is also perfectly consistent with the different patterns obtained for biogas flames in CC maps, which show almost a half cycle more than the methane ones. The coherent results obtained for two biogas blends demonstrate the flexibility of the method with respect to the fuel used. Moreover, to the author's knowledge, the discussed documents are the first ones where FTF of biogas flames have been shown and analyzed in details.

In summary, the method analyzed can be considered a valuable tool to assess various aspects of the dynamics of flames, starting from the actual contribution of each flame area to the global response. In particular, various insights about FTF characteristics could be gained. This result is particularly important for the FTF phase, since, as it will be shown in the next section, this parameter governs the (in)stability of a thermoacoustic system.

It would be worth performing further analyses using CCM, in particular considering different flame conditions, e.g. with different shape (conical, trumpet) or with different type of air-fuel injections (partially premixed or non-premixed). In particular, the assessment of partially premixed flames may yield interesting results, since an analysis about the CC output in conditions of multiple dynamic inputs superposed (namely, Φ' and u') could lead to other advantages of the method proposed for the analysis of flame dynamics, not evidenced by the present study.

3.4 Prediction of natural un/stable modes of a thermoacoustic system

3.4.1 *Introduction*

As mentioned in Section 3.1.1, the main parameters involved in the thermoacoustic response of a burner are the fluctuations of pressure inside the system, p', of heat released by the flame, Q', and of inlet velocity of the air-fuel mixture at the entrance of the combustion chamber, u' (equivalence ratio fluctuation is not considered since this work deals with perfectly premixed flames). Also, the magnitude of each variable is not important *per se*, but it is their mutual interaction what defines if a system will be thermoacoustically stable or if it will present unstable oscillations. The Rayleigh's criterion [6] is formulated in this sense, focusing more on the relative phase between p' and Q' than on the magnitude of each fluctuation.

Due to the high importance of avoiding flame dynamics in industrial facilities, various authors have developed models in order to predict the natural oscillation modes of a burner and whether these modes could result unstable and, so, lead the system to a limit cycle condition. These models result particularly useful during the design of the system, to know in advance if it could present some unstable conditions and, if so, to take remedial actions (e.g. by modifying the initial design or by installing dampers).

These models can have very different degrees of complexity, depending on how many of the variables and physical effects involved in the problem are considered. The relevant parameters could be roughly grouped as follows:

- Geometrical configuration of the system;
- Acoustic boundary conditions;
- Main thermal and fluid-dynamic parameters;
- Dynamic flame response;
- Irreversible losses.

So, thermoacoustic models can range from the simple equations describing the Rijke tube response [89-91] to comprehensive CFD models [92, 93]; of course, the more complex the model is, the more the computational effort required will be, and the accuracy of each model depends on how well the system studied fits with the simplifications applied.

In this context, low-order network models represent a good compromise between the computational effort required and the achieved accuracy. This approach has been applied in a number of works (e.g. [2, 21, 34, 57, 94]) and consists of modeling each burner element in terms of transfer (or scattering) matrix, using linear acoustics. These matrices are, then, connected in series, the outputs of a matrix representing the inputs for the following one. A detailed description of the transfer matrix for the most common elements of a combustor can be found in [21].

Some works suggest that the description of burner elements using linear acoustics is valid also in non-linear conditions (limit cycle), apart from the flame response [37, 95]. Therefore, an accurate description of the non-linear response of the flame (i.e. the flame describing function, FDF) combined with simple transfer matrix of the other burner elements may provide accurate prediction of the natural modes of a combustor (see, e.g. [37, 60, 95, 96]).

The disadvantage of implementing the low-order network model with FDF is, precisely, the availability of the flame describing function. In fact, as shown in Section 3.1.2 (Fig. 3.5), the FDF depends both on the frequency and on the magnitude of u'; so a family of curves is needed to implement the model, possibly for a wide range of u' amplitudes. The collection of these experimental data may be a challenging task, depending on the flame studied and on the necessary equipment to obtain the FDF.

However, a few studies have been found that successfully used FTF as input to the low-order network model in limit cycle conditions [36, 38, 97, 98]. The use of FTF instead of FDF significantly simplifies the inputs to the model. It reduces the efforts needed to collect the flame dynamic response (only one curve is needed) and to run the model to obtain the modes of the burner. The results obtained using FTF in previous works are promising, so this approach has been explored here in a systematic way for a wide range of operational conditions, in order to evaluate the feasibility of predicting unstable modes based on simplified descriptions of the system and, especially, of the flame response.

While Section 3.3 has been dedicated to investigate the actual contribution of each flame zone to FTF, and to relate FTF and flame characteristics, this section will focus on the use of the linear flame response to predict non-linear combustor modes. Experimental results will be analyzed and compared with theoretical ones, in order to assess the suitability of the FTF to predict unstable modes reaching non-linear regimes.

Moreover, among the operational variations proposed, the use of two different blends (pure methane and biogas (60-40)) is considered. So, the analysis can also focus on differences due to the addition of CO_2, in terms of both p' amplitude and frequency, and offers a good opportunity to verify whether the FTFs measured include (together with other physical parameters needed for the model) the necessary information to correctly predict unstable modes and, hence, to account for the impact of changes in fuel composition.

The results presented in this section have been also discussed in Paper 3 [47], which can be consulted in Section 4 for further details.

3.4.2 *Dispersion equation*

The experimental facility in Fig. 3.6 can be simplified as a two-cavity system, where the first one is represented by the injection duct and the second one by the combustion chamber.

The transfer matrices for this geometry can be condensed in a single equation, called "dispersion equation", under certain hypotheses:

- 1-D system, so the waves are supposed to propagate just along the longitudinal direction (forward and backward);
- Linear acoustics describes well the phenomena happening in both elements;
- Steady state;
- Low Mach number;
- Flame is a 0-D element;
- Constant temperature in each cavity;
- Same pressure and specific heat ratio (γ) in the two elements.

Apart from assuming a constant temperature in the whole combustion chamber, the other hypotheses can be considered suitable for the cases analyzed. In particular, the approximation of the flame as a 0-D element is admissible if the flame length is much shorter than the wavelength considered [21]. For the frequencies of interest (hundreds of Hz) this condition is respected, so the approximation made can be considered acceptable.

The two-cavity system is sketched in Fig. 3.25, where S_1 and S_2 denote the inlet of the injection duct (1) and the outlet of the combustion chamber (2), respectively. Hereafter, the same notation (subscripts 1-2) will be used for all the magnitudes referred to one of the two cavities. $R_{1,2}$ represents the reflection coefficient at the boundaries of the system, and $A_{1,2}^{+,-}$ designate the amplitudes of plane waves travelling forward (+)/backward (-) inside the two cavities. x defines the longitudinal variable along the burner, measured from the upstream end of the injection duct (x=0), with x=b at the dump plane and x=L at the outlet of the combustion chamber. In this model, the flame is supposed to be located exactly at the discontinuity between the injection and the combustion chamber, that is, at x=b.

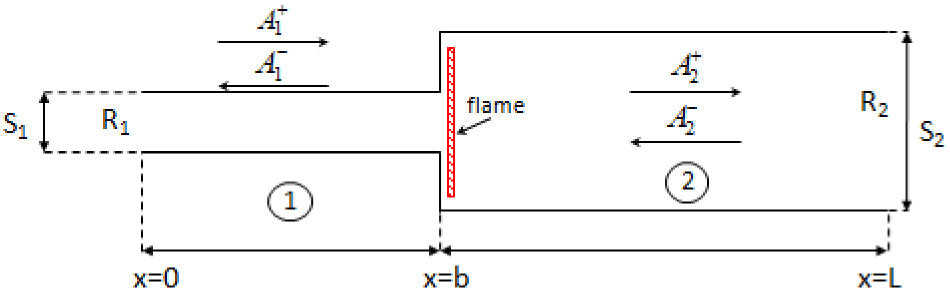

Fig. 3.25. Sketch of a two-cavity system

The main steps that lead to the final formulation used will be briefly described in this section; for further details about the derivation of dispersion equation, references [34, 35, 38] are recommended.

According to linear acoustic theory, pressure amplitude is conserved at the discontinuity (x=b), whereas a sudden jump can be observed in velocity fluctuation, dependent on the ratio between the two areas ($S_{1,2}$) and on the fluctuation of the heat release rate, Q'. These two conditions are expressed in Eqs. (3.22)-(3.23), where $b_{+,-}$ indicates right (+)/left (-) handed limits, as x approaches b

$$p'(b_-) = p'(b_+) \tag{3.22}$$

$$S(b_+) \cdot u'(b_+) - S(b_-) \cdot u'(b_-) = \frac{\gamma - 1}{\gamma \bar{p}} Q' \tag{3.23}$$

Assuming harmonic variation of the acoustic variables and of the heat release rate, Eqs. (3.22)-(3.23) can be rearranged as follows, where $\bar{\rho}$ and c represent the mean density and the speed of sound, respectively. k indicates the wave number, defined as $k^{\pm} = \omega/(c \pm \bar{u})$, whereas i is the imaginary unit.

$$A_2^+ + A_2^- = A_1^+ \cdot e^{-ik_1^+ b} + A_1^- \cdot e^{ik_1^- b} \tag{3.24}$$

$$\frac{S_2}{\bar{\rho}_2 c_2} \cdot (A_2^+ - A_2^-) = \frac{S_1}{\bar{\rho}_1 c_1} \cdot (A_1^+ \cdot e^{-ik_1^+ b} - A_1^- \cdot e^{ik_1^- b}) + \frac{\gamma - 1}{\gamma \bar{p}} Q' \tag{3.25}$$

The upstream and downstream reflection coefficients can be defined as:

$$R_1 = \frac{A_1^+}{A_1^-} \;\; ; \;\; R_2 = \frac{A_2^- \cdot e^{ik_2^-(L-b)}}{A_2^+ \cdot e^{-ik_2^+(L-b)}} \tag{3.26}$$

Rearranging Eqs. (3.24)-(3.25) in order to make explicit R_1 and R_2, the final expression for the dispersion equation is obtained:

$$\begin{aligned}&(1+\mathit{\Gamma}_1+\mathit{\Gamma}_2\cdot FTF)\left(R_1R_2\cdot e^{-i\left[b(k_1^{+}+k_1^{-})+(L-b)(k_2^{+}+k_2^{-})\right]}-1\right)+\\&(1-\mathit{\Gamma}_1-\mathit{\Gamma}_2\cdot FTF)\left(R_2\cdot e^{-i(L-b)(k_2^{+}+k_2^{-})}-R_1\cdot e^{-ib(k_1^{+}+k_1^{-})}\right)=0\end{aligned} \qquad (3.27)$$

Where the coefficients $\mathit{\Gamma}_1$ and $\mathit{\Gamma}_2$ depend on both physical parameters and geometrical dimensions of the rig:

$$\mathit{\Gamma}_1=\frac{\bar{\rho}_2c_2S_1}{\bar{\rho}_1c_1S_2}\ ;\ \mathit{\Gamma}_2=\frac{\bar{\rho}_2c_2}{\bar{\rho}_1c_1S_2}\frac{\gamma-1}{\bar{\rho}_1c_1^2}\frac{\bar{Q}}{\bar{u}} \qquad (3.28)$$

The solutions of Eq. (3.27) in terms of ω (hidden in the wave numbers, k) represent the natural modes of the system considered. The results will be complex numbers, where the real part indicates the natural oscillation frequency of the system, whereas the sign of the imaginary part reveals if the solution is stable ($Im(\omega) > 0$) or unstable ($Im(\omega) < 0$).

3.4.3 *Experimental data*

A vast experimental campaign has been carried out in order to obtain results for a broad range of operational conditions. Two different combustor lengths have been tested (900 and 1,250 mm) for two different fuels: methane and biogas (60-40). For each fuel and length, experiments have been carried out on five different values of Φ: 0.98, 0.92, 0.86, 0.80, 0.72. Moreover, for the shorter combustor, the inlet reflection coefficient R_1 has been varied by adjusting the position of the crenelated plug; this position is identified by the coordinate H, which expresses the length of the plug teeth inserted into the duct, so H=0 mm means that the tip of the teeth is aligned with the base of the injection duct and H=25 mm indicates that the plug completely obstructs the inlet. Five different acoustic conditions at the inlet of the facility have been tested: H=0, 10, 15 and 20 mm plus the condition where the plug is completely retired (fully open inlet), which will be indicated as H=-inf.

Most of the operational conditions tested present self-induced pressure oscillations which reach a condition of limit cycle, with a magnitude of hundreds or even thousands of Pa. The frequency and amplitude of this natural fluctuation have been recorded for each test according to the methodology exposed in Section 3.2.3.

Since the FTF is also a required input to solve Eq. (3.27), it was obtained for each fuel and Φ by applying the experimental procedure described in Section 3.2.3.

Three out of five conditions considered have already been discussed as a part of the analysis performed for CCM, so the related FTF have been already shown and their relative characteristics analyzed (see Fig. 3.9 and Section 3.3.4). The other two conditions (Φ=0.92 and 0.80) just increase the granularity of the operational conditions investigated, but no major differences have been observed with respect to the data presented above. The obtained results are shown in Fig. 3.26, but a detailed comparison of them will be skipped, for the sake of conciseness.

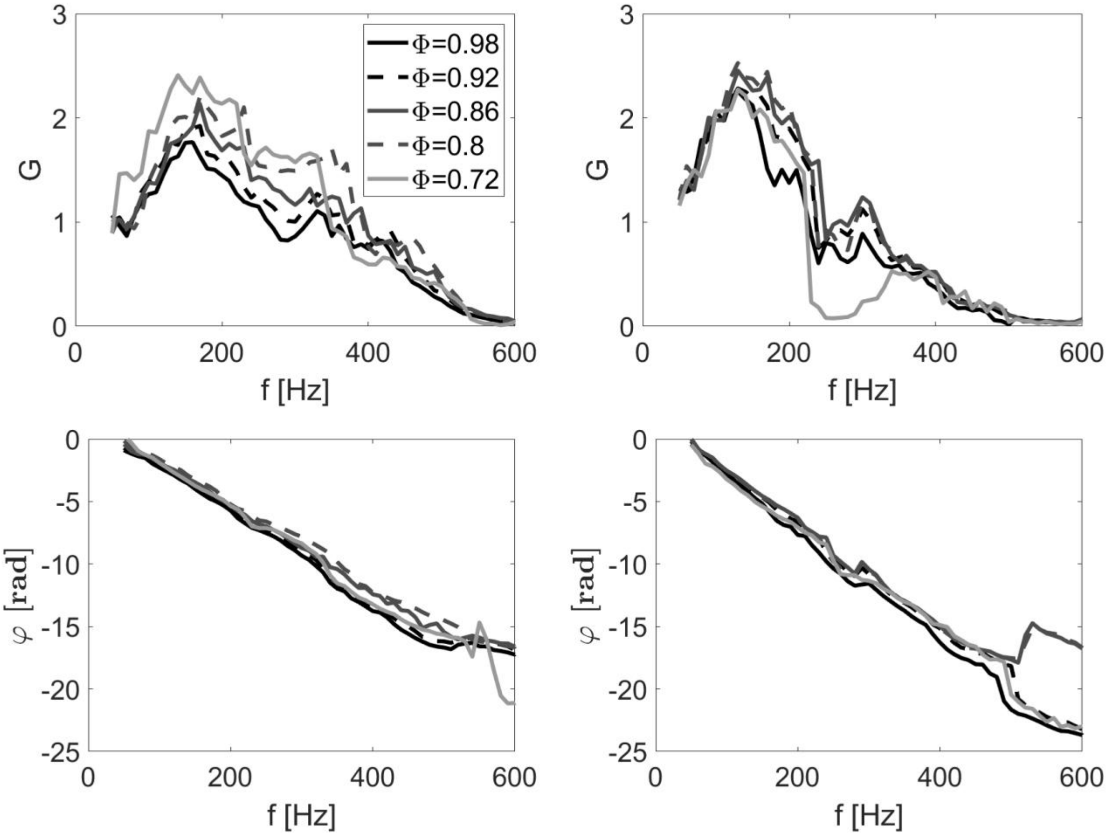

Fig. 3.26. Gain (top row) and phase (bottom row) for flames of pure methane (left column) and biogas (60-40) (right column) at different values of Φ

Since the outlet of the combustion chamber is open to the atmosphere, the downstream reflection coefficient R_2 can be considered equal to -1 [21], whereas the value of R_1 has been determined experimentally for each value of H tested, following a similar methodology to the one applied to derive FTF. A loudspeaker was located at the top of the combustion chamber and the facility was excited at the same frequencies considered in FTF measurements (see Section 3.2.3). p' data were acquired through the five pressure transducers located along the injection duct, sampling for 4 s at 4 kHz per each frequency; the Riemann invariants for p' (and, hence, also for u') were estimated from the data collected using the multi-microphone method and the reflection coefficient could be obtained. Experiments were performed for the two combustor lengths considered and injecting a variable air mass flow to the rig, between 0 and 40 Nm^3/h; the values obtained barely change with these parameters, so R_1 can be considered a function only of H. The gain and phase of R_1 are depicted in Fig. 3.27 for the various levels of restriction. The phases obtained for H from 0 to 20 mm display an almost linear trend, with a slope that slightly increases with H, whereas the angles obtained for H=-inf. are almost constant with values around π, resembling the acoustic condition of an open boundary. Gain values display significant fluctuations in the frequency range explored, so no clear interpretation can be inferred about this parameter from the data collected.

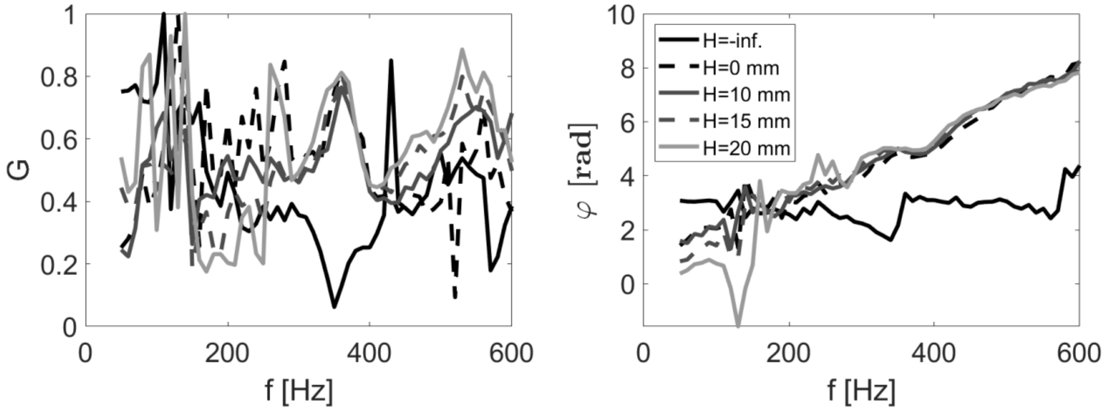

Fig. 3.27. R_1 gain (left) and phase (right) for various restriction levels

3.4.4 Results and discussion

The amplitudes of the pressure fluctuations obtained for methane and biogas (60-40) are shown in Fig. 3.28-a. Both fuels display high p' amplitudes, with values ranging from 200 to 2,600 Pa and generally higher as the mixture becomes leaner. Methane flames reach greater limit cycle amplitudes than biogas ones, especially for low values of Φ, where the difference between the p' registered for the two fuels is about 4 times.

Methane flames also show higher unstable frequencies than those recorded for biogas (Fig. 3.28-b). This difference is higher for richer flames, and decrease with air addition to the mixture, mainly due to a decreasing in the frequency registered for CH_4 cases (biogas frequency is almost constant). The lower frequency for biogas flames could be justified by the lower temperatures reached with this blend, where CO_2 absorbs part of the heat released during the combustion process; this is also in line with the behavior depicted by the frequencies of methane flames with respect to Φ. Nevertheless, a more careful analysis (not shown here for brevity) evidenced that the assumption of temperature as the unique element affecting the limit cycle frequency may result in omitting other phenomena which could affect this parameter in a comparable measure. Therefore, a more comprehensive analysis should be conducted, where all the parameters involved in the definition of the oscillating frequencies are accounted for.

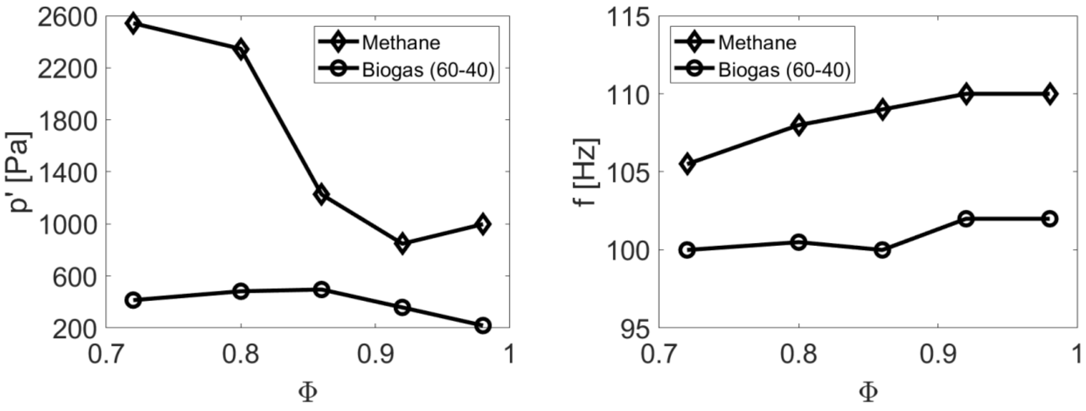

Fig. 3.28. Amplitude (left) and frequency (right) of the main peak in p′ spectra for methane and biogas (60-40). Combustor length=1,250 mm, H=-inf.

The magnitudes of p' reached with the combustion chamber of 900 mm are shown in the top row of Fig. 3.29 for methane (left) and biogas (right) as a function of H. Methane flames show a stable behavior for the condition of a completely open inlet, whereas the strength of the instability grows with the obstruction of the injection duct. Moreover, it can be observed that leaner flames are more responsive than richer ones to a variation in the inlet acoustic condition; in fact, they start showing instability for lower values of H than at richer conditions, being Φ=0.8 the most unstable condition for every restriction tested.

Biogas, as methane, shows very low values of p' for H=-inf, with the instability triggered as the injection inlet is closed. However, in this case pressure amplitude does not increase monotonically with the restriction level, but it presents a peak for H=0 mm, with other conditions showing dynamics quite similar among each other, independently of H and Φ values. The same is valid for unstable frequencies obtained with biogas flames: almost the same frequency is obtained for each restriction tested, and it barely varies with the equivalence ratio.

Frequencies for methane flames, instead, appear to be switching between two characteristic modes of the facility: ~150 and ~135 Hz. These two modes do not depend on the equivalence ratio, while they are sensitive to the value of H. In particular, the first characteristic frequency is typical of a completely open inlet, whereas the second is triggered by a higher restriction level. H=0 mm represents an intermediate condition, where both modes are recorded depending on the equivalence ratio.

For the cases analyzed, it is clear that the inlet acoustic condition significantly affects the dynamics of the rig, whereas the interpretation of the frequency variation with other magnitudes, such as temperature, is not evident.

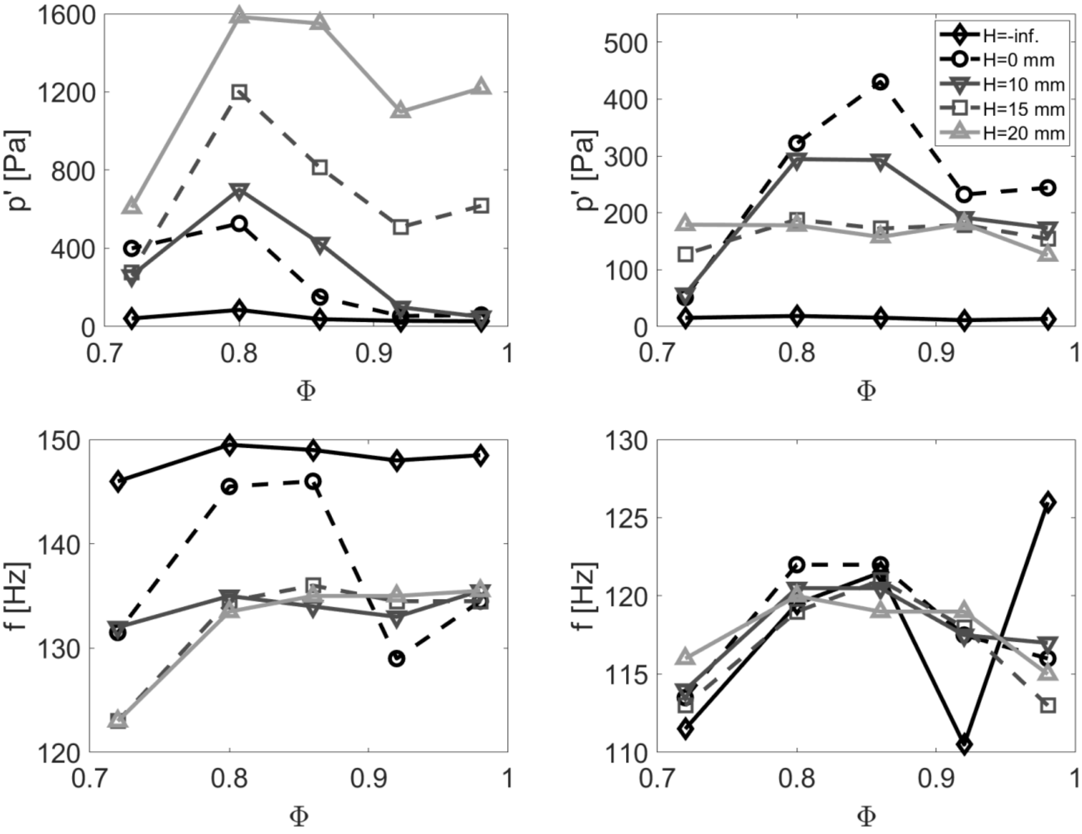

Fig. 3.29. p′ amplitude (top) and oscillation frequency (bottom) for methane (left) and biogas (right), for different upstream reflection coefficient. Combustor length=900 mm

The previous analysis clarifies that the characteristic modes of the rig are not determined by a single variable, but the whole bunch of physical parameters involved in the thermoacoustics of the system should be considered to define correctly the characteristic modes for each operational condition. Therefore, the dispersion equation has been used in order to include all the relevant magnitudes into the modal analysis.

The natural modes of the rig have been identified for all the pairs of unknowns (real and imaginary part of ω) for which Eq. (3.27) is satisfied. In order to find the solutions, the angular frequency plane has been swept: from 50 to 600 Hz, with 0.5 Hz steps, for the real part and from -1,000 to 1,000 rad/s, with 1 rad/s, steps for the imaginary part.

As mentioned before, the temperature inside the combustion chamber (T_2) must also be defined. The adiabatic temperature is not considered a good approximation in this case, due to the significant heat losses through the quartz and metal walls of the combustion chamber (see Section 3.2.1). This was experimentally confirmed, with temperatures around 400° C measured at the outlet of the 1,250 mm combustor. A systematic investigation has been conducted to find the best alternative to define the average gas temperature inside the combustion chamber, by varying its value as a fraction of the adiabatic temperature and comparing the output of the dispersion equation versus the experimental values for a fully open inlet. It has been observed that the correspondence between experimental and theoretical results reaches an optimum when the temperature in the combustion chamber was set at 50% of the adiabatic flame temperature, in K, for each operational condition (Fig. 3.30).

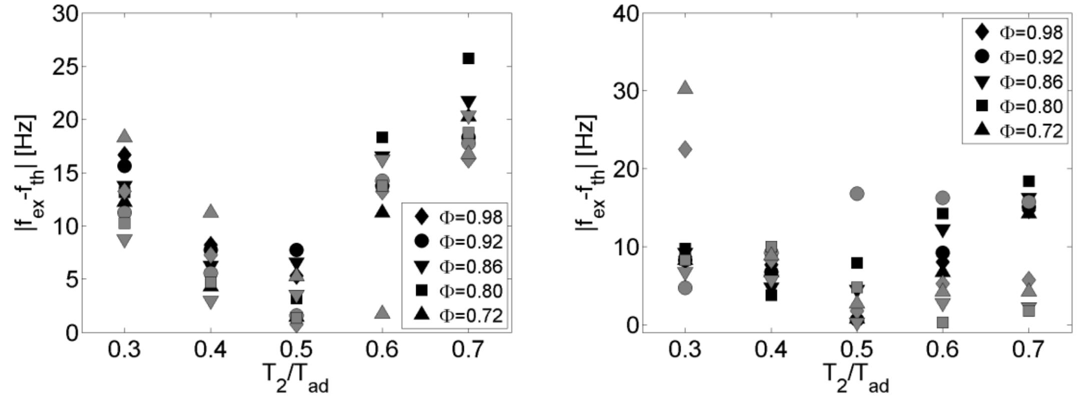

Fig. 3.30. Error obtained in the dispersion equation predictions varying the T_2 value for a burner length of 1,250 mm (right) and 900 mm (left). Black and grey markers represent methane and biogas cases, respectively; H=-inf.

Another factor to be considered to obtain correct results is a correction of the burner length; in fact, to apply correctly the acoustic condition of a completely open outlet, the burner must be artificially elongated by a factor $\delta = 0.85 \cdot D/2$, where D designates the hydraulic diameter of the combustion chamber [34, 35].

The differences between the frequencies obtained with the dispersion equation (f_{th}) and the experimental ones (f_{ex}) are represented in Fig. 3.31. The values of f_{th} have been chosen as the solutions found which presented the lower real part and a negative imaginary part. Overall, differences are below 10 Hz in 90% of cases, with a maximum difference of 16 Hz.

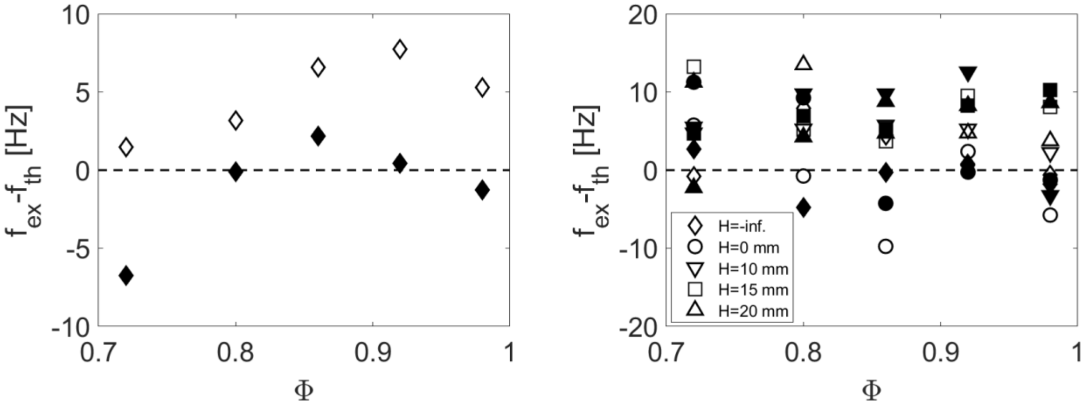

Fig. 3.31. Differences between experimental and predicted frequencies. Hollow markers: methane cases; full markers: biogas cases. Left: burner of 1,250 mm, H=-inf. Right: burner of 900 mm for different inlet restriction settings

So, despite the simplification of adopting a linear description of the flame response (FTF) to model non-linear situations, the results obtained are reasonably accurate for a broad variety of cases (changes in equivalence ratio, inlet restriction, burner length, fuel). The good match obtained between predictions and experimental results might be linked to the low sensitivity of the natural modes to the magnitude (gain) of the flame response. In fact, the gain parameter is the one distinguishing FTF and FDF, so the results obtained seem to be mainly determined by the phase of flame response, irrespectively of the gain this function presents. That is the reason why the predictions obtained are in line with the experiments, since FTF and FDF phases are very similar for the same operational condition.

An important objective of this study was to assess the suitability of the dispersion equation for different fuels. It has been observed that, despite the different dynamic response of the two mixtures, the precision of the outputs for both blends is comparable, for the whole range of Φ tested. So, the information brought into the equation by the FTF is sufficient to allow distinguishing between the dynamic response for the two fuels tested.

3.4.5 *Conclusions*

A systematic variation of operational parameters has been performed in order to study how these changes affect both the amplitude and the frequency of unstable modes obtained in the experimental facility for methane and biogas (60-40) flames.

The two fuel blends tested showed a different dynamic behavior when varying operational parameters, such as equivalence ratio, acoustic reflection coefficient at the inlet of the rig and burner length. In particular, the natural frequencies obtained are not well described if the problem is simplified in order to consider just one variable, but all the parameters affecting the thermoacoustics of the system should be included to obtain suitable results.

It has been considered that a two-cavity system could be used as a good description of the rig used throughout this work. Using a low-order network model approach, the thermoacoustics of such system is completely described by a unique equation, called "dispersion equation". The dispersion equation has been applied for the whole set of experiments carried out, using as an input the linear-regime response of the flames tested (FTF).

The results obtained using the dispersion equation have shown a good match with the experimental frequencies measured, highlighting that the FTF can be used also to predict modes in which the flame shows a strong non-linear condition. This fact suggests that solutions of the dispersion equation strongly depend on the FTF phase (very similar to the FDF one), whereas the FTF magnitude barely affects the estimated natural modes. Of course, this deduction should be properly validated, but it would allow a strong simplification in the prediction of the unstable modes of a burner (i.e., the use of only one curve, FTF, instead of a family of curves, FDF).

The same information has been used for the two different fuels tested, obtaining a similar accuracy in the final results. This means that the FTF contains sufficient information to describe the impact of changes in fuel composition on the estimated modes of the system using low-order network models.

3.5 Pseudo-active control of thermoacoustic instabilities

3.5.1 Introduction

An accurate prediction of natural unstable modes of gas turbine facilities is essential at the design stage, but also for the implementation of control systems (especially passive ones), aimed at suppressing the onset of limit cycle situations.

Instability control methods can be divided in two main categories: passive [39] and active [40] systems. Passive systems consist of devices aimed at damping the acoustic energy generated by the coupling of pressure and thermal fluctuations; some examples are quarter-wave tubes, Helmholtz resonators [41], perforated plates or acoustic liners [42]. The main advantages of passive systems are their structural simplicity and high durability, as well as their effectiveness in damping the onset of instabilities [41, 99-102]. Nevertheless, they are generally optimized to damp oscillations at a defined frequency, lacking flexibility when modes different from the one they have been designed for are triggered (in order to overcome this limitation, tunable devices have been proposed [101, 103, 104], which modify their natural frequency by varying their geometry). Moreover, the optimal location of passive system on the engine is usually difficult to be accomplished at theoretical level, and often the installation of these devices is experience-guided or based on "trial-and-error" experiments.

Active systems typically operate in closed-loop with a reference signal of the unstable condition (normally, p'), activating a dynamic element (a loudspeaker or a high-frequency valve) which generates an additional acoustic input aimed at decoupling the interaction between p' and Q'. Various works have investigated this approach (e.g. [105-108], in Ref. [108] an application at full-scale is presented) whose major advantage with respect to passive systems is its adaptability to frequency variations of the instabilities. However, the elevated cost of the equipment, the limited bandwidth of the pulsating valves and their potential of making the system unstable [38] are important drawbacks that are hindering its use in industrial applications.

Among the possible active control configurations, one often proposed is the injection of a secondary flow of pure fuel in the core of the main flame. It has been observed that, in general, the presence of a pilot flame in the combustion chamber represents, per se, a source of stability for the system [7, 109-113], even though some communications report cases in which pilot injection supports instabilities [109, 114]. Moreover, further reduction of the amplitude of p' into the burner by up to tens of decibels can be accomplished if the pure fuel injection is properly modulated in order to induce an out-of-phase oscillation between p' and the heat released by the pilot flame [114-118].

The implementation of this type of control should be preceded by a careful study of the acoustic response of the pilot line, since it determines the magnitude and phase of the velocity of the pilot fuel at the combustion chamber inlet [119]. Some authors have proposed to take advantage of this natural acoustic response to replace the dynamic element (in this case, the pulsating valve), using the pressure fluctuation generated in the combustion chamber as the driving force which causes the oscillation in the heat released. However, the applications proposed for this type of control are mainly focused on the main fuel injection [120-124]. Only Richards and co-workers [43, 44] have proposed the implementation on a secondary fuel injection in the main air-fuel mixture, upstream of the combustion chamber (therefore the mechanisms involved in the flame dynamics are substantially different from the ones that govern the dynamics of a pure injection into the burner).

In this work, a novel control system has been proposed, named as 'pseudo-active control', which has been implemented and tested on the experimental rig. It is based on the tuning of the acoustic impedance of the pilot line, which injects a small amount of pure fuel directly in the combustion chamber. The instantaneous mass flow rate of secondary fuel will oscillate according to the acoustic response of the pilot injection to the p' oscillation generated in the burner, so the goal is to achieve an out-of-phase oscillation of the heat released by the pilot flame with respect to p'. The implementation of a similar strategy has not been found in the literature, so this system can be considered as a fully new concept, at least to the author's knowledge.

The proposed control system is composed of just purely passive elements, so it should be classified as a passive method [124]. Nevertheless, the effect sought is comparable with the one obtained with active methods, therefore the system has been called "pseudo-active instability control" (PAIC). The final goal is a control which presents the cost and robustness of passive systems and the versatility of active ones.

It could be inferred from the PAIC description that the knowledge of three magnitudes is essential for the correct design of such a system:

- The unstable mode(s) of the facility, since the response of PAIC should be calibrated according to the p' frequencies
- The acoustic impedance of the pilot line, which determines how the pilot fuel flow is modulated
- The dynamic response of the diffusion flame, which eventually leads to the damping effect sought

The first magnitude can be obtained from suitable thermoacoustic modeling, like the one described in Section 3.4, whereas the acoustic response can be obtained either through experiments or through acoustic models of simple elements (see [21]). A major challenge in the PAIC design is represented by the pilot flame response, since the configuration tested implies that the pilot flame is burning in the core of the main premixed flame, making the assessment of its dynamics very difficult, as it will be explained in the following paragraphs.

In this section, the rationale behind the PAIC system, as well as its design and implementation and the results obtained, will be summarized. For further details, Paper 4 [48] and Paper 5 [49] describe the main findings about the PAIC system; they can be found in Section 4. It is worth underlining that the results obtained represent a first proof of concept of the possibilities that the system proposed would give, but further work is needed to achieve a reliable and accurate control system to be implemented at industrial scale.

3.5.2 *Pseudo-active instability control*

The logic behind PAIC implementation is sketched in Fig. 3.32 (top), where Z^{-1} is the acoustic admittance (inverse of the acoustic impedance, defined in Eq. (3.29)), and the subscripts p and d refer to the main flame/fuel (*premixed* flame) and to the pilot injection (*diffusion* flame), respectively.

$$Z(\omega) = \frac{\hat{p}(\omega)/\bar{\rho}\bar{c}}{\hat{u}(\omega)} \tag{3.29}$$

The dynamic pressure in the combustion chamber generates fluctuations in the pilot fuel flow (u'_d) determined by Z_d^{-1}. In turn, the heat released by the pilot flame, Q'_d, oscillates with a magnitude and a phase that depend on the flame transfer function $\mathrm{FTF_d}$. The effect sought is represented in Fig. 3.32 (bottom), with Q'_d in opposition of phase with respect to p'.

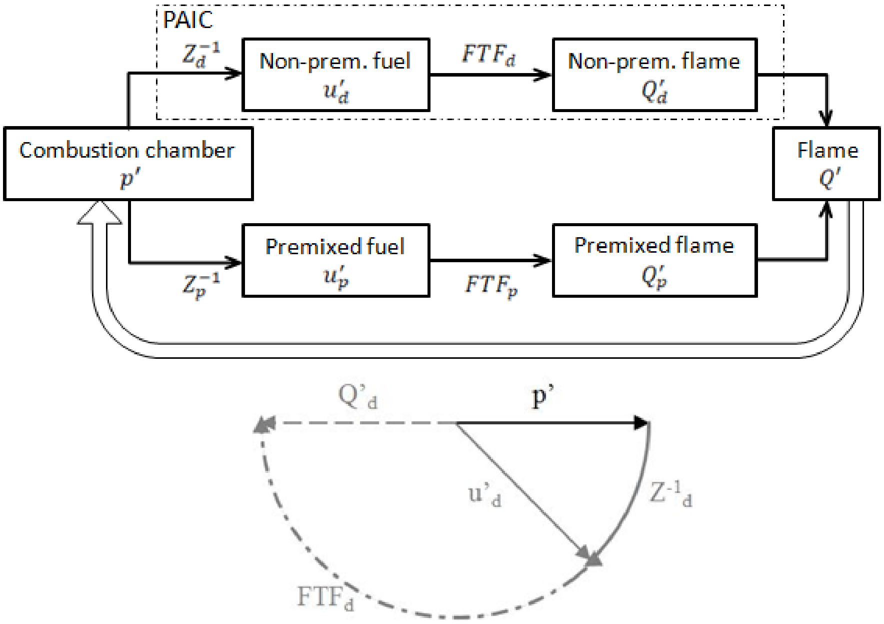

Fig. 3.32. Conceptual diagram of PAIC (top) and ideal phase distribution (bottom)

As mentioned above, a correct design of the PAIC system strongly relies on the knowledge of both Z_d^{-1} and $\mathrm{FTF_d}$. In particular, the time delay characteristic of $\mathrm{FTF_d}$ results fundamental to suitably design the pilot line in order to obtain a Z_d^{-1} value which leads to the phase distribution depicted in Fig. 3.32.

However, the determination of the response of a pilot flame burning in the core of a main premixed one is not trivial. The response of the tiny diffusion flame is masked by the heat released by the (much bigger) main premixed flame, and no reliable techniques have been found in the literature that could be suitable to characterize the dynamics of small non-premixed flames under such conditions. Some works have tackled this problem using CFD (e.g., [112, 125]), whereas recently Li et al. [126] proposed a model based on G equation, with good results in linear range, but presenting low precision in non-linear regimes (i.e. limit cycle).

Since a CFD approach is out of scope for this work, and the system is aimed to act during strong self-sustained instability, for this first exploration PAIC has been designed considering the uncertainty related with flame response. Therefore, a set of Z_d^{-1} values has been tested, which have been obtained according to criteria which will be explained later in detail.

The first results obtained were encouraging, and from them an attempt of estimating the phase of $\mathrm{FTF_d}$ has been made. However, further tests revealed that the effects measured in combustion chamber were not solely due to the PAIC system, but are also related to other purely acoustical phenomena, superposed to the one caused by PAIC. This superposition does not allow performing the estimations of FTF_d initially proposed, but the results obtained anyhow confirmed a major dynamic effect caused by the PAIC system.

3.5.3 Strategy for the design of the pilot fuel line

Theoretical considerations

In principle, the pilot impedance can be freely adjusted by modifying its geometry (in this case, its length). However, since PAIC works as a purely passive system, this limits the values of Z_d^{-1} that can be achieved.

This can be easily deduced if Z_d^{-1} is expressed as a function of the reflection coefficient of the duct, R, defined as

$$R(\omega) = \frac{f(\omega)}{g(\omega)} \tag{3.30}$$

where f and g are the Riemann invariants, representing, respectively, the plane waves travelling forward and backward with respect to the flow direction. Z_d^{-1} can be calculated from $R = |R|\angle\alpha$ as

$$Z_d^{-1} = \frac{|R|\angle\alpha - 1}{|R|\angle\alpha + 1} = \frac{|R|^2 - 1 + i\,2|R|\sin\alpha}{(|R| - 1)^2 + 2|R|(1 + \cos\alpha)} \tag{3.31}$$

For a passive element the amplitude of the reflected wave $|f|$ at its bottom cannot be greater than the incident one $|g|$, so that $|R| \leq 1$, while its phase presents no particular constraint. This condition implies that the real part of Z_d^{-1} is always negative (see Eq. (3.31)), confining the Z_d^{-1} values to the left half of the complex plane. Also, it can be demonstrated that, for a given $|R|$ (so, a circumference in the complex domain), the values of Z^{-1} also describe a circumference whose radius diverges for $|R|$ tending to 1 (see Fig. 3.33).

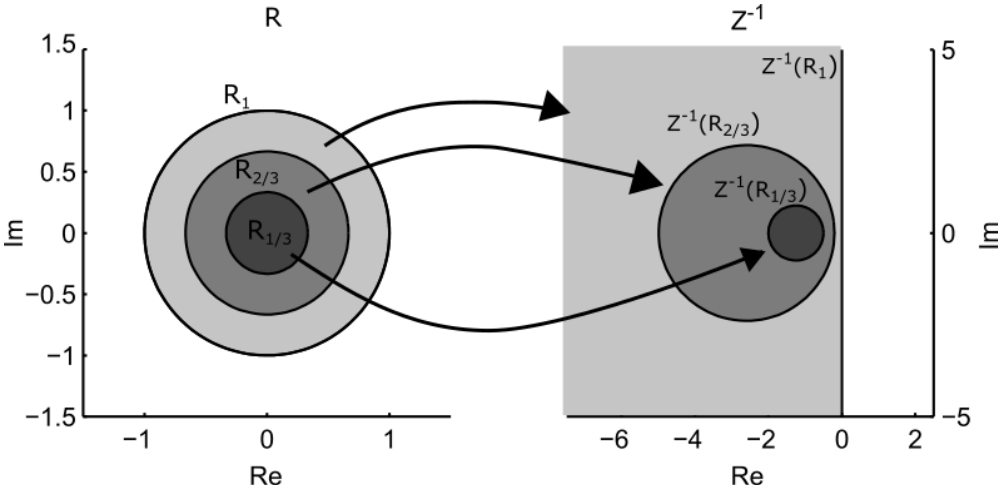

Fig. 3.33. Possible values of Z^{-1} for a given module of R, with the constraint $|R| \leq 1$. The transformation of the curves for $|R|$=1, 1/3 and 2/3 are shown.

These considerations lead to important conclusions about Z_d^{-1}; in particular its absolute value can increase theoretically up to infinity, whereas its phase is limited to the interval [90°, 270°]; therefore, the phase between p' and u_d' can only be adjusted in this range. Since the final target is to obtain a Q_d' oscillation out of phase with respect to p', the constraints analyzed represent an important limitation (that is, only half of the possible values) to the optimization of PAIC system.

PAIC design and validation

Once determined the physical limitations of Z_d^{-1}, the other, and most important, limitation for PAIC design is the lack of information about FTF_d. Due to the impossibility of an *a priori* knowledge of FTF_d, the PAIC lengths have been set based on the following guidelines:

- The modulus of Z_d^{-1} should be high, to maximize the amplitude of the velocity fluctuations at the injector;
- The Z_d^{-1} phase should cover most of the physically possible range (180°, as shown before), to analyze the effect of the time delay between p' and u_d'.

These two conditions should increase the pilot flame response in absolute value and allow exploring a range in phase as wide as possible, in order to investigate a set of cases that may give solid indications about the effectiveness of PAIC.

Since the unstable oscillation for the combustion chamber considered is around 110 Hz (see Section 3.4), the values of Z_d^{-1} have been optimized to comply with the bullets above in the neighborhood of this frequency.

To define the values sought, a 1-D acoustic model was developed to assist in the design of the pilot line and, in particular, to select the most convenient tube lengths, L (due to the geometrical characteristics of the system proposed, the value of L is the one to which Z_d^{-1} is more sensitive).

The pilot injection has been modeled as an acoustic network composed of the orifice, the tube and the final injection. The choked orifice installed at the upstream end of the polyamide tube (see Fig. 3.6) represents the upstream boundary condition of the system analyzed, and it can be suitably modeled as a closed end, that is, R=1 [127]. For the two parts of the pilot pipe (the polyamide and the stainless steel one) the model proposed by Peters et al. [128] has been applied, which takes into account both the thermal and the viscous damping happening in the pipe through the shear and the Prandtl numbers, as well as the roughness of the duct surface through an empirical coefficient C_d (set as 1 and 2 for the stainless steel and the polyamide tube, respectively). The model of the final injector is a combination of a sudden area change (from 8 to 2.5 mm in diameter) and a straight tube of 2.5 mm in diameter and 5 mm in length. The model used for a sudden area change has been described in [21]. Further details about the model developed can be found in Papers 4 [48] and 5 [49].

The model led to five values of L compliant with the characteristics defined above: L=1.30, 1,50, 1.65, 1.85 and 2.10 m; the correspondent Z_d^{-1} present absolute values greater than 10 and a phase range of 125° over a maximum of 180° physically admissible (Table 3.4). The validation of the model has been performed by measuring, in cold conditions, the velocity fluctuations induced at the exit of the pilot line by means of a hot wire anemometer, and externally exciting the rig with the loudspeakers. The comparison between the experimental values and the theoretical ones showed a good match for the 5 lengths defined (see Fig. 3.34), supporting the suitability of the model proposed. A more detailed description about the experimental methods used for the validation of the developed model can be found in Paper 4 [48].

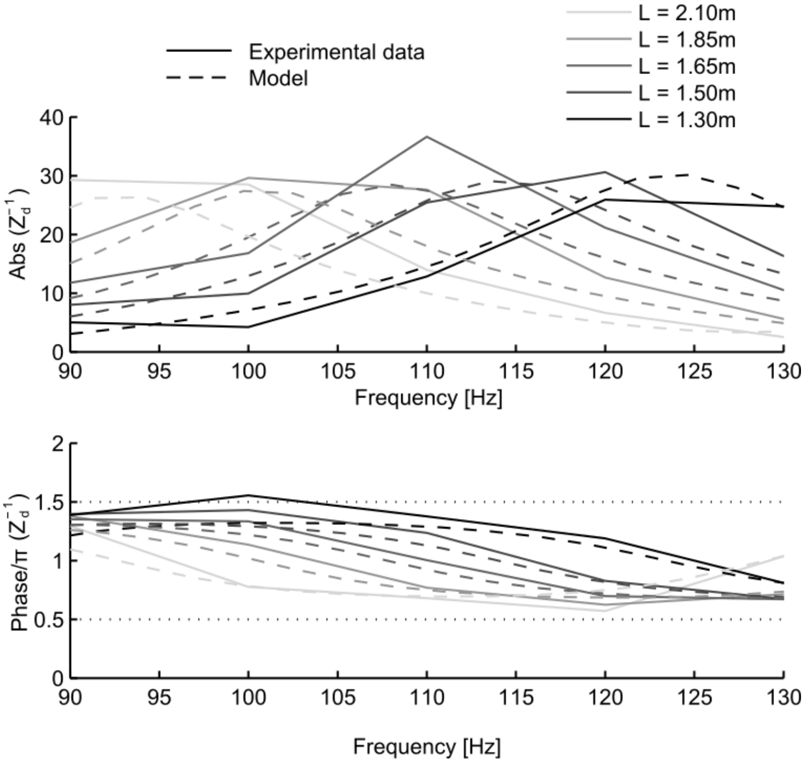

Fig. 3.34. Theoretical and experimental values of Z_d^{-1} for the selected values of L

Table 3.4. Lengths of polyamide tubes selected for the tests and relative values of Z_d^{-1} at 110 Hz

Case	1	2	3	4	5
L [m]	2.10	1.85	1.65	1.50	1.30
Abs (Z_d^{-1})	13.96	27.59	36.65	25.44	12.84
$\angle(Z_d^{-1})$ [°]	110	126	168	210	235

3.5.4 *Test matrix*

A first test campaign was carried out (see Paper 4) using, as a benchmark, three lengths of the polyamide tube (L=0.85, 0.75, 0.65 m) which should yield much lower contributions to the dynamics of the system than the lengths listed in Table 3.4. In fact, these lengths present absolute values of Z_d^{-1} ten times lower than the ones shown in Table 3.4, whereas the phase range covered is comparable.

Table 3.5. Values of Z_d^{-1} at 110 Hz for the PAIC lengths used in the first test series

Case	7	8	9
L [m]	0.85	0.75	0.65
Abs (Z_d^{-1})	2.38	1.63	2.27
$\angle(Z_d^{-1})$ [°]	218	175	132

A pilot mass flow, $\dot{V}_d$, of 0.05 Nm^3/h (1.66% of the main fuel injected into the combustion chamber) of pure CH_4 was injected through the pilot channel for each PAIC length. Tests were carried out setting the equivalence ratio of the main flame to 0.98, 0.86, 0.72; each experiment was repeated twice to ensure the repeatability of the values obtained. To compare the dynamics induced by varying the value of L, p' amplitude inside the combustion chamber was measured. The 8 PAIC lengths tested were designated from 1 to 8, from the longest to the shortest one (see Table 3.4 and Table 3.5).

A second campaign was carried out (see Paper 5), in which the PAIC effects of the lengths defined in Table 3.4 were compared for two different values of $\dot{V}_d$ (0.05 and 0.08 Nm3/h) in order to assess the effects of the amount of pilot fuel. Moreover, the same tests were also carried out in absence of pilot fuel injection, in order to quantify (and verify) the dynamic effects specifically induced by the PAIC through the fluctuations in the heat released in the pilot flame.

3.5.5 Results and discussion

The amplitudes of the dynamic pressure for the tests performed in the first campaign are represented in Fig. 3.35 against the phase of Z_d^{-1} for each tube length tested. The results present good repeatability and highlight a big difference between the configurations with a high absolute value of Z_d^{-1} (cases 1-5) and those presenting a low module of their acoustic admittance (cases 6-8), with the former presenting a much lower dynamic pressure than the latter. Moreover, p' values considerably vary also among cases 1-5, presenting a minimum almost at the center of the phase range swept.

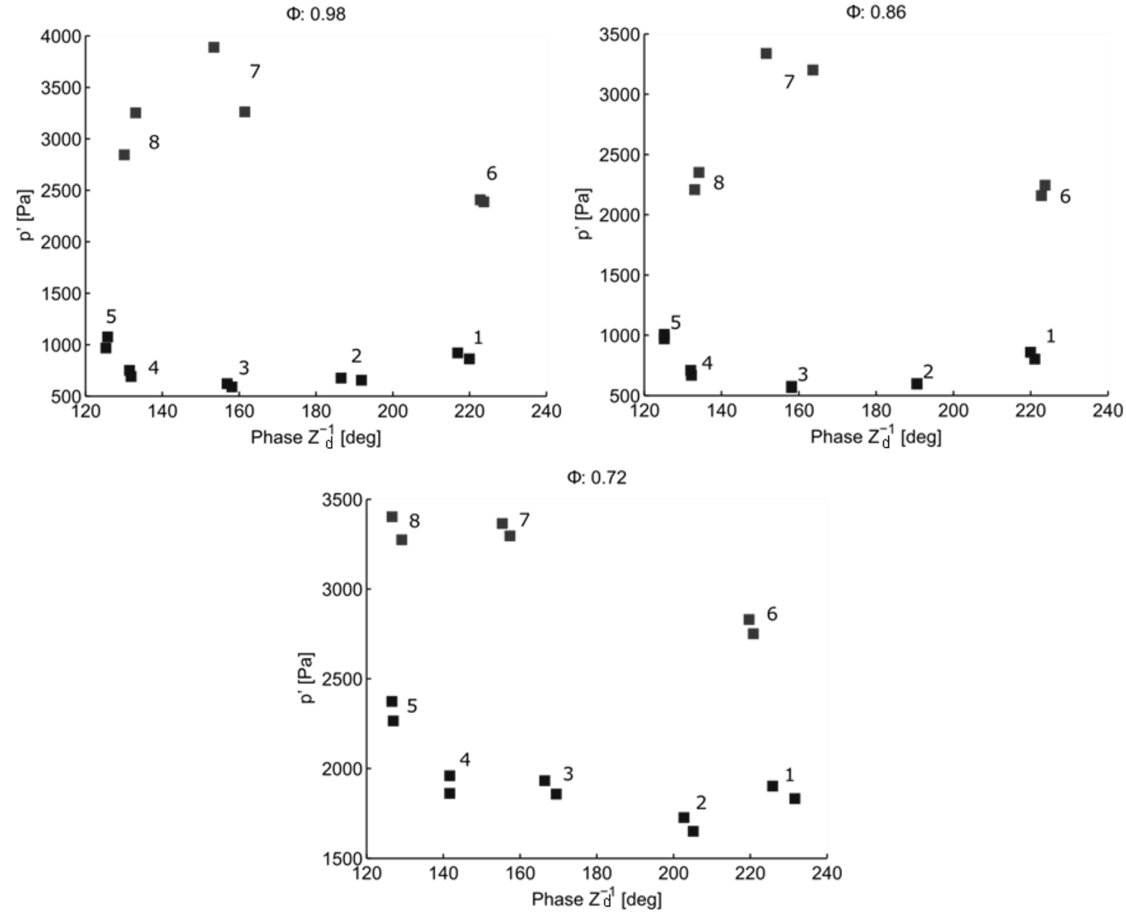

Fig. 3.35. p' amplitude versus Z_d^{-1} phase for configurations with high (cases 1-5) and low (cases 6-8) Z_d^{-1} modules

The results obtained show how the interaction between the tiny pilot flame and the main premixed one leads to changes in the dynamics of the system. In particular, pilot line lengths with a higher $|Z_d^{-1}|$ strongly damp the dynamic pressure with respect to those with smaller $|Z_d^{-1}|$, and this difference should be attributed to the magnitude of the fluctuation of u'_d, being this parameter the only difference between cases 1-5 and cases 6-8.

The patterns obtained can be considered as a first evidence that the system proposed can considerably reduce the dynamic pressure self-induced in a rig during a limit cycle condition. Moreover, a variation in the phase of Z_d^{-1} seems to open the possibility to further reductions in p'.

The variation with Z_d^{-1} phase could be related to an optimization of the phase of Q'_d, with the minimum representing a condition perfectly out of phase with respect to p'. In the lack of information about $\mathrm{FTF_d}$, and according to this interpretation, the patterns obtained can be used to estimate the phase of $\mathrm{FTF_d}$. The values of the two repetitions for cases 1-5 have been averaged, and the results have been interpolated through a quadratic curve to identify the Z_d^{-1} phase corresponding to the minimum. Once this reference point has been defined, it is quite straightforward to determine the FTF$_d$ phase for each case tested. The phasorial diagrams in Fig. 3.36 represent the results obtained. It should be noted that, in these graphs, the amplitude of Q_d' phasors is represented proportional to the corresponding u_d', since no further indication can be obtained from this analysis about the gain of FTF$_d$.

This is just one of the possibilities that could explain the results obtained; another one could be some dependence of the damping efficacy of the system on the magnitude of the modulation induced by Z_d^{-1}, even though the results obtained for Φ=0.72 do not seem to support this hypothesis. Also, the values obtained for cases 6-8 depict an opposite trend with respect to the one observed for cases 1-5, despite the phase range is almost the same. These data do not seem consistent with the approach proposed; however, the values of $|Z_d^{-1}|$ for the cases considered are, as mentioned before, really low (Table 3.5), and for case 7 (the one presenting the p' peak) it is almost half of the other two. So, the projection of Q_d' on the real axis for cases 6 and 8 might be greater than that for case 7, even if the phase of the latter is, in principle, more favorable to damp instabilities. Of course, this discussion can be considered just as a hypothesis, due to the impossibility of having reliable data about FTF$_d$ that could confirm it.

In any case, the results have shown great potentialities for the PAIC system to reduce the strength of thermoacoustic instabilities induced by the constructive coupling between the acoustic field of the combustion chamber and the heat released by the main flame. In order to further explore the possibilities of PAIC system, a second test campaign was carried out. In particular, the first objective was to assess if a higher value of $\dot{V}_d$ (0.08 Nm^3/h) could induce greater variations in p' and, to set a reference, tests were also performed without injecting any pilot fuel. Unexpectedly, this last set of tests provided particularly interesting results for the evaluation of the actual role of the PAIC strategy proposed as well as to identify other phenomena not initially considered.

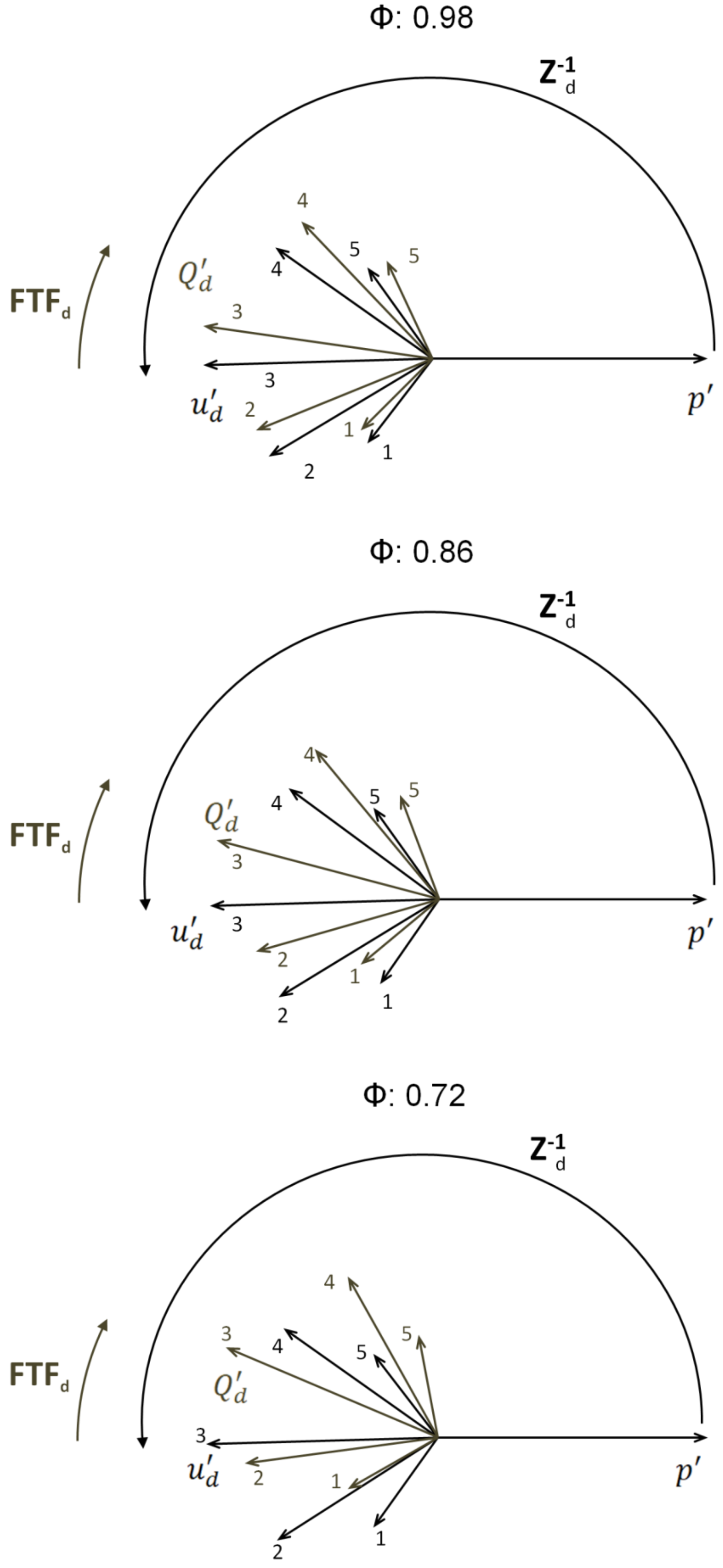

Fig. 3.36. Estimated phase of FTF_d *for different equivalence ratios*

The results obtained for the three pilot injections tested are shown in Fig. 3.37. Also for these cases, the experiments have been repeated twice but, due to the good repeatability shown (as for Fig. 3.35) and to improve the readability of the plot, just the average of the two values has been represented.

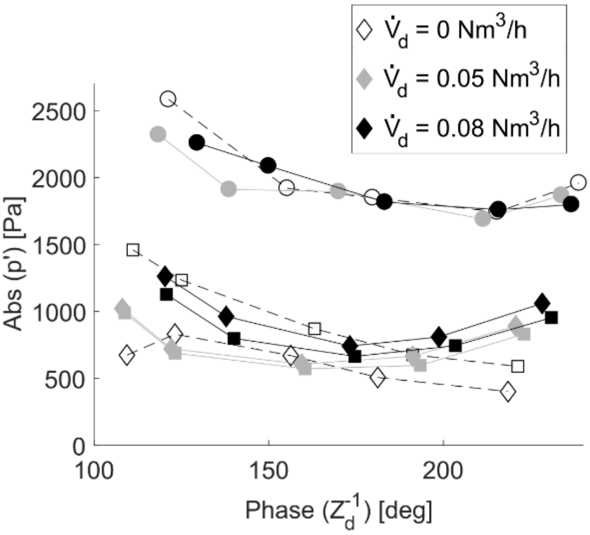

Fig. 3.37. Peak value of p' *vs. the phase of* Z_d^{-1}*. Test conditions identified by shape and colour of the symbols: white/grey/black for 0/0.05/0.08* Nm^3/h*; ○/□/◇ for* Φ*=0.72/0.86/0.98.*

It can be observed that a greater pilot injection does not sensibly affect the dynamic pressure, with very similar values for the leanest case and slightly higher for richer ones when $\dot{V}_d$ is increased.

The tests without pilot fuel injection depict a considerable variation in p', whereas an almost constant value was expected. Moreover, they show a different pattern (which decreases with the phase of Z_d^{-1}) with respect to the one obtained with pilot flame for Φ=0.98 and 0.86, whereas this difference disappears for Φ=0.72, with p' magnitudes quite similar to the ones obtained with secondary injection.

In order to exclude some external effect that could affect the dynamic pressure obtained, the same tests were repeated plugging the secondary injection orifice: in this case, the p' values obtained showed an almost constant value, so that various insights are gained by this comparison:

- the simple variation of Z_d^{-1} causes an acoustic phenomenon which affects p' in a measure comparable to the one observed with a secondary flame;
- the two different patterns observed for the richer conditions with and without pilot flame highlight how the interaction of a secondary flame

with the main one has an additional effect on the dynamics of the system, which superposes to the one induced by Z_d^{-1};
- the additional effect induced by the pilot flame disappears for Φ=0.72, with very similar p' values independently of the presence of the pilot flame.

In order to make the analysis more systematic, the mechanisms induced by the pilot flame presence will be analyzed separately from the ones caused by the pilot injection.

Analysis of the interaction with the pilot flame

The differences observed in Fig. 3.37 between the cases with and without pilot flame can only be ascribed to phenomena induced by the dynamics caused by the presence of secondary, non-premixed fuel. To better assess these differences, Fig. 3.38 shows, for each Φ tested, the ratio between p' amplitudes obtained with 0.05 Nm^3/h of CH$_4$ from the pilot line (designated as $p'_{0.05}$) and those measured without pilot injection (p'_0).

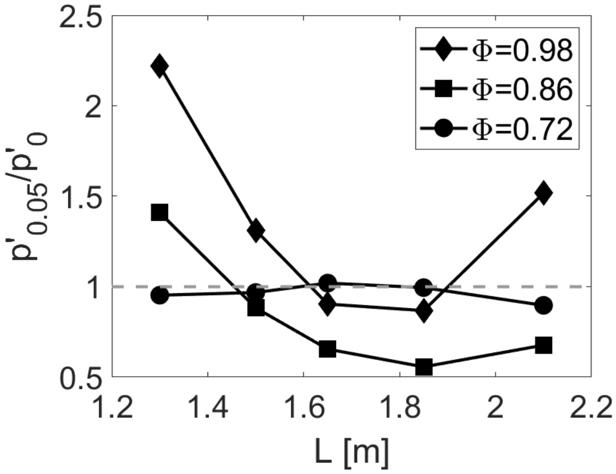

Fig. 3.38. Ratio between p' amplitudes measured with $\dot{V}_d$=0.05 and 0 Nm³/h, for different equivalence ratios, as a function of the length of the pilot fuel injection.

As observed above, the values are practically the same for Φ=0.72, whereas they show noticeable differences for richer flames as L is changed. In particular, at Φ=0.98 the dynamic pressure is amplified for the shortest and the longest PAIC tubes tested, while the intermediate lengths shows no major effect induced by pilot flame. When Φ is set to 0.86, the secondary flame strongly damps the dynamic pressure in the combustion chamber for almost all the PAIC lengths tested, except for the shortest one, which shows an amplification of p'.

The behaviors observed clearly support that PAIC system can significantly influence the dynamic pressure of the system; in particular, for Φ=0.98 and 0.86, respectively, p' increases and diminishes by a factor of ~2. Moreover, these variations are not constant with L; hence, the effects observed are not ascribable to an offset caused by the introduction of a pilot flame into the system, but they must be attributed to the dynamic interaction between the tiny diffusion flame and the main premixed one.

Instead, the leanest condition tested does not show any major variation due to pilot injection. This might be due to an enhanced dispersion of the pilot fuel before burning. In fact, the luminosity of the flame near the injection was reduced as the flame becomes leaner, which also causes a delayed ignition of the non-premixed fuel, so that it can be entrained into the main jet and its combustion is thought to take place, at least partially, in premixed mode. This might explain why for Φ=0.98 and 0.86 relevant differences have been observed with and without secondary injection, whereas no difference can be seen for Φ=0.72. However, these are just tentative conclusions, and a more specific analysis would be needed about how the Φ value could affect the interaction between the main premixed flame and the tiny diffusive one (this analysis can be considered as a part of the more vast investigation needed to properly design PAIC system, that is, a proper definition of FTF_d).

In an attempt to better assess how the main flame and the pilot one interact, OH* filtered images were collected and analyzed both injecting pilot fuel (0.05 Nm^3/h) and without pilot injection for Φ=0.98. The diffusion flame is not clearly discernible in the images collected, due to the very low power released (1.66%) with respect to the main one. To improve the visibility of the secondary flame, some images were recorded changing the filter wavelength from OH* to CH* (431 nm) but the resolution of the main flame resulted worse and the pilot flame was invisible anyway.

Several post-processings of the bandfiltered images have been applied in order to obtain flame maps that could reveal differences between the cases with and without pilot flame, but most of them have not shown any visible variation in cases with pilot injection with respect to the ones without any secondary flame. The only exception are the CC maps, which allowed detecting some differences for some PAIC lengths worth to be analyzed more in depth.

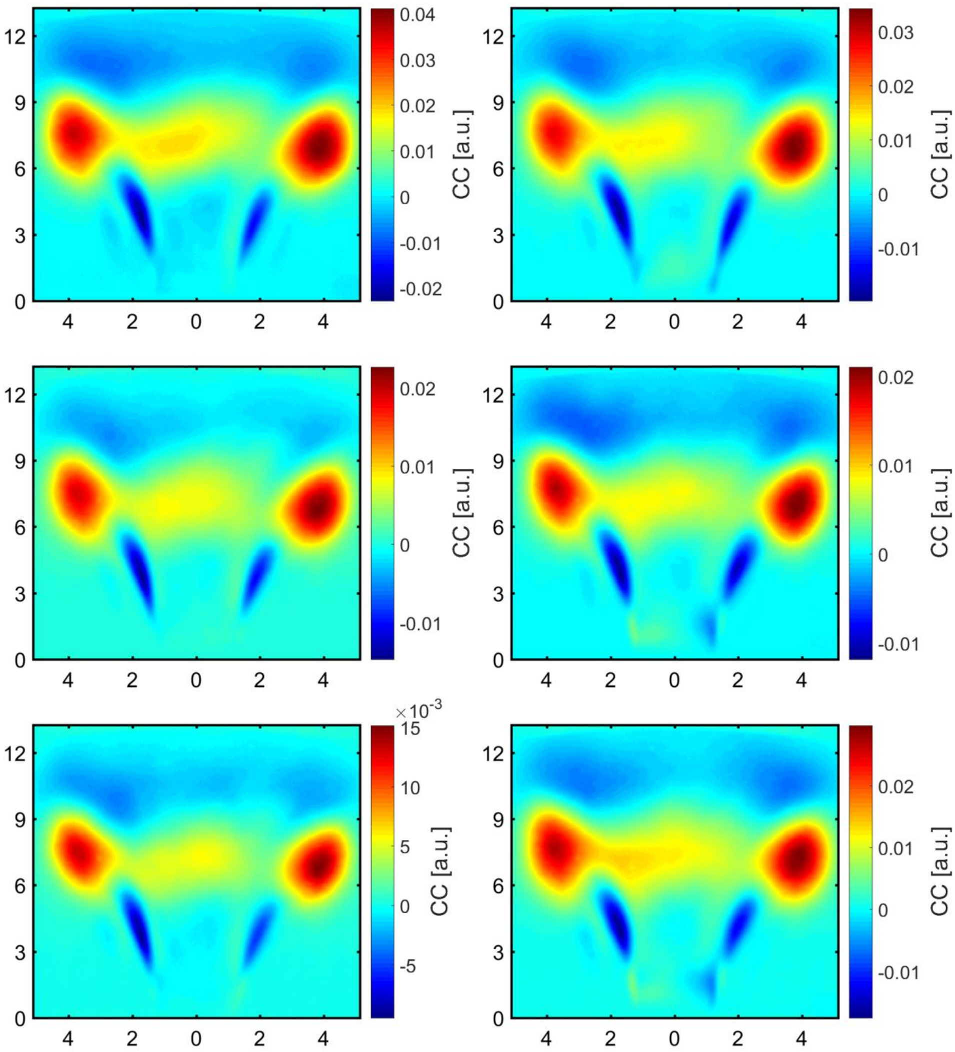

Fig. 3.39. Cross correlation maps at Φ=0.98 for different tube lengths, from top to bottom: L= 2.1, 1.5 and 1.3 m. Left: no pilot flame; right: $\dot{V}_d$=0.05 Nm^3/h

The maps shown in Fig. 3.39 represent the CC representations without (left) and with (right) pilot injection for L=2.1, 1.5 and 1.3 m. It is clearly visible how the cases with a secondary flame display active areas at the base of the flame, close to the dump plane, whereas the same areas present almost null values with no diffusion flame. Therefore, recalling the meaning of CC maps (see Section 3.3), this is a clear sign that pilot flame is contributing, either in a constructive or in a destructive way, to the main dynamic response of the flame in a slight yet non negligible way. In particular, the shortest lengths tested (L=1.5 and 1.3 m) show opposite values at the two sides of the flame, which could reveal precession-related phenomena in that area. For L=2.10 m this antisymmetric pattern is not apparent; instead, compared to the case with no secondary fuel, the presence of the pilot flame seems to cause an elongation of the negative spots aligned with the V flame.

The other two PAIC lengths, instead, show no major difference in CC maps both injecting pilot fuel and in absence of pilot flame (and, so, they have been not reported, for brevity). This is perfectly aligned with the global dynamic information shown in Fig. 3.38: the p' values obtained for L=1.85 and 1.65 m are practically identical both with secondary flame and without it, and so CC maps do not show any relevant difference. Instead, cases presenting consistent differences in p' values (that is, L=2.1, 1.5 and 1.3 m) highlight also a difference in CC maps. A further confirmation has been obtained by repeating the test for Φ=0.72: CC maps have not revealed any difference for $\dot{V}_d$=0.05 Nm^3/h compared with the same cases with no pilot flame, perfectly in line with the global results obtained in Fig. 3.38.

The analysis carried out clearly shows that the dynamic interaction of the two flames has significant effects on the amplitude of the pressure fluctuation inside the combustion chamber, leading to important increase/decrease of p' up to a factor of 2. Further analysis is needed to better understand the physics of this interaction, but CC maps clearly identified a difference at the basis of the flame, which may (should) be attributed to the presence of the diffusion flame; this difference disappears where no major variation in p' is registered, so there is a consistent correlation between the two phenomena.

Effects of pilot line length variation with no secondary fuel

As shown in Fig. 3.37, the variation of L causes a remarkable variation in p' values, even in the absence of a pilot flame. The patterns obtained depict a decreasing trend with the phase of Z_d^{-1}, and tests performed with the pilot injector plugged confirmed that the variations observed can only be caused by the change in the acoustic admittance of the pilot line.

So, a first hypothesis is that the pilot tube acts as a tunable resonator, and the change of its length modifies its effectiveness in damping the instability. To verify the plausibility of this hypothesis, the order of magnitude of the losses caused by the secondary line has been compared with acoustic energy production.

The acoustic losses, Σ, have been calculated according to Eq. (3.32), where S_d is the cross sectional area of the injector and $\angle p'u_d'$ is the phase between both variables. From the definition of the acoustic admittance, it can be easily deduced that the cosine can be expressed as its real part, Re (Z_d^{-1}).

$$\Sigma = \frac{1}{T}\int_T \int_{S_d} p'(t)\, \boldsymbol{u'_d}(t) \cdot d\boldsymbol{S}\, dt \;\; \approx -\frac{p'u'_d}{2}\cos(\, \angle p'u'_d)\, S_d = -\frac{1}{2}\frac{p'^2}{\bar{\rho}\bar{c}}\, \text{Re}\left(Z_d^{-1}\right) S_d \qquad (3.32)$$

The estimated Σ values range between almost zero losses up to around 1 W, depending on the operational condition and, of course, on the value of Z_d^{-1}. Therefore, some fraction of the acoustic energy generated in the combustion chamber is expected to dissipate in the pilot line depending on the value of L and operational conditions.

In order to understand if these losses can be the cause for the variations observed in p' values, the acoustic source term, E, has been calculated through Eq. (3.33), where q' represents the heat fluctuation released per unit of volume (also considered harmonic in time), V the flame volume and γ the ratio of specific heat capacities. Assuming that the flame is acoustically compact, p' can be assumed constant over the flame volume and the integral can be approximated as shown in the right hand side of Eq. (3.33).

$$E = \frac{1}{T}\int_T \int_V \frac{(\gamma - 1)p'(t)q'(t)}{\bar{\rho}\bar{c}^2} \cdot dV\, dt \approx \frac{p'Q'}{2}\cos(\angle p'Q')\frac{\gamma - 1}{\bar{\rho}\bar{c}^2} \qquad (3.33)$$

Equation (3.33) has been applied for the various cases tested, yielding estimated values of E below 10 W. Although higher, these values are of the same order of acoustic dissipation and, hence, the latter may contribute to the observed reduction in the amplitude of p'.

As a further analysis, the relationship between the dynamic pressure of the combustion chamber and the acoustic losses has been explored for the cases tested. The acoustic dissipation tends to reduce the acoustic energy and, at the same time, it is proportional to p'^2, so the effectiveness of the dissipation caused by PAIC is better represented by the normalized dissipation, Σ / p'^2, which is proportional to $-$Re (Z_d^{-1}) (see Eq. (3.32)). This latter is always a positive number, since it is physically impossible that the real part of Z_d^{-1} be positive, as shown above.

The calculation has been performed for a wide set of data, i.e. the different acoustic admittances tested, with different amounts of pilot fuel (0, 0.05, 0.08 Nm^3/h). The plot clearly shows an inverse relationship, so the dissipation increases with $-$Re (Z_d^{-1}), further confirming that the purely passive dissipation at the pilot orifice can contribute to the damping observed in some tests.

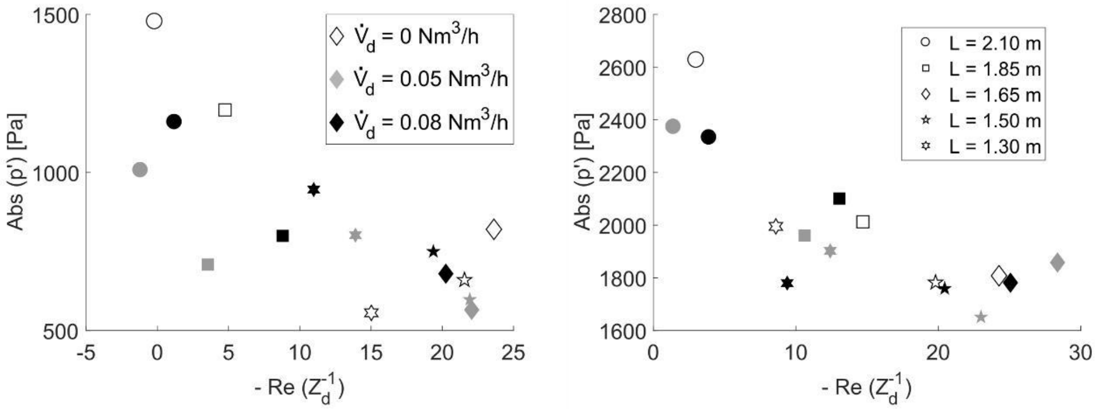

Fig. 3.40. Amplitude of the limit cycle with normalized acoustic losses, as a function of the flow rate of pilot fuel and tube lengths (denoted, respectively, by the different colors and symbols). Left: Φ=0.86, Right: Φ=0.72.

The data points display a more defined trend for Φ=0.72 (right plot of Fig. 3.40), probably due to the low influence of the pilot flame in this case. That is probably why, for Φ=0.86 (left plot of Fig. 3.40), the values are more scattered, and the same happens for Φ=0.98 (the pattern obtained is very similar to the one obtained for Φ=0.86, so data have not been shown for brevity).

Finally, some additional experiments were carried out in cold conditions, in order to exclude that some thermal or fluid-dynamic effect could be responsible for the p' variations in the absence of a pilot flame. For these tests the combustion chamber length was set to 750 mm, since this length presents a resonant frequency of 100 Hz at ambient temperature, close to the one for which PAIC lengths have been optimized; external excitation was provided by the loudspeakers.

The results clearly show a well-defined, negative correlation, further supporting that the variation of dynamic pressure observed in absence of pilot flame are caused by dissipation induced by the pilot fuel channel.

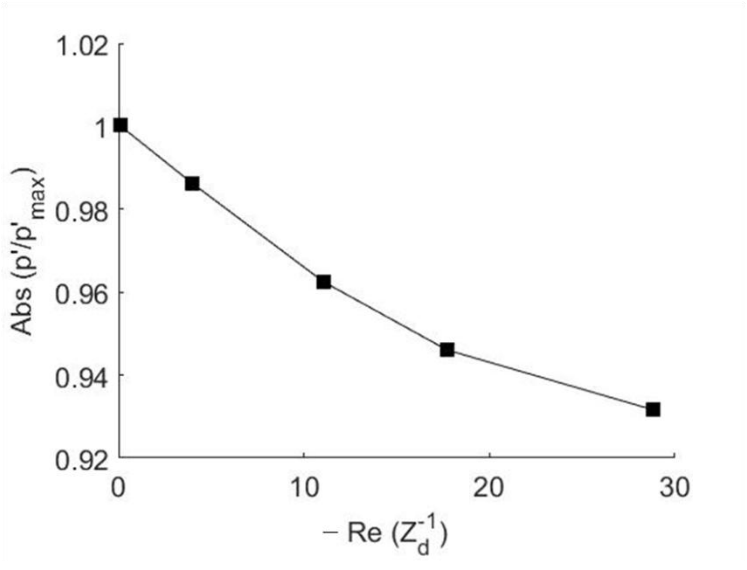

Fig. 3.41. p′ amplitude vs acoustic losses, both normalized, for tests performed in cold conditions

This is a result of practical interest, since it widens the possibility of PAIC; in fact, a proper combination of acoustic dissipation (caused by Z_d^{-1}) and thermoacoustic damping (induced by an out-of-phase oscillation of Q_d' with respect to p') would possibly lead to a very effective decrease of the amplitude of a self-induced instability.

In summary, the significant damping obtained with PAIC is due to the superposition of two effects: dynamic interaction between the pilot and the main flame, and purely passive dissipation at the orifice. It should be noted that this in part invalidates the analysis attempted in Fig. 3.36, that is, an estimation of $\mathrm{FTF_d}$ phase, since this reasoning considers Q_d' as the sole cause of damping. This might also explain why cases 6-8 in the first test campaign yielded so different p' magnitudes with respect to cases 1-5. So, the superposition of the two phenomena (the heat release oscillation in the pilot flame and the pure acoustic response of the pilot tube) should be accounted for in order to properly estimate $\mathrm{FTF_d}$.

3.5.6 *Conclusions*

A novel strategy conceived to reduce the amplitude of p' in limit cycle conditions has been proposed and tested in an experimental combustion rig. The system proposed seeks to mimic the effects induced by active controls, but involving only passive elements, so that it has been called *pseudo-active instability control* (PAIC). The strategy consists in producing an oscillation in a tiny, pilot flame (injected in the core of the main flame) out of phase with the pressure amplitude of the system, in order to damp the acoustic energy released. The acoustic response of the injection duct to p' is the driving force which induces the oscillations in the pilot flame.

The main difficulty found in the design of the system is the impossibility of defining the flame transfer function of the diffusion flame, $\mathrm{FTF_d}$. Therefore, a wide range of PAIC acoustic responses has been tested, in order to see if the system is sensitive to the acoustic characteristics of the secondary injection and to look for some conditions in which p' is effectively reduced. The implementation of PAIC on the experimental rig has led, in some cases, to variation of almost two times in the amplitude of p' with respect to the value obtained without pilot flame, either amplifying or reducing the amplitude, depending on the operating conditions. This can be considered as a clear proof of the proposed concept. So, these preliminary results suggest that the system proposed can be considered as a possible alternative to control thermoacoustic instabilities, even though further research is needed to achieve robust PAIC designs.

A key piece needed to make PAIC a reliable system is the knowledge of $\mathrm{FTF_d}$. The results make clear that the dynamic interaction between the two flames causes important variations in p' amplitude, but it was impossible to isolate the response of the diffusion flame which would be needed to optimize the system by achieving out-of-phase heat release in the main and pilot flames. Also, another interesting result is the low effectiveness of PAIC when leaner conditions are set, probably due to a different combustion behavior of the pilot flame when the air surplus is higher. Finally, it has been observed that the dynamics of the system is also affected when no pilot flame is present, the pilot injection acting as an acoustic resonator which is more or less effective in damping the pressure fluctuations depending on its acoustic impedance. This makes PAIC even more interesting, since, if suitably designed, it can modulate the dynamic pressure in two ways.

In summary, this preliminary investigation on PAIC demonstrates a good potential, making it worth for further analysis. Nevertheless, some key pieces would be needed to make the system robust and reliable, the most important being the description of the dynamic response of the pilot flame. Therefore, future work about PAIC should be focused firstly on the study of $\mathrm{FTF_d}$, and secondly on the analysis of the differences in the combustion behavior of the pilot flame with high and low excess of air. Progress along those lines could help to properly design the PAIC system, and so to exploit all its possibilities for the control of thermoacoustic instabilities.

3.6 Conclusions and future work

The investigation carried out pivots on the flame transfer function, FTF, as a key magnitude in thermoacoustics. In fact, the flame response to acoustic inputs results fundamental to conduct a thermoacoustic analysis and, at the same time, it still presents grey areas worth of being analyzed more in depth.

Throughout this work, various facets of thermoacoustic instabilities generated in gas turbine burners have been investigated and, in all of them, the flame response assumes a fundamental role. In fact, in many cases the FTF has been either the objective of the research carried out or a most important input to achieve the results.

The study combines experimental and modeling approaches, in order to gain comprehensive insight into the nature and characteristics of thermoacoustic instabilities. In particular, great effort has been devoted to conduct a broad range of experiments, to give a solid support to the theoretical results obtained.

Noteworthy, the tests have been performed on both pure methane and biogas flames. To the best of the author's knowledge, the literature about the dynamics of the latter is limited and, in particular, its FTF has not been reported before. Therefore, the analysis of the dynamics of biogas flames and the assessment of their FTF represent a further, important added value of this work.

The first part of the present study is dedicated to a novel procedure to process chemiluminiscence flame images. The method proposed is based on the joint analysis of local and global fluctuation of the heat released in the flame, to obtain the so-called "cross-correlation maps", CCM. According to the rationale behind CCM, the cross-correlation maps highlight the contribution of each flame parcel to its global dynamic response (that is, to FTF) both in magnitude and in quality (i.e. supporting or damping). The experimental CCM maps obtained for both methane and biogas flames show a quite good match with the expected theoretical patterns. These representations also reveal that vortex shedding is the mechanism which rules the dynamics of the flame analyzed. In particular, the zone in which the vortex roll-up occurs has been identified as the one which contributes the most to the global flame response.

The CCM has revealed itself as a simple yet effective method to gain insights into the dynamics of the flame analyzed. Three different applications of CCM have been proposed, the simplest one needing just a series of bandfiltered flame images. In case other relevant parameters were known, CC values can be converted into variables with notable physical meaning, quantifying the "local effective gain" as well as the net contribution a flame zone gives to the global FTF.

The analysis performed on final CC maps has led to important insights on some features of the local response of each flame zone, also confirmed by local FTF measurements. As an example of the potential of CCM in gaining information on the dynamics of the flame studied, an assessment of the characteristic flame length has been proposed. This magnitude is strictly related to the FTF time length, and the regions where CC peaks are found (ascribed to vortex roll-up) have been identified as a suitable reference to define this geometrical magnitude for the flames analyzed.

It has been observed that methane and biogas flames share similar patterns in terms of CC maps, highlighting that vortex shedding represents the dominant mechanism of instability for both fuels. Nevertheless, the characteristic lengths determined for biogas are greater than for methane, so confirming what was observed in the global FTFs: a higher time delay for biogas flames than for methane, which corresponds to longer flames at equal equivalence ratio. All these collateral analyses about differences and similarities in the FTF as well as the comparison between flame geometries have been duly reported throughout the document.

In summary, the method proposed can represent a suitable option for the analysis of the dynamics of premixed flames, since the features captured by CCM are not evidenced by the other post processing methods used in the literature. This means that CCM should be considered not as alternative to other analysis, but as complementary, in order to make an assessment about the flame dynamics more complete. The results obtained opens the way for future analyses: CCM has been tested just on perfectly premixed flame, and it would be interesting for the future also to apply the method on partially premixed flames, where two contributions superpose in the observed flame dynamics (namely, simultaneous fluctuations in inlet velocity and equivalence ratio).

The second part of this work consists of a systematic analysis in which various operational parameters have been varied in order to study the variation in unstable frequency. Tests have been performed for both methane and biogas flames, so that an in-depth comparison has been carried out about similarities and differences in the dynamic behaviors of the two flames for a broad variety of operational conditions. Generally speaking, biogas shows lower instability amplitudes with respect to methane, even though each condition tested shows peculiar characteristics. Also, the frequency of oscillation is generally lower for biogas flames than for methane ones.

This second parameter has been deeply analyzed. Firstly, a simple model (quarter-wave tube) has been used to estimate the unstable modes of the combustor, but predictions were not in line with experimental results. Therefore, a slightly more complex model has been adopted: a two-cavity system, representing the main features of the experimental facility, has been described through the so-called dispersion equation. One of the major differences with the quarter-wave tube model is that dispersion equation allows including the flame response (in terms of its FTF) as an input. The solutions obtained match with the experimental results, so confirming that the dynamic response of a flame represents a most important input to accurately describe the dynamics of a thermoacoustic system. Moreover, the difference in the modes between methane and biogas are well captured by the dispersion equation, whereas the variations in unstable frequencies, ultimately due to the differences in flame dynamics, cannot be predicted when a simpler model is used. Therefore, FTF contains enough information to distinguish between two different fuels, and no other input is needed to the model in this regard.

Even though the study has included a notably comprehensive test campaign, addressing the effects of a wide range of operational parameters, a further confirmation of the robustness of the analysis could come from tests with partially premixed flames or flames produced by other fuels. In the first case, a suitable FTF, describing the fluctuations generated by both the injection velocity and the equivalence ratio, should be used, to assess if, even in the case of a superposition of inputs, the FTF measured in the linear regime contains enough information to lead to correct values of the unstable modes of the system.

The final part of the study is focused on a novel system to control thermoacoustic instabilities. This control strategy is intended to damp the instability in the burner by spontaneously modulating the heat released by a pilot flame injected into the combustion chamber, so exploiting the same mechanisms used in an active control. However, the system proposed is only composed of passive elements, and the fluctuations are naturally induced by the acoustic response of the system to the pressure oscillation generated in the combustion chamber by the thermoacoustic instability. So, the device has been called “pseudo-active instability control”, PAIC.

A major difficulty encountered in the PAIC design is the impossibility of describing the response of the pilot flame for the configuration studied. In this context, the strategy followed consisted in exploring a range of cases with widely differing acoustic properties of the pilot line injection, as a means to evaluate the sensitivity of the response (i.e. limit cycle amplitude) to the particular conditions and, hence, the actual impact of the proposed strategy. With this aim, the length of the pilot injection has been modified, to vary the acoustic response of the system so as to cover the widest set of possible cases. The results have shown a relevant influence of the pilot flame on the dynamics of the system, with changes in the dynamic pressure amplitude by a factor of two in some cases (both amplifying and reducing the amplitude). Therefore, PAIC can be considered as a suitable option to suppress instabilities in a gas turbine burner, even if the design and the effects induced should be investigated more in depth. Moreover, PAIC has shown, unexpectedly, a considerable effect on the dynamics of the burner even in absence of the pilot flame. It has been verified that this influence is caused by the injection line, which acts as an acoustic resonator. This could represent a further advantage for PAIC, since the pressure oscillation can be controlled by two different methods, which can lead to a important mitigations of the instability strength if suitably combined.

As mentioned above, a relevant limitation in this investigation is represented by the impossibility of quantifying the acoustic response of the pilot flame; some attempts have been made in this work, but the results were not conclusive. Therefore, future research on the topic should focus on properly defining this function. This would allow for an optimization of the PAIC system and, so, for a solid confirmation of the effectiveness of this novel control strategy.

This report is based on five different papers published either in scientific journals or in international congresses, and it is intended as a summary of them. Further details on this research work can be found in these publications, which are enclosed to this document.

3.7 References

[1] B. Cosic, Nonlinear Thermoacoustic Stability Analysis of Gas Turbine Combustion Chambers, Ph.D. Thesis, Berlin University (2014)

[2] A. Dowling, S. R. Stow, Acoustic Analysis of Gas Turbine Combustors, J. Propul. Power 19 (2003) 751-764

[3] T. Lieuwen, B. T. Zinn, Theoretical investigation of combustion instability mechanisms in lean premixed gas turbines, 36th AIAA Aerospace Sciences Meeting and Exhibit (1998), paper AIAA-98-0641

[4] Y. Huang, V. Yang, Dynamics and stability of lean-premixed swirl-stabilized combustion, Prog. Energy Combust. Sci. 35 (2009) 293-364

[5] T. García Armingol, Operational issues and advanced monitoring in lean premixed syngas combustion, Ph.D. Thesis, University of Zaragoza (2014)

[6] J. W. S. Rayleigh, The explanation of certain acoustical phenomena, Nature 18 (1878) 319-321

[7] T. García-Armingol, Á. Sobrino, E. Luciano, J. Ballester, Impact of fuel staging on stability and pollutant emissions of premixed syngas flames, Fuel 185 (2016) 122-132

[8] Q. Sun, H. Li, J. Yan, L. Liu, Z. Yu, X. Yu, Selection of appropriate biogas upgrading technology-a review of biogas cleaning, upgrading and utilisation, Renew. Sust. Energ. Rev. 51 (2015) 521-532

[9] K. C. Surendra, D. Takara, A. G. Hashimoto, S. K. Khanal, Biogas as a sustainable energy source for developing countries: Opportunities and challenges, Renew. Sust. Energ. Rev. 31 (2014) 846-859

[10] S. E. Hosseini, M. A. Wahid, Development of biogas combustion in combined heat and power generation, Renew. Sust. Energ. Rev. 40 (2014) 868-875

[11] C. J. Mordaunt, W. C. Pierce, Design and preliminary results of an atmospheric-pressure model gas turbine combustor utilizing varying CO2 doping concentration in CH4 to emulate biogas combustion, Fuel 124 (2014) 258-268

[12] H. Nikpey, M. Assadi, P. Breuhaus, P. T. Mørkved, Experimental evaluation and ANN modeling of a recuperative micro gas turbine burning mixtures of natural gas and biogas, Appl. Energ. 117 (2014) 30-41

[13] (Eds), Biogas Handbook, University of Southern Denmark Esbjerg, 2008

[14] T. Leung, I. Wierzba, The effect of hydrogen addition on biogas non-premixed jet flame stability in a co-flowing air stream, Int. J. Hydrogen Energy 33 (2008) 3856-3862

[15] M. Saediamiri, M. Birouk, J. A. Kozinski, On the stability of a turbulent non-premixed biogas flame: Effect of low swirl strength, Combust. Flame 161 (2014) 1326-1336

[16] W. Dai, C. Qin, Z. Chen, C. Tong, P. Liu, Experimental studies of flame stability limits of biogas flame, Energy Convers. Manage. 63 (2012) 157-161

[17] K. Lee, H. Kim, P. Park, S. Yang, Y. Ko, CO2 radiation heat loss effects on NOx emissions and combustion instabilities in lean premixed flames, Fuel 106 (2013) 682-689

[18] Y. Lafay, B. Taupin, G. Martins, G. Cabot, B. Renou, A. Boukhalfa, Experimental study of biogas combustion using a gas turbine configuration, Exp. Fluids 43 (2007) 395-410

[19] S. Candel, Combustion dynamics and control: Progress and challenges, Proc. Combust. Inst. 29 (2002) 1-28

[20] T. Lieuwen, Modeling Premixed Combustion–Acoustic Wave Interactions: A Review, J. Propul. Power 19 (2003) 765-781

[21] P. R. Alemela, Measurement and scaling of acoustic transfer matrices of premixed swirl flames, Ph.D. Thesis, Technische Universität München (2009)

[22] T. Lieuwen, Nonlinear kinematic response of premixed flames to harmonic velocity disturbances, Proc. Combust. Inst. 30 (2005) 1725-1732

[23] B. D. Bellows, M. K. Bobba, A. Forte, J. M. Seitzman, T. Lieuwen, Flame transfer function saturation mechanisms in a swirl-stabilized combustor, Proc. Combust. Inst. 31 (2007) 3181-3188

[24] D. Durox, T. Schuller, S. Candel, Combustion dynamics of inverted conical flames, Proc. Combust. Inst. 30 (2005) 1717-1724

[25] K. Oberleithner, S. Schimek, C. O. Paschereit, Shear flow instabilities in swirl-stabilized combustors and their impact on the amplitude dependent flame response: A linear stability analysis, Combust. Flame 162 (2015) 86-99

[26] S. Ducruix, D. Durox, S. Candel, Theoretical and experimental determinations of the transfer function of a laminar premixed flame, Proc. Combust. Inst. 28 (2000) 765-773

[27] P. Palies, T. Schuller, D. Durox, S. Candel, Modeling of premixed swirling flames transfer functions, Proc. Combust. Inst. 33 (2011) 2967-2974

[28] T. Schuller, D. Durox, S. Candel, A unified model for the prediction of laminar flame transfer functions: comparisons between conical and V-flame dynamics, Combust. Flame 134 (2003) 21-34

[29] P. Subramanian, R. S. Blumenthal, W. Polifke, R. I. Sujithc, Distributed Time Lag Response Functions for the Modelling of Combustion Dynamics, Combust. Theor. Model. 19 (2015) 223-237

[30] A. Gentemann, C. Hirsch, F. Kiesewetter, T. Sattlemayer, W. Polifke, Validation of flame transfer function reconstruction for perfectly premixed swirl flames, ASME Turbo Expo 2004 (2004), paper GT2004-53776

[31] D. Durox, T. Schuller, N. Noiray, S. Candel, Experimental analysis of nonlinear flame transfer functions for different flame geometries, Proc. Combust. Inst. 32 (2009) 1391-1398

[32] K. T. Kim, J. G. Lee, B. D. Quay, D. A. Santavicca, Spatially distributed flame transfer functions for predicting combustion dynamics in lean premixed gas turbine combustors, Combust. Flame 157 (2010) 1718-1730

[33] R. Balachandran, B. O. Ayoola, C. F. Kaminski, A. P. Dowling, E. Mastorakos, Experimental investigation of the nonlinear response of turbulent premixed flames to imposed inlet velocity oscillations, Combust. Flame 143 (2005) 37-55

[34] F. Richecoeur, T. Schuller, A. Lamraoui, S. Ducruix, Analytical and experimental investigations of gas turbine model combustor acoustics operated at atmospheric pressure, C. R. Mecanique 341 (2013) 141-151

[35] A. Lamraoui, F. Richecoeur, S. Ducruix, T. Schuller, Experimental analysis of simultaneous non-harmonically related unstable modes in a swirled combustor ASME Turbo Expo (2011), paper GT 2011-46701

[36] V. Bellucci, B. Schuermans, D. Nowak, P. Flohr, C. O. Paschereit, Thermoacoustic Modeling of a Gas Turbine Combustor Equipped With Acoustic Dampers, Journal of Turbomachinery 127 (2005) 372-379

[37] J. Peterleithner, N. V. Stadlmair, J. Woisetschläger, T. Sattelmayer, Analysis of Measured Flame Transfer Functions With Locally Resolved Density Fluctuation and OH-Chemiluminescence Data, J. Eng. Gas Turb. Power 138 (2015) 031504 1-9

[38] H. J. Kim, J. P. Cha, J. K. Song, Y. S. Ko, Geometric and number effect on damping capacity of Helmholtz resonators in a model chamber, J. Sound Vib. 329 (2010) 3266-3279

[39] G. A. Richards, D. L. Straub, E. H. Robey, Passive Control of Combustion Dynamics in Stationary Gas Turbines, J. Propul. Power 19 (2003) 795-810

[40] K. R. McManus, T. Poinsot, S. M. Candel, A review of active control of combustion instabilities, Prog. Energy Combust. Sci. 19 (1993) 1-29

[41] C. H. Sohn, J. H. Park, A comparative study on acoustic damping induced by half-wave, quarter-wave, and Helmholtz resonators, Aerosp. Sci. Technol. 15 (2011) 606-614

[42] J. D. Eldredge, A. P. Dowling, The absorption of axial acoustic waves by a perforated liner with bias flow, J. Fluid Mech. 485 (2003) 307-335

[43] G. A. Richards, J. M. Yip, Oscillating Combustion &om a Premix Fuel Nozzle, Combustion Institute/American Flame Research Committee Meeting (1995), paper DOE/METC/C-95/7189

[44] G. A. Richards, J. M. Yip, R. Gemmen, Design Factors for Stable Lean Premix Combustion, Advanced Coal-Fired Power Systems 95 Review Meeting (1995), paper DOE/METC/C-96/7210

[45] E. Luciano, J. Ballester, Analysis of the dynamic response of premixed flames through chemiluminescence cross-correlation maps, Combust. Flame 194 (2018) 296-308

[46] E. Luciano, J. Ballester, Analysis of the Dynamics of Premixed Methane and Biogas Flames Based on Cross-correlation Maps, Combust. Sci. Technol. 191 (2019) 1-26

[47] E. Luciano, E. Tizné, J. Ballester, Use of Flame Transfer Function to Predict Combustor Unstable Modes, 24th International Congress on Sound and Vibration (2017), paper 905

[48] J. Oliva, E. Luciano, J. Ballester, Damping of Combustion Instabilities Through Pseudo-Active Control, ASME Turbo Expo 2018: Turbomachinery Technical Conference and Exposition (2018), paper 51067

[49] E. Luciano, J. Oliva, Á. Sobrino, J. Ballester, Analysis of a Pseudo-active Approach for the Control of Thermoacoustic Instabilities, Combust. Sci. Technol. 192 (2020) 1-28

[50] https://ec.europa.eu/clima/policies/strategies/2020_en#tab-0-1, as of 25/01/2020

[51] http://www.cop21paris.org/, as of 25/01/2020

[52] https://ec.europa.eu/clima/policies/strategies/2030_en#tab-0-1, as of 25/01/2020

[53] I. E. Agency, World Energy Outlook 2019, (2019)

[54] M. A. Nemitallah, A. A. Abdelhafez, M. A. Habib, Premixed Combustion for Gas-Turbine Applications, in: Medhat A. Nemitallah, Ahmed A. Abdelhafez and Mohamed A. Habib (Eds.), Approaches for Clean Combustion in Gas Turbines Vol. Springer International Publishing, Cham, 2020, pp. 13-97

[55] S. M. Correa, A review of NOx formation under gas-turbine combustion conditions, Combust. Sci. Technol. 87 (1993) 329-362

[56] P. Palies, D. Durox, T. Schuller, P. Morenton, S. Candel, Dynamics of premixed confined swirling flames, C. R. Mecanique 337 (2009) 395-405

[57] T. Lieuwen and V. Yang (Eds), Combustion Instabilities in Gas Turbine Engines: Operational Experience, Fundamental Mechanisms, and Modeling, PrAA, AIAA, 2005

[58] S. Terhaart, O. Krüger, P. C. Oliver, Flow field and flame dynamics of swirling methane and hydrogen flames at dry and steam diluted conditions, J. Eng. Gas Turb. Power 137 (2014) 1-10

[59] D. Kim, J. G. Lee, B. D. Quay, D. A. Santavicca, K. Kim, S. Srinivasan, Effect of flame structure on the flame transfer function in a premixed gas turbine combustor, J. Eng. Gas Turb. Power 132 (2010)

[60] P. Palies, D. Durox, T. Schuller, S. Candel, Nonlinear combustion instability analysis based on the flame describing function applied to turbulent premixed swirling flames, Combust. Flame 158 (2011) 1980-1991

[61] D. Kim, J. G. Lee, B. D. Quay, D. A. Santavicca, K. Kim, S. Srinivasan, Effect of flame structure on the flame transfer function in a premixed gas turbine combustor, J. Eng. Gas Turb. Power 132 (2010) 021502 1-7

[62] J. Ballester, T. García-Armingol, Diagnostic techniques for the monitoring and control of practical flames, Prog. Energy Combust. Sci. 36 (2010) 375-411

[63] B. O. Ayoola, R. Balachandran, J. H. Frank, E. Mastorakos, C. F. Kaminski, Spatially resolved heat release rate measurements in turbulent premixed flames, Combust. Flame 144 (2006) 1-16

[64] Y. Hardalupas, M. Orain, Local measurements of the time-dependent heat release rate and equivalence ratio using chemiluminescent emission from a flame, Combust. Flame 139 (2004) 188-207

[65] C. S. Panoutsos, Y. Hardalupas, A. M. K. P. Taylor, Numerical evaluation of equivalence ratio measurement using OH∗ and CH∗ chemiluminescence in premixed and non-premixed methane–air flames, Combust. Flame 156 (2009) 273-291

[66] Z. Han, S. Balusamy, S. Hochgreb, Spatial Analysis on Forced Heat Release Response of Turbulent Stratified Flames, J. Eng. Gas Turb. Power 137 (2015) 061504 1-8

[67] K. T. Kim, J. G. Lee, H. J. Lee, B. D. Quay, D. Santavicca, Characterization of Forced Flame Response of Swirl-Stabilized Turbulent Lean-Premixed Flames in a Gas Turbine Combustor, J. Eng. Gas Turb. Power 132 (2010) 041502 1-8

[68] M. G. De Giorgi, A. Sciolti, S. Campilongo, A. Ficarella, Image processing for the characterization of flame stability in a non-premixed liquid fuel burner near lean blowout, Aerosp. Sci. Technol. 49 (2016) 41-51

[69] P. Palies, D. Durox, T. Schuller, S. Candel, The combined dynamics of swirler and turbulent premixed swirling flames, Combust. Flame 157 (2010) 1698-1717

[70] A. J. De Rosa, J. Samarasinghe, S. J. Peluso, B. D. Quay, D. A. Santavicca, Flame Area Fluctuation Measurements in Velocity-Forced Premixed Gas Turbine Flames, J. Eng. Gas Turb. Power 138 (2015) 041507 1-9

[71] N. A. Bunce, B. D. Quay, D. A. Santavicca, Interaction Between Swirl Number Fluctuations and Vortex Shedding in a Single-Nozzle Turbulent Swirling Fully-Premixed Combustor, J. Eng. Gas Turb. Power 136 (2013) 021503 1-11

[72] S. Schimek, J. P. Moeck, C. O. Paschereit, An Experimental Investigation of the Nonlinear Response of an Atmospheric Swirl-Stabilized Premixed Flame, J. Eng. Gas Turb. Power 133 (2011) 101502 1-7

[73] S. Balusamy, L. K. B. Li, Z. Han, S. Hochgreb, Extracting flame describing functions in the presence of self-excited thermoacoustic oscillations, Proc. Combust. Inst. 36 (2017) 3851-3861

[74] M. C. Lee, J. Yoon, S. Joo, J. Kim, J. Hwang, Y. Yoon, Investigation into the cause of high multi-mode combustion instability of H2/CO/CH4 syngas in a partially premixed gas turbine model combustor, Proc. Combust. Inst. 35 (2015) 3263-3271

[75] M. Emadi, K. Kaufman, M. W. Burkhalter, T. Salameh, T. Gentry, A. Ratner, Examination of thermo-acoustic instability in a low swirl burner, Int. J. Hydrogen Energy 40 (2015) 13594-13603

[76] D. M. Kang, F. E. C. Culick, A. Ratner, Combustion dynamics of a low-swirl combustor, Combust. Flame 151 (2007) 412-425

[77] Y. Huang, Combustion dynamics of swirl-stabilized lean premixed flames in an acoustically-driven environment, Ph.D. Thesis, University of Iowa (2008)

[78] M. Hauser, M. Lorenz, T. Sattelmayer, Influence of Transversal Acoustic Excitation of the Burner Approach Flow on the Flame Structure, J. Eng. Gas Turb. Power 133 (2010) 041501 1-8

[79] E. Luciano, Á. Sobrino, J. Ballester, A Novel Approach for the Evaluation of Local and Global Flame Time Lag from OH* Filtered Images, 22nd International Congress on Sound and Vibration (2015), paper 1089

[80] A. J. De Rosa, S. J. Peluso, B. D. Quay, D. A. Santavicca, The Effect of Confinement on the Structure and Dynamic Response of Lean-Premixed, Swirl-Stabilized Flames, J. Eng. Gas Turb. Power 138 (2015) 061507 1-10

[81] Z. Han, S. Hochgreb, The response of stratified swirling flames to acoustic forcing: Experiments and comparison to model, Proc. Combust. Inst. 35 (2015) 3309-3315

[82] F. Duchaine, F. Boudy, D. Durox, T. Poinsot, Sensitivity analysis of transfer functions of laminar flames, Combust. Flame 158 (2011) 2384-2394

[83] J. C. Román Casado, Nonlinear behavior of the thermo acoustic instabilities in the limousine combustor, Ph.D. Thesis, University of Twente (2013)

[84] L. Tay-Wo-Chong, S. Bomberg, A. Ulhaq, T. Komarek, W. Polifke, Comparative Validation Study on Identification of Premixed Flame Transfer Function, J. Eng. Gas Turb. Power 134 (2011) 021502 1-8

[85] D. Kim, S. W. Park, Forced and self-excited oscillations in a natural gas fired lean premixed combustor, Fuel Process. Technol. 91 (2010) 1670-1677

[86] V. N. Kornilov, M. Manohar, L. P. H. de Goey, Thermo-acoustic behaviour of multiple flame burner decks: Transfer Function (de)composition, Proc. Combust. Inst. 32 (2009) 1383-1390

[87] https://www.grc.nasa.gov/www/CEAWeb/, as of 31/08/2020

[88] T. Guiberti, Analysis of the topology of premixed swirl-stabilized confined flames, Ph.D. Thesis, École Centrale Paris (2015)

[89] A. P. Dowling, A. S. Morgans, FEEDBACK CONTROL OF COMBUSTION OSCILLATIONS, Annual Review of Fluid Mechanics 37 (2005) 151-182

[90] F. Weng, S. Li, D. Zhong, M. Zhu, Investigation of self-sustained beating oscillations in a Rijke burner, Combust. Flame 166 (2016) 181-191

[91] K. I. Matveev, Thermoacoustic instabilities in the Rijke tube: experiments and modeling, Ph.D. Thesis, California Institute of Technology (2003)

[92] W. Polifke, A. Gentemann, Order and Realisability of Impulse Response Filters for Accurate Identification of Acoustical Multi-ports from Transient CFD, Int. J. Acoust. Vib. 9 (2004) 139-148

[93] B. Schuermans, H. Luebcke, D. Bajusz, P. Flohr, Thermoacoustic Analysis of Gas Turbine Combustion Systems Using Unsteady CFD, ASME Turbo Expo 2005: Power for Land, Sea, and Air (2005), paper GT2005-68393

[94] T. Z. Liewven, B.T., Theoretical investigation of combustion instability mechanisms in lean premixed gas turbines, 36th AIAA Aerospace Sciences Meeting and Exhibit (1998), paper 641

[95] N. Noiray, D. Durox, T. Schuller, S. Candel, A unified framework for nonlinear combustion instability analysis based on the flame describing function, J. Fluid Mech. 615 (2008) 139-167

[96] J. Li, A. S. Morgans, Time domain simulations of nonlinear thermoacoustic behaviour in a simple combustor using a wave-based approach, J. Sound Vibrat. 346 (2015) 345-360

[97] K. T. Kim, D. Santavicca, Linear stability analysis of acoustically driven pressure oscillations in a lean premixed gas turbine combustor, J. Mech. Sci. Technol. 23 (2009) 3436-3447

[98] N. Noiray, D. Durox, T. Schuller, S. Candel, Self-induced instabilities of premixed flames in a multiple injection configuration, Combust. Flame 145 (2006) 435-446

[99] W. Krebs, S. Bethke, J. Lepers, P. Flohr, B. Prade, C. Johnson, S. Sattinger, Thermoacoustic design tools and passive control: Siemens Power Generation approaches, in: Timothy C. Lieuwen and Victor Yang (Eds.), Combustion Instabilities in Gas Turbine Engines, in Progress in Astronautics and Aeronautics Vol. 210, AIAA, 2005, pp. 89-112

[100] I. D. J. Dupère, A. P. Dowling, The Use of Helmholtz Resonators in a Practical Combustor, J. Eng. Gas Turb. Power 127 (2005) 268-275

[101] D. Zhao, A. S. Morgans, Tuned passive control of combustion instabilities using multiple Helmholtz resonators, J. Sound Vib. 320 (2009) 744-757

[102] S. Li, Q. Li, L. Tang, B. Yang, J. Fu, C. A. Clarke, X. Jin, C. Z. Ji, H. Zhao, Theoretical and experimental demonstration of minimizing self-excited thermoacoustic oscillations by applying anti-sound technique, Appl. Energy 181 (2016) 399-407

[103] J. M. de Bedout, M. A. Franchek, R. J. Bernhard, L. Mongeau, Adaptive-passive noise control with self-tuning Helmholtz Resonators, J. Sound Vib. 202 (1997) 109-123

[104] S. J. Estève, M. E. Johnson, Adaptive Helmholtz resonators and passive vibration absorbers for cylinder interior noise control, J. Sound Vib. 288 (2005) 1105-1130

[105] A. P. Dowling, A. S. Morgans, Feedback control of combustion oscillations, Annu. Rev. Fluid Mech. 37 (2005) 151-182

[106] S. S. Sattinger, Y. Neumeier, A. Nabi, B. T. Zinn, D. J. Amos, D. D. Darling, Sub-Scale Demonstration of the Active Feedback Control of Gas-Turbine Combustion Instabilities, J. Eng. Gas Turb. Power 122 (2000) 262-268

[107] Y. Neumeier, B. T. Zinn, Experimental demonstration of active control of combustion instabilities using real-time modes observation and secondary fuel injection, Symp. (Int.) Combust. 26 (1996) 2811-2818

[108] J. Hermann, S. Hoffmann, Implementation of active control in a full-scale gas-turbine combustor, in: Tim Lieuwen and Vigor Yang (Eds.), Combustion Instabilities in Gas Turbine Engines, in Progress in Astronautics and Aeronautics Vol. 210, AIAA, Whashington, 2005, pp. 611-634

[109] J. Li, S. Peluso, B. Quay, D. A. Santavicca, Effect of pilot flame on flame macrostructure and combustion instability, ASME Turbo Expo 2017: Turbomachinery Technical Conference and Exposition (2017), paper GT2017-64079

[110] R. Riazi, M. Farshchi, M. Shimura, M. Tanahashi, T. Miyauchi, An Experimental Study on Combustion Dynamics and NOx Emission of a Swirl Stabilized Combustor with Secondary Fuel Injection, J. Therm. Sci. Tech. 5 (2010) 266-281

[111] G.-M. Choi, M. Tanahashi, T. Miyauchi, Control of oscillating combustion and noise based on local flame structure, Proc. Combust. Inst. 30 (2005) 1807-1814

[112] J. Shinjo, S. Matsuyama, Y. Mizobuchi, S. Ogawa, Study on flame dynamics with secondary fuel injection control by large eddy simulation, Combust. Flame 150 (2007) 277-291

[113] M. Tanahashi, S. Murakami, T. Miyauchi, G.-M. Choi, Control of oscillating combustion and measurements of turbulent flames, Proceedings of 5th Symposium on Smart Control of Turbulence (2004), paper 3.2

[114] J. Moeck, M. Bothien, D. Guyot, C. Paschereit, Phase-shift control of combustion instability using (combined) secondary fuel injection and acoustic forcing, in: R. King (Eds.), Active Flow Control Vol. 95, Springer, 2007, pp. 408-421

[115] D. Guyot, M. Röbler, M. R. Bothien, C. O. Paschereit, Active control of combustion instability using pilot and premix fuel modulation, 14th International Congress on Sound and Vibration (2007), paper 235

[116] J. G. Lee, K. Kim, D. A. Santavicca, Effect of injection location on the effectiveness of an active control system using secondary fuel injection, Proc. Combust. Inst. 28 (2000) 739-746

[117] S. Tachibana, L. Zimmer, Y. Kurosawa, K. Suzuki, Active control of combustion oscillations in a lean premixed combustor by secondary fuel injection coupling with chemiluminescence imaging technique, Proc. Combust. Inst. 31 (2007) 3225-3233

[118] J. G. Lee, D. A. Santavicca, Experimental Diagnostics for the Study of Combustion Instabilities in Lean Premixed Combustors, J. Propul. Power 19 (2003) 735-750

[119] M. P. Auer, C. Gebauer, K. G. Mösl, C. Hirsch, T. Sattelmayer, Active Instability Control: Feedback of Combustion Instabilities on the Injection of Gaseous Fuel, J. Eng. Gas Turb. Power 127 (2004) 748-754

[120] G. A. Richards, E. H. Robey, Effect of Fuel System Impedance Mismatch on Combustion Dynamics, J. Eng. Gas Turb. Power 130 (2008) 1-7

[121] G. Richards, D. Straub, E. Robey, Control of Combustion Dynamics Using Fuel System Impedance, ASME Turbo Expo 2003: International Joint Power Generation Conference (2003), paper GT2003-38521

[122] G. A. Richards, D. L. Straub, E. H. Robey, Dynamic Response of a Premix Fuel Injector, ASME Turbo Expo 2001: Power for Land, Sea, and Air (2001), paper GT2001-0036

[123] A. Huber, W. Polifke, Impact of Fuel Supply Impedance on Combustion Stability of Gas Turbines, ASME Turbo Expo 2008: Power for Land, Sea and Air (2008), paper GT2008-51193

[124] N. Noiray, D. Durox, T. Schuller, S. Candel, Dynamic phase converter for passive control of combustion instabilities, Proc. Combust. Inst. 32 (2009) 3163-3170

[125] C. O. Paschereit, P. Flohr, E. J. Gutmark, Combustion Control by Vortex Breakdown Stabilization, J. Turbomach. 128 (2002) 679-688

[126] C. Li, S. Li, X. Cheng, M. Zhu, Measurements and Modeling of the Dynamic Response of a Pilot Stabilized Premixed Flame Under Dual-Input Perturbation, ASME Turbo Expo 2017: Turbomachinery Technical Conference and Exposition (2017), paper GT2017-63843

[127] J. J. Keller, Thermoacoustic oscillations in combustion chambers of gas turbines, AIAA journal 33 (1995) 2280-2287

[128] M. Peters, A. Hirschberg, A. Reijnen, A. Wijnands, Damping and reflection coefficient measurements for an open pipe at low Mach and low Helmholtz numbers, J. Fluid Mech. 256 (1993) 499-534

4

Papers

Combustion and Flame 194 (2018) 296–308

Contents lists available at ScienceDirect

Combustion and Flame

journal homepage: www.elsevier.com/locate/combustflame

Analysis of the dynamic response of premixed flames through chemiluminescence cross-correlation maps

Ennio Luciano[a], Javier Ballester[b,*]

[a] Laboratory of Research on Fluid Dynamics and Combustion Technologies (LIFTEC), CSIC – University of Zaragoza, Spain
[b] Fluid Mechanics Group/LIFTEC, CSIC – University of Zaragoza, Spain

A R T I C L E I N F O

Article history:
Received 8 December 2017
Revised 3 May 2018
Accepted 4 May 2018
Available online 25 May 2018

Keywords:
Cross-correlation maps
Thermoacoustic instability
Chemiluminescence imaging
Flame transfer function

A B S T R A C T

This work proposes a novel methodology to extract useful information on flame dynamics from instantaneous chemiluminescence images in terms of the ‘effective local response’, by means of the so-called cross-correlation maps (CCM). Theoretical considerations suggest that CCM presents some advantages with respect to other options: it allows filtering out some spurious heat release rate fluctuations, not related to the acoustic excitation (either natural or forced) and generates a map of the ‘effective gain’, which can be interpreted as the actual contribution of each flame parcel to the global dynamic response. The method has been applied to an experimental dataset collected for premixed V flames of methane and CO_2/methane blends, covering a wide range of operating conditions. The results are fully consistent with the physical interpretation proposed for the cross-correlation maps, and confirm their potential for diagnosing the effective contribution of the different flame regions to the global dynamic response, as quantified, for example, in terms of the flame transfer function. With further hypotheses (e.g., n-τ formulation), CCM can provide further information about some features of the dynamic flame response, such as the characteristic flame length related to convective time lag and, hence, to the phase of the FTF. Cross-correlation maps are also compared with the spatial distribution of the local Rayleigh index, revealing a qualitatively similar pattern but also some essential differences, related to the different nature of both magnitudes. CC maps reflect the intrinsic dynamic response of the flame, whereas the Rayleigh index is related to the spontaneous instability and, hence, depends on the coupling between flame and the rest of the system.

1. Introduction

Due to the very low values of pollutant emissions achieved, lean premixed combustion has prevailed among other solutions in the gas turbines field, and nowadays represents the leading technology for these plants [1]. However, lean flames are more prone to combustion dynamics [2], a phenomenon due to in-phase coupling between pressure fluctuation (p') and heat release oscillation (Q') in the combustion chamber [3]. The instability grows due to the acoustic energy supplied by the flame, in a way determined by its dynamic response. Hence, even though these are system instabilities, an adequate description of flame response is one of the main objectives in this field.

The flame transfer function (FTF) is normally used to characterize the linear, global flame response, in terms of Q' amplitude, to inputs which can affect heat release rate fluctuation (equivalence ratio, Φ', and/or inlet velocity, u' [4,5]), as a function of frequency. The paramount importance of this parameter in the study of thermoacoustics justifies the large number of works devoted to determine FTF and to investigate its characteristics in different configurations. For the most common case of perfectly premixed, V-shaped flames, many studies coincide in that their FTF presents a low-pass filter behavior in gain and an almost linear trend in phase [6–12].

The global response of the flame, as quantified by its FTF, is the result of the dynamic response of different flame regions, each contributing with widely different magnitudes and phases. Hence, the bulk Q' could actually reflect the dynamics of some flame portions, whereas other regions may even present negative contributions and, so, would tend to damp the response to an acoustic excitation. Since all these features are lost in the spatial

---

[*] Corresponding author. Present address: Fluid Mechanics Group, School of Engineering and Architecture, María de Luna, 3, 50018 Zaragoza, Spain.
E-mail address: ballester@unizar.es (J. Ballester).

https://doi.org/10.1016/j.combustflame.2018.05.005

Nomenclature

Latin

f	frequency
G	gain of flame transfer function
I	intensity of bandfiltered radiation
i	normalized radiation intensity
K	constant, as defined in Eq. (10)
L	characteristic convective length
N_{im}	number of images
N_{px}	number of pixels per image
n	gain of the $n-\tau$ model
p	pressure
Q	heat release rate
q	normalized heat release rate
T	integration time
t	time
u	injection velocity
V	mean convective velocity

Acronyms

CCM	cross correlation map
FFT	fast Fourier transform
FTF	flame transfer function
PMT	photomultiplier tube
PT	pressure transducer
RI	Rayleigh index

Greek

σ	standard deviation
τ	time delay of the $n-\tau$ model
φ	phase of flame transfer function
Φ	equivalence ratio
ω	angular frequency

Overscripts

$\overline{()}$	mean quantity
$\widehat{()}$	fast Fourier transform

Superscripts

$()'$	fluctuation

Subscripts

ex,f	relative to external acoustic forcing
x	denotes a local value of the variable at a generic location x

integration of Q', some kind of space-resolved diagnostic should be employed to analyze the local contribution of different flame zones to the global response. The proportionality between the chemiluminescence emission at certain wavelengths (e.g., CH* or OH* bands) and the instantaneous heat release rate [9,13–15] makes the analysis of bandfiltered images of the flame a most valuable tool in this respect, although the process needed to extract the relationship between global and local response is not so obvious.

Some information about the flame dynamic behavior can be obtained from time averaged maps of the heat released by the flame (analyzed either from line-of-sight integrated or Abel-deconvoluted images [9,10,16–18]), by extracting selected geometric characteristics of the flame, such as length, angle, aspect ratio (see, for example, [17,19]), which have been used as inputs to model the global response of laminar V flames [20,21] and turbulent, swirl-stabilized ones [22]. Local time averaged values, however, are not representative of the local dynamic response of the flame parcels. Alternatively, the standard deviation of the chemiluminescence intensity recorded at different locations could be used as a measure of local fluctuations [23–26]. It should be noted, however, that fluctuation maps could be influenced by spurious contributions such as spatial flame movements (e.g., wobbling), broadband fluctuations (e.g., due to turbulence) or noise, which do not actually contribute to the global thermoacoustic response of the flame, as represented by the FTF.

Phase-locked chemiluminescence images have been widely applied for the analysis of flame instabilities (e.g., [10,18,26–30]). This is a most valuable tool to reconstruct and interpret the dynamic flame behavior along an oscillation cycle. However, how to extract from phase-resolved maps statistically meaningful information on the effective contribution of different regions to the global Q' is not at all obvious. As a possibility, phase-locked images can be further processed to obtain the spatial distribution of the Rayleigh index (see, e.g., [31–34]). This is a most relevant magnitude in thermoacoustics, since it expresses the acoustic energy generated by the coupling of pressure and heat release oscillations [3]. Therefore, the RI map describes the role of different flame areas, in which acoustic energy can be either generated or damped (respectively due to in-phase or out-of-phase oscillation with respect to p'). Nevertheless, it is important to note that RI maps describe the coupling between the flame and the acoustics of the whole system and, hence, do not inform on the intrinsic response of the flame.

Alternatively, if chemiluminescence images are acquired at high frame rates, the frequency content of local heat release rate oscillations can be determined by performing the fast Fourier transform (FFT) on every pixel. Among other advantages, this procedure filters out spurious fluctuations not related to the acoustic excitation or to a specific oscillation mode. This approach has been applied in a few works [16,35], demonstrating the very good potential of local FFT to describe in detail the dynamics of the flame. However, as it will be discussed later, the effective role of different zones in building global Q' cannot be ascertained directly from these maps and further processing of FFT would be required, in particular to evaluate the actual synchrony between local oscillations and global flame response.

Therefore, the magnitude of local oscillations in a given flame region may not be indicative of its actual contribution to the global response of the flame, as quantified in terms of bulk Q' or FTF. In this work, the approach proposed to address such analysis is the evaluation of the '*effective local contribution*' of different portions of the flame to its global response and, to this end, a novel methodology based on '*cross-correlation maps*' (CCM) is proposed. In its simplest form, this approach only requires a series of instantaneous, low frame rate, bandfiltered flame images, which are converted into 2D maps directly related to the magnitude of the share of global response associated with different flame portions. A very preliminary version was presented in [36], showing its potential for the qualitative assessment of distributed dynamic response. That development was parallel to the method used in [37], based on the so-called '*heat release rate index maps*', which was successfully applied to diagnose the role of different flame zones in the global dynamic response.

In this article, the physical interpretation of CC maps is discussed and expressed in terms of the parameters of local and global FTF. The results of CCM analysis are illustrated here for a wide range of swirl-stabilized, perfectly premixed flames of methane and CO_2/methane blends. First, the experimental facility, instrumentation and conditions of the tests carried out are described. Section 3 summarizes the main features of the flames studied, in terms of FTF and various chemiluminescence maps. The rationale behind the cross-correlation method is explained in Section 4. The analysis and discussion of the results obtained is performed in Section 5, while the main conclusions are summarized in Section 6.

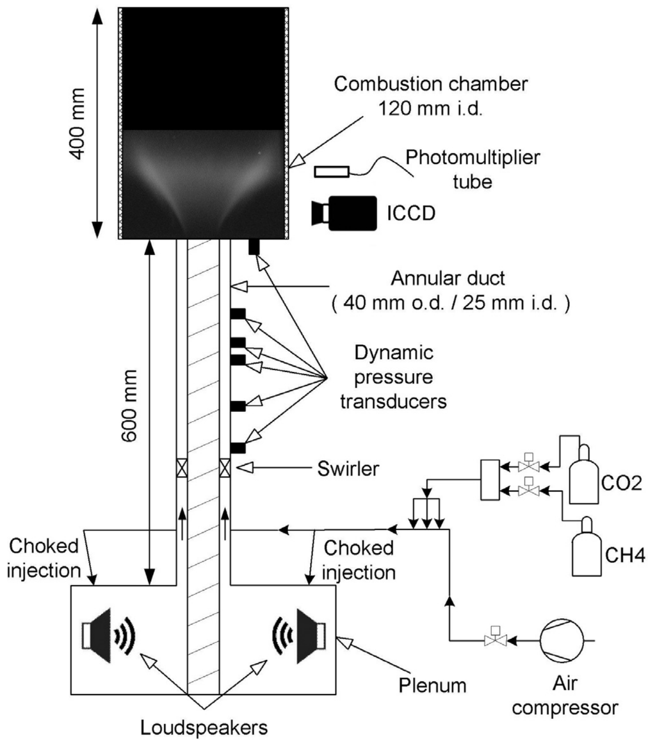

Fig. 1. Experimental rig and instrumentation.

2. Experimental Method

2.1. Experimental rig

The experiments were carried out in the combustion rig sketched in Fig. 1. It is an atmospheric, swirl-stabilized premixed combustor, consisting of a plenum, an annular duct and an optically accessible quartz combustion chamber. Compressed air is conveyed through a pipeline in which the fuel, supplied from pressurized tanks, is injected through a multi-orifice injector. Both air and fuel flows are regulated in closed-loop with thermal mass flow controllers. The air-fuel mixture is then split into two branches of the same length and is injected into the plenum through two choked orifices. This configuration guarantees perfect premixing and, at the same time, decoupling of air and fuel flow rates from pressure fluctuations in the combustion chamber. So, fluctuations in equivalence ratio and mass flow rates are negligible and the flame dynamics is solely due to modulation in the burner injection velocity.

The plenum is connected to the combustion chamber by means of an annular duct with outer and inner diameters of 40 and 25 mm, respectively. An axial swirler with six 30° vanes (geometrical swirl number $S = 0.48$) is located 380 mm upstream of the dump plane. The combustion chamber is cylindrical, with 120 mm in diameter and a total length of 400 mm. The first 220 mm are made up of a quartz tube, providing full optical access to the flame. A stainless steel tube forms the last 180 mm, with the exit open to the atmosphere (acoustically open end condition).

2.2. Instrumentation

Five piezoelectric pressure transducers (PT thereafter, PCB 103B02) were installed along the annular duct at different positions between the swirler and the injection plane. The multi-microphone method [38] was applied to determine velocity oscillation at the injection plane from the five pressure signals. Another PT located at the back plate was used to measure pressure fluctuations inside the combustion chamber.

A photomultiplier tube (PMT thereafter, Hamamatsu H5784-03), fitted with an interference filter (310 ± 5 nm, suitable for the OH* band), was mounted perpendicular to the quartz section at a radial distance of 370 mm, in order to determine the instantaneous heat release rate from the whole flame volume. An intensified CCD camera (ICCD, Hamamatsu C8484-05) equipped with a UV lens and a band-pass filter (310 ± 5 nm) was employed to record the spatial distribution of the chemiluminescence emission due to OH*. The exposure time was set at 80 µs, much shorter than the period of the highest frequencies detected in the flame (<1000 Hz), so that the ICCD images can be considered as instantaneous. Global heat release rate fluctuation, Q', may be derived from both the photomultiplier signal or, by summing up all pixels, from ICCD images. In fact, the consistence of the results obtained with both methods was specifically verified, so that the photomultiplier is not actually necessary as the ICCD camera could provide all radiation information.

Two loudspeakers (350 W, 10″, Eminence DELTA-10A) powered in phase by the same amplifier were installed at both ends of the plenum in which the air-fuel mixture is injected. They provided the acoustic excitation necessary to study the dynamic response of the flame in terms of both the FTF and OH* chemiluminescence maps.

2.3. Tests performed

The experiments were performed on pure methane flames, at three different equivalence ratios ($\Phi = 0.98$, 0.86 and 0.72), in order to cover a broad range, from nearly stoichiometric to lean conditions. The air mass flow rate was adjusted to set the equivalence ratio values, while the fuel flow rate was maintained constant (3 Nm^3/h).

Two different diagnostics were carried out for each condition: FTF measurement and recording of OH* filtered flame images. FTF was measured by exciting flames from f_{ex}=50 to 600 Hz (above 600 Hz, the flames did not show any response to excitation) with 10 Hz steps. Both pressure and photomultiplier signals were sampled at 4 kHz during 4 s (16,000 data) for each excitation frequency.

For each Φ tested, 500 OH* chemiluminescence images were recorded with the ICCD at a frequency of 7 fps, both without and with external excitation; in these tests, four excitation frequencies (90, 150, 230, and 400 Hz) were selected to study flame dynamics for widely different frequencies and to compare it with unforced flames. The dynamic pressure in the combustion chamber and the PMT signal were sampled at 20 kHz and recorded together with the ICCD trigger, with a common temporal reference in order to synchronize the images with the pressure fluctuation and to calculate local and global Rayleigh indices.

In all tests, the dynamic response of the flame to acoustic forcing was within the linear range. This was specifically verified by increasing the magnitude of the input voltage up to 2.5 V, and checking that the FTF measured presented negligible variations in the entire range of frequency tested. Due to this, the input signal to the amplifier was set to a constant voltage (2.5 V), although the u' amplitude achieved for each condition varies due to the different response in frequency of both loudspeakers and facility. Table 1 lists the normalized amplitudes reached at the frequencies for the tests using the ICCD.

The same experiments were performed also on biogas flames (blends of methane and CO$_2$, at 85–15 and 60–40% by volume, respectively). Addition of CO$_2$ led to changes in the dynamic response of the flames, which is primarily ascribed to a decrease in flame temperature due to dilution, since the tests were designed to keep constant the values of Φ and $\bar{u}$ with respect to

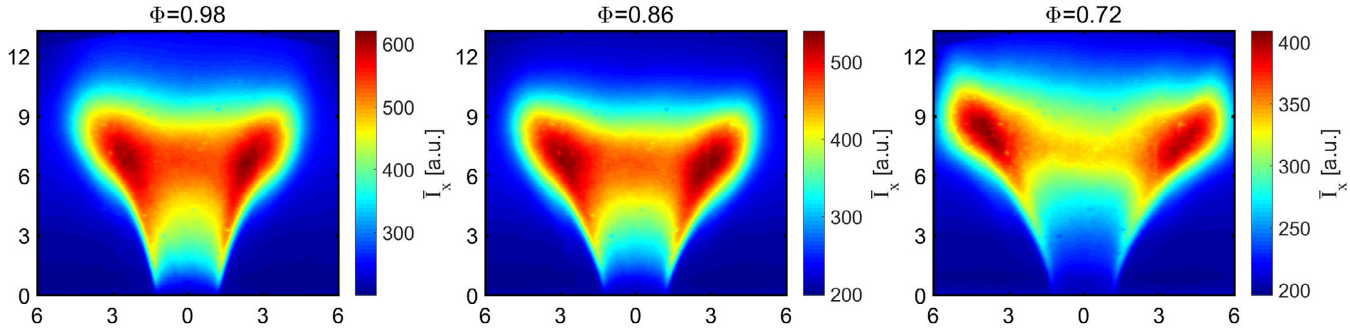

Fig. 2. Mean OH* chemiluminescence maps at different equivalence ratios. Axes scale in cm.

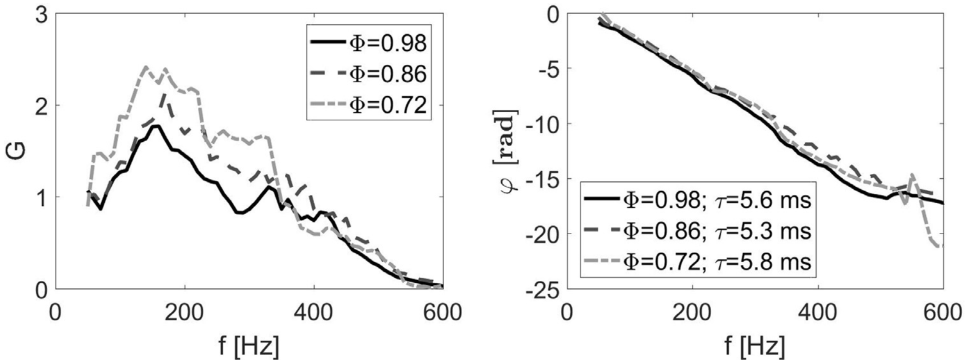

Fig. 3. FTF gains (left) and phases (right) varying Φ. τ values calculated from the slope of the phase plot are also indicated.

Table 1
Values of $|u'|/\bar{u}$ for the ICCD tests.

Φ	f_{ex} [Hz]			
	90	150	230	400
0.98	4.0%	6.6%	15.0%	3.0%
0.86	7.0%	5.5%	15.0%	2.8%
0.72	4.4%	4.7%	12.7%	2.5%

pure methane cases. For brevity, biogas cases have been omitted throughout most of this article to avoid redundancy in the presentation and discussion of the results since, as briefly summarized in the Conclusions section, those results just confirmed the findings obtained from methane flames regarding the application and interpretation of the cross-correlation method.

3. Analysis of the flame dynamics

In the first place, the main features and the dynamic response of the flames studied in this work will be described in terms of OH* chemiluminescence maps and FTF measurements. The flames display the usual V shape, as shown in Fig. 2 for different stoichiometries, without acoustic forcing. These pictures are the average of 500 instantaneous ICCD frames and, hence, are depth-integrated maps of local mean OH* chemiluminescence (designated as $\bar{I}_x$). A consistent evolution of the flame shape and dimensions with fuel-air ratio is apparent and some reduction in peak intensities can be observed for lean flames, in spite of maintaining an almost constant heat input; this is ascribed to the fact that OH* emission decreases as the mixture becomes leaner [15,39,40]. No significant variation in flame length and shape can be observed in mean flame maps when acoustic excitation is applied; for example, Fig. 2-left is a non-forced case which can be compared with the bottom-left image in Fig. 4.

The FTF measured at the three different Φ studied are represented in Fig. 3. In all cases, the gain (G) of the FTF behaves as a low-pass filter and the phase (φ) depicts an almost straight line. Similar results have been reported in previous works for CH_4 flames [10,11,22,27]. The linear behavior of the FTF phase can be interpreted as a constant time delay (τ) between the Q' and u' signals, irrespectively of excitation frequency. The value of τ was calculated from the slope of the phase diagram and the results are indicated in the legend of Fig. 3b.

To analyze more in depth the phenomena involved in the flame dynamics, Abel-deconvoluted maps of the average heat released by the flame along a cycle have been examined. The reference to phase-lock the images is the pressure fluctuation recorded by the PT at the dump plane; the pressure cycle has been divided into 34 parts (≈10.6° each), with a minimum of 12 images per phase interval. Since the dynamics of the flame was very similar across the cases tested, only one condition will be analyzed here ($\Phi = 0.98$, f_{ex}=230 Hz), in terms of phase-resolved maps at 45° steps along the pressure cycle (Fig. 4). Average line-of-sight and Abel-deconvoluted maps, as well as the line-of-sight fluctuation map are included.

Maps clearly show how the main fluctuations of the heat release rate are produced by the movement of the upper region of the flame. This flapping motion begins at 135°, where the downstream part of the flame starts to wrap itself towards the outer zone. This rolled zone increases its intensity and dimensions and moves downstream along the cycle, until 315°. Here the wrapped structure gradually disappears and the flame tip recovers the original V shape and, after 90°, the cycle starts again.

This fluctuating mechanism is apparently due to coherent macrostructures shed at the dump plane and convected downstream. These vortices impinge on the flame front, and drag it along their rotating direction. The flame tip winds around the vortex kernel when the coherent structure reaches the downstream zone of the flame, causing large periodic perturbations in that region, whereas the visible effect of vortices is much weaker at the flame base. The nature and role of the vortex shedding phenomenon as one of the main instability mechanisms in lean

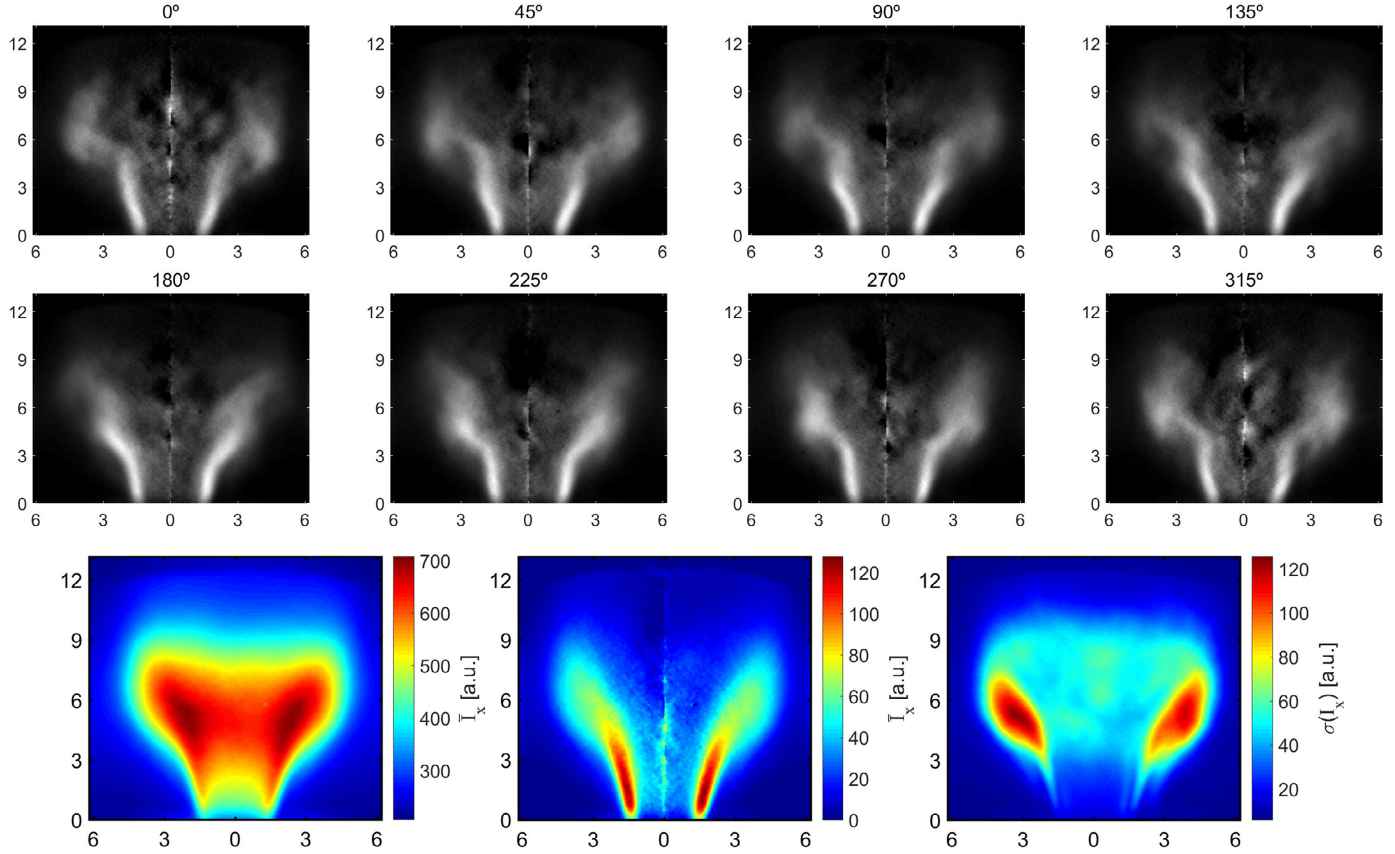

Fig. 4. Top and middle row: Abel-deconvoluted maps of the heat released (averaged within 10.6° intervals) along the pressure cycle at $\Phi = 0.98$, f_{ex}=230 Hz. Bottom row: mean intensity map, depth-integrated (left) and Abel-transformed (center), and line-of-sight fluctuation map $\sigma(I_x)$ (right) for the same condition.

premixed flames has been reported and analyzed in many previous works (e.g., [4,9,11,12,18,24,41]).

As mentioned before, also the presence of the swirler may generate fluctuations of heat release rate due to the modulation in swirl number. These fluctuations would result in a breathing movement of the internal recirculation zone of the flame, causing cyclic changes in the flame angle which can be easily detected from fluctuations of the heat released at the flame base [24,26]. However, the flame angle barely varies for the case analyzed, suggesting that no significant variations in instantaneous swirl number occurs for the flames studied. Also, the rms map included in Fig. 4 clearly shows that the highest heat release fluctuation is produced at the vortex roll-up region, whereas the flame base presents very low magnitudes, indicating that swirl number fluctuations barely contribute to flame dynamics in these particular cases. Finally, the shape of FTF gain curves shown in Fig. 3a also supports this conclusion. Fluctuations in swirl number generally cause peaks and hollows in the gain curve, due to the constructive/destructive interference between the flame tip and the flame base oscillations (respectively induced by vortices and swirl number fluctuations) [16,24]; the smooth variation of FTF gains observed further confirms a negligible role of swirl number modulation in this case.

The same behavior was observed for the other cases analyzed. It is worth mentioning that this undulating evolution of the V flame is much less appreciable in phase-locked maps obtained for f_{ex}=400 Hz. This is probably due in part to the low level of $|u'|/\bar{u}$ achieved for this excitation frequency and to the fact that the flames analyzed are more responsive to lower frequency excitations than to higher frequency ones, as evidenced by the low-pass filter behavior depicted by the FTF gains (Fig. 3a).

4. Cross-correlation maps

This work describes a novel method to extract meaningful information on the dynamic response of the different regions of the flame from chemiluminescence images. A notably simple procedure is applied to obtain the so-called ‘cross-correlation maps’ (CCM), revealing flame patterns very different from most of the maps normally analyzed, like average or, in some cases, fluctuation of the intensity. As already explained for earlier versions of the CCM method [36], cross-correlation maps present the advantages of filtering out all heat release rate fluctuations but those caused by injection velocity oscillation and of showing the actual contribution, either positive or negative, of each flame parcel to the global Q'. The theoretical basis of the CCM as well as the procedure to derive them from chemiluminescence images are detailed in this section.

4.1. General formulation of CCM

The flame transfer function is defined as in Eq. (1) (where the overscript ‘^’ indicates the Fourier transform of the variable and i the imaginary unit), and it can be generally described by a gain, G, and a phase delay, φ, both only depending on frequency, since the flame response is considered linear in this work.

$$FTF(\omega_f) = \frac{\hat{Q}(\omega_f)/\bar{Q}}{\hat{u}(\omega_f)/\bar{u}} = G(\omega_f) \cdot \exp\left[-i\varphi(\omega_f)\right] \tag{1}$$

Considering a harmonic oscillation for the injection velocity at the forcing frequency, ω_f, (Eq. (2)) the flame response induced can be obtained by applying the corresponding FTF gain, G, and the phase delay, φ, at the considered frequency, as shown in Eq. (3).

$$u'(t) = u'_0 \cdot \cos\left(\omega_f t\right) \tag{2}$$

$$Q'(t) = \frac{u'_0}{\bar{u}} \cdot \bar{Q} \cdot G(\omega_f) \cdot \cos\left[\omega_f t - \varphi(\omega_f)\right] \tag{3}$$

In real, turbulent flames, other fluctuations may occur simultaneously to those due to acoustic excitation. So, heat release rate oscillation at position x, Q'_x, can be split in two contributions (Eq. (4)): the first one is the fluctuation due to the acoustic forcing at ω_f (designated as Q'_{x,ω_f}) while the second one is due to effects not related to u' and includes all frequencies ω_j different from ω_f (indicated as Q'_{x,ω_j}).

$$Q'_x(t) = Q'_{x,\omega_f}(t) + Q'_{x,\omega_j}(t) \tag{4}$$

The dynamic response at point x due to the acoustic forcing can be expressed, using flame transfer function de-composition [10,42], in terms of the local FTF (characterized by gain G_x and phase φ_x: $FTF_x(\omega_f) = G_x(\omega_f) \cdot \exp[-i\varphi_x(\omega_f)]$) as:

$$Q'_{x,\omega_f}(t) = \frac{u'_0}{\bar{u}} \cdot \bar{Q}_x \cdot G_x(\omega_f) \cdot \cos\left[\omega_f t - \varphi_x(\omega_f)\right] \tag{5}$$

The global dynamic response, quantified in terms of $Q'(t)$, is the outcome of the combined response of all flame elements, $Q'_x(t)$. However, the magnitude of Q' not only depends on those of local fluctuations, but also on how well they are synchronized. Therefore, both the amplitude and phase of local and global heat release rates need to be analyzed in order to extract the part of $Q'_x(t)$ actually contributing to $Q'(t)$ (and, hence, to the FTF). The method proposed here, based on Eq. (6), is thought to constitute a simple yet effective method to achieve that goal. The integral in Eq. (6) is the average cross-correlation of the variables $Q'(t)$ and $Q'_x(t)$ for zero time lag, averaged over a length of time, T, much longer than the period of the forcing signal. The local heat release rate, $Q'_x(t)$, can be split as indicated in Eq. (4):

$$\begin{aligned} Q' * Q'_x &= \frac{1}{T}\int_0^T Q'(t) \cdot Q'_x(t)dt = \frac{1}{T}\int_0^T Q'(t) \cdot Q'_{x,\omega_f}(t)dt \\ &+ \frac{1}{T}\int_0^T Q'(t) \cdot Q'_{x,\omega_j}(t)dt \end{aligned} \tag{6}$$

The last term is the average product of a periodic signal, of angular frequency ω_f, with a sum of periodic signals of different frequencies. If this integral is averaged over a sufficient long period of time, the result goes to zero. Therefore, all the spurious heat fluctuations, not related to the acoustic forcing, are filtered out in Eq. (6).

On the contrary, the first integral represents the product of two waves of the same frequency, so its final result will not be null. If the global and local heat release rates are written as a function of their respective transfer functions, the first term in Eq. (6) can be written as:

$$\begin{aligned} Q' * Q'_x &= \frac{1}{T}\int_0^T \left(\frac{u'_0}{\bar{u}}\right)^2 \cdot \bar{Q} \cdot \bar{Q}_x \cdot G(\omega_f) \\ &\cdot G_x(\omega_f) \cdot \cos\left[\omega_f t - \varphi(\omega_f)\right] \cdot \cos\left[\omega_f t - \varphi_x(\omega_f)\right]dt \end{aligned} \tag{7}$$

Using the trigonometric identity $2 \cdot \cos(a) \cdot \cos(b) = \cos(a-b) + \cos(a+b)$, and since the second term of this identity also vanishes when averaged over a sufficiently long time, T, the final result is given in Eq. (8).

$$\begin{aligned} Q' * Q'_x &= \frac{1}{2}\left(\frac{u'_0}{\bar{u}}\right)^2 \bar{Q} \cdot \bar{Q}_x \cdot G(\omega_f) \cdot G_x(\omega_f) \\ &\cdot \cos\left[\varphi_x(\omega_f) - \varphi(\omega_f)\right] \end{aligned} \tag{8}$$

The function $Q' * Q'_x$ can then be normalized by the average heat release rates with all space-independent parameters grouped in a lumped constant, $K(\omega_f)$, to give:

$$q' * q'_x = \frac{Q' * Q'_x}{\bar{Q}_x \cdot \bar{Q}} = K(\omega_f) \cdot G_x(\omega_f) \cdot \cos\left[\varphi_x(\omega_f) - \varphi(\omega_f)\right] \tag{9}$$

$$K(\omega_f) = \frac{1}{2}\left(\frac{u'_0}{\bar{u}}\right)^2 \cdot G(\omega_f) \tag{10}$$

The function $q' * q'_x$ is, therefore, proportional to the gain of the local FTF, $G_x(\omega_f)$, but also depends on the relative phase between global and local heat release rate. The cosine term introduces a correction on the local gain, related to the synchrony between local and global fluctuations of the heat release rate. For example, if $\varphi_x(\omega_f) = \varphi(\omega_f)$, all the fluctuations in heat release rate at flame position x contribute to global Q', whereas the parcels at which $\varphi_x(\omega_f) - \varphi(\omega_f) = \pi$ have a damping effect on the response to the acoustic excitation, or they do not contribute at all if $\varphi_x(\omega_f) - \varphi(\omega_f) = \pi/2$. Therefore, $q' * q'_x$ properly describes the spatial distribution of the '*effective*' local FTF gain and provides an alternative description of the flame topology with respect to its dynamic response, which may reveal effects not visible in the various types of flame maps normally used in the field.

At this point, it should be noted that there exists a parallelism between some of the expressions included above and the definition of Rayleigh index, with the difference that the latter involves the pressure signal $p'(t)$ instead of $Q'(t)$. Despite the obvious formal similarity, there are fundamental differences between the results, and their interpretation, obtained with both approaches. For the sake of clarity, this discussion is postponed and will be specifically addressed at the end of Section 5.

The CCM method will be applied to the flames studied in this work. To do so, OH* chemiluminescence maps have been processed according to Eq. (9). Assuming that the intensity at pixel x, I_x, is proportional to local heat release rate, Q_x (both are depth-integrated values), cross-correlation (CC) maps can be calculated from experimental data through Eq. (11), where $i' * i'_x$ denotes the value of $q' * q'_x$ as estimated from chemiluminescence images:

$$i' * i'_x = \frac{\sum_{j=1}^{N_{im}} \left(I'_x \cdot \sum_{k=1}^{N_{px}} \left(I'_x\right)_k \right)_j}{N_{im} \cdot \bar{I}_x \cdot \bar{I}} \tag{11}$$

$\bar{I}_x$ and I'_x represent respectively the mean and fluctuating component of the intensity collected at pixel x, while $\bar{I}$ is the mean OH* intensity for the whole flame, calculated by summing up all pixels of the mean, line-of-sight integrated map. The calculations are done over N_{im} instantaneous images, each one consisting of N_{px} pixels.

4.2. Formulation for n-τ model

Further insight into characteristic parameters related to the flame response may be gained for some particular functional forms of the FTF, namely for the n-τ model. This FTF model has been chosen since it suitably approximates the dynamic response of the flame studied, in particular because of the almost linear variation of the phase with f_{ex} (see Fig. 3). In the following analysis, the global and local dynamic response will be expressed using the parameters (n, τ) for the global FTF and (n_x, τ_x) for the local one. So, following the usual notation, FTF gains will be written in terms of the proportionality factors ($n(\omega_f) \equiv G(\omega_f)$ and $n_x(\omega_f) \equiv G_x(\omega_f)$), while the FTF phase can be expressed as proportional to a sensitive time lag, so that $\varphi(\omega_f) = \omega_f \cdot \tau$, $\varphi_x(\omega_f) = \omega_f \cdot \tau_x$. So, Eq. (9) can be rewritten as:

$$q' * q'_x = K(\omega_f) \cdot n_x(\omega_f) \cdot \cos\left[\omega_f \cdot (\tau_x - \tau)\right] \tag{12}$$

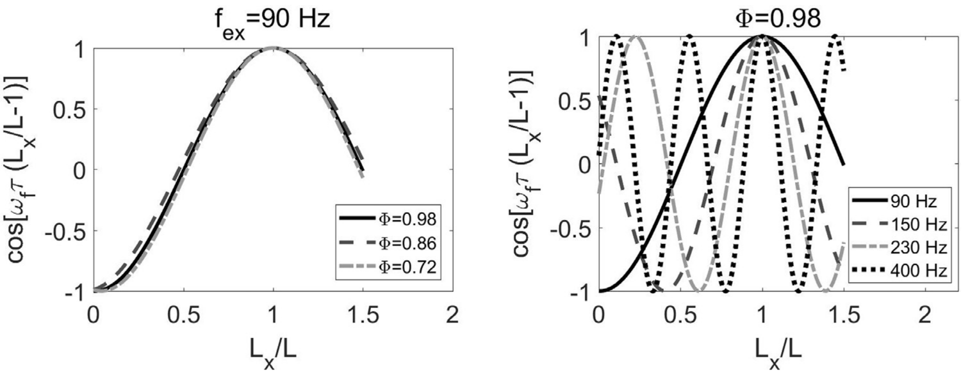

Fig. 5. Theoretical patterns obtained from Eq. (13) for different Φ (left) and f_{ex} (right).

Sensitive time lags can be related to characteristic velocities and lengths. Whereas plausible values can be proposed for the characteristic propagation velocities (depending on the coupling mechanism, it can be the speed of sound, the velocity in the premixing duct or a relevant flow velocity along the flame), much less obvious is to identify suitable characteristic lengths in some cases. As it has been shown in previous works, in general at least three characteristic dimensions are needed to describe an FTF of a turbulent, perfectly premixed, swirling flame (two concerning the flame and one representative of the swirl effect [19,22,26]). For example, time lags associated with swirl number modulation should be related to the distance between swirler and injection plane. Convective distances in the flame should represent the length 'typically' traveled by a fluid parcel between injection and the location where it is burnt. In this case, however, there are no geometrical references that can be used and representative flame distances need to be derived from some kind of flame map.

Various studies have investigated the characteristic convective flame length, L, involved in the FTF time lag. The definition of this distance not always coincides among different works: L has been defined by some authors as the total flame length [38] or as different fractions of it [5,11,12,18]; some works identify L as the distance at which the maximum heat release occurs [17,35,43–45] while others relate it to the center of mass of the flame [19,27,46]. In this context, CC maps could represent a valid alternative to identify a flame zone suitable to define this characteristic flame distance. It is important to note that, by no means, this implies that L is always the only relevant length related to the sensitive time lag. As mentioned before, the delay in the flame may need to be combined, for example, with that of swirl perturbations inside the premixing duct (see, e.g., [19]). However, in the flames analyzed in this work, no significant effects due to swirl number modulation were detected, so that the sensitive time lag can be only ascribed to the convective delay along the flame. Therefore, τ can be estimated as the ratio between a characteristic flame length, L, and a related propagation velocity, V. Similar considerations can also be applied to the distributed FTF and, so, $\tau_x \sim L_x/V_x$. If the convective velocity is considered to be approximately constant along the jet path, $V \sim V_x$ and $\tau_x/\tau \sim L_x/L$. So, the cosine term in Eq. (12) can be reformulated as

$$\cos\left[(\omega_f\cdot(\tau_x-\tau)\right]=\cos\left[\omega_f\cdot\tau\cdot\left(\frac{L_x}{L}-1\right)\right] \tag{13}$$

This suggests that the cross-correlation maps should exhibit along the jet path a sinusoidal evolution with respect to the distance to the injection plane. This is illustrated in Fig. 5, where Eq. (13) is plotted for different cases. Figure 5a shows the results for flames excited at a fixed frequency of 90 Hz and three Φ values, with very similar results, due to the small differences in τ (see Fig. 3). As shown in Fig. 5b, higher excitation frequencies result in a corresponding decrease in the spatial wavelength of $q' * q'_x$ along the flame path. As it will be shown later, these theoretical patterns are reproduced in the experiments when the function $q' * q'_x$, as determined from experimental data, is plotted against the distance L_x. Since the cosine exhibits a peak at $L_x = L$, this sort of curves could provide a valid alternative to easily identify a characteristic flame length associated to the global convective time delay, τ.

5. Results and discussion

5.1. Experimental results

Eq. (11) has been applied to the chemiluminescence images recorded for the case at $\Phi = 0.98$ forced at 230 Hz and the cross-correlation map obtained, in terms of $i' * i'_x$, is represented in Fig. 6a. It is interesting to compare the flame pattern revealed by this CC map with the images shown in Fig. 4 for the same test. Whereas the mean intensity and the standard deviation show significant values, respectively, over most of the flame volume and at the outer edge of the flame, the CC map displays a sequence of spots, with alternating negative/positive values, aligned with the V flame sheet. To better assess the position of these areas with respect to the flame region, the location of the V flame has been overlapped in Fig. 6b. These shadowed areas were determined as the pixels in the Abel-transformed map (Fig. 4) with intensity exceeding 45% of the peak value; the white, solid lines mark the center of these regions. In general, the zones with significant values (both negative and positive) in the CC map are located at the outer edge of the flame sheet. These spots gradually move outwards, so that most of the last peak falls outside the V flame (their relative position with respect to the flame cone is clearly seen by comparing the enhanced zones with the white line). The relative location of the peak values, both positive and negative, in the CC map with respect to the shadowed area is considered a relevant and revealing result: first, this demonstrates that the strongest dynamics may perfectly occur outside the main average flame location (and, hence, average intensity maps should not be used to determine variables related to dynamic response) and, second, the pattern revealed by the CC map is perfectly consistent with vortex shedding as the main instability mechanism in this case, causing intermittent heat release at pockets located at the outer edge of the flame.

A distinct, fundamental feature of CC maps is the existence of areas with negative values, indicating oscillations in heat release rate which are out of phase with respect to the global Q'. Hence, these regions tend to damp the response of the flame to acoustic forcing, in contrast with other regions showing high positive values and, hence, contributing to the total Q' or, equivalently, to the FTF. This oscillating pattern can be observed more clearly in Fig. 6c, where the solid line represents the evolution with the

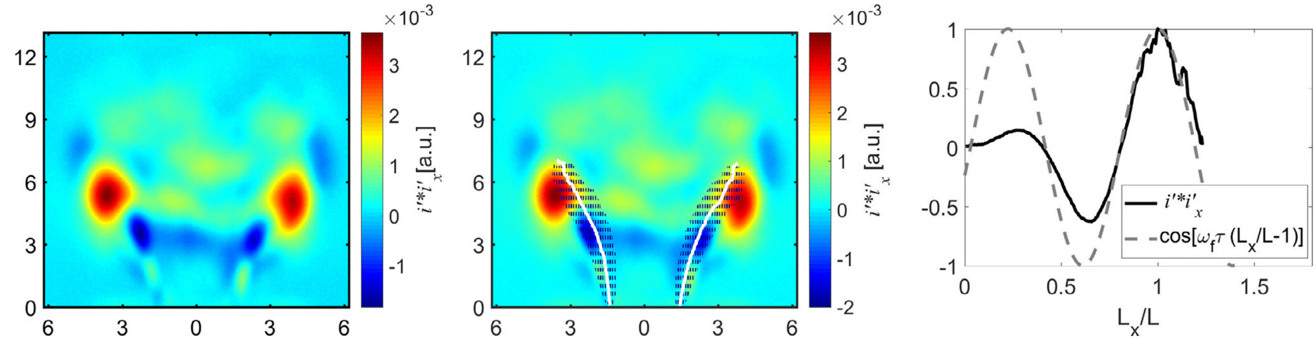

Fig. 6. a) CC map for a methane flame at $\Phi = 0.98$ and forced at 230 Hz; b) Superposition of the combustion zone (shadowed area), as identified from the Abel map of Fig. 4, on the CCM map (the white, solid line indicates the center of this area); c) comparison between $i' * i'_x$ values along the shadowed area in (b) and the theoretical curve (dashed line) predicted from Eq. (13) for 230 Hz and τ=5.6 ms.

axial distance, L_x, of $i' * i'_x$ integrated across the width of the shadowed area. Both axes have been normalized in order to compare the obtained pattern with the theoretical one expressed by Eq. (13) (deduced under the assumptions of proportionality between τ_x and L_x, and global and local FTF described by an $n - \tau$ model), which has also been plotted in Fig. 6c. Once the Y and X axes are normalized respectively with the magnitude and L_x at the $i' * i'_x$ peak, the experimental results display a remarkable similarity with the theoretical curve, supporting the validity of the theoretical considerations behind the CCM method and, hence, the physical interpretations proposed for the cross-correlation maps. According to Eq. (9), the continuous increase of the amplitude of $i' * i'_x$ oscillations in Fig. 6c can be ascribed to an almost monotonic increment of the local FTF gain, G_x, with L_x, since $K(\omega_f)$ is a constant for a given operational condition (this point will be analyzed below in greater detail). Also, these results may serve to determine a flame zone suitable to define the 'characteristic flame length' (associated with the convective delay between u' and Q'). This characteristic length was noted as L in Eq. (13) and, according to Fig. 6c, it can be easily determined as the distance at which the $i' * i'_x$ peak occurs. The intuitive interpretation as well as the theoretical derivation of L obtained from the CC maps are thought to clearly make it a physically plausible and valid option, among other definitions obtained from different kinds of chemiluminescence maps.

In general, the initial value of the theoretical sinusoidal function has to be taken into account when matching experimental and theoretical patterns. In fact, the combination of Eq. (13) behavior with that of the local gain (which, according to the observations, tends to zero at the dump plane and increases monotonically with L_x) could lead to discrepancies between the two curves when L_x tends to zero (unless also the theoretical oscillation goes to zero for $L_x = 0$, as for the case in Fig. 6). However, these differences are limited to the very first portion of the curves. Very similar conclusions to those derived from Fig. 6 can be obtained for other experimental conditions when analyzing the CCM results.

CC maps have been calculated from depth-integrated chemiluminescence images, but other options could be considered. An alternative would be, for instance, to first calculate tomography-transformed images before applying the CCM analysis. However, since the CC maps reveal essentially toroidal structures with very low values at the inner flame core, the distortion due to line-of-sight integration is almost negligible with respect to the actual radial profiles, at least for the considered cases.

The CCM method was applied to analyze the spatial patterns representing dynamic flame response for the different combustion conditions explored in this work; the results are shown in Fig. 7. The cross-correlation values represented in those maps have been post-processed by dividing $i' * i'_x$, calculated with Eq. (11), by $K(\omega_f)$, as defined in Eq. (10). $K(\omega_f)$ is a constant for a given test (and, hence, CC map) and is only a function of data involved in FTF calculation: gain and normalized velocity fluctuation for each equivalence ratio and forcing frequency. This is an alternative way to analyze cross-correlation results. Non-normalized data, as those shown in Fig. 6a, can be directly obtained from chemiluminescence images, with the advantage of not requiring FTF information. But if FTF is known, CC values normalized in this way can provide additional information. According to Eq. (9), this normalization yields:

$$\frac{i' * i'_x}{K(\omega_f)} \approx \frac{q' * q'_x}{K(\omega_f)} = G_x(\omega_f) \cdot \cos\left[\varphi_x(\omega_f) - \varphi(\omega_f)\right] \tag{14}$$

The right-hand side of Eq. (14) not only depends on the gain of the local FTF but also accounts for the phase difference between global and local heat release rate. Therefore, normalized CC maps calculated with Eq. (14) directly quantify the contributions of the different flame regions to the global dynamic response of the flame to acoustic excitation, which justifies describing them as '*effective local gain*'.

In most cases, Fig. 7 display flame patterns very similar to that observed in Fig. 6. There is, however, the exception of the tests forced at 400 Hz, with a much more noisy appearance, which will be discussed below. As in Fig. 6, the CC maps for frequencies of 90, 150 and 230 Hz show alternating positive/negative spots along the outer edge of the V flame, with absolute magnitude growing with axial distance. The number of cycles increases with the forcing frequency, in coincidence with the behavior predicted by combining CC mapping and the n-τ model (see Eq. (13) and Fig. 5b). Peak values in the range 5–13 have been obtained, which, according to the interpretation proposed above, indicate a very high 'effective local gain' over small toroidal volumes, always located surrounding the flame tip. It should be noted that, in all cases, those peak values exceed by far the gain of the global FTF (G in the interval 1–3 for those frequencies, see Fig. 3). Obviously, this difference is explained by the fact that the global FTF gain is an average (weighed with $\bar{Q}_x$) of local contributions, which also include flame portions with weak response (e.g., near the dump plane) and with negative contributions (even < -5, immediately upstream of the regions with largest positive values). Kim et al. [10] obtained analogous results, with local gains significantly higher than the global one, for CH_4–H_2 M-flames (although the local gain data in [10] were determined with a different method and represent an average over the cross section).

This behavior is thought to be perfectly consistent with fluctuating heat release due to vortex shedding, which, as discussed in Section 3 when analyzing Fig. 4, appears to be the dominant mechanism of the instability for the cases analyzed. The spots indicate the impingement of the coherent structures on the flame front, causing flame area fluctuations at the outer edge of the shear layer

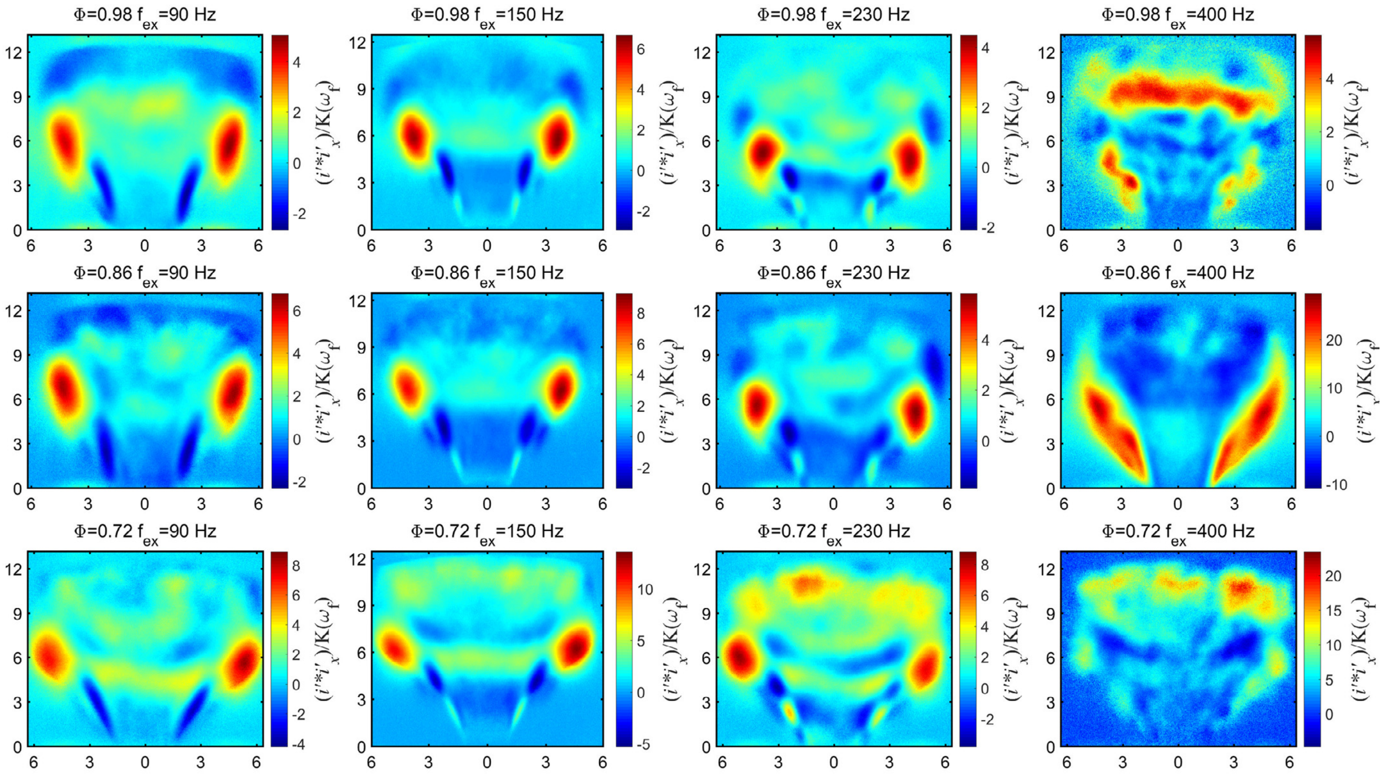

Fig. 7. Normalized CC maps, $(i' * i'_x)/K(\omega_f)$, for different equivalence ratios and forcing frequencies.

clearly highlighted by CC maps. The toroidal volume with peak local gain mentioned above coincides with the vortex roll-up zone seen in Section 3, where the highest instantaneous heat release occurs and which mostly determines the global Q' (and hence, global FTF). At the same time, the CC maps demonstrate that the regions immediately upstream of those peak values exhibit heat fluctuations which are out-of-phase with the bulk response of the flame.

Most of the maps obtained for 400 Hz do not show the oscillating pattern along the flame jet path, at least as clearly as observed for lower frequencies. This is ascribed to the causes already discussed in Section 3, which result in small amplitude oscillations along the flame, more affected by experimental uncertainties and causing the noisy profiles obtained. A consequence of this is the low G value at this frequency, which, together with the low amplitude of u' (both included in the denominator of Eq. (14)) magnify the effect of noise in normalized CC maps, reaching peak values >15, probably unrealistic.

The $(i' * i'_x)/K(\omega_f)$ maps shown in Fig. 7 describe the 'effective local gain' of the FTF. This is a useful description of the dynamic response of the flame but it should be noted that, since the intensity fluctuation has been normalized by the average value $\bar{I}_x$, $(i' * i'_x)/K(\omega_f)$ values do not inform on the absolute contribution of a flame portion to the global FTF. As indicated, e.g., in [10], the global FTF can be calculated from the local ones as a summation weighed with the mean value of the local heat release rate, $\bar{I}_x$. Therefore, this defines an alternative formulation of CC maps in terms of $(i' * I'_x)/K(\omega_f)$, obtained by multiplying $(i' * i'_x)/K(\omega_f)$ by the average local intensity, $\bar{I}_x$. Both magnitudes have different physical interpretations: $(i' * I'_x)/K(\omega_f)$ is a measure of the absolute contribution of a flame portion to the global FTF, whereas $(i' * i'_x)/K(\omega_f)$ is the 'effective local gain', as defined in Eq. (14).

Figure 8 displays this alternative definition for a few cases, which can be directly compared with the corresponding normalized form in Fig. 7 (second row). Even though the peak areas at the flame tip become slightly smaller, the general pattern is very similar since, for the cases analyzed, $\bar{I}_x$ is almost constant along the shear layer; this also produces $(i' * I'_x)/K(\omega_f)$ values almost proportional to those of $(i' * i'_x)/K(\omega_f)$ maps. So, the differences between the two CC formulations are considered important for a quantitative analysis and for the calculation of global FTF from local contributions, and they can offer two alternative descriptions of the flame dynamics. Nevertheless, as the general pattern obtained for the particular cases tested is very similar, and the values proportional to those of Fig. 7, no further analysis will be performed in terms of $(i' * I'_x)/K(\omega_f)$ for the flames studied (however, this similarity is not thought to necessarily occur for the general case).

The sinusoidal shape of the effective local gain can be better illustrated by means of its evolution along the V flame. The same procedure described above to build Fig. 6c was applied to all cases, with the results shown in Fig. 9. The curves exhibit the features already noted above. First, the wavelength is inversely proportional to the forcing frequency, as predicted by Eq. (13) and illustrated in Fig. 5 under the assumptions of $n-\tau$ response and constant convective velocity. Second, the amplitude of the oscillation gradually grows until reaching a maximum near the tip of the flame. According to Eq. (14), the curves shown in Fig. 9 could be further analyzed to determine the local FTF gain, G_x, from the local maxima/minima along the different curves. These points almost satisfy $\varphi_x(\omega_f) - \varphi(\omega_f) = k\pi$ (where k is an integer) and, hence, $\cos = \pm 1$. The results are shown in Fig. 10 and indicate that, in all cases, the local gain gradually increases until reaching a maximum (some scattering is shown, probably related to the fact that the first peak does not satisfy the condition of $\cos = \pm 1$ for all conditions, as explained above). Actually, to derive Fig. 9 it was assumed that the FTF obeys the $n-\tau$ model and, hence, the local gain so estimated is $n_x(\omega_f)$. This parameter was

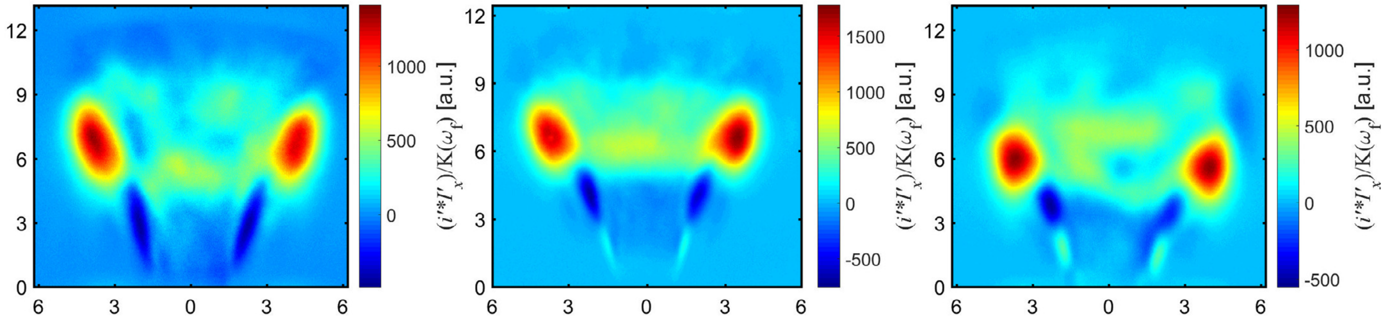

Fig. 8. $(i' * I'_x)/K(\omega_f)$ maps for methane flames at $\Phi = 0.86$ forced at 90 (left), 150 (middle) and 230 Hz (right).

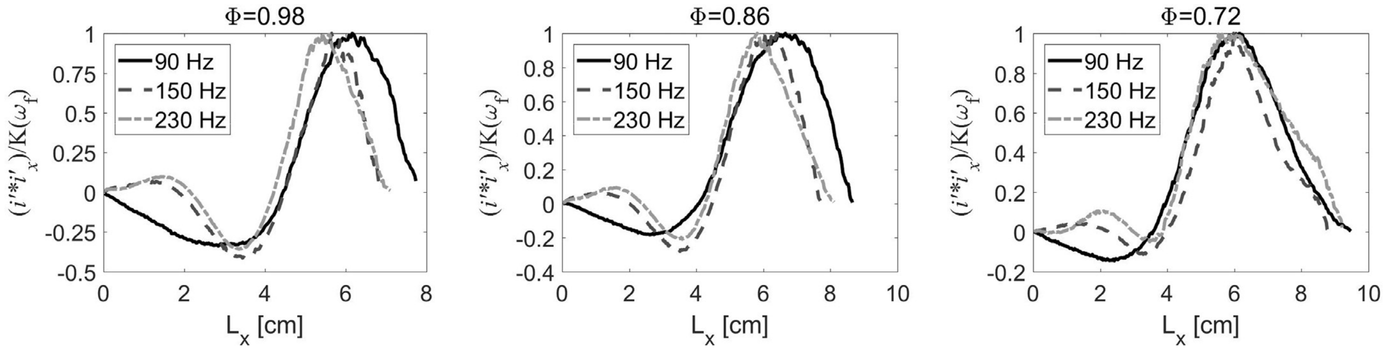

Fig. 9. Oscillations along the jet path for CC maps of Fig. 7.

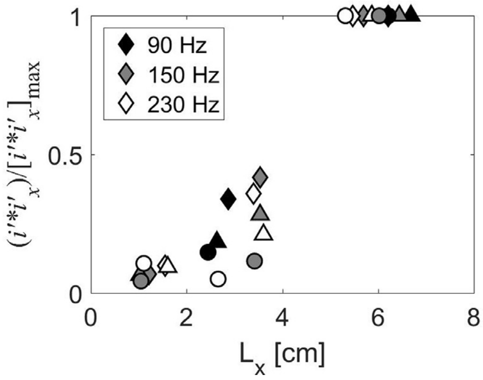

Fig. 10. Evolution of $(i' * i'_x)$ local maxima/minima values (normalized with the respective peak value) along the flame axial distance. Symbols: (◊)$\Phi = 0.98$; (Δ)$\Phi = 0.86$; (o)$\Phi = 0.72$ – grey levels vary with f_{ex}, as indicated in the legend.

also determined from local FTF measurements in [10] for CH_4–H_2, M-shaped flames, with results very similar to those obtained here, only based on OH* chemiluminescence images.

5.2. Comparison with other chemiluminescence maps

Cross-correlation maps are thought to provide a different and original perspective of the local flame dynamics, complementary to other chemiluminescence maps, such as the ones representing either the mean heat release rate or its fluctuation. Nevertheless, other processing methods give results that are more closely linked with the information contained in CC maps, so it seems worth comparing the different approaches.

As mentioned in the introduction, FFT processing can be applied locally as a means to analyze the magnitude of the local response. This approach has been successfully applied in some previous works to investigate the nature of flame dynamics in different situations [16,35]. However, it must be noted that the FFT value at a point informs about the amplitude of the local response but it does not describe the actual contribution of the flame zone to the global flame response, since this also depends on how well Q' and Q'_x are synchronized. Therefore, the FFT results at each pixel would need to be corrected by taking into account the phase with respect to the global $Q'(t)$, which may result in a significantly different result, not only in magnitude but also even in the sign. Whereas this post-processing could be performed to determine CC maps from local FFT data, it requires additional operations and also high frame rate images. The CCM has much lower requirements in this respect, since the Nyquist criterion does not need to be fulfilled and the cross correlation can be calculated from image series with much longer intervals, as long as the image series are sufficiently representative of the whole cycle.

The parallelism between CC and RI formulation has been already pointed out in Section 4. In fact, the oscillating pattern observed in the CC maps is visually similar to the Rayleigh index maps for forced flames reported in [32–34]. Also, the definition of the local Rayleigh index (Eq. (15)) exhibits a remarkable formal similarity with that for the cross correlation (Eq. (6)), except that in the RI formula $Q'(t)$ has been replaced by the pressure fluctuation, $p'(t)$.

$$RI_x = \frac{1}{T}\int_0^T p'(t)\cdot Q'_x(t)dt \qquad (15)$$

Since, $p'(t)$ is practically constant over the flame volume and fluctuates at the same frequency as $Q'(t)$, the similarities between both maps is not surprising at all. As an example, both CC and RI maps are shown in Fig. 11 for a methane flame at $\Phi = 0.98$, forced at 230 Hz; in order to better visualize and compare both variables, Fig. 11c represents their evolution along the flame sheet, following the same procedure described above for Fig. 6c. As shown in Fig. 11, both maps exhibit practically the same pattern, apparently only differing in the spatial phase. Also, the curves in Fig. 11c for CC and RI display very similar shapes (sinusoidal evolution with amplitude growing with axial distance), but with a phase

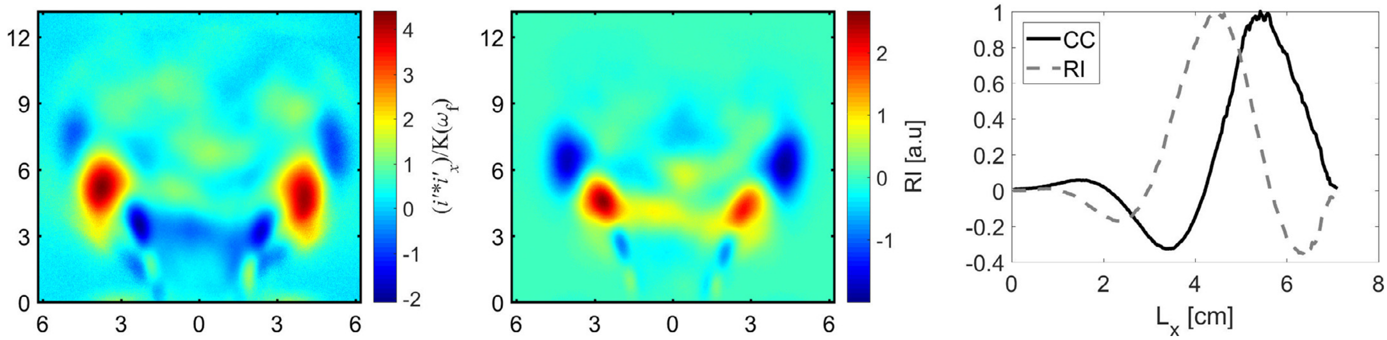

Fig. 11. (a) CC and (b) RI maps for methane flame at $\Phi = 0.98$ externally excited at 230 Hz; (c) normalized oscillations pattern along the jet path.

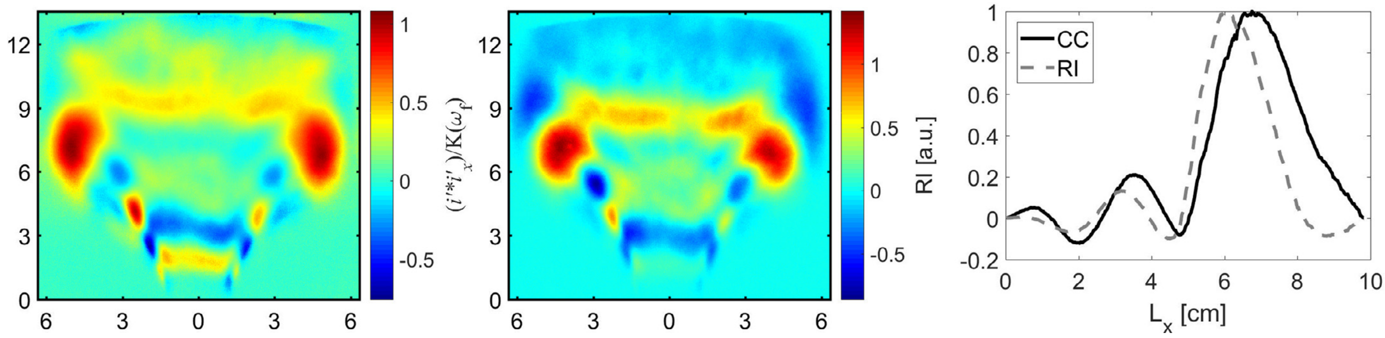

Fig. 12. (a) CC and (b) RI maps for CH_4–CO_2 (60-40% in volume) flame at $\Phi = 0.98$ in a condition of self-sustained instability; (c) normalized oscillations pattern along the jet path.

difference close to $\pi/2$. Practically the same lag was determined between $p'(t)$ and $Q'(t)$ signals (not shown here for brevity), consistently with the different variables involved in RI and CC definitions.

However, this shift in the oscillating patterns, and the consequent different values associated to each flame area, is by no means a secondary aspect, but reveals an essential difference between CC and RI maps. In fact, the inherent physical meaning of the two magnitudes is different. As it has been discussed, CC maps are only related to the dynamics of the flame and describe the effective contribution of the different flame zones to the global FTF. In contrast, RI is a measure of the production or suppression of acoustic energy, as a result of the coupling between the flame response and the acoustics of the whole system. Therefore, for example, a positive RI value of a flame zone does not imply that this area is contributing to the global flame response to u' (or any other instability mechanism), as it can be clearly observed by comparing Fig. 11a and b. These substantial differences make the results obtained with CCM and RI complementary for what concerns the thermoacoustic analysis, but absolutely not correlated (the only option would be to reprocess the data by accounting for the phase between p' and Q' to transform RI into CC maps).

According to this interpretation, the only case in which the two maps would be expected to show similar results is when $p'(t)$ and $Q'(t)$ signals oscillate perfectly in-phase, as it approximately happens in limit-cycle situations. Pure methane flames did not present a sustained pressure oscillation at any operational condition, therefore a mixture of CH_4 and CO_2 (60-40% in volume, respectively) was used. At $\Phi = 0.98$, this fuel showed a moderate, self-sustained pressure fluctuation at 240 Hz. Figure 12 shows the two maps (CC and RI) obtained for this condition, as well as their associated fluctuation patterns calculated along the jet path. As expected, in this case, the CC and RI maps display a remarkable resemblance, and the respective curves (Fig. 12c) fluctuate almost in phase (and so do the temporal oscillations of $p'(t)$ and $Q'(t)$). Therefore, CC and RI maps lead to the same results uniquely in the case of a perfect synchronization between the two global variables considered by both methods (it should be noted that even in unstable cases CC and RI maps may not coincide, since the phase between $p'(t)$ and $Q'(t)$ may adopt any value between $-\pi/2$ and $\pi/2$). As it has been noted above, the information contained in CC maps could be obtained by correcting RI values according to the relative phase between $p'(t)$ and $Q'(t)$. However, this adds unnecessary complications, since CC calculations are quite straightforward from a series of chemiluminescence images, and do not require the phase-locked analysis involved in Rayleigh index processing or even the measurement of $p'(t)$. Moreover, the quantitative analysis afforded by normalized CC maps in terms of local gain is not possible from RI maps. Finally, it should be noted that, whereas cross-correlation is expected to yield meaningful information on the dynamic response of flames for both forced and non-forced conditions, in general the Rayleigh index concept does not apply to velocity-forced flames.

6. Conclusions

In this work, a novel method, based on the so-called ‘cross-correlation maps’ (CCM), has been presented as a valid tool to determine the effective local response of the various flame zones. The theoretical analysis indicates that this flame mapping method is an effective way to determine the actual contribution of the different flame regions to the global flame dynamics. Moreover, significant practical advantages of this method are its notably low instrumentation and processing requirements.

Different versions of CC maps can be obtained, depending on the information available. In its simplest form, CC mapping only requires a series of instantaneous chemiluminescence images, representative of the oscillation cycle, but which do not need to be phase-locked or acquired at high frame rates. CC maps calculated by simply applying cross-correlation processing on instantaneous OH* images can be interpreted as a qualitative description of the synchronism of the local response of the flame with respect to the global heat release fluctuation. If the global FTF is known, those primary results can be normalized to obtain a quantitative description, in terms of the 'effective gain' of the local FTF (i.e., its component in phase with the global flame response), or to estimate the net contribution of the different flame regions to the global FTF.

This method has been applied to a wide range of situations involving turbulent, swirling premixed V flames. The CC maps derived from recorded OH* images display a sequence of spots alternating negative/positive values along the outer border of the flame sheet, whose number and magnitude increase, respectively, with the forcing frequency and with the axial distance from the dump plane. This pattern, and the fact that peaks in CC maps fall on the outer edge of the main flame, are thought to well highlight vortex shedding as the main instability mechanism in the flames studied. More detailed information and further confirmation of the proposed physical interpretation of CC maps can be gathered if both global and local FTF are described by $n-\tau$ models:

- The proportionality between the wavelength of the alternating spots in CC maps and the forcing frequency is easily explained.
- Local FTF gain monotonically increases from the dump plane to the flame tip.
- The characteristic flame length associated with the convective time lag normally found in the FTF can be determined from the location of the peak value in CC maps.

Although not shown here for brevity, the same procedure was applied to biogas flames. The addition of CO_2 resulted in some quantitative differences with respect to analogous methane cases (e.g., longer flames, longer $u'-Q'$ delay times). However, from the point of view of the applicability and interpretation of the CCM method, which is the main objective of this work, biogas tests served to confirm all the conclusions described for methane flames for a wide range of situations.

A comparison of the CC method with others which can provide similar information has been performed, and, in particular, a parallelism between the CCM process and the Rayleigh index one has been analyzed. CC and Rayleigh index maps present similar oscillating patterns, due to the formal similarity of their respective formulations. However, a difference in phase can be noticed between the two maps, which varies according to the thermoacoustic conditions. This is an essential difference between both maps, related to their different physical meaning. The information provided by CC maps, in terms of the 'effective local response' might be also obtained from other descriptions of flame response (like RI maps or local FFT data), if they are suitably post-processed, so as to obtain precisely the same magnitude as that calculated in the cross-correlation analysis.

In summary, cross-correlation maps derived from chemiluminescence images are thought to provide an alternative and useful perspective of the flame pattern regarding its dynamic response. Also, remarkable advantages of the CCM method are the very limited information required and the simplicity of the data processing involved.

Acknowledgments

This work was supported by the Spanish Ministry of Science and Innovation, through Project CSD2010-00011 (Program Consolider-Ingenio), and by the Ministry of Economy, Industry and Competitiveness and by the European Union (FEDER), through Project RTC-2016-4845-3 (Program Retos-Colaboración).

References

[1] A. Dowling, S.R. Stow, Acoustic Analysis of Gas Turbine Combustors, J. Propul. Power 19 (2003) 751–764.
[2] T. Lieuwen, B.T. Zinn, Theoretical investigation of combustion instability mechanisms in lean premixed gas turbines, 36th AIAA Aerospace Sciences Meeting and Exhibit (1998) paper AIAA-98-0641.
[3] L. Rayleigh, The explanation of certain acoustical phenomena, Nature 18 (1878) 319–321.
[4] S. Candel, Combustion dynamics and control: Progress and challenges, Proc. Combust. Inst. 29 (2002) 1–28.
[5] T. Lieuwen, Modeling premixed combustion-acoustic wave interactions: a review, J. Propul. Power 19 (2003) 765–781.
[6] S. Ducruix, D. Durox, S. Candel, Theoretical and experimental determinations of the transfer function of a laminar premixed flame, Proc. Combust. Inst. 28 (2000) 765–773.
[7] P. Subramanian, R.S. Blumenthal, W. Polifke, R.I. Sujithc, Distributed time lag response functions for the modelling of combustion dynamics, Combust. Theor. Model. 19 (2015) 223–237.
[8] A. Gentemann, C. Hirsch, F. Kiesewetter, T. Sattlemayer, W. Polifke, Validation of flame transfer function reconstruction for perfectly premixed swirl flames, ASME Turbo Expo 2004 (2004) paper GT2004-53776.
[9] R. Balachandran, B.O. Ayoola, C.F. Kaminski, A.P. Dowling, E. Mastorakos, Experimental investigation of the nonlinear response of turbulent premixed flames to imposed inlet velocity oscillations, Combust. Flame 143 (2005) 37–55.
[10] K.T. Kim, J.G. Lee, B.D. Quay, D.A. Santavicca, Spatially distributed flame transfer functions for predicting combustion dynamics in lean premixed gas turbine combustors, Combust. Flame 157 (2010) 1718–1730.
[11] D. Durox, T. Schuller, N. Noiray, S. Candel, Experimental analysis of nonlinear flame transfer functions for different flame geometries, Proc. Combust. Inst. 32 (2009) 1391–1398.
[12] D. Durox, T. Schuller, S. Candel, Combustion dynamics of inverted conical flames, Proc. Combust. Inst. 30 (2005) 1717–1724.
[13] J. Ballester, T. García-Armingol, Diagnostic techniques for the monitoring and control of practical flames, Prog. Energy Combust. Sci. 36 (2010) 375–411.
[14] B.O. Ayoola, R. Balachandran, J.H. Frank, E. Mastorakos, C.F. Kaminski, Spatially resolved heat release rate measurements in turbulent premixed flames, Combust. Flame 144 (2006) 1–16.
[15] Y. Hardalupas, M. Orain, Local measurements of the time-dependent heat release rate and equivalence ratio using chemiluminescent emission from a flame, Combust. Flame 139 (2004) 188–207.
[16] Z. Han, S. Balusamy, S. Hochgreb, Spatial analysis on forced heat release response of turbulent stratified flames, J. Eng. Gas Turbines Power 137 (2015) 061504 1-8.
[17] K.T. Kim, J.G. Lee, H.J. Lee, B.D. Quay, D. Santavicca, Characterization of forced flame response of swirl-stabilized turbulent lean-premixed flames in a gas turbine combustor, J. Eng. Gas Turbines Power 132 (2010) 041502 1-8.
[18] P. Palies, D. Durox, T. Schuller, P. Morenton, S. Candel, Dynamics of premixed confined swirling flames, C. R. Mécanique 337 (2009) 395–405.
[19] Z. Han, S. Hochgreb, The response of stratified swirling flames to acoustic forcing: Experiments and comparison to model, Proc. Combust. Inst. 35 (2015) 3309–3315.
[20] T. Schuller, D. Durox, S. Candel, A unified model for the prediction of laminar flame transfer functions: comparisons between conical and V-flame dynamics, Combust. Flame 134 (2003) 21–34.
[21] T. Lieuwen, Nonlinear kinematic response of premixed flames to harmonic velocity disturbances, Proc. Combust. Inst. 30 (2005) 1725–1732.
[22] P. Palies, T. Schuller, D. Durox, S. Candel, Modeling of premixed swirling flames transfer functions, Proc. Combust. Inst. 33 (2011) 2967–2974.
[23] M.G. De Giorgi, A. Sciolti, S. Campilongo, A. Ficarella, Image processing for the characterization of flame stability in a non-premixed liquid fuel burner near lean blowout, Aerosp. Sci. Technol. 49 (2016) 41–51.
[24] P. Palies, D. Durox, T. Schuller, S. Candel, The combined dynamics of swirler and turbulent premixed swirling flames, Combust. Flame 157 (2010) 1698–1717.
[25] A.J. De Rosa, J. Samarasinghe, S.J. Peluso, B.D. Quay, D.A. Santavicca, Flame area fluctuation measurements in velocity-forced premixed gas turbine flames, J. Eng. Gas Turbines Power 138 (2015) 041507 1-9.
[26] N.A. Bunce, B.D. Quay, D.A. Santavicca, Interaction Between Swirl Number Fluctuations and Vortex Shedding in a Single-Nozzle Turbulent Swirling Fully-Premixed Combustor, J. Eng. Gas Turbines Power 136 (2013) 021503 1-11.
[27] D. Kim, J.G. Lee, B.D. Quay, D.A. Santavicca, K. Kim, S. Srinivasan, Effect of flame structure on the flame transfer function in a premixed gas turbine combustor, J. Eng. Gas Turbines Power 132 (2010) 021502 1-7.
[28] J. Peterleithner, N.V. Stadlmair, J. Woisetschläger, T. Sattelmayer, Analysis of measured flame transfer functions with locally resolved density fluctuation and oh-chemiluminescence data, J. Eng. Gas Turbines Power 138 (2015) 031504 1-9.
[29] S. Schimek, J.P. Moeck, C.O. Paschereit, An experimental investigation of the nonlinear response of an atmospheric swirl-stabilized premixed flame, J. Eng. Gas Turbines Power 133 (2011) 101502 1-7.
[30] S. Balusamy, L.K.B. Li, Z. Han, S. Hochgreb, Extracting flame describing functions in the presence of self-excited thermoacoustic oscillations, Proc. Combust. Inst. 36 (2017) 3851–3861.
[31] M.C. Lee, J. Yoon, S. Joo, J. Kim, J. Hwang, Y. Yoon, Investigation into the cause of high multi-mode combustion instability of H2/CO/CH4 syngas in a partially premixed gas turbine model combustor, Proc. Combust. Inst. 35 (2015) 3263–3271.

[32] M. Emadi, K. Kaufman, M.W. Burkhalter, T. Salameh, T. Gentry, A. Ratner, Examination of thermo-acoustic instability in a low swirl burner, Int. J. Hydrogen Energy 40 (2015) 13594–13603.

[33] D.M. Kang, F.E.C. Culick, A. Ratner, Combustion dynamics of a low-swirl combustor, Combust. Flame 151 (2007) 412–425.

[34] Y. Huang, Combustion dynamics of swirl-stabilized lean premixed flames in an acoustically-driven environment Ph.D. Thesis, University of Iowa, 2008.

[35] M. Hauser, M. Lorenz, T. Sattelmayer, Influence of Transversal Acoustic Excitation of the Burner Approach Flow on the Flame Structure, J. Eng. Gas Turbines Power 133 (2010) 041501 1-8.

[36] E. Luciano, Á. Sobrino, J. Ballester, A novel approach for the evaluation of local and global flame time lag from OH* filtered images, 22nd International Congress on Sound and Vibration (2015) paper 1089.

[37] A.J. De Rosa, S.J. Peluso, B.D. Quay, D.A. Santavicca, The effect of confinement on the structure and dynamic response of lean-premixed, swirl-stabilized flames, J. Eng. Gas Turbines Power 138 (2015) 061507 1-10.

[38] P.R. Alemela, Measurement and scaling of acoustic transfer matrices of premixed swirl flames Ph.D. Thesis, Technische Universität München, 2009.

[39] T. García-Armingol, J. Ballester, A. Smolarz, Chemiluminescence-based sensing of flame stoichiometry: Influence of the measurement method, Measurement 46 (2013) 3084–3097.

[40] J. Ballester, R. Hernández, A. Sanz, A. Smolarz, J. Barroso, A. Pina, Chemiluminescence monitoring in premixed flames of natural gas and its blends with hydrogen, Proc. Combust. Inst. 32 (2009) 2983–2991.

[41] B.D. Bellows, M.K. Bobba, A. Forte, J.M. Seitzman, T. Lieuwen, Flame transfer function saturation mechanisms in a swirl-stabilized combustor, Proc. Combust. Inst. 31 (2007) 3181–3188.

[42] V.N. Kornilov, M. Manohar, L.P.H. de Goey, Thermo-acoustic behaviour of multiple flame burner decks: Transfer Function (de)composition, Proc. Combust. Inst. 32 (2009) 1383–1390.

[43] F. Duchaine, F. Boudy, D. Durox, T. Poinsot, Sensitivity analysis of transfer functions of laminar flames, Combust. Flame 158 (2011) 2384–2394.

[44] J.C. Román Casado, Nonlinear behavior of the thermo acoustic instabilities in the limousine combustor Ph.D. Thesis, University of Twente, 2013.

[45] L. Tay-Wo-Chong, S. Bomberg, A. Ulhaq, T. Komarek, W. Polifke, Comparative validation study on identification of premixed flame transfer function, J. Eng. Gas Turbines Power 134 (2011) 021502 1-8.

[46] D. Kim, S.W. Park, Forced and self-excited oscillations in a natural gas fired lean premixed combustor, Fuel Process. Technol. 91 (2010) 1670–1677.

COMBUSTION SCIENCE AND TECHNOLOGY
https://doi.org/10.1080/00102202.2019.1662407

Taylor & Francis
Taylor & Francis Group

Analysis of the Dynamics of Premixed Methane and Biogas Flames Based on Cross-correlation Maps

Ennio Luciano[a] and Javier Ballester[b]

[a]Laboratory of Research on Fluid Dynamics and Combustion Technologies (LIFTEC), CSIC – University of Zaragoza, Zaragoza, Spain; [b]Fluid Mechanics Group/LIFTEC, CSIC-University of Zaragoza, Zaragoza, Spain

ABSTRACT

In this study, the cross-correlation method (CCM) has been investigated in detail and applied to analyze the dynamic response of premixed methane and biogas flames. CCM mapping was proposed in a recent study as an effective, and notably simple, method to evaluate the actual contribution of different flame zones to its global dynamic response. The physical interpretation of cross-correlation maps has been further investigated and validated by means of spatially resolved measurements of the local flame transfer function along the flame. The results obtained are consistent with vortex shedding being the phenomenon governing the dynamics of the flames studied. Methane and biogas flames exhibited different response to fluctuations. The analysis of cross-correlation maps revealed changes in the location of regions with strongest response to velocity fluctuations. Furthermore, this method was applied to determine the variations in the convective length associated with the phase delay between the oscillations in velocity and in heat release rate. In spite of the broad differences among the flames studied, all of them were consistent with the perturbations traveling along the flame at approximately one half of the flow velocity, in coincidence with the findings of some recent works.

ARTICLE HISTORY
Received 15 April 2019
Revised 28 August 2019
Accepted 28 August 2019

KEYWORDS
Cross-correlation method; flame transfer function; thermoacoustic instability; biogas flames; flame dynamics

Introduction

The interaction between a fluctuating heat source and the acoustic field in which it is contained, firstly described by Rayleigh (1878), has become a relevant phenomenon to be taken into account for the correct operation of gas turbine plants. In fact, lean premixed combustion, adopted in the majority of these plants because of their low NO_x emissions, has shown proneness to generate thermoacoustic instabilities (Lieuwen and Zinn (1998), Dowling and Stow (2003)).

These are system instabilities, whose growth is determined by the acoustic properties of the combustion equipment and by the dynamic response of the flame. This response is usually quantified in terms of the flame transfer function, FTF (or the flame describing function, FDF when non-linear conditions are reached), by relating the amplitude and phase of the oscillations of heat released by the flame (Q') with respect to those of equivalence ratio fluctuations, Φ', and/or inlet velocity oscillations, u', as a function of

CONTACT Javier Ballester ✉ ballester@unizar.es Fluid Mechanics Group, School of Engineering and Architecture, María de Luna, 3, Zaragoza 50018, Spain

Color versions of one or more of the figures in the article can be found online at www.tandfonline.com/gcst.

frequency (Candel (2002), Lieuwen (2003)). The knowledge of the FTF allows determining the ranges of stability for a given combustion condition or to determine the influence of the various operating conditions which affect flame properties (Lamraoui et al. (2011), Richecoeur et al. (2013), Kim et al. (2010c)). This is also true for changes in fuel properties, whose effect on thermo-acoustic stability for a given combustion facility depends on the variations in FTF (Kim et al. (2010c)). Hence, this is the sort of information required to evaluate potential changes in dynamic stability characteristics of combustion equipment due to fuel switching.

Among other options, biogas offers a good potential for energy generation in gas turbine engines. In fact, its estimated potential growth is really high, representing both a great percentage of renewable sources in EU27 countries plans to get 2020 goals (Sun et al. (2015)) and an opportunity for rural zones of developing countries to exploit this resource and, in this way, raise their living standards (Chen et al. (2014), Zhen et al. (2016), Surendra et al. (2014)). Biogas is mainly obtained from anaerobic digestion process of different kinds of organic material in either digesters or landfills. Final product is a mixture of principally CH_4 and CO_2, which concentration can vary depending on substrate used, fermentation technology and collection method (Sun et al. (2015)). Typical concentration range are 35–70% in volume for CH_4 and 15–40% in volume for CO_2 (Sun et al. (2015)).

Due to this potential, various works have investigated the combustion characteristics of biogas (e.g., Hinton and Stone (2014), Cohé et al. (2009), Wei et al. (2016), Kobayashi et al. (2007)) and the technical issues due to switching from natural gas to biogas (Hosseini and Wahid (2014), Mordaunt and Pierce (2014), Nikpey et al. (2014)). The impact of biogas composition on stability limits has been analyzed in some studies, with particular attention to blow-out (Leung and Wierzba (2008), Saediamiri, Birouk, and Kozinski (2014), Dai et al. (2012), Mordaunt and Pierce (2014)). A few works (Lee et al. (2013), Lafay et al. (2007)) have addressed the thermoacoustic behavior of biogas flames, although the FTF of biogas flames has not been specifically studied. Hence, the analysis of the FTF for biogas flames and its comparison with traditional fuels seems an important piece still missing in literature.

In the common case of perfectly premixed, V-shaped flames, many experimental and theoretical studies (e.g., Ducruix, Durox, and Candel (2000), Subramanian et al. (2015), Gentemann et al. (2004), Balachandran et al. (2005), Durox et al. (2009), Durox, Schuller, and Candel (2005)) have shown that the gain, G, of the FTF presents a low-pass filter behavior and its phase, φ, varies linearly with the frequency. This global flame response is the result of the combination of the local response at each location; more specifically, the global FTF can be calculated as the volume integral of local FTFs, weighed with the local heat release rate from each flame portion (Kornilov, Manohar, and de Goey (2009), Kim et al. (2010c)). Hence, the local contribution to the global dynamic response of the flame may be very different according to the flame zone analyzed, and these differences may not be related exclusively to the different value of the local heat released. In fact, each flame spot responds with different amplitudes and phases to oscillations in, e.g., injection velocity (Kim et al. (2010c)). Hence, the description and analysis of the relative contributions of different parts of the flame to its global response appears to be an important objective in order to better understand the flame dynamic behavior. In particular, this can be an effective method to describe the changes caused by variations in fuel properties on the dynamic response of the flame and, finally, on its thermo-acoustic stability.

The analysis of a series of images filtered at a chemiluminescent band is the technique commonly used to analyze the dynamic response of local areas of the flame, due to the proportionality of some chemiluminescent radical (e.g., CH* or OH*, both emitting at well-defined wavelengths) with the instantaneous heat released (Ballester and Garcia-Armingol (2010), Balachandran et al. (2005), Ayoola et al. (2006), Hardalupas and Orain (2004), Kim et al. (2010c)). Various post-processing techniques have been proposed in the literature, which give as a result different maps containing valuable information about the dynamic behavior of the flame; some examples often used in studies are the mean intensity map (Han, Balusamy, and Hochgreb (2015), Balachandran et al. (2005), Palies et al. (2009), Kim et al. (2010c)), the map of the standard deviation of the local heat released (De Giorgi et al. (2016), Palies et al. (2010), De Rosa et al. (2015b), Bunce, Quay, and Santavicca (2013)) or the Rayleigh index map (Lee et al. (2015), Emadi et al. (2015), Kang, Culick, and Ratner (2007), Huang (2008)), just to name the most commonly used.

In this context, the so-called “cross-correlation method” (CCM) (De Rosa et al. (2015a), Luciano, Sobrino, and Ballester (2015)) represents a simple yet suitable option to analyze the actual contribution of a flame parcel to its global dynamics. In a recent work, Luciano and Ballester (2018) have analyzed in-depth this methodology and showed that the cross-correlation map informs on the “local effective gain” of each flame parcel. This and other conclusions mentioned below were supported both by theoretical analysis and by the experimental results for a range of tests with premixed flames.

In order to seek further evidences, a first objective of this work was to compare CC maps with measurements of the local FTF of perfectly premixed, V-shaped, swirling flames at selected flame zones. The diagnostic methods afforded by cross-correlation maps were applied to analyze the dynamic response of a range of flames, including methane and CH_4-CO_2 blends with different proportions, representative of the biogas. So, the second objective was to exploit the possibilities of the CC method to analyze similarities and differences between methane and biogas flames, in terms of the flame transfer function, the spatial distribution of their dynamic response and of representative parameters such as the sensitive time lag or the convective length.

Experimental method

The dynamic response of premixed flames was studied in the combustion rig shown in Figure 1. A detailed description was provided by Luciano and Ballester (2018) and only the essential elements and the additional instrumentation used for this work are listed here. The tests were conducted under perfectly premixed conditions with fixed equivalence ratio, which was guaranteed by injecting the fuel-air mixture through choked orifices into the plenum. The mixture flows along an annular duct containing an axial swirler (geometrical swirl number = 0.48). Five piezoelectric pressure transducers (PTs) were installed along the injection tube to determine velocity fluctuations (u') at the injection with the multi-microphone method (Alemela (2009)). Another PT was located at the dump plane (see Figure 1), to record the pressure fluctuations in the combustion chamber.

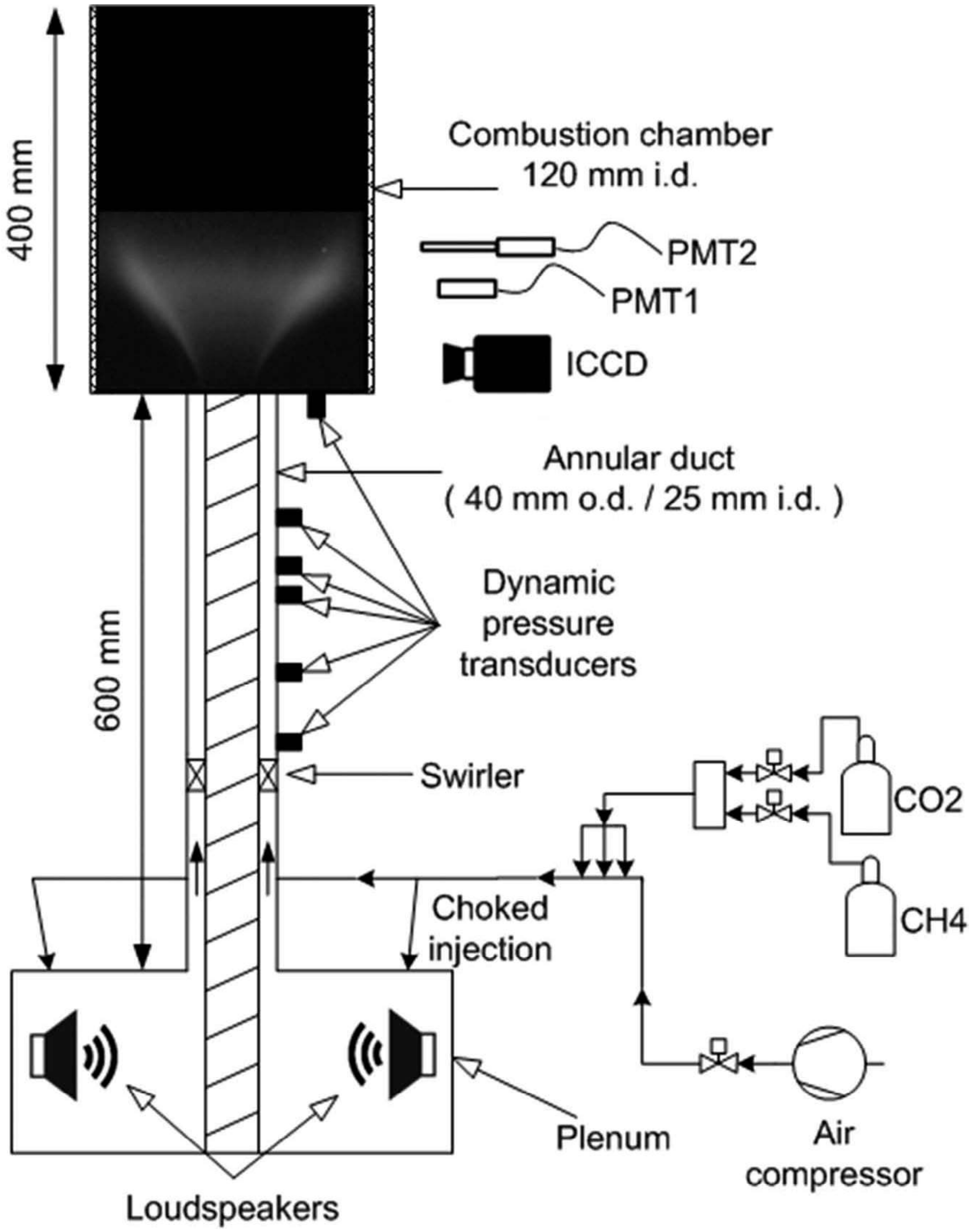

Figure 1. Sketch of the experimental facility and instrumentation used.

All flames studied displayed the usual V shape, normally found in swirl-stabilized dump combustors. The combustion chamber consisted of a quartz tube (120 mm i.d.), allowing unrestricted optical access. This study extensively uses OH* chemiluminescence images recorded with an intensified CCD camera (ICCD, Hamamatsu C8484-05) fitted with an OH* interference filter (310 ±5 nm). Each sequence comprised 500 frames, recorded with an exposure time of 80 µs. Two photomultiplier tubes (Hamamatsu H5784-03) were used to measure bandfiltered radiation in the OH* band. One of them (PMT1, thereafter) collected the total emission from the whole flame, whereas the other one (PMT2) was fitted with a tube acting as a diaphragm to select smaller measuring volumes. Figure 2 shows the location of both sensors. PMT1 is placed at a radial distance

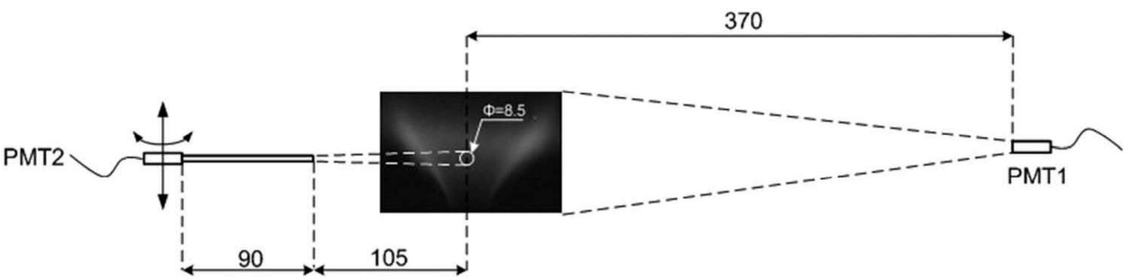

Figure 2. Location of the two PMTs relative to the flame. All dimensions in mm.

long enough to see the whole flame. As it was explained by García-Armingol et al. (2014), the view angle of PMT2 was limited by means of a tube (i.d. 4 mm, length 90 mm), so that the field of view included a slightly conical volume with a diameter of 8.5 mm at the flame axis. The PMT2+tube assembly was mounted on a 2D traverse system, which allowed selecting measuring volumes at different axial and radial distances, as explained below.

The tests reported here include flames of methane and two CH_4-CO_2 blends, which simulate two typical biogas compositions (85–15% and 60–40% by volume, denoted as biogas 85–15 and 60–40, respectively). As shown in Figure 1, the blends are prepared on-line by mixing the streams of CH_4 and CO_2, regulated in closed loop by mass flow controllers. The three fuels were tested at three different equivalence ratios (Φ= 0.98, 0.86 and 0.72). For each fuel, its mass flow rate was fixed and the equivalence ratio was changed by varying the airflow rate. For methane flames, the mass flow rate of methane was set to 3 Nm^3/h, so that the injection velocity at the dump plane was $\bar{u}$= 12.7, 14.3 and 16.8 m/s for Φ= 0.98, 0.86 and 0.72, respectively. For the biogas blends the flow rates were adjusted so as to maintain the same injection velocities indicated above for pure methane mixtures at the same equivalence ratio. This resulted in small variations in thermal input, up to only 7% in the worst case (CH4 vs. biogas (60–40) at Φ= 0.98).

Local and global Flame Transfer Functions (FTF) were measured in tests with acoustic forcing, using the two loudspeakers installed in the plenum (see Figure 1), from 50 to 600 Hz with 10 Hz steps. At each frequency, the signals from the dynamic pressure transducers and photomultipliers were acquired simultaneously for 4 s at a sampling frequency of 4 kHz. Following the common practice (Balachandran et al. (2005), Ayoola et al. (2006), Hardalupas and Orain (2004)), OH* chemiluminescence was assumed to be proportional to the instantaneous heat release rate and the signals from photomultipliers PMT1 and PMT2 were interpreted, respectively, in terms of the global and local heat release rates involved in the calculation of flame transfer functions. Flame images were recorded and analyzed for some selected excitation frequencies: f_{ex}= 90, 150, 230 Hz. In all cases, the forcing amplitudes yielded flame oscillations within the linear range (more details in Luciano and Ballester (2018)).

The tube installed in front of PMT2, as shown in Figure 2, restricted the field of view to circles of 8.5 mm at the flame, which can be compared with the values recorded with the ICCD camera at the same location. Results will be shown for the nine spots identified in Figure 3, at the axial (H) and radial (R) coordinates listed in Table 1. Seven of them are located along the V-flame sheet, as identified from Abel-transformed images (see Figure 3, left). Local FTF measured as a function of the distance from injection can be directly

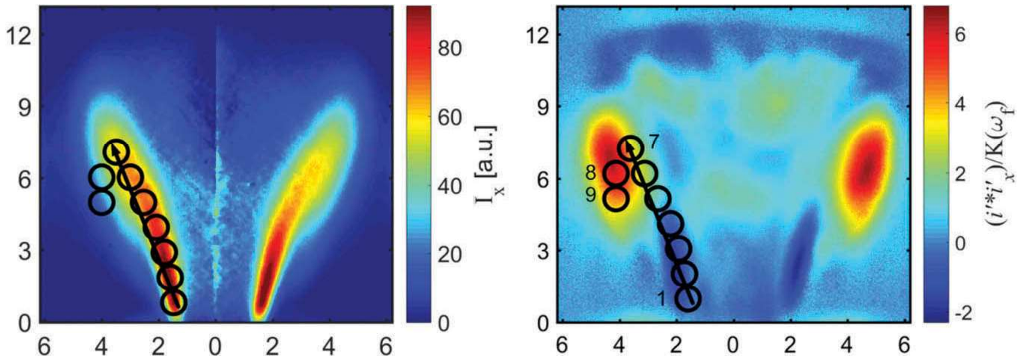

Figure 3. Flame areas selected to measure local FTF, superposed on an Abel-transformed map (left) and a cross-correlation map (right). Coordinates in cm.

Table 1. Axial and radial coordinates of the flame zones analyzed with PMT2.

Point code	1	2	3	4	5	6	7	8	9
H [cm]	1.0	2.0	3.0	4.0	5.0	6.0	7.0	6.0	5.0
R [cm]	1.7	1.8	1.9	2.2	2.7	3.1	3.7	4.1	4.1

compared with the interpretation on the influence of L_x on the sensitive time lag. Spots 8 and 9 correspond to the area displaying the peak values in the CC maps (see Figure 3, right), in order to determine whether the magnitude of average cross-correlation calculated from chemiluminescence images is effectively related to that of the local FTF. All the data reported on local FTF correspond to a pure methane flame with $\Phi = 0.86$. Additional measurements performed for other equivalence ratios and fuels, as well as at other locations in the flame (e.g., inside the V flame), yielded results fully consistent with those reported here and, so, are not included for brevity.

Cross-correlation maps vs. local FTF

The analysis of flame dynamics based on cross-correlation maps was recently proposed by Luciano and Ballester (2018) as an effective method to determine the relative contribution of different flame zones to its global dynamic response. That paper provides a detailed description and, for convenience, only the essential ideas are summarized in Appendix A. In particular, the following relevant information can be extracted from cross-correlation maps:

The normalized cross-correlation, denoted as $\left(i'{*}i'_x\right)/K(\omega_f)$, is equivalent to the effective local gain, expressed as $G_x \cdot \cos\left(\varphi_x - \varphi\right)$, where G_x is the gain of the local FTF and φ_x, φ are the phases of the local and global FTF, respectively.

The sensitive time lag, τ, of the FTF (in $n - \tau$ formulation) is related to a characteristic flame length, L, which can be determined as the distance between the injection and the peak value in the CC map; so CCM represents a notably simple, physically based and unambiguous method to define L.

The results reported in Luciano and Ballester (2018) clearly supported these postulates. In this work, a new set of tests, with more detailed measurements, were conducted to experimentally verify both the physical interpretation of CC maps and the underlying hypotheses.

The global FTF obtained for Φ= 0.86 is shown in Figure 4 (black thick line). The usual dynamic response of perfectly premixed, V-shaped flame is obtained: low-pass filter behavior in gain and a linear trend in phase (associated time lag is 5.04 ms). The global FTF was measured again each time a local FTF was determined; therefore, 10 repeated measurements of the global dynamics were performed. Values obtained showed a good repeatability, with a maximum deviation always below 10% of the reported data. The experimental procedure was further verified by repeating some of the local FTF determinations, again showing good coincidence with deviations also <10%.

As observed in Luciano and Ballester (2018) from phase-locked images, the flame dynamics, and so the FTF obtained, is attributed to the vortex shedding phenomenon, i.e., the impingement on the outer shear layer of coherent macrostructures shed at the dump plane and convected downstream. In particular, the combustion products wind around these vortices at the flame tip, creating a strong heat fluctuation in this zone, a phenomenon known as vortex roll-up; this mechanism has been analyzed extensively in the literature as one of the main processes responsible of thermoacoustic instabilities (Durox, Schuller, and Candel (2005), Candel (2002), Durox et al. (2009), Palies et al. (2010), Bellows et al. (2007), Palies et al. (2009), Balachandran et al. (2005)). Also, the fluctuations induced by the swirler might represent another important instability source (Bunce, Quay, and Santavicca (2013), Palies et al. (2010)), but synchronized images indicated negligible contribution of this mechanism for the cases studied (Luciano and Ballester (2018)).

The magnitude and the phase of the local FTF obtained for points 1–7, located along the flame sheet, are also shown in Figure 4. The local gain, G_x, shows an almost flat evolution with frequency over the first half of the flame (points 1–3). Instead, the points located farther downstream (5–7) present a low-pass filter behavior, with the gain peaking in the range 100–200 Hz, whereas point 4 represents a transition between both behaviors. Gain values consistently increase with the distance along the flame, at least for low frequencies, including the ones investigated in Luciano and Ballester (2018) (90, 150, 230 Hz); at higher frequencies, the low-pass filter behavior at the downstream zones leads to G_x values similar to those registered closer to the injection plane. This different

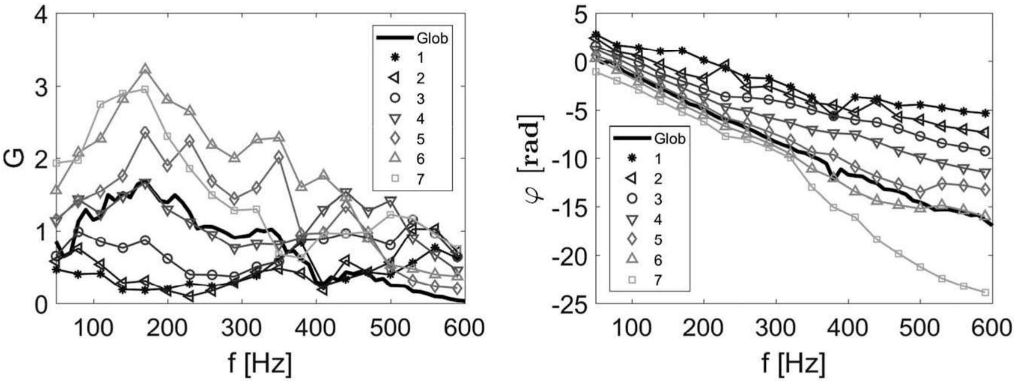

Figure 4. Gain (left) and phase (right) of the global and local FTF measured at points 1–7 for Φ= 0.86.

response may be due to the different impact of vortices along the flame height, as proposed and discussed in Durox, Schuller, and Candel (2005). Near the injection, the coherent macrostructures are still small and their effects are rather modest; as they move downstream, they grow in dimension and strength, but also neighbor vortices mutually obstruct their dragging of burning gases, due to their equal rotating direction. This creates just cusps and hollows on the flame edge, while at the flame tip there is no obstacle to the ingestion of gases by the vortex and the roll-up phenomenon happens (see Durox, Schuller, and Candel (2005) for a more detailed explanation). The observed increment in flame response along its height is consistent with this description. The higher the excitation frequency is, the smaller the macrostructures formed will be, so also their dragging force will diminish; this might be the reason why the local FTF develop low-pass filter behaviors as the probed points approach the flame tip.

Local FTF gains show both lower and higher values than the magnitude of the global FTF. This is consistent with the fact that the global response of the flame can be interpreted as the sum of the local responses weighed with the mean heat rate locally released (Kornilov, Manohar, and de Goey (2009), Kim et al. (2010c)), so that the higher gains obtained will contribute in an amount dictated by their respective $\bar{Q}_x$ values. The phase of both global and local FTF displays almost linear trends, with slopes increasing with H. The phase curve for the global FTF practically coincides with that of the local response at H= 6 cm. Kim et al. (2010c) obtained a similar evolution of both the local gain and phase along the flame height, even though their local FTF measurements were integrated across the flame width.

The local FTF functions measured at points 1–7 are a useful reference to analyze the physical information contained in cross-correlation maps, like that shown in Figure 3-right. The conclusions can be contrasted, on the one hand, with the expression postulated for the general case (see appendix, Eq. (A-4)). On the other hand, the linear tendency of the φ_x values with f_{ex} observed for the measured FTFs indicates that the flame can be suitably described by $n - \tau$ models, both regarding the global and local dynamic response. Hence, the expressions used in the previous study (Eqs. (A-6)–(A-7) of the appendix) are actually applicable in the cases studied.

Apart from describing the effective contribution of the different areas to the global flame response, the CCM was postulated by Luciano and Ballester (2018) to constitute an effective and physically sound method to determine the convective length associated to the sensitive time lag between the velocity excitation at the injection and the global heat release fluctuation, Q' (represented by τ in $n - \tau$ models). According to Luciano and Ballester (2018) (see Eqs. (A-6)–(A-7) of the appendix), the characteristic length representative of the bulk response of the flame, L, coincides with the distance L_x at which the time lag for the local FTF coincides with that of the global FTF.

Figure 5-left represents the time lags, τ_x, calculated as the slope of the phase curves for the seven local FTFs measured along the flame. This plot depicts an approximately linear evolution, as an additional evidence of the proportionality between distance along the flame and sensitive time lag. The value of τ for the global FTF is also indicated as a horizontal dashed line and is only slightly higher than the time lag τ_x derived from the local FTF measured at point 6. Therefore, the location of point 6 is representative of the average convective length traveled by a perturbation until it generates a fluctuation in

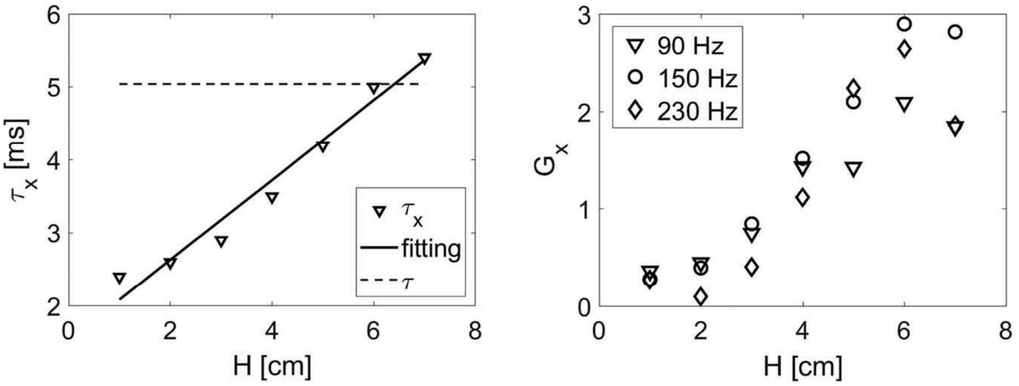

Figure 5. Left: Variation of local time lag, τ_x,with the axial coordinate, *H*; right: Evolution of local gain, G_x,as a function of *H* at f_{ex}= 90, 150 and 230 Hz.

heat release rate; that is, $L \approx L_x$ at point 6. This conclusion is to be compared with the CCM map shown in Figure 3-right, where the peak value is located, precisely, near point 6 (actually, between points 6 and 7). Figure 5-right shows the variation of the gain of local FTF along the distance from the injection, for three different forcing frequencies. In all cases, G_x displays a continuous growth until point 6, which again pinpoints this area of the flame as the most responsive to perturbations among those probed along the V flame, in fully agreement with the pattern observed in the CCM map (see Figure 3-right). The trend depicted in Figure 5-right is fully consistent with the evolution indirectly estimated from cross-correlation maps by Luciano and Ballester (2018), as an additional confirmation of the rationale behind the development and interpretation of this kind of flame mapping.

Additionally, the local FTF was measured at points 8 and 9, located in the vortex roll-up area (see Figure 3-right) where, according to the CC map, the dynamic activity is expected to be very strong. The gain and phase diagrams are represented in Figure 6, along with those for points 5 and 6 and for the global FTF. The phase curves (Figure 6b) are very similar in all cases, as a clear indication that the zone defined around points 6 (in the V-flame) and 9 (in the vortex roll-up) is representative of the sensitive time lag (and associated convective length) exhibited by the bulk FTF. Nevertheless, some differences

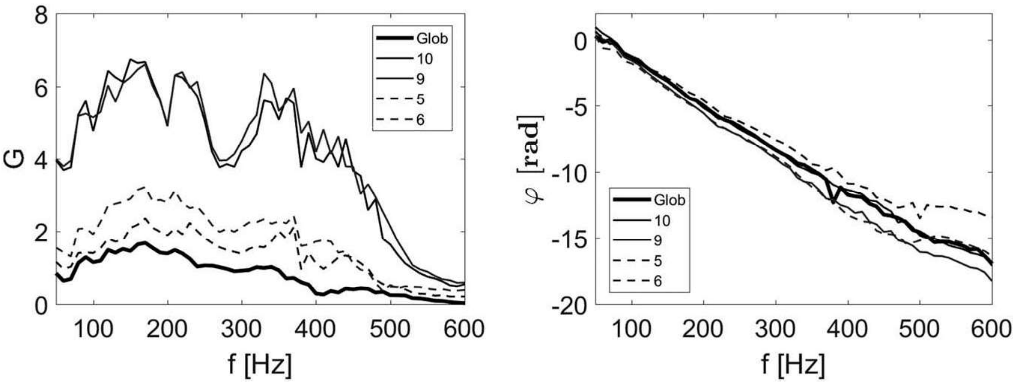

Figure 6. Gain (left) and phase (right) of the global FTF (black line) and of the local ones measured both at points 9–10 (solid lines) and at 5–6 (dashed line).

can be still observed between the phase curves for the 4 points, with a greater time lag (i.e., steeper decay) for points 6 and 8; on the contrary, the slope is very similar between the pairs of points located at the same height (5/9 and 6/8). All this is again consistent with the concept of a sensitive time lag associated with convective delays.

All the local gain curves (Figure 6a) display values significantly higher than those of the global FTF; i.e. this part of the flame has a strong dynamic activity, well above the average over the flame. Points 8 and 9, located in the VR zone, show remarkably high peak gains, reaching values close to 7, clearly demonstrating the high susceptibility of the heat released at the vortex in response to injection velocity perturbations. However, the actual contribution of a given flame parcel not only depends on the local gain, but is also proportional to the magnitude of local heat release rate (Luciano and Ballester (2018), Kim et al. (2010c), Kornilov, Manohar, and de Goey (2009)), as discussed below.

The FTF for the global flame can be calculated from the local functions, $\mathrm{FTF_x}$, as (Kornilov, Manohar, and de Goey (2009), Kim et al. (2010c))

$$FTF = \sum FTF_x \frac{\bar{Q}_x}{\bar{Q}} \tag{1}$$

Hence, the gain of the global FTF can be expressed as

$$G = \sum G_x e^{i\left(\varphi_x - \varphi\right)} \frac{\bar{Q}_x}{\bar{Q}} \tag{2}$$

Since G is a real number, this can be simplified to

$$G = \sum G_x \cos\left(\varphi_x - \varphi\right) \frac{\bar{Q}_x}{\bar{Q}}, \tag{3}$$

i.e., the gain of the global FTF can be calculated as the sum of the projections in the complex plane of $\mathrm{FTF_x}$, weighed by the magnitude of the mean heat release rate at each point x. In this work, Eq. (3) has been applied to the nine local FTF determined at locations 1–9 (see Figure 3 and Table 1), and the result is compared in Figure 7 with the global FTF actually measured. In spite of the small number of points, covering only a narrow zone, the coincidence is notably good (probably because these points cover the region with the highest contribution to the global flame oscillations).

Alternatively, and according to the proposed interpretation for CCM, it should be also possible to decompose the global FTF in terms of local cross-correlation data. In fact, according to the formulation of CC method (see Eqs. (A-2) and (A-4) of the appendix), the calculation described in Eq. (3) can be expressed as a summation over the cross-correlation map, weighed at each point by the corresponding local heat release rate:

$$G = \sum_x \frac{i' * i'_x}{K(\omega_f)} \frac{\bar{Q}_x}{\bar{Q}} \tag{4}$$

where the 'effective local gain', $G_x \cdot \cos\left(\varphi_x - \varphi\right)$, has been replaced by the normalized cross-correlation value, $i' * i'_x / K(\omega_f)$. Hence, all local values involved in Eq. (4) can be easily extracted from chemiluminescence maps (in particular, mean local heat release rate and

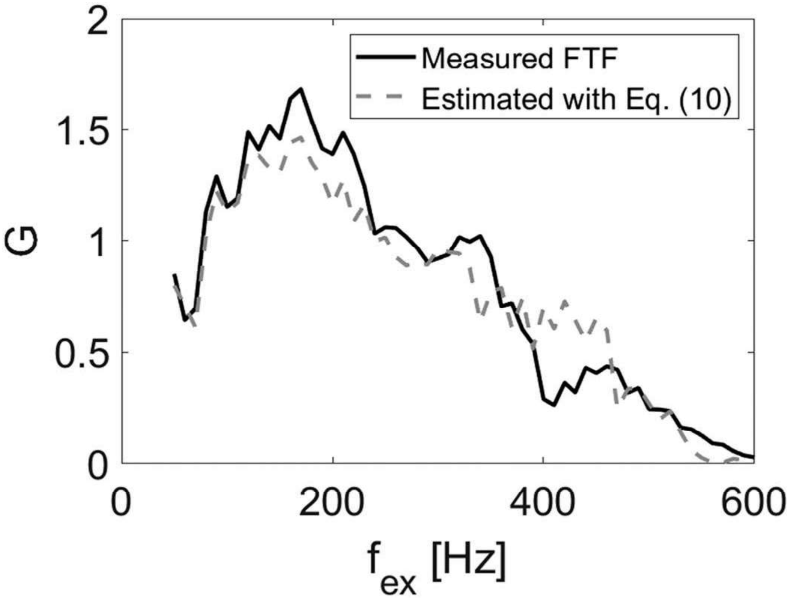

Figure 7. Global FTF and its estimate by applying Eq. (3) to the FTF_x measured at points 1–9.

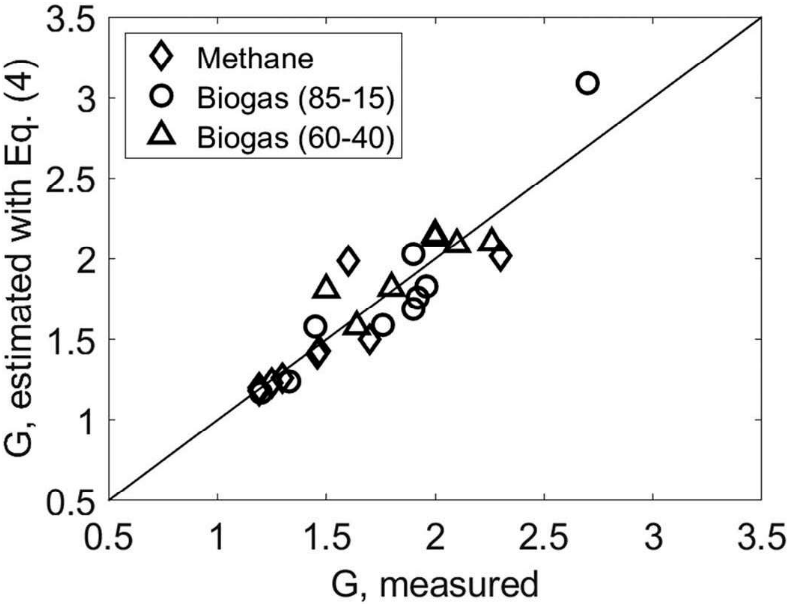

Figure 8. Comparison between measured values of G and the corresponding estimates from cross-correlation maps through Eq. (4).

normalized cross-correlation ones). This exercise was applied to three different fuels, for three different equivalence ratios (0.72, 0.86, 0.98) and three forcing frequencies (90, 150, 230 Hz). The results are compared with the gain of the corresponding FTF in Figure 8. The difference only exceeded 15% in one case (out of 27 tests), which again confirms the consistence of the procedure and the methodology proposed.

This was just a global verification proof, but the CCM may provide much richer information. For example, it is interesting to analyze the widely different nature of the contributions from different flame zones. Figure 9 represents the two factors in Eq. (4) for

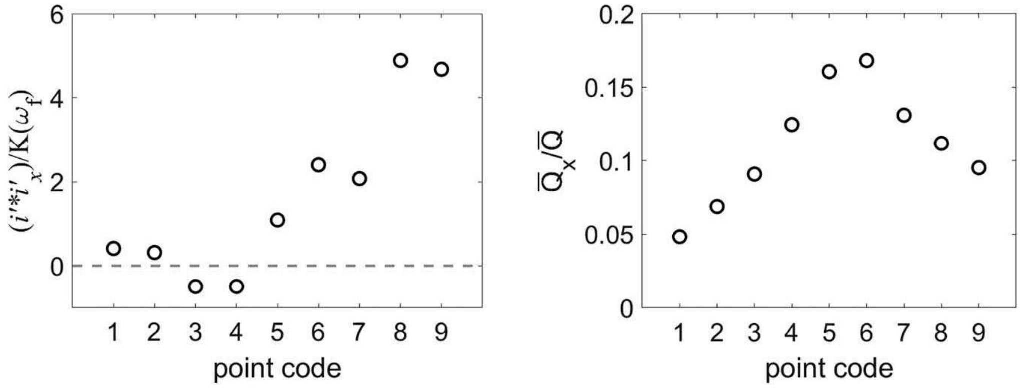

Figure 9. Magnitudes of the two factors in Eq. (4): left: Effective local gain; right: Fraction of total heat release rate at each probed point.

the 9 points listed in Table 1 and identified in Figure 3, for the tests with methane, Φ= 0.86 and forcing frequency of 230 Hz. As the measuring volume moves from points 1 to 7 along the V flame, the 'effective local gain', as estimated from $i' * i'_x/K(\omega_f)$, exhibits zones of positive and negative sign and reaches a maximum at point 6. This effective gain, however, is much higher at points 8 and 9, located at the vortex roll-up zone. Therefore, the flame includes zones contributing to the oscillation ($i' * i'_x > 0$) whereas other zones tend to damp it ($i' * i'_x < 0$), and also some points (8 and 9) exhibiting very high local gains. However, the global thermoacoustic behavior must be evaluated from the global FTF, which combines all the flame parcels (with high/low, positive/negative effective gains), weighted by the magnitude of the local heat release rate (higher along the V flame). All these considerations are duly accounted for in Eq. (4), in terms of data directly extracted from chemiluminescence images by applying cross-correlation mapping.

In summary, all the verifications attempted in terms of both local and global FTF confirmed the validity of the theoretical reasoning behind cross-correlation mapping, as described in the previous section and in Luciano and Ballester (2018), as well as the physical interpretation proposed for CC maps. In the next section, this method will be applied to analyze chemiluminescence images recorded for premixed methane and biogas flames.

Effect of fuel and equivalence ratio on flame dynamics and associated parameters

Cross-correlation mapping was applied to evaluate the influence of fuel composition and equivalence ratio on some aspects of the dynamic response of lean premixed flames. As it was explained in Section 2, the test matrix included nine cases: three equivalence ratios (Φ =0.72, 0.86, 0.98) and three fuel compositions (pure CH_4 and two CH_4/CO_2 blends, 85/15% and 60/40% by volume, respectively). On the one hand, this set of experiments allowed studying the effect of fuel composition in a relatively simple case, since the addition of CO_2 modifies flame temperatures but is not expected to significantly affect combustion chemistry; and, on the other hand, the tests are relevant for the use of biogas in lean premixed combustors, since this alternative fuel contains as major constituents CH_4 and CO_2 in similar proportions.

A general impression on the effects of both stoichiometry and fuel composition can be obtained from Figure 10, representing the average OH* intensity maps for different flames. The first row displays the images for pure methane flames at different equivalence ratios. As the flame becomes leaner, the axial and radial dimensions of the flame gradually increase. Similar changes in flame geometry were obtained when methane is diluted with CO_2. In Figure 10, the changes when the proportion of CO_2 increases from 15% to 40% for fixed Φ=0.86 (bottom row) are qualitatively similar to those observed between CH_4 flames with Φ=0.86 and Φ=0.72 (top row). For example, the leanest methane flame (Φ=0.72) exhibits a flame pattern similar to the case with 40% CO_2 and Φ=0.86. This coincidence is consistent with the CO_2 addition having primarily a dilution effect, resulting in lower flame temperature, as it also happens when the equivalence ratio decreases.

Figure 10 also reveals significant variations in peak intensity between the different cases. This can be more clearly observed in Figure 11, representing the average values of radiation measured by the photomultiplier tube PMT1, which detects OH* chemiluminescence emitted from the whole flame. In all cases, for a fixed fuel composition, the intensity increases as the flame becomes richer. This is a well-known fact, extensively characterized experimentally (García-Armingol, Ballester, and Smolarz (2013), Hardalupas and Orain (2004), Ballester et al. (2009)) and also reproduced in kinetic studies (García-Armingol et al. (2014), Hardalupas and Orain (2004)). Also, the results clearly demonstrate that as CO_2 is added to the fuel, the radiation intensity, $\bar{I}$, gradually decreases, especially for rich flames. Results similar to those shown in Figure 11 were obtained by Lafay et al. (2007), although with some differences in the observed trends, probably due to the different operational condition imposed (here, the air mass flow is changed in order to obtain the same inlet velocity for each blend at equal Φ, whereas in Lafay et al. (2007) the airflow is kept constant and the fuel flow varied among the tests). Again, the results shown in Figure 11 indicate a similar trend of radiation intensity both when the excess air is increased by lowering Φ and when CO2 is added to the fuel for fixed Φ.

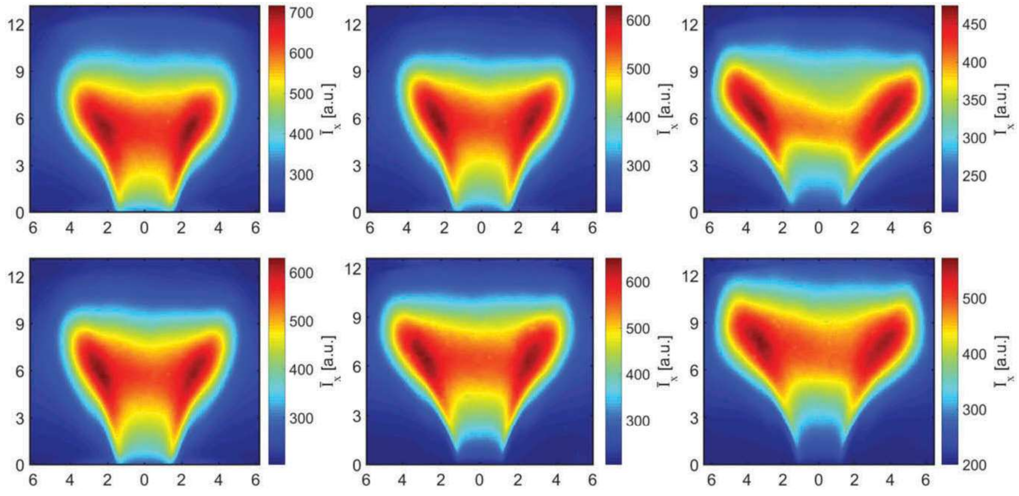

Figure 10. Average images of depth-integrated OH* chemiluminescence. Top row: pure methane flames at Φ= 0.98 (left), Φ= 0.86 (middle), Φ= 0.72 (right). Bottom row: flames at Φ= 0.86 of pure CH_4 (left), CH_4-CO_2 = 85%-15% (middle), CH_4-CO_2 = 60%-40% (right).

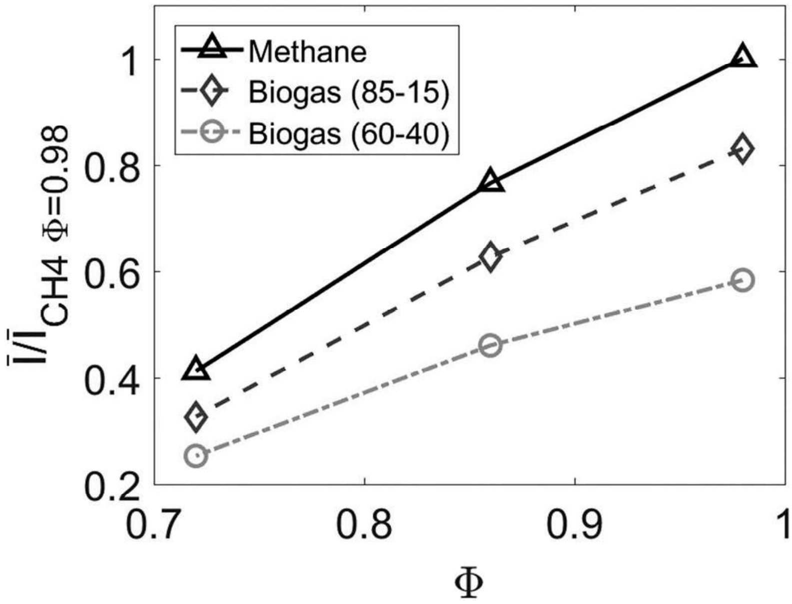

Figure 11. Evolution of the average intensity emitted by the flames studied as a function of Φ and fuel composition. Data normalized by the value measured at Φ= 0.98 with pure methane.

The FTFs obtained for each blend and Φ are shown in Figure 12. Again, every operational condition depicts the typical dynamic response of swirling, V-shaped flames (low-pass filter behavior in gain and linear trend in phase). In most instances, leaner flames display higher gains over most of the frequency range. The only exception is the case of biogas (60–40) at Φ=0.72, which, as commented below, exhibits a different flame configuration. Similarly, to the effect observed as Φ decreases, the addition of CO_2 gradually increases the FTF gain for most of the frequency range (up to 400 Hz), whereas the response becomes weaker for higher frequencies. The exception observed for biogas (60–40) at Φ=0.72, with a sudden drop at ~250 Hz, is ascribed to its different configuration, passing from the typical V shape of all other cases to a trumpet one (Terhaart,

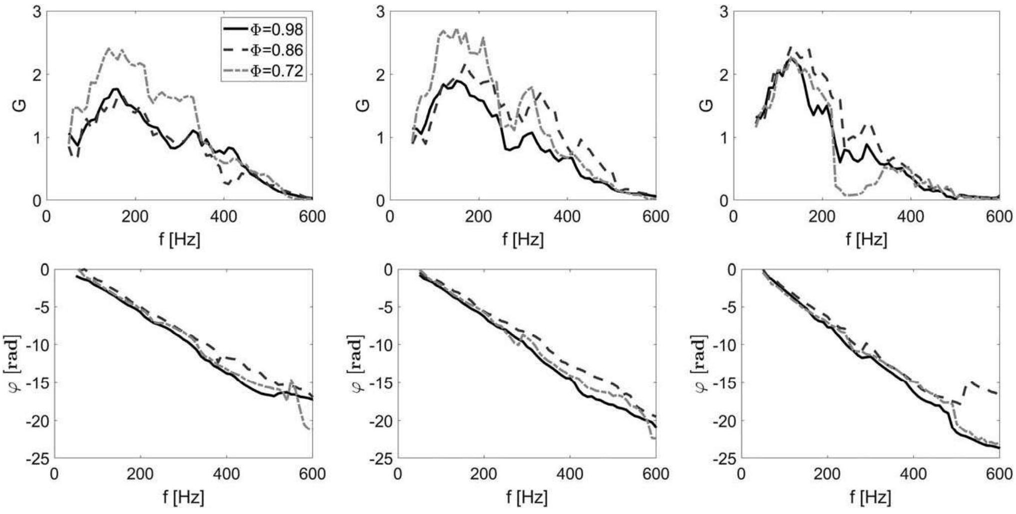

Figure 12. FTF gain (top row) and phase (bottom row) for each blend and Φ tested. Methane: left column; biogas (85–15): central column; biogas (60–40): right column.

Krüger, and Oliver (2014)). This shape change occurred when the excitation approached the natural frequency of the combustion chamber (220–250 Hz, depending on the temperature). As a matter of fact, dedicated experiments (not shown here for brevity) demonstrated that trumpet-shaped flames could be obtained for the other blends tested, but at greater forcing amplitudes, while the combination of a high quantity of CO_2 and air (low Φ) makes the flame more susceptible to this alteration. However, this shape modification seems not to sensibly affect the phase values, through which the time lag is calculated.

All the phase plots exhibit nearly linear trends, indicating that the flame response can be characterized by an approximately constant sensitive time lag, τ. The value of τ for each test was calculated by linear fitting and the results are plotted in Figure 13 for the different fuels, as a function of Φ. Changes in equivalence ratio resulted in a non-monotonic variation, with the lowest values of τ found at Φ=0.86. The addition of CO_2 to the fuel leads to an increased time lag in all cases, especially when the proportion increased from 15% to 40%.

As it has been discussed in the previous section, τ can be interpreted as the ratio between a characteristic flame length and a mean convective velocity along the flow path. Both are expected to vary between the different cases. On the one hand, the average velocity depends on the velocity at the injection plane and also on the flame temperature, and both vary with CO_2 content and with Φ, although with opposite trends (e.g., an increase in Φ leads to lower injection velocity and higher temperature). On the other hand, Figure 10 demonstrates that the dimensions of the flame clearly change with the particular conditions: the total flame length increases for high CO_2 proportion and for low equivalence ratios. However, the FTF time lag is not related to the total flame length but to a characteristic convective length, L, representative of the distance traveled by a fuel parcel between injection (where velocity disturbances are measured) and the location where it is

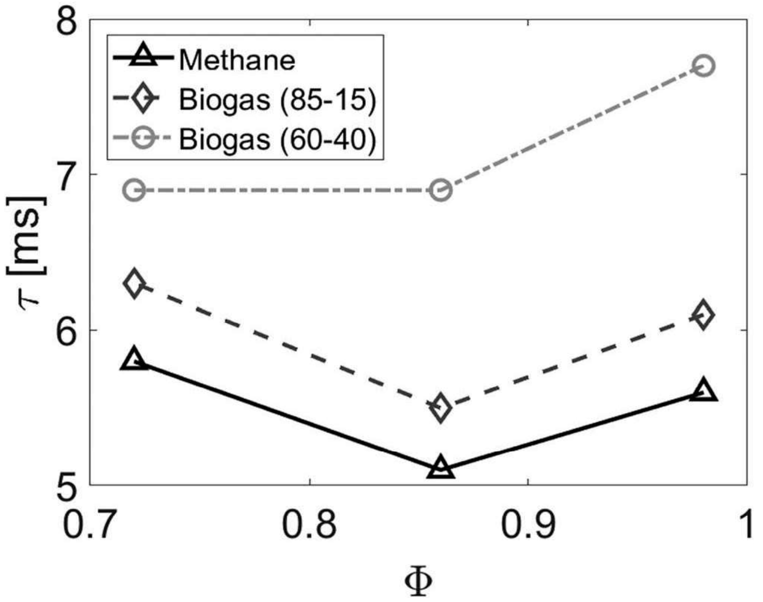

Figure 13. Variation of the time delay calculated from the FTF, τ, with the equivalence ratio, Φ, for the fuels tested.

burnt, causing a fluctuation in heat release rate. Although there is no discussion on the concept of the convective length, there is also no general agreement in the literature on the method to determine it from experimental data. In some works, L is measured as the total flame length (Alemela (2009)), or different fractions of it (Lieuwen (2003), Durox et al. (2009), Palies et al. (2009)), whereas in other works it is determined as the distance to the point at which the maximum heat release occurs (Duchaine et al. (2011), Román Casado (2013), Kim et al. (2010d), Hauser, Lorenz, and Sattelmayer (2010), Tay-Wo-Chong et al. (2011)) or to the center of mass of the flame (Kim et al. (2010a), Kim and Park (2010), Han and Hochgreb (2015)). As it has been discussed above, the approach proposed in this work is based on the analysis of CC maps which is thought to provide a relatively simple and physically plausible method to determine L.

Cross-correlation maps for nine of the tests are displayed in Figure 14, in terms of the normalized cross-correlation value which, as discussed (and verified) above, should be interpreted as the 'local effective gain', namely:

$$\frac{i' * i'_x}{K(\omega_f)} \approx G_x(\omega_f) \cdot \cos\left[\varphi_x(\omega_f) - \varphi(\omega_f)\right] \tag{5}$$

The nine cases shown in Figure 14 are thought to adequately summarize the effects observed and the rest of the maps (up to a total of 27 cases) will not be shown for brevity.

As it was analyzed by Luciano and Ballester (2018), the highest values (both negative and positive) in the CC maps lie on the outer border of the V flame sheet and gradually move farther outwards (suitably reflecting the phenomenon of vortices growing in strength and impinging on the flame layer). The CC map reveals oscillating patterns, the number of cycles increasing with the forcing frequency (as suggested by Eq. (A-6) in the appendix). This can be clearly seen in the top row of Figure 14, corresponding to three flames of methane at Φ =0.86, forced, respectively, at 90, 150 and 230 Hz.

The oscillation pattern obtained barely varies with the Φ value (middle row of Figure 14), due to the similarity among the time lags obtained for the three equivalence ratios tested. This difference increases as CO_2 is added to the fuel, as it can be appreciated in the bottom row of Figure 14: biogas maps show almost half cycle more than the pure CH_4 flame. The effect of equivalence ratio can be observed in the middle row, where the CC maps for pure methane are, respectively, represented at three equivalence ratios (0.98, 0.86 and 0.72). The qualitative pattern is similar, whereas the peaks are gradually displaced downstream, similarly, to the changes in flame shape shown in Figure 10; i.e., the flame patterns exhibit a gradual increase in length, divergence angle, and diameter as the equivalence ratio diminishes. The results for the three fuels can be compared for the common conditions of Φ =0.86 and f =90 Hz. As it was already noted for the mean intensity maps (Figure 10), the location of the peaks in the cross-correlation map is displaced to larger radii as the amount of CO_2 increases. Also, the first negative peak (dark blue area) gradually moves away from the burner. This is due to the difference in the global time delay of the three fuels tested (see Figure 13) which, in turn, affects the oscillating pattern along the flame sheet, according to Eq. (5).

A more quantitative analysis can be attempted in terms of the convective length, L, as defined above, i.e., the distance traveled by a perturbation and the point where, in average,

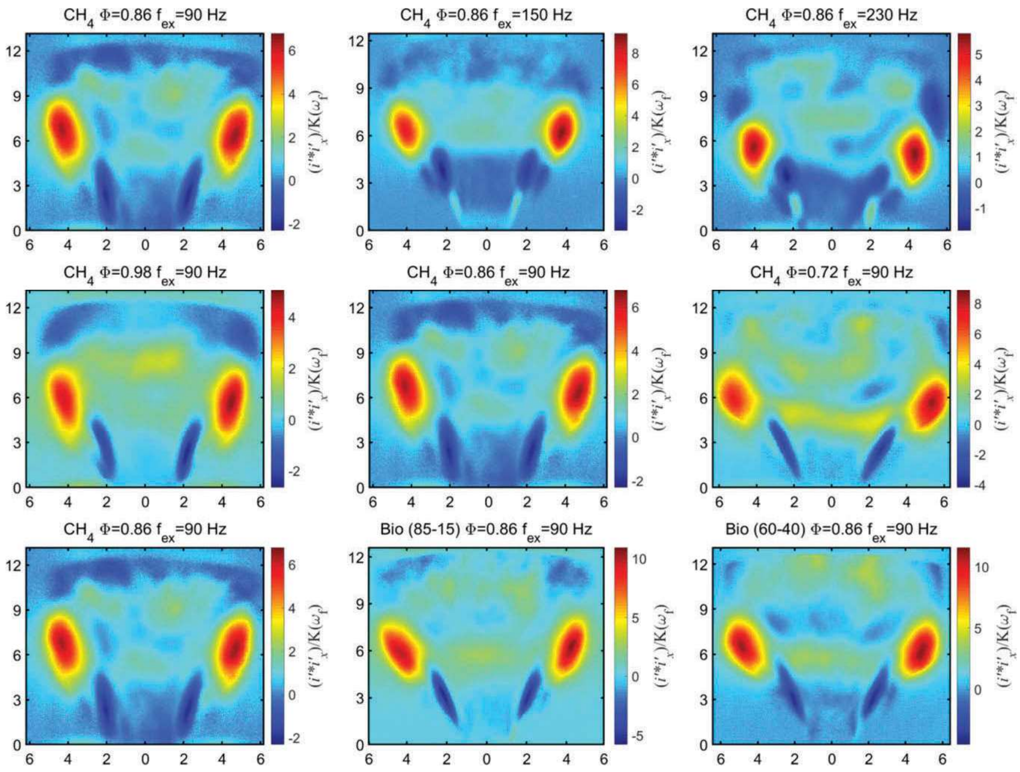

Figure 14. CC maps for different operational conditions. Top row: CH_4 flames, Φ= 0.86, from left to right f_{ex}= 90, 150, 230 Hz. Middle row: CH_4 flames, f_{ex}= 90 Hz, from left to right Φ= 0.98, 0.86, 0.72. Bottom row: f_{ex}= 90 Hz, Φ= 0.86, from left to right pure methane, biogas (85–15) and biogas (60–40) flames.

it produces a fluctuation in heat release rate. This length can be easily identified in CC maps from the location of the peak values, as it was discussed by Luciano and Ballester (2018) and further verified in the previous section. At the same time, these red pockets represent the vortex roll-up zones, which are the main contributors to the global flame dynamics for the cases studied. Durox, Schuller, and Candel (2005) analyzed the dynamics of laminar flames in which the flame response was governed by vortex shedding and identified as the characteristic flame length the distance between injection and the vortex roll-up region, which is fully consistent with the conclusions reached from the analysis of CC maps. This result is also confirmed for non-linear regimes in Durox et al. (2009), confirming that this distance can be considered representative of a flame dynamic response governed by vortex shedding phenomenon.

Therefore, the characteristic convective length was determined for each test as the distance between the center of the peak in the CC maps and the corner of the center body (Figure 1), and designated as *D* (the test with biogas (60–40) at Φ=0.72 has not been considered, due to the shape change described before). The distances *D* obtained are plotted in Figure 15 as a function of Φ and fuel composition. Each data point is calculated as the average of the distances determined for the three forced frequencies. Figure 15 shows that the measured distances increase with CO_2 content and with the air mass flow, confirming in a more quantitative manner the trends observed in CC maps. The only exception is the case of biogas (85–15) at Φ=0.98, whose *D* value is greater than that obtained for the same fuel at Φ=0.86.

The convective lengths extracted from CC maps can be related to the sensitive time lags derived from the flame transfer functions (Figure 13) through an estimated mean velocity, *V*, representing the velocity with which the flow transports the perturbations from the injection plane to the regions where they produce a variation in instantaneous heat release. However, there is not an obvious method to estimate *V* and different options can be found in the literature. Some authors defined it as the injection velocity of the mixture into the combustion chamber ($\bar{u}$) (Duchaine et al. (2011), Kim and Park (2010)), others as the bulk velocity of the flow along the flame jet path (Lieuwen (2003), Kim et al. (2010a)) or as a fraction of the latter (Durox, Schuller, and Candel (2005)). In general, it could be considered that the convective velocity, *V*, is related to the flow velocity along the path followed by the perturbations. Alemela (2009) measured the velocity field in a configuration very similar to the one used in these tests (swirl-stabilized, dump combustor) and proposed the following relationship between some characteristic parameters of the problem and the maximum flow velocity along the V-flame, designated here as u^*:

$$u^* = \bar{u}\left[1 + C\left(\frac{T_h}{T_c} - 1\right)\right] \tag{13}$$

According to this formulation, u^* is proportional to the mean injection velocity, $\bar{u}$, and also depends on the ratio between the adiabatic flame temperature T_h and that of the fresh mixture at the inlet, T_c. The second term accounts for the acceleration effect due to the temperature increase, where *C* is a coefficient characteristic of the burner used. Alemela (2009) adjusted it empirically at *C*=0.08 from PIV measurements. In the lack of detailed velocity data, in this work *C* was set at 0.1, very similar to the value used by Alemela (2009) for a similar burner configuration.

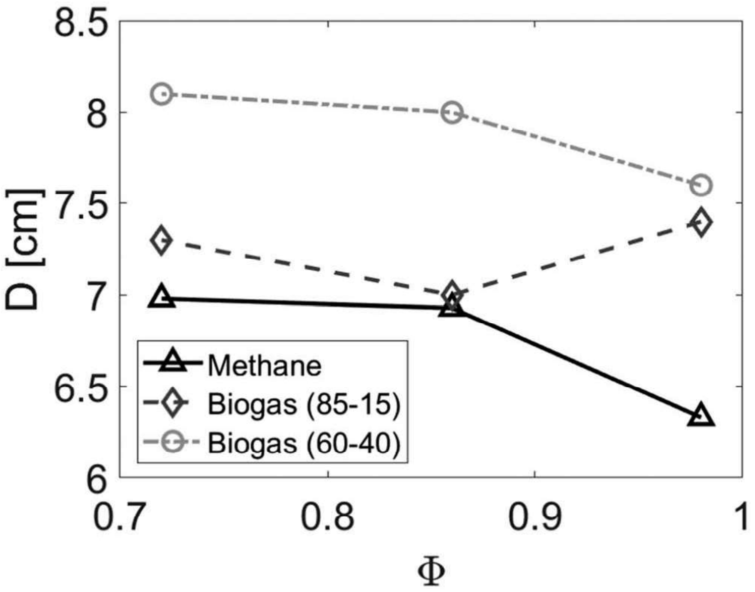

Figure 15. Distance between injector and CC peak, *D*, as a function of the equivalence ratio, Φ, and fuel composition.

The average flow velocity along the jet path estimated with the correlation proposed by Alemela can be compared with the convective velocity, V, calculated by dividing the convective length determined from CC maps, D, with the sensitive time lag derived from the FTF, τ. Table 2 displays the results obtained for the nine flames studied in this work, revealing important differences between both velocities, with $V = D/\tau$ being always much lower than the estimated flow velocity, u^*. Assuming that both should be correlated, it could be assumed, for example, a proportionality relationship, $V = ku^*$. The factor k so defined has been calculated for the different cases and shown in the last column of Table 2. The values obtained oscillate in a rather narrow range, between 0.4 and 0.6, with an average value around 0.5. These results, obtained for a wide range of conditions, clearly demonstrate that the perturbations travel at about one half of the peak flow velocity. This behavior is ascribed to the fact that the perturbations are not actually convected by the jet but are propagated along the flame due to the evolution of the vortices, which travel at a different speed. This result is fully consistent with the findings of Guiberti (2015), who concluded that the vortices are convected downstream with about one half of the maximum flow velocity the gases reach along the flame sheet. Also, similar values have been obtained by Durox, Schuller, and Candel (2005) and Durox et al. (2009) for laminar V flames. The similarity between the convective velocity estimated from CC maps and the motion speed of vortices found in the quoted studies still further confirms that, in the cases studied, flame dynamics is driven by the vortex shedding phenomenon, as it had been inferred from the patterns observed in the cross-correlation maps.

The tests with CH_4/CO_2 blends have shown significant effects on flame dynamics due to variations in fuel composition, which can be of the order of those existing between natural gas and biogas. Obviously, these results are not enough to evaluate the actual impact on stability ranges in a particular facility, which should be analyzed by considering also the geometric and acoustic properties of the whole system (e.g., by means of acoustic network models). However, it should be noted that thermo-acoustic stability is largely determined by the phase of the FTF, as it affects the nature of the coupling between the flame response and the resonance modes (Kim et al. (2010c), Kim and Santavicca (2009), Noiray et al. (2006)). As it has been shown, there is a close connection between the phase and the geometrical pattern of the CC maps (more specifically, the location of peaks).

Table 2. Estimated convective velocity for the cases analyzed.

Φ	$\bar{u}$ [m/s]	T_h [K]	D [cm]	τ [ms]	u^*[m/s]	$V=D/\tau$ [m/s]	k $\left(\frac{D}{\tau u^*}\right)$
Methane							
0.98	12.7	2210	6.33	5.6	19.34	11.30	0.53
0.86	14.3	2078	6.93	5.0	21.26	13.75	0.59
0.72	16.8	1866	6.98	5.8	24.05	12.04	0.46
Biogas (85–15)							
0.98	12.7	2177	6,81	6.3	19.22	11.55	0.55
0.86	14.3	2048	6,41	6.0	21.14	11.65	0.50
0.72	16.8	1842	6,67	7.1	23.94	10.45	0.40
Biogas (60–40)							
0.98	12.7	2091	6.88	7.7	18.93	9.87	0.48
0.86	14.3	1967	7.38	6.9	20.83	11.65	0.51
0.72	16.8	1777	7.46	6.9	23.64	11.76	0.46

Therefore, although in a rather qualitative way, the cross-correlation analysis can provide some useful hints on the expected shift in phase values and also some insight into their relation with changes in flame pattern.

Conclusions

Cross-correlation mapping has been applied to characterize the dynamics of premixed flames of methane and two methane/CO_2 blends, representative of biogas composition. In a recent work, this image processing method was demonstrated to constitute a reliable tool to quantify the actual contribution of different flame regions to the oscillation in global heat release rate, which is finally the magnitude eventually involved in thermo-acoustic coupling.

In the first place, a detailed analysis was conducted to verify the physical interpretation of cross-correlation maps. This technique was compared with measurements of local flame transfer functions, obtained through independent tests, which provided the actual phase and gain associated with local fluctuations in heat release rate due to external forcing. The analysis fully confirmed that the magnitudes represented in CC maps quantitatively correspond to the actual contribution of a given flame parcel to global heat release rate oscillations, Q' (effective local gain). Also, the results are consistent with tentative conclusions proposed in a previous work on the nature of the oscillations of the V flames: the dynamics is governed by the vortex shedding phenomenon, the amplitude of local flame response gradually increases along the flame and the time delay is practically proportional to the distance traveled. Since the response is correctly described by $n - \tau$ models, the phase information can be summarized in terms of a characteristic time lag, τ, both for the global and local flame transfer functions. The analysis conducted demonstrates that the characteristic length associated to τ can be determined in a notably straightforward manner by simply identifying the location of the areas with the highest cross-correlation values. All these conclusions were derived from the analysis of flames with a relatively broad range of properties (a total of 27 tests: 3 fuels, 3 equivalence ratios, 3 forcing frequencies).

The differences between fully premixed flames of methane and biogas were specifically addressed. The variations in terms of FTF were consistent with those observed in cross-correlation maps, which also revealed the impact of fuel composition on the spatial distribution of flame response. In general, biogas flames display higher phase and time lag values than methane flames for the same equivalence ratio. This can be justified by the longer distance at which the strongest dynamic response occurs, as identified by the peak values in the CC maps. The usual relationship between sensitive time delay and a characteristic flame length is analyzed here, making use of the distance measured in CC maps. The estimated mean velocity with which perturbations are convected along the flame is estimated to be around one half of the maximum velocity along the V jet. This finding is fully consistent with the conclusions proposed in recent works on the motion of vortices along V flames, as further confirmation of the interpretations proposed.

Finally, it is noteworthy that all the results point to a close connection between the phase of the dynamic response and the geometrical flame pattern revealed by CC maps. Given the strong influence of phase on the thermo-acoustic stability of a flame-combustor system, the proposed cross-correlation analysis can provide some useful hints on the expected impact of changes in flame patterns due, among others, to variations in fuel composition.

Funding

This work was supported by the Ministry of Economy and Competitiveness and by the European Union (FEDER), through Project [RTC-2016-4845-3] (Program Retos-Colaboración).

References

Alemela, P. R. 2009. Measurement and scaling of acoustic transfer matrices of premixed swirl flames. PhD Thesis, Technische Universität München

Ayoola, B. O., R. Balachandran, J. H. Frank, E. Mastorakos, and C. F. Kaminski. 2006. Spatially resolved heat release rate measurements in turbulent premixed flames. *Combust. Flame* 144:1–2. doi:10.1016/j.combustflame.2005.06.005.

Balachandran, R., B. O. Ayoola, C. F. Kaminski, A. P. Dowling, and E. Mastorakos. 2005. Experimental investigation of the nonlinear response of turbulent premixed flames to imposed inlet velocity oscillations. *Combust. Flame* 143:1–2. doi:10.1016/j.combustflame.2005.04.009.

Ballester, J., and T. García-Armingol. 2010. Diagnostic techniques for the monitoring and control of practical flames. *Prog. Energy Combust. Sci.* 36(4). doi:10.1016/j.pecs.2009.11.005.

Ballester, J., R. Hernández, A. Sanz, A. Smolarz, J. Barroso, and A. Pina. 2009. Chemiluminescence monitoring in premixed flames of natural gas and its blends with hydrogen. *Proc. Combust. Inst.* 32(2). doi:10.1016/j.proci.2008.07.029.

Bellows, B. D., M. K. Bobba, A. Forte, J. M. Seitzman, and T. Lieuwen. 2007. Flame transfer function saturation mechanisms in a swirl-stabilized combustor. *Proc. Combust. Inst.* 31(2). doi:10.1016/j.proci.2006.07.138.

Bunce, N. A., B. D. Quay, and D. A. Santavicca. 2013. Interaction between swirl number fluctuations and vortex shedding in a single-nozzle turbulent swirling fully-premixed combustor. *J. Eng. Gas Turb. Power* 136(2). doi:10.1115/1.4025361.

Candel, S. 2002. Combustion dynamics and control: progress and challenges. *Proc. Combust. Inst.* 29(1). doi:10.1016/S1540-7489(02)80007-4.

Chen, Y., W. Hu, Y. Feng, and S. Sweeney. 2014. Status and prospects of rural biogas development in China. *Renew. Sust. Energ. Rev.* 39. doi:10.1016/j.rser.2014.07.119.

Cohé, C., C. Chauveau, I. Gökalp, and D. F. Kurtulus. 2009. CO2 addition and pressure effects on laminar and turbulent lean premixed CH4 air flames. *Proc. Combust. Inst.* 32(2). doi:10.1016/j.proci.2008.06.181.

Dai, W., C. Qin, Z. Chen, C. Tong, and P. Liu. 2012. Experimental studies of flame stability limits of biogas flame. *Energy Convers. Manage.* 63. doi:10.1016/j.enconman.2012.03.021.

De Giorgi, M. G., A. Sciolti, S. Campilongo, and A. Ficarella. 2016. Image processing for the characterization of flame stability in a non-premixed liquid fuel burner near lean blowout. *Aerosp. Sci. Technol.* 49. doi:10.1016/j.ast.2015.11.030.

De Rosa, A. J., S. J. Peluso, B. D. Quay, and D. A. Santavicca. 2015a. The effect of confinement on the structure and dynamic response of lean-premixed, swirl-stabilized flames. *J. Eng. Gas Turb. Power* 138(6). doi:10.1115/1.4031885.

De Rosa, A. J., J. Samarasinghe, S. J. Peluso, B. D. Quay, and D. A. Santavicca. 2015b. Flame area fluctuation measurements in velocity-forced premixed gas turbine flames. *J. Eng. Gas Turb. Power* 138(4). doi:10.1115/1.4031708.

Dowling, A., and S. R. Stow. 2003. Acoustic analysis of gas turbine combustors. *J. Propul. Power* 19 (5). doi:10.2514/2.6192.

Duchaine, F., F. Boudy, D. Durox, and T. Poinsot. 2011. Sensitivity analysis of transfer functions of laminar flames. *Combust. Flame* 158(12). doi:10.1016/j.combustflame.2011.05.013.

Ducruix, S., D. Durox, and S. Candel. 2000. Theoretical and experimental determinations of the transfer function of a laminar premixed flame. *Proc. Combust. Inst.* 28(1). doi:10.1016/S0082-0784(00)80279-9.

Durox, D., T. Schuller, and S. Candel. 2005. Combustion dynamics of inverted conical flames. *Proc. Combust. Inst.* 30(2). doi:10.1016/j.proci.2004.08.067.

Durox, D., T. Schuller, N. Noiray, and S. Candel. 2009. Experimental analysis of nonlinear flame transfer functions for different flame geometries. *Proc. Combust. Inst.* 32(1). doi:10.1016/j.proci.2008.06.204.

Emadi, M., K. Kaufman, M. W. Burkhalter, T. Salameh, T. Gentry, and A. Ratner. 2015. Examination of thermo-acoustic instability in a low swirl burner. *Int. J. Hydrogen Energy* 40. doi:10.1016/j.ijhydene.2015.08.016.

García-Armingol, T., J. Ballester, and A. Smolarz. 2013. Chemiluminescence-based sensing of flame stoichiometry: Influence of the measurement method. *Measurement* 46(9). doi:10.1016/j.measurement.2013.06.008.

García-Armingol, T., Y. Hardalupas, A. M. K. P. Taylor, and J. Ballester. 2014. Effect of local flame properties on chemiluminescence-based stoichiometry measurement. *Exp. Therm Fluid Sci.* 53. doi:10.1016/j.expthermflusci.2013.11.009.

Gentemann, A., C. Hirsch, F. Kiesewetter, T. Sattlemayer, and W. Polifke 2004. Validation of flame transfer function reconstruction for perfectly premixed swirl flames. ASME Turbo Expo 2004, paper GT2004-53776

Guiberti, T. 2015. Analysis of the topology of premixed swirl-stabilized confined flames. PhD Thesis, École Centrale Paris

Han, Z., S. Balusamy, and S. Hochgreb. 2015. Spatial analysis on forced heat release response of turbulent stratified flames. *J. Eng. Gas Turb. Power* 137(6). doi:10.1115/1.4029056.

Han, Z., and S. Hochgreb. 2015. The response of stratified swirling flames to acoustic forcing: experiments and comparison to model. *Proc. Combust. Inst.* 35(3). doi:10.1016/j.proci.2014.05.047.

Hardalupas, Y., and M. Orain. 2004. Local measurements of the time-dependent heat release rate and equivalence ratio using chemiluminescent emission from a flame. *Combust. Flame* 139(3). doi:10.1016/j.combustflame.2004.08.003.

Hauser, M., M. Lorenz, and T. Sattelmayer. 2010. Influence of transversal acoustic excitation of the burner approach flow on the flame structure. *J. Eng. Gas Turb. Power* 133(4).

Hinton, N., and R. Stone. 2014. Laminar burning velocity measurements of methane and carbon dioxide mixtures (biogas) over wide ranging temperatures and pressures. *Fuel* 116. doi:10.1016/j.fuel.2013.08.069.

Hosseini, S. E., and M. A. Wahid. 2014. Development of biogas combustion in combined heat and power generation. *Renew. Sust. Energ. Rev.* 40. doi:10.1016/j.rser.2014.07.204.

Huang, Y. 2008. Combustion dynamics of swirl-stabilized lean premixed flames in an acoustically-driven environment. PhD Thesis, University of Iowa

Kang, D. M., F. E. C. Culick, and A. Ratner. 2007. Combustion dynamics of a low-swirl combustor. *Combust. Flame* 151(3). doi:10.1016/j.combustflame.2007.07.017.

Kim, D., J. G. Lee, B. D. Quay, D. A. Santavicca, K. Kim, and S. Srinivasan. 2010a. Effect of flame structure on the flame transfer function in a premixed gas turbine combustor.*J. Eng. Gas Turb. Power* 132:1–7.

Kim, D., and S. W. Park. 2010. Forced and self-excited oscillations in a natural gas fired lean premixed combustor. *Fuel Process. Technol.* 91(11). doi:10.1016/j.fuproc.2010.07.003.

Kim, K., J. Lee, B. Quay, and D. Santavicca. 2010c. Spatially distributed flame transfer functions for predicting combustion dynamics in lean premixed gas turbine combustors. *Combust. Flame* 157 (9). doi:10.1016/j.combustflame.2010.04.016.

Kim, K. T., J. G. Lee, H. J. Lee, B. D. Quay, and D. Santavicca. 2010d. Characterization of forced flame response of swirl-stabilized turbulent lean-premixed flames in a gas turbine combustor. *J. Eng. Gas Turb. Power* 132(4). doi:10.1115/1.3204532.

Kim, K. T., and D. Santavicca. 2009. Linear stability analysis of acoustically driven pressure oscillations in a lean premixed gas turbine combustor. *J. Mech. Sci. Technol.* 23(12). doi:10.1007/s12206-009-0924-0.

Kobayashi, H., H. Hagiwara, H. Kaneko, and Y. Ogami. 2007. Effects of CO2 dilution on turbulent premixed flames at high pressure and high temperature. *Proc. Combust. Inst.* 31(1). doi:10.1016/j.proci.2006.07.159.

Kornilov, V. N., M. Manohar, and L. P. H. de Goey. 2009. Thermo-acoustic behaviour of multiple flame burner decks: Transfer function (de)composition. *Proc. Combust. Inst.* 32(1). doi:10.1016/j.proci.2008.05.022.

Lafay, Y., B. Taupin, G. Martins, G. Cabot, B. Renou, and A. Boukhalfa. 2007. Experimental study of biogas combustion using a gas turbine configuration. *Exp. Fluids* 43(2). doi:10.1007/s00348-007-0302-6.

Lamraoui, A., F. Richecoeur, S. Ducruix, and T. Schuller 2011. Experimental analysis of simultaneous non-harmonically related unstable modes in a swirled combustor, ASME Turbo Expo paper GT 2011-46701

Lee, K., H. Kim, P. Park, S. Yang, and Y. Ko. 2013. CO2 radiation heat loss effects on NOx emissions and combustion instabilities in lean premixed flames. *Fuel* 106. doi:10.1016/j.fuel.2012.12.048.

Lee, M. C., J. Yoon, S. Joo, J. Kim, J. Hwang, and Y. Yoon. 2015. Investigation into the cause of high multi-mode combustion instability of H2/CO/CH4 syngas in a partially premixed gas turbine model combustor. *Proc. Combust. Inst.* 35(3). doi:10.1016/j.proci.2014.07.013.

Leung, T., and I. Wierzba. 2008. The effect of hydrogen addition on biogas non-premixed jet flame stability in a co-flowing air stream. *Int. J. Hydrogen Energy* 33(14). doi:10.1016/j.ijhydene.2008.04.030.

Lieuwen, T. 2003. Modeling premixed combustion–acoustic wave interactions: A review. *J. Propul. Power* 19(5). doi:10.2514/2.6193.

Lieuwen, T., and B. T. Zinn 1998. Theoretical investigation of combustion instability mechanisms in lean premixed gas turbines. 36th AIAA Aerospace Sciences Meeting and Exhibit paper AIAA-98-0641

Luciano, E., and J. Ballester. 2018. Analysis of the dynamic response of premixed flames through chemiluminescence cross-correlation maps. *Combust. Flame* 194. doi:10.1016/j.combustflame.2018.05.005.

Luciano, E., Á. Sobrino, and J. Ballester 2015. A novel approach for the evaluation of local and global flame time lag from oh* filtered images. 22nd International Congress on Sound and Vibration, paper 1089

Mordaunt, C. J., and W. C. Pierce. 2014. Design and preliminary results of an atmospheric-pressure model gas turbine combustor utilizing varying CO2 doping concentration in CH4 to emulate biogas combustion. *Fuel* 124. doi:10.1016/j.fuel.2014.01.097.

Nikpey, H., M. Assadi, P. Breuhaus, and P. T. Mørkved. 2014. Experimental evaluation and ANN modeling of a recuperative micro gas turbine burning mixtures of natural gas and biogas. *Appl. Energ.* 117. doi:10.1016/j.apenergy.2013.11.074.

Noiray, N., D. Durox, T. Schuller, and S. Candel. 2006. Self-induced instabilities of premixed flames in a multiple injection configuration. *Combust. Flame* 145(3). doi:10.1016/j.combustflame.2006.01.006.

Palies, P., D. Durox, T. Schuller, and S. Candel. 2010. The combined dynamics of swirler and turbulent premixed swirling flames. *Combust. Flame* 157(9). doi:10.1016/j.combustflame.2010.02.011.

Palies, P., D. Durox, T. Schuller, P. Morenton, and S. Candel. 2009. Dynamics of premixed confined swirling flames. *C. R. Mécanique* 337:6–7. doi:10.1016/j.crme.2009.06.001.

Rayleigh, J. W. S. 1878. The explanation of certain acoustical phenomena. *Nature* 18:455. doi:10.1038/018319a0.

Richecoeur, F., T. Schuller, A. Lamraoui, and S. Ducruix. 2013. Analytical and experimental investigations of gas turbine model combustor acoustics operated at atmospheric pressure. *C. R. Mecanique* 341(1). doi:10.1016/j.crme.2012.11.011.

Román Casado, J. C. 2013. Nonlinear behavior of the thermo acoustic instabilities in the limousine combustor. PhD Thesis, University of Twente

Saediamiri, M., M. Birouk, and J. A. Kozinski. 2014. On the stability of a turbulent non-premixed biogas flame: effect of low swirl strength. *Combust. Flame* 161(5). doi:10.1016/j.combustflame.2013.11.002.

Subramanian, P., R. S. Blumenthal, W. Polifke, and R. I. Sujith. 2015. Distributed time lag response functions for the modelling of combustion dynamics. *Combust.Theor.Model.* 19(2):223–237.

Sun, Q., H. Li, J. Yan, L. Liu, Z. Yu, and X. Yu. 2015. Selection of appropriate biogas upgrading technology-a review of biogas cleaning, upgrading and utilisation. *Renew. Sust. Energ. Rev.* 51. doi:10.1016/j.rser.2015.06.029.

Surendra, K. C., D. Takara, A. G. Hashimoto, and S. K. Khanal. 2014. Biogas as a sustainable energy source for developing countries: opportunities and challenges. *Renew. Sust. Energ. Rev.* 31. doi:10.1016/j.rser.2013.12.015.

Tay-Wo-Chong, L., S. Bomberg, A. Ulhaq, T. Komarek, and W. Polifke. 2011. Comparative validation study on identification of premixed flame transfer function. *J. Eng. Gas Turb. Power* 134(2):1–8.

Terhaart, S., O. Krüger, and P. C. Oliver. 2014. Flow field and flame dynamics of swirling methane and hydrogen flames at dry and steam diluted conditions. *J. Eng. Gas Turb. Power* 137(4):1–10.

Wei, Z. L., C. W. Leung, C. S. Cheung, and Z. H. Huang. 2016. Effects of equivalence ratio, H2 and CO2 addition on the heat release characteristics of premixed laminar biogas-hydrogen flame. *Int. J. Hydrogen Energy* 41. doi:10.1016/j.ijhydene.2016.01.170.

Zhen, H. S., C. W. Leung, C. S. Cheung, and Z. H. Huang. 2016. Combustion characteristic and heating performance of stoichiometric biogas–Hydrogen–Air flame. *Int. J. Heat Mass Transfer* 92. doi:10.1016/j.ijheatmasstransfer.2015.09.040.

Appendix A. Cross-correlation method

Cross-correlation maps can be readily obtained from a sequence of OH* chemiluminescence images, each frame providing the intensity I_x at every pixel$x$. The total intensity can be calculated as $I = \sum_{k=1}^{N_{px}} (I_x)_k$, where N_{px} is the total number of pixels. Both total and local intensities, I and I_x, can be decomposed into their mean and fluctuating components $(\bar{I}, I'; \bar{I}_x, I_x^{'})$. The CC map can be obtained from N_{im} flame images by assigning to each pixel x the magnitude denoted as $i' * i_x^{'}$ and given by the following expression:

$$i' * i_x^{'} = \frac{\sum_{j=1}^{N_{im}} \left(I_x^{'} \cdot \sum_{k=1}^{N_{px}} \left(I_x^{'} \right)_k \right)_j}{N_{im} \cdot \bar{I}_x \cdot \bar{I}} \qquad (A-1)$$

If proportionality between OH* emission and heat release rate is assumed, local CC values, $i' * i_x^{'}$, are equivalent to the normalized cross-correlations between global and local heat release rates, Q and Q_x:

$$i' * i_x^{'} \approx q^{'} * q_x^{'} = \frac{Q' * Q_x^{'}}{\bar{Q}_x \cdot \bar{Q}} \qquad (A-2)$$

$$Q' * Q_x^{'} = \frac{1}{T} \int_0^T Q'(t) \cdot Q_x^{'}(t) dt \qquad (A-3)$$

Equation (A-3) is the cross-correlation of $Q'(t)$ and $Q_x^{'}(t)$ for zero time lag, averaged over a length of time, T, much longer than the period of the oscillations. As it was discussed in Luciano and Ballester (2018), it expresses the contribution of the fluctuation of heat release rate $Q_x^{'}$ in a given flame location, x, to the total response of the flame, Q'. The integration in Eq. (A-3) automatically selects the fluctuations of the same frequency and in phase with the bulk heat release oscillations, discarding the rest, so providing an effective and simple means to determine the effective participation of different flame portions in the global dynamic response of the flame, as quantified by Q'. This method can be applied both to natural oscillations and to studies with external forcing. In particular, cross-correlation values can be related to the parameters of flame transfer functions. If global and local FTF are expressed as $FTF(\omega_f) = G(\omega_f) \cdot \exp[-i\varphi(\omega_f)]$ and $FTF_x(\omega_f) = G_x(\omega_f) \cdot \exp[-i\varphi_x(\omega_f)]$), respectively, it can be easily deduced that, for the case of an external excitation of relative amplitude $(u_0^{'}/\bar{u})$ at frequency ω_f, Eq. (A-4) holds.

$$q^{'} * q_x^{'} = \frac{Q' * Q_x^{'}}{\bar{Q}_x \cdot \bar{Q}} = K(\omega_f) \cdot G_x(\omega_f) \cdot \cos[\varphi_x(\omega_f) - \varphi(\omega_f)] \qquad (A-4)$$

$$K(\omega_f) = \frac{1}{2} \left(\frac{u_0^{'}}{\bar{u}} \right)^2 \cdot G(\omega_f) \qquad (A-5)$$

Since $K(\omega_f)$ is constant for the whole flame, Eq. (A-4) clearly expresses that $q' * q_x^{'}$ is proportional to the 'effective local FTF gain', i.e., to the product of the local gain, $G_x(\omega_f)$, by a correction factor, $\cos[\varphi_x(\omega_f) - \varphi(\omega_f)]$, accounting for the phase difference between local and global fluctuations. The same information is contained in the CC maps, in terms of $i' * i_x^{'}$, as defined in Eq. (A-1). Therefore, cross-correlation maps are directly related to local FTF and, more specifically, to the contribution of each flame portion to the bulk heat release rate fluctuations. Further analysis and physical insight can be gained if the flame dynamics can be described by the well-known $n - \tau$ model, both at global and local levels. In that case, global and local FTF can be expressed as $FTF(\omega_f) = n(\omega_f) \cdot \exp[-i\omega_f\tau]$ and $FTF_x(\omega_f) = n_x(\omega_f) \cdot \exp[-i\omega_f\tau_x]$), respectively, and Eq. (A-4) becomes:

$$q' * q_x' = K(\omega_f) \cdot n_x(\omega_f) \cdot \cos\left[\omega_f \cdot (\tau_x - \tau)\right] \qquad (A-6)$$

Sensitive time lags, τ and τ_x, are commonly interpreted in terms of a convective velocity and a characteristic length traveled by a fuel parcel until it is burnt and releases heat. The definition of such length is very simple for the local FTF and is the distance between a given point x and the injection, denoted as L_x. However, as discussed in Luciano and Ballester (2018), the definition of an appropriate convective length for the whole flame, L, associated to the global FTF, is much less obvious and different procedures have been proposed to measure it from flame images, leading to different results.

CC maps enable determining L in a notably straightforward manner. If the convective velocity is considered to be approximately constant along the jet path, $V \sim V_x$ and $\tau_x/\tau \sim L_x/L$. So, the cosine term in Eq. (A-6) can be reformulated as

$$\cos\left[(\omega_f \cdot (\tau_x - \tau)\right] = \cos\left[\omega_f \cdot \tau \cdot \left(\frac{L_x}{L} - 1\right)\right] \qquad (A-7)$$

That is, the cross-correlation map is expected to exhibit a sinusoidal evolution along the flame (i.e., as L_x increases), as it was in fact shown in Luciano and Ballester (2018). From the study of the oscillations obtained in the CCM, it was concluded that the convective length related to the global sensitive time lag can be simply identified as the peak along the sinusoidal curve, where $L_x = L$.

24th INTERNATIONAL CONGRESS ON SOUND AND VIBRATION
23–27 July 2017, London

USE OF FLAME TRANSFER FUNCTION TO PREDICT COMBUSTOR UNSTABLE MODES

Ennio Luciano, Eduardo Tizné and Javier Ballester

Laboratory for Research on Fluid Dynamics and Combustion Technologies (LIFTEC), CSIC - University of Zaragoza, María de Luna 10, 50018 Zaragoza, Spain
email: eluciano@liftec.unizar-csic.es

The use of low-order network models to predict the natural modes of a burner is a very useful tool especially during the early stage of combustor design. In particular, the prediction of the unstable modes, which can generate limit cycle conditions, is a major objective of these simulations. A few studies have shown that the flame transfer function (FTF), i.e. linear flame response, can also be used to predict unstable, non-linear modes, both in their frequency and in their growth rate. In order to further assess the validity of this approach, predictions with this simplified method have been compared with experimental results for a broad range of conditions, in most cases reaching limit cycle regimes. Two different fuels, methane and biogas, have been studied for two different burner lengths and varying both the equivalence ratio and the upstream reflection coefficient. The results of the model coincide quite well in their real part with the experimental frequencies measured, while the imaginary part of the solution reveals the instability of the modes obtained. So, the results validate the viability of this approach for a broad range of operational conditions, including the differences in dynamic flame response between methane and biogas.

Keywords: Flame Dynamics, Dispersion Equation, Limit Cycle, Flame Transfer Function

1. Introduction

Lean premixed combustion has become the leading technology in gas turbines field because of its high efficiency combined with very low pollutant emissions [1]. However, combustion dynamics has risen as a major problem since lean combustion has shown proneness to the coupling of flame heat flux fluctuation (Q') with pressure oscillations in the combustion chamber (p').

According to Rayleigh's criterion [2], the in-phase oscillation of these two magnitudes, if their product is greater than irreversible losses, produces a strong increment of p' fluctuation, eventually reaching limit cycle conditions, which can cause serious damages to the hardware.

Prediction of instability modes is an important objective, especially at the early stage of combustor design. Two main approaches can be followed [3]: on the one hand, the direct calculation of both acoustic waves and unsteady heat release through CFD simulations is a possibility, even if really onerous at computational level. On the other hand, the development of simplified network models, in which burner elements are modelled using linear acoustics (in terms of transfer or scattering matrices) and, then, are connected in series, has shown a high potential to identify unstable ranges.

Previous works suggest that linear acoustics correctly describes the behaviour of the system, except for the flame response [3, 4].Therefore, an accurate model of non-linear flame dynamics combined with simple transfer matrices of the other elements may provide good predictions of the unstable modes of the system studied.

In this context, many authors have performed simulations combining linear models of the burner elements and non-linear flame dynamics (e.g., [3-6]), which can be resumed by a family of curves called flame describing function (FDF). Nevertheless, some studies successfully used the flame transfer function (FTF), i.e. the linear flame response, for the prediction of natural unstable modes [7-10]. The use of FTF, instead of FDF, as an input to the model significantly simplifies the procedure to describe the dynamic response of the flame and, so, it reduces the effort and time required to predict combustor stability. The results obtained in previous works are encouraging, and the objective here is to explore in a systematic way a relatively wide range of operational conditions, including fuel composition, in order to evaluate the feasibility of predicting unstable modes based on simplified descriptions of the system and, especially, of the flame response.

In this work, a simplified model, called *dispersion equation*, has been used to predict unstable modes of a lab-scale, gas turbine burner using FTF as an input. A wide range of possible situations has been explored, which includes variations in geometry (burner length, upstream reflection coefficient), equivalence ratio and fuel composition. In particular, a specific objective was to evaluate the ability of the model and of the FTF to successfully capture the impact of changes in fuel properties on combustor stability. With this aim, the experimental results for both methane and biogas flames have been compared with the predictions of the model. The formulation of the dispersion equation is developed in Section 2, while Section 3 describes the experimental rig as well as experiments performed and instrumentation used. Section 4 is dedicated to the results discussion, and the main conclusions are summarized in Section 5.

2. Dispersion equation

Figure 1 shows a simplified scheme of the burner used for the experiments, which will be used as a reference to develop the model. Further details are given in Section 3. This combustion rig can be modelled as a two-cavity system and, for the frequencies of interest, the flame can be considered compact. Therefore, the low-order network model of the entire system can be reduced to a single equation, called *dispersion equation*. The main steps which lead to the final formulation of the model are outlined in this section; for a more in-depth analysis, references [7, 11, 12] are recommended.

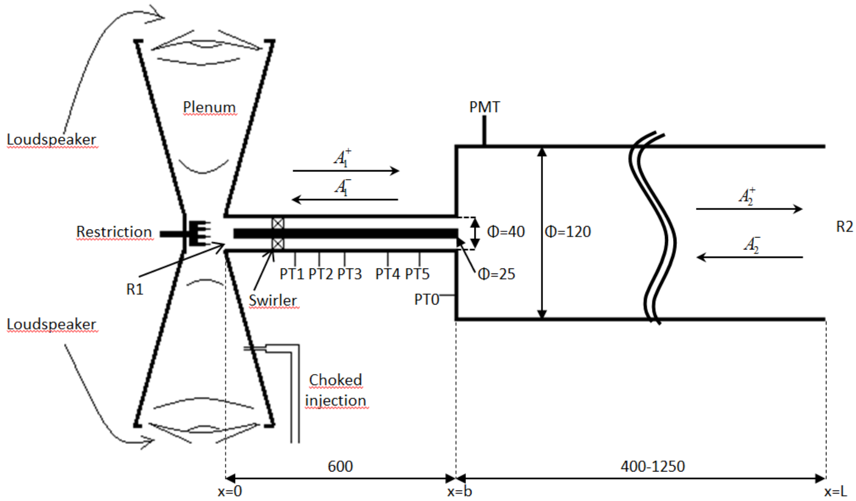

Figure 1. Scheme of the burner (all dimensions in mm).

$A_{1,2}^{+,-}$ represents plane waves travelling forward (+)/backward (-) inside the injection duct (1) and combustion chamber (2). The same notation will be used from now on to designate variables in both sections (1, 2) and propagation directions (+, -). Supposing small values of Mach number and constant mean pressure (p) and specific heat ratio (γ) in both elements, according to linear acoustic theory pressure fluctuation is conserved at the discontinuity ($x=b$), while there is a sudden jump in velocity oscillation, dependent on the area (S) variation and on the fluctuation of heat release rate, Q'

(the flame is assumed to be located very close to the dump plane).These conditions are expressed in Eqs. (1-2), where $b_{+,-}$ indicates right (+)/left (-) handed limits, as x approaches b.

$$p'(b_-) = p'(b_+) \tag{1}$$

$$S(b_+)\cdot u'(b_+) - S(b_-)\cdot u'(b_-) = \frac{\gamma - 1}{\gamma \cdot p} Q' \tag{2}$$

Assuming a harmonic variation of both acoustic variables and heat release rate, continuity conditions can be reformulated as in Eqs. (3-4), where ρ and c represent the mean density and the speed of sound, respectively. k is the wave number, defined as $k^{\pm} = \omega/(c \pm u)$, with ω and u designating angular frequency and mean flow velocity, respectively.

$$A_2^+ + A_2^- = A_1^+ e^{-ik_1^+ b} + A_1^- e^{ik_1^- b} \tag{3}$$

$$\frac{S_2}{\rho_2 c_2}(A_2^+ - A_2^-) = \frac{S_1}{\rho_1 c_1}(A_1^+ e^{-ik_1^+ b} - A_1^- e^{ik_1^- b}) + \frac{\gamma - 1}{\gamma \cdot p} Q' \tag{4}$$

Upstream and downstream reflection coefficients (R_1 and R_2) can be defined as in Eq. (5), where L indicates the total length of the rig:

$$R_1 = \frac{A_1^+}{A_1^-}; R_2 = \frac{A_2^- e^{ik_2^-(L-b)}}{A_2^+ e^{-ik_2^+(L-b)}} \tag{5}$$

Rearranging Eq. (3) and (4), in order to make R_1, R_2 and FTF explicit, leads to the dispersion equation (Eq. (6)), which completely describes the burner acoustics:

$$\begin{aligned}(1+\Gamma_1+\Gamma_2\cdot FTF)\cdot\left(R_1\cdot R_2\cdot e^{-i[b(k_1^+ + k_1^-)+(L-b)\cdot(k_2^+ + k_2^-)]} - 1\right) + \\ (1-\Gamma_1-\Gamma_2\cdot FTF)\cdot\left(R_2\cdot e^{-i\cdot(L-b)\cdot(k_2^+ + k_2^-)} - R_1\cdot e^{-i\cdot b\cdot(k_1^+ + k_1^-)}\right) = 0\end{aligned} \tag{6}$$

Γ_1 and Γ_2 are two variables dependent on physical parameters and rig dimensions, as shown in Eq. (7), where Q indicates the mean heat flux.

$$\Gamma_1 = \frac{\rho_2 c_2 S_1}{\rho_1 c_1 S_2}; \Gamma_2 = \frac{\rho_2 c_2}{\rho_1 c_1 S_2} \frac{\gamma - 1}{\rho_1 c_1^2} \frac{Q}{u} \tag{7}$$

Solutions of Eq. (6) in terms of ω (hidden into k values) are the natural modes of the burner. The solutions are complex numbers, whose real part indicates oscillation frequency, while the sign of the imaginary part reveals if the solution is stable ($Im(\omega)>0$) or unstable ($Im(\omega)<0$). The dispersion equation has been applied to the experimental conditions explained in the next section.

3. Experimental method

3.1 Experimental rig

Tests have been performed in an atmospheric, swirl-stabilized, premixed combustor facility consisting of a plenum, an annular duct and a combustion chamber (main dimensions as in Fig. 1). Fuel is premixed with air upstream of the plenum and injected into it through two choked orifices in order to prevent ER fluctuations. The air-fuel mixture flows into the annular duct, passing through an axial swirler (six 30º vanes) located 380 mm upstream of the dump plane. The acoustic boundary condition R_1 at the entrance of the injection duct can be modified by manipulating an adjustable restriction. As sketched in Fig. 1, this restriction is shaped as a crenelated plug, with eight, 25 mm high teeth. The relative position between the plug and the duct entrance can be adjusted. This setting will be identified by the coordinate H, expressing the length of the teeth inserted into the duct: H=0 means that the tips are aligned with the duct inlet, which is gradually restricted as H increases until completely closed for H=25 mm. H=-infinity indicates that the plug is withdrawn and the inlet is fully open.

The combustion chamber is composed of a first, optically accessible, quartz section (220 mm in length) followed by a second stainless steel one, whose length can be changed by installing different segments, so that the total chamber length can be set to 400, 900 or 1250 mm.

Five piezoelectric pressure transducers (PT1-5 in Fig. 1, PCB 103B02) are located at various positions along the annular duct, while another one (PT0) measures *p'* in the combustion chamber. Flame heat flux is determined using a photomultiplier tube (PMT, Hamamatsu H5784-03), fitted with an OH* band interference filter (310±5 nm). Two loudspeakers (10", Eminence DELTA-10A), powered by the same amplifier, are installed at both sides of the plenum to provide acoustic excitation to the premixed flow. Another loudspeaker (8", HQ Power VDSSP8/8) can be installed, in absence of flame, at the combustor exit to acoustically excite the facility from the top.

3.2 Flame and rig characterization

Apart from physical magnitudes (such as densities, speeds of sound etc.) and geometrical dimensions, some parameters involved in the dispersion equation have to be determined experimentally. In particular, FTF and reflection coefficients must be determined in ad-hoc tests, as explained in the following sub-sections.

3.2.1 Upstream reflection coefficient

The combustion chamber outlet was open to the atmosphere in all tests and, hence, the downstream reflection coefficient was taken as R_2=-1 for the calculations. Instead, R_1 value can be changed by modifying the position of the restriction and so it had to be measured. To do so, an 8" loudspeaker was located in front of the combustor outlet to provide acoustic forcing at frequencies from 50 to 600 Hz with 10 Hz step. *p'* was measured (4 s, 4 kHz) with the five PTs located along the annular duct and the multi-microphone method [13] was applied in order to determine the two Riemann invariants in the duct, and so the value of R_1. The results for different H settings are shown in Fig. 2 and were used as an input for the dispersion equation model. The tests were repeated for different combustor lengths, forcing amplitudes and air mass flows injected into the rig (from 0 to 40 Nm^3/h); however, R_1 displayed negligible differences and so it was taken as constant for all test conditions. R_1 results show similar patterns for *H* values from 0 to 20 mm in magnitude and phase, with the latter depicting an almost linear trend with frequency whose slope slightly increases with restriction level. A different behaviour is obtained for the fully open inlet (*H*=-inf), especially for the phase, which is almost constant around π, resembling the acoustic condition of an open end.

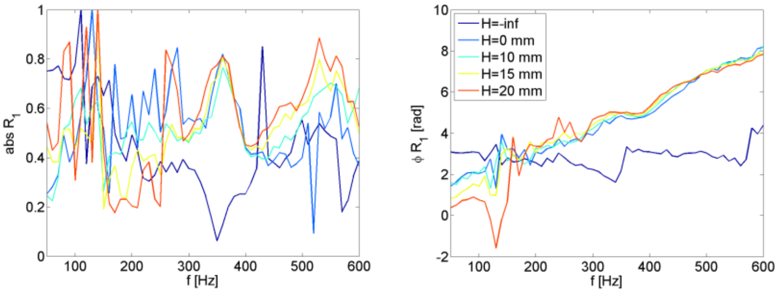

Figure 2. R_1 absolute value and phase for various restriction levels

3.2.2 FTF tests

The flame transfer function was measured for the short combustion chamber (400 mm), in order to avoid self-excited instabilities, which otherwise would strongly affect the results. Acoustic forcing was provided by the two loudspeakers located in the plenum, for the same sampling frequency, recording time and excitation frequencies described above for R_1 tests. The amplitude was regulated at sufficiently high levels to obtain meaningful results but always within the linear regime. The multi-microphone method was applied to calculate *u'* value at the dump plane, while both mean and fluctuating value of heat flux were measured with PMT. FTF tests were performed at five different ER (0.98, 0.92, 0.86, 0.80, 0.72) for two different fuels: methane and a CH_4-CO_2 blend (60-40% in volume), representative of biogas. Methane flow rate was kept constant at 3 Nm^3/h in all tests, changing the air mass flow in order to vary ER. For biogas cases, the air-fuel mass flow was set to achieve the same ER and mean injection velocity as in CH_4 tests. As a consequence, power cannot be the same for the two fuels, however differences are really low (7% in the worst case). FTF results are shown in Fig. 3.

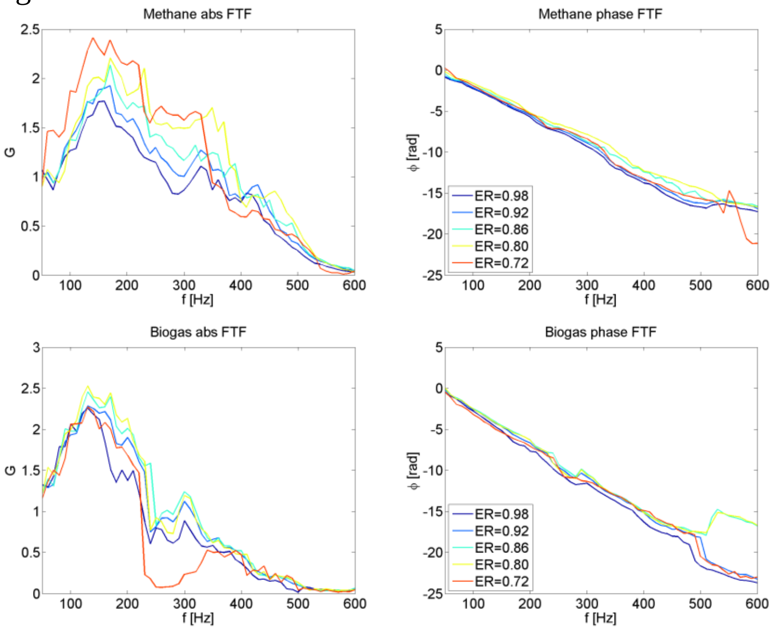

Figure 3. FTF magnitude and phase for methane (top) and biogas (bottom) varying ER

3.3 Limit cycle tests

Strong limit cycle conditions are naturally established with combustor lengths of both 1,250 and, in most of the cases, 900 mm. So, these two geometries were selected for these tests, where Q' and p' signals in the combustor were recorded, respectively, with PT0 and PMT (both, for 4 s at 4 kHz).

Experiments were carried out for the same fuels and ER as in FTF tests. With the 1,250 mm combustor, measurements were performed only with the inlet fully open, while all restriction settings listed above for the R_1 measurements were tested with the length of 900 mm. The experimental results and the comparison with predictions are discussed in the following section.

4. Results and discussions

4.1 Limit cycle results

Pressure amplitudes obtained with the burner of 1,250 mm for both CH_4 and biogas and different ER values can be observed in Fig. 4-a, while Fig. 4-b shows the frequency of the main peak in the pressure spectra (the frequency correspondence between Q' and p' has been verified for all tests).

Both fuels present high p' values, ranging from a minimum of about 200 Pa to a maximum of more than 2,500 Pa, with amplitude increasing as the mixture becomes leaner. CH_4 flames show higher pressure oscillations than biogas ones for all the ER tested, especially at lean conditions, where the difference is of about 4 times.

Methane flames present also higher oscillation frequencies than biogas, with values that increase almost linearly with ER. On the contrary, frequency results almost constant for biogas, with a slight change between ER=0.92 and 0.86.The changes in frequency are explained in part by the variation in flame temperature (and, so, in speed of sound), which gradually increases with ER and is higher for methane than for biogas. This effect, however, does not fully justify the variations observed for changes in fuel properties or fuel-air ratio. Most probably, the changes in FTF shown in Fig. 3 should also be accounted for, but this requires a more comprehensive analysis, combining both FTF and burner acoustics, for example using the dispersion equation, as shown below.

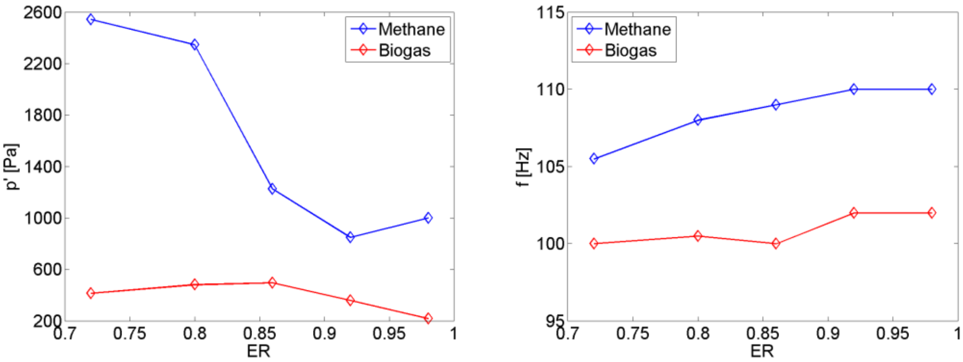

Figure 4. Amplitude and frequency of the main peak in *p'* spectra for methane and biogas. Combustor length=1,250 mm, *H*=-inf

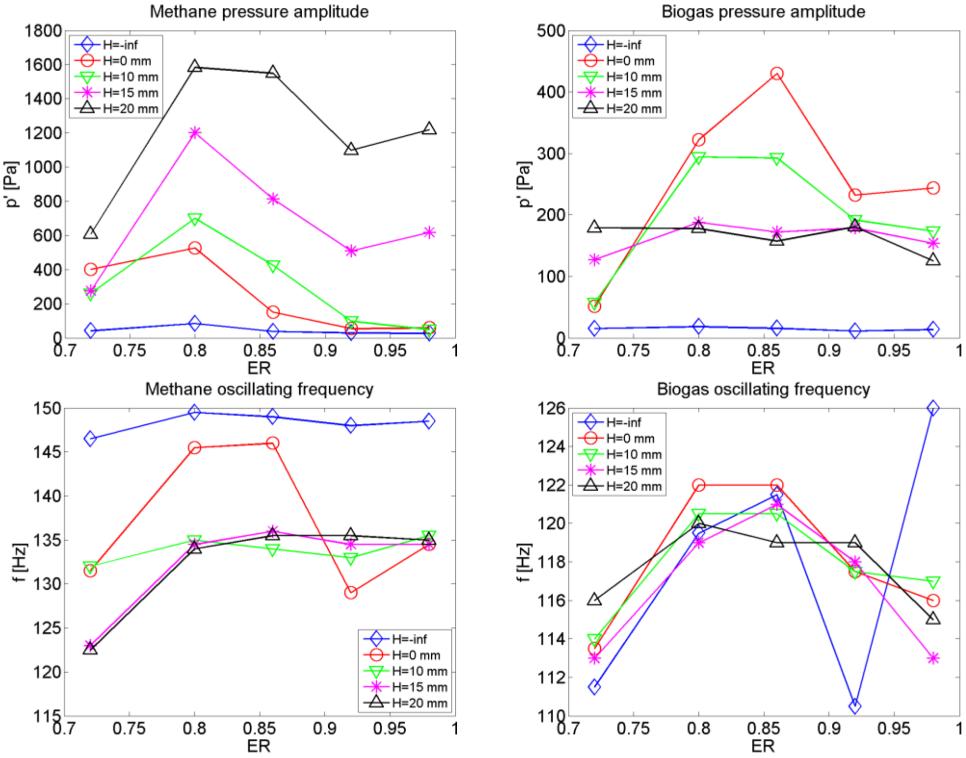

Figure 5. *p'* amplitude (top) and oscillation frequency (bottom) for methane (left) and biogas (right), for different upstream reflection coefficient. Combustor length=900 mm

Figure 5 shows *p'* amplitudes and frequencies obtained with the combustion chamber of 900 mm changing the upstream reflection coefficient. Methane shows very low *p'* amplitudes for an inlet completely open, while the instability tends to increase as the inlet is progressively closed (*H* increasing). The amplitude of the instability varies with the restriction level, but in all cases the strongest limit cycle occurs for ER=0.8.

Biogas, as methane, shows very low pressure fluctuations for fully open inlet (*H*=-inf), with instabilities triggered as the restriction is closed. However, in this case the dynamics does not increase monotonically with restriction level, but the most unstable case is represented by *H*=0 mm. Further increase in the inlet restriction causes a decrease in the combustion dynamics and only ER=0.72 suffers a slight increment of pressure fluctuation. Differently to methane, *p'* level is almost constant for any ER for the highest restriction tested (*H*=20 mm).

Biogas frequencies are almost the same for a given ER, irrespectively of the inlet restriction, while methane flames appear to shift between two characteristics frequencies, at 150 and 135 Hz approximately. The first mode is typical of a completely open inlet, whereas the second appears at high restriction levels. The intermediate condition with *H*=0 mm leads to an oscillating behaviour between both modes depending on the ER value. Frequency values are less interpretable in terms of temperature in this case and are probably more conditioned by the reflection coefficient value and by the acoustic of the system.

4.2 Dispersion equation results

All tests presented in the previous section have been simulated using the dispersion equation. The solutions were identified as those yielding a result of approximately zero for Eq. (6). With that purpose, the angular frequency plane has been swept: from 50 to 600 Hz with 0.5 Hz steps for the real frequency and from -1000 to 1000 rad/s, with 1 rad/s steps, for the imaginary component.

The temperature inside the combustor is not known. Adiabatic temperature is not a good approximation, due to significant heat losses: the combustion chamber is cooled by 50 Nm^3/h of air flowing, in parallel and cocurrent with burnt gases, between the combustion chamber wall and an outer concentric shield, which in turn is refrigerated by a water jacket along its first 400 mm. Therefore, the temperature is significantly lower than the adiabatic one and, moreover, it varies noticeably along the axial distance (preliminary tests showed a temperature down to 400°C at the outlet for the 1,250 mm combustor). Since the dispersion equation requires a single temperature value for the whole combustion chamber, it was set at 50% of the adiabatic temperature (as calculated for different fuels and ER), as a reasonable approximation.

Another factor to be considered for a correct simulation is the burner length considered in the model: to represent a completely open outlet the combustor length must be artificially increased by $\delta=0.85\cdot D/2$, where D is the hydraulic diameter of the combustor [11, 12].

Due to space limitations, the analysis will be focused on the differences between experimental and predicted oscillation frequencies in order to assess the ability of this simple approach to identify the instability modes under limit cycle conditions. Figure 6-a and b present the difference between experimental frequencies (f_{ex}) and the modes predicted with the dispersion equation (f_{th}) for combustor lengths of 1,250 and 900 mm, respectively. Values of f_{th} have been chosen among the different solutions provided by the dispersion equation as the lowest frequency with a negative imaginary part. Overall, the differences obtained are below 10 Hz in 90% of the cases, with a maximum difference of 16 Hz.

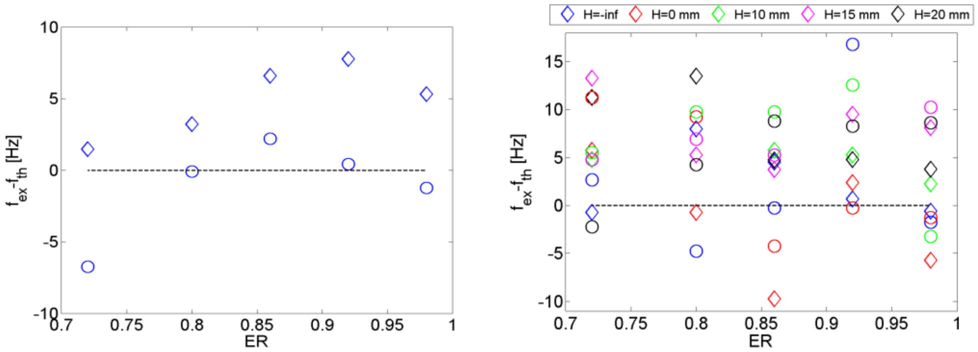

Figure 6. Differences between experimental and predicted frequencies; (◊) methane cases, (o) biogas cases. Left: burner of 1,250 mm, *H*=-inf. Right: burner of 900 mm for different inlet restriction settings

So, despite the simplifications involved, the use of linear FTF to simulate strong non-linear limit cycle conditions has shown to correctly predict unstable modes for a large variety of cases, including changes in conditions of very different nature (geometry, ER, fuel). A particular objective of this work was to test these methods against changes in the composition of the fuel, also with good results, in spite of the significant changes in flame properties for methane and for biogas. The description of the dynamic response of the flame in terms of the FTF measured for linear regimes seems to provide the information required to anticipate limit-cycle behaviour for different fuels.

The fact that the FTF gain does not describe the actual flame behaviour in non-linear conditions does not seem to lead to significant errors in the predictions of oscillation modes. The reason could be that these results are mainly determined by the phase (rather than the gain) of the FTF, which barely changes from FTF to FDF, at least for the flame shape studied (V-flame). Nevertheless, further investigation would be required to verify this interpretation.

5. Conclusions

The FTF of two different fuels has been used as an input to a simplified network model to predict unstable modes for a wide range of operational conditions. The results obtained have been compared with experiments in which high pressure fluctuations are naturally obtained, reaching limit cycle conditions. Theoretical unstable modes obtained show a very good agreement with experimental frequencies, so indicating that the FTF contains the information required to predict instability modes, irrespectively of operational parameters. Apparently, the phase information contained in the FTF may be accurate enough (i.e., similar to the phase in non-linear conditions, as described by the FDF) to successfully identify the natural oscillation modes when the system reaches a limit cycle. Nevertheless, further work to confirm this conclusion is needed. The results presented are expected to complement the findings of previous works by extending the range of validation tests with a systematic study of different conditions, including biogas flames and their differences with respect to methane.

ACKNOWLEDGEMENTS

This work was supported by the Spanish Ministries of Science and Innovation, and of Industry and Competitiveness, through research projects CSD2010-00011 and 2016-4845, respectively.

REFERENCES

1 Dowling, A. and Stow, S. R. Acoustic Analysis of Gas Turbine Combustors, *Journal of Propulsion and Power,* **19** (5), 751-764, (2003)

2 Rayleigh, L. The explanation of certain acoustical phenomena, *Nature,* **18** 319-321, (1878)

3 Han, X., Li, J. and Morgans, A. S. Prediction of combustion instability limit cycle oscillations by combining flame describing function simulations with a thermoacoustic network model, *Combustion and Flame,* **162** (10), 3632-3647, (2015)

4 Noiray, N., Durox, D., Schuller, T. and Candel, S. A unified framework for nonlinear combustion instability analysis based on the flame describing function, *Journal of Fluid Mechanics,* **615** 139-167, (2008)

5 Palies, P., Durox, D., Schuller, T. and Candel, S. Nonlinear combustion instability analysis based on the flame describing function applied to turbulent premixed swirling flames, *Combustion and Flame,* **158** (10), 1980-1991, (2011)

6 Li, J. and Morgans, A. S. Time domain simulations of nonlinear thermoacoustic behaviour in a simple combustor using a wave-based approach, *Journal of Sound and Vibration,* **346** 345-360, (2015)

7 Kim, K. T., Lee, J. G., Quay, B. D. and Santavicca, D. A. Spatially distributed flame transfer functions for predicting combustion dynamics in lean premixed gas turbine combustors, *Combustion and Flame,* **157** (9), 1718-1730, (2010)

8 Kim, K. T. and Santavicca, D. Linear stability analysis of acoustically driven pressure oscillations in a lean premixed gas turbine combustor, *Journal of Mechanical Science and Technology,* **23** (12), 3436-3447, (2009)

9 Bellucci, V., Schuermans, B., Nowak, D., Flohr, P. and Paschereit, C. O. Thermoacoustic Modeling of a Gas Turbine Combustor Equipped With Acoustic Dampers, *Journal of Turbomachinery,* **127** (2), 372-379, (2005)

10 Noiray, N., Durox, D., Schuller, T. and Candel, S. Self-induced instabilities of premixed flames in a multiple injection configuration, *Combustion and Flame,* **145** (3), 435-446, (2006)

11 Lamraoui, A., Richecoeur, F., Ducruix, S. and Schuller, T. Experimental analysis of simultaneous non-harmonically related unstable modes in a swirled combustor *Proceedings of GT 2011*, Vancouver, Canada, (2011)

12 Richecoeur, F., Schuller, T., Lamraoui, A. and Ducruix, S. Analytical and experimental investigations of gas turbine model combustor acoustics operated at atmospheric pressure, *Comptes Rendus Mécanique,* **341** (1), 141-151, (2013)

13 Alemela, P. R., *Measurement and scaling of acoustic transfer matrices of premixed swirl flames*, Ph.D. Thesis, Technische Universität München, (2009)

Proceedings of ASME Turbo Expo 2018: Turbomachinery Technical Conference and Exposition
GT2018
June 11-15, 2018, Oslo, Norway

GT2018-77102

DAMPING OF COMBUSTION INSTABILITIES THROUGH PSEUDO-ACTIVE CONTROL

Jesús Oliva, Ennio Luciano and Javier Ballester
Laboratory of Research on Fluid Dynamics and Combustion Technologies (LIFTEC)
CSIC – University of Zaragoza
Maria de Luna 10, 50018, Zaragoza, Spain
E-mail: ballester@unizar.es

ABSTRACT

Active instability control techniques have demonstrated very good capabilities to correct combustion oscillations but, due to high costs and other practical reasons, have not achieved the success expected in gas turbines engines. A different approach, named here as 'pseudo-active instability control', has been explored and the first results are presented in this work. In this case, the flow of non-premixed pilot fuel is modulated by passive methods: the pressure oscillation in the combustion chamber induces a velocity fluctuation at the secondary fuel injector. In principle, damping of the instability may be achieved if the heat release oscillations due to the secondary fuel are out of phase with those of the main flame.

This work reports a first exploration of this strategy, aimed mainly at performing a proof of the concept. An experimental study has been carried out in a laboratory premixed combustor with pilot fuel injection. The relationship between the fluctuations of pressure in the combustion chamber and those of velocity at the injector was studied both experimentally (hot wire anemometry) and theoretically (1-D acoustic model of the injection line). Combustion tests in limit cycle conditions demonstrated that modifications in the geometry of the secondary injection affected the pressure fluctuations inside the combustion chamber. Depending on the geometry (and, hence, acoustic impedance), the instability was enhanced or damped. This demonstrates that the proposed 'pseudo-active control' can produce similar effects (at least, qualitatively) to those of active control, but only using passive means, as initially postulated.

[Keywords: Combustion instability, premixed combustion, pseudo-active instability control.]

INTRODUCTION

Due to the very low amount of pollutant emissions generated, lean premixed combustion has become the most widely adopted technology in gas turbine facilities [1]. However, a major drawback of lean flames is their proneness to thermoacoustic instabilities [2], generated by the in-phase coupling between pressure oscillation and heat flux fluctuation in the combustion chamber, which could lead to unbearable levels of dynamic pressure for the engine.

Different solutions have been proposed and developed for the control of this phenomenon, leading to a range of configurations which can be subdivided in two groups: passive and active methods. Passive systems, such as quarter-wave tubes or Helmholtz resonator [3], mitigate the pressure fluctuation of the system by acting as dampers of the acoustic energy generated in the burner. The structural simplicity and the high durability of these devices as well as their effectiveness in reducing the amplitude of the dynamic pressure have favored the use of passive dampers in industrial plants [3-7]. However, these devices are generally adequate to dissipate oscillations only at the design frequency, so they lack the flexibility required to act on different modes of the system (even if tunable devices have been proposed [6, 8, 9] , which modify their natural frequency by varying their geometry). Moreover, their optimal sizing and location on the engine are difficult to model and can be quite onerous if performed by "trial-and-error".

Active instability control is based on the modulation of fuel flow rate by means of a high-frequency valve which, operating in closed-loop with a sensor signal, modifies the thermoacoustic response of the system in order to decouple the constructive interaction between the dynamic pressure and the heat release fluctuation. Contrarily to passive dampers, the active systems present the advantage of being adaptable to variations in the unstable frequencies of the burner, but the elevated cost of the equipment, the limited bandwidth of the pulsating valves and their potential of making the system unstable (in case of some failure in the logic of control) make the application of this technology still very limited at industrial level. Several authors have studied the active systems in depth (e.g. [10-13]) and, among the various solutions adopted, one often proposed is the modulation of a secondary injection of small amounts of non-premixed fuel into the combustion chamber [14-18]. These studies have demonstrated that, if designed correctly, this modulated pilot injection can lead to important reductions in the pressure amplitude.

This work explores an alternative method to modulate the flow rate of pilot fuel, by means of the natural acoustic response of the secondary line to the pressure fluctuations produced inside the combustion chamber, and the possibility to adjust it as required to damp combustion instabilities. The obvious advantage would be to avoid the use of pulsed valves and other ancillary systems, which finally are the main practical drawback for the implementation of active instability control. Since the mechanism sought is the same as in active instability control, for brevity the proposed strategy will be named as pseudo-active instability control (PAIC).

This general idea is not fully new, as the occurrence and potential of naturally-induced fuel modulation has already been studied in a number of relevant previous works.

The effect of the acoustic response of the pilot line was already addressed by Auer et al. [18], in the context of active instability control, demonstrating that the dynamic pressure can induce oscillations in the flow rate of pilot fuel and that these effects must be taken into account in order to achieve the desired fuel modulation. Although this work was oriented to active control, their results are relevant for this work and suggest that the proposed PAIC strategy may significantly impact combustor dynamics. Richards et al. [19, 20] studied the response of a secondary injection on the dynamics of a burner. However, differently to the strategy analyzed here, in these works the secondary line did not directly discharge into the combustion chamber (and, so, a pilot flame was not formed) but bypassed a small amount of fuel which was finally injected into the premixing duct.

Other studies have been focused on the application of strategies analogue to PAIC, but based on the modulation of the main fuel flow. Richards et al. [21, 22] demonstrated substantial reduction of the dynamics for a broad range of operational conditions by tuning a resonator installed in the primary feeding line. Huber and Polifke [23] studied the effectiveness of a similar system simulating the flame response to fluctuations in both equivalence ratio and injection velocity; they also observed that a modification of the fuel line response can represent a suitable tool to influence the stability of the facility. Considering a burner with two injectors, Richards et al. [24] achieved a further reduction of the instability, with respect to the case with only one injection, mismatching the two impedances. Noiray et al [25] applied a similar strategy in a burner with multiple injectors.

All these previous works point to the possibility to achieve significant modulation of fuel flow rate due to the acoustic interaction with the pressure fluctuation in the combustion chamber. The way in which this is implemented in the proposed PAIC strategy is explained in the following section.

GENERAL DESCRIPTION OF PSEUDO-ACTIVE INSTABILITY CONTROL

As in conventional active instability control, the objective is to naturally induce a modulation of pilot fuel that could interact, and finally damp, the instability of the main, premixed flame. This is sketched in Figure 1, where the subscripts d and p refer to the secondary and primary injection, while p', u' and Q' represent the pressure, velocity and heat flux fluctuation, respectively.

The dynamic pressure in the combustion chamber induces velocity fluctuations in the different injections, including both the main premixed fuel-air stream and the pilot fuel. For convenience, the relationship between p' and u' will be expressed in terms of the inverse of the acoustic impedance,

$$Z^{-1}(\omega) = \left(\frac{p'(\omega)/\bar{\rho}\,\bar{c}}{u'(\omega)}\right)^{-1} \qquad (1)$$

Z_p^{-1} and Z_d^{-1} designate the inverse of the acoustic impedances of the premixed and pilot fuel lines, as determined at their plane of injection into the combustion chamber. For a given pressure fluctuation in the flame, p', the fluctuation in the velocity at their outlet will be $u_p' = (p'/\bar{\rho}\bar{c})Z_p^{-1}$ and $u_d' = (p'/\bar{\rho}\bar{c})Z_d^{-1}$ for the premixed stream and for the pilot fuel, respectively. The transfer function of the (main) premixed flame, $\mathrm{FTF_p}$, converts u_p' into an oscillation of heat release rate which, in absence of other mechanisms, will finally determine the thermo-acoustic behavior of the system.

The oscillations in pilot fuel flow, however, also affects the dynamics of the flame by inducing additional heat flux fluctuations. This could be quantified in terms of the transfer function of the diffusion flame created by the pilot fuel, $\mathrm{FTF_d}$. According to the Rayleigh criterion, this secondary fuel will tend to damp an existing instability if the oscillation in heat release rate in the diffusion flame is out of phase with the pressure fluctuation existing in the combustion chamber (and generated by the unstable main, premixed flame). Therefore, the PAIC configuration should be designed so as to ideally achieve the phase diagram shown at the bottom of Fig. 1. The phase difference between Q' and $p'$is the sum of the phases of $\mathrm{FTF_d}$ and of Z_d^{-1}. Therefore, a hypothetical PAIC application could be optimized by acting on any of both. In principle, the adjustment (and, as discussed below, even the measurement) of the flame transfer function of the diffusion flame is much less obvious than modifying the acoustic impedance of the secondary injection line. This study has focused on the effects of changes in Z_d^{-1}, achieved through changes in the geometry, on the dynamic behavior of a premixed combustor.

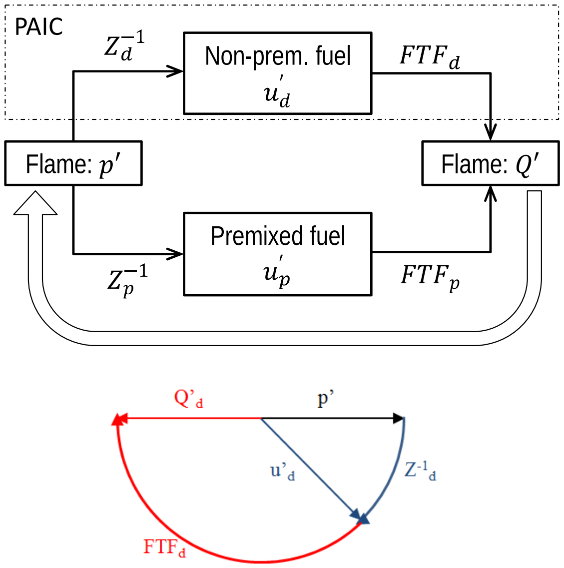

Fig. 1. Schematic representation of the PAIC strategy: main elements (top) and the ideal phase diagram (bottom)

EXPERIMENTAL FACILITY

The tests were performed in the atmospheric, swirl-stabilized combustion facility sketched in Fig. 2.

The primary fuel is supplied by a pure CH_4 pressurized tank and is on-line blended with the air supplied by a compressor; both flows are regulated by mass flow controllers. The mixture is injected into a plenum through two choked orifices which acoustically isolate the feeding line from the rig, so that the blend can be considered perfectly premixed with constant equivalence ratio. The air-fuel mix flows in an annular duct where a swirler (swirl number $S \approx 0.48$) is located 380 mm upstream of the dump plane. The combustion takes place inside a cylindrical combustion chamber composed of a quartz tube (220 mm in length), which guarantees optical access to the flame, followed by a stainless steel extension of the same diameter, for a total length of 1,250 mm.

The pilot fuel is injected by means of a central gun installed coaxially with the annular premix duct. Methane is fed from a pressurized tank and its mean flow rate is automatically regulated by a mass flow controller. A choked orifice installed downstream of the control valve represents a well-defined acoustic boundary condition. The orifice dimensions were chosen to choke the entrance with the minimum flow allowed by the mass flow controller (0.05 Nm^3/h); choked conditions were verified by measuring the static pressure upstream of the choked section. The orifice discharges into a 8 mm line, composed of a first polyamide section of variable length and a second stainless steel one which is a part of the central gun and, hence, of fixed length. The pilot fuel injector is a round orifice of 5 mm in thickness and 2.5 mm in diameter (mean injection velocity is 3 m/s for a methane flow rate of 0.05 Nm^3/h).
A pressure transducer (PCB 103B02) is located at the dump plane of the combustion chamber to record the pressure fluctuations generated. The rig can be externally excited by means of two loudspeakers (Eminence Delta 10-A, 10", 350 W) which are in-phase powered by the same amplifier. Photomultipliers with interference filters were used to determine heat flux fluctuations and flame transfer functions, but these results have not been reported here for brevity.

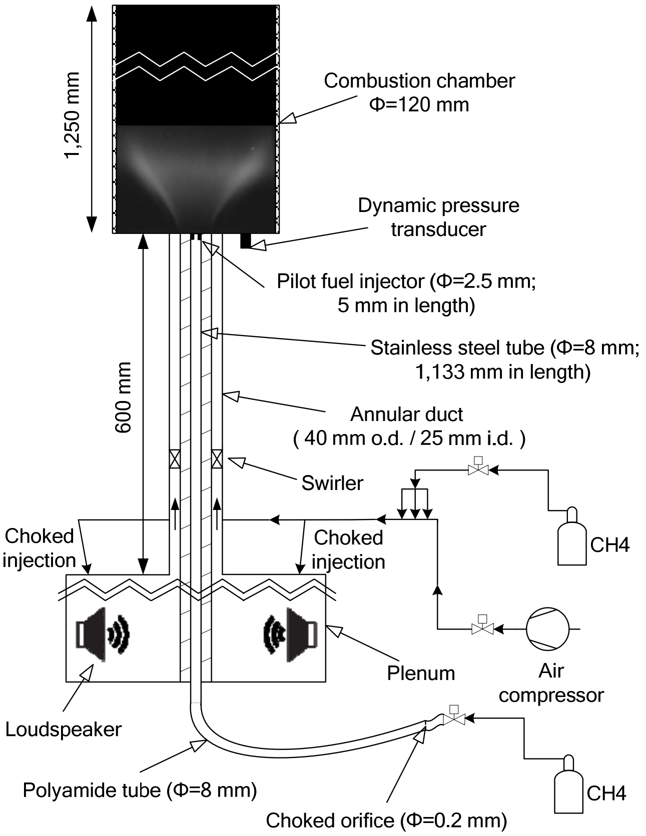

Fig. 2. Sketch of the experimental facility

ANALYSIS OF THE ACOUSTIC IMPEDANCE

In principle, the acoustic behavior of the fuel line can be freely adjusted by modifying its impedance. However, there is a limit in the range of possible values. This can be easily deduced by expressing the inverse impedance in terms of the reflection coefficient, $|R|\angle\alpha$ (for simplicity, Z_d^{-1} will be just denoted as Z^{-1} hereafter):

$$Z^{-1} = \frac{|R|\angle\alpha - 1}{|R|\angle\alpha + 1} = \frac{|R|^2 - 1 + i\,2|R|\sin\alpha}{(|R|-1)^2 + 2|R|(1+\cos\alpha)} \qquad (2)$$

Since $|R| \leq 1$, the real part of the numerator of Eq. (2) is always negative, while the denominator is always positive. Therefore, all the possible values of Z^{-1} are restricted to the left-hand half-plane of the complex domain. Moreover, it can be demonstrated (not shown here for brevity) that, given a certain value of $|R|$ (i.e., a circumference in the complex plane), the correspondent values of Z^{-1} also depict a circumference whose radius increases with $|R|$. In the limit of $|R|$ tending to 1, (denoted as R_1 in Fig. 3), the circumference is transformed into the imaginary axis. Therefore, the range of possible values of Z^{-1} is restricted to the left half plane (negative real part).

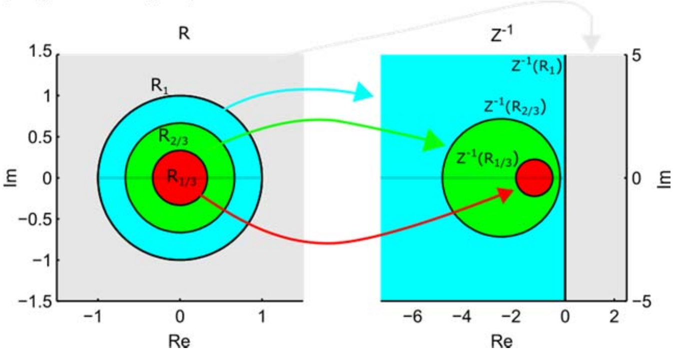

Fig. 3. Possible values of Z^{-1} for a given module of R, with the constraint $|R| \leq 1$

Transposing these results to the physical plane, this analysis defines that the amplitude of Z^{-1} can theoretically increase up to infinity and that its angle is always included in the range between 90º and 270º. Therefore, the phase of u'_d with respect to p' is restricted to a range of 180º (see Fig. 4). This may constitute an important limitation in a hypothetical PAIC implementation since, depending on the phase imposed by the $\mathrm{FTF_d}$, the possibilities to place Q'_d out of phase with respect to p' may be hindered. In the worst case, if the phase of $\mathrm{FTF_d}$ is 180º, in theory any configuration of the secondary fuel injection would yield Q'_d in-phase with p' (see Fig. 1) and, hence, it would always enhance the instability.

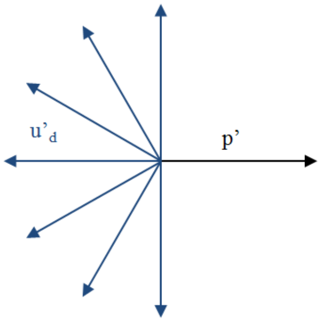

Fig. 4. Possible range of phases between u'_d and p'

Therefore, the details on the dynamic behavior of the diffusion flame are fundamental in the implementation of PAIC. However, assessing the pilot flame response, in terms of $\mathrm{FTF_d}$, in the considered situation (a diffusion flame in the core of a premixed flame) is an extremely difficult task. This would require a reliable measurement of the heat flux fluctuation, Q'_d, exclusively due to the diffusion flame. If the usual method based on chemiluminescence intensity is to be applied, a first difficulty is to establish a valid relationship between emission in selected bands and heat release rate. In any case, due to the very small power of the diffusion flame, the signal due to the diffusion flame is probably hidden by the fluctuations in the much stronger emission from the main flame. So, the most common approach found in literature is based on computational analyses (e.g., [26, 27]), as no experimental technique has been found to differentiate the response of the two flames. Li et al. [28] have recently proposed a theoretical model of the FTFs of a flame similar to the one considered in this work; however, apart from minor differences in their facility and resultant flame, their method showed applicability only for linear regimes, while in this case limit cycle conditions are studied.

The strategy followed in this study consisted in testing a wide range of configurations of the secondary fuel injection. This allows evaluating the impact of the PAIC configuration used in the tests on the severity of the instability as well as to indirectly derive some conclusions on the expected phase of the dynamic response of the pilot flame.

A 1D linear acoustic model was used to calculate the impedance of the fuel line for the different lengths of the polyamide section. The line can be decomposed into a number of elements connected in series: choked orifice, polyamide tube, stainless steel tube and injector. The global model was built by suitably combining their respective submodels. The choked orifice was described through a reflection coefficient formulation proposed in [29], which gives a final result very similar to the reflection coefficient of a closed end ($R = 1$). The 8 mm tube was modeled as plane acoustic waves propagatin along a straight duct with damping, according to the model proposed in [30]. The damping effect is quantified through the shear and the Prandtl numbers and through an empirical coefficient C_d which takes into account the wall roughness (C_d was set to 1 and 2 for the stainless steel and the polyamide tubes, respectively). The injection orifice was described as a sudden area change (from 8 to 2.5 mm in diameter), as described in [31], followed by a straight tube of 5 mm in length.

The predictions of the model were firstly contrasted with experimental results to assess its reliability. The velocity fluctuations at the injector were measured using a constant temperature hot wire anemometer (TSI Instruments, IFA 300). The hot wire element (1.5 mm in length) was located 1 mm downstream of the injection orifice (Fig. 5) to measure the u'_d amplitude generated by a given pressure fluctuation and their relative phase (the distance between the orifice and the hot wire can be considered short enough to not affect the fluctuations generated at the dump plane). The pressure fluctuation was measured by the pressure transducer installed at the dump plane. The signals of both sensors were recorded for 4s, at a sampling rate of 4 kHz. The system was acoustically excited using the two loudspeakers installed at both sides of the plenum (see Fig. 2), from 50 to 250 Hz with 10 Hz steps.

Figure 6 compares, in magnitude and phase, the measured values of Z^{-1} (solid lines) and the ones predicted by the model (dashed lines) for a methane flow rate of 0.05 $\mathrm{Nm^3/h}$ in the pilot line and without installing any polyamide tube (L=0).

Model predictions agree quite well with the experimental results, therefore the acoustic model can be considered reliable to calculate the impedances for the various pilot line configurations used to assess the results with pseudo-active control on the rig.

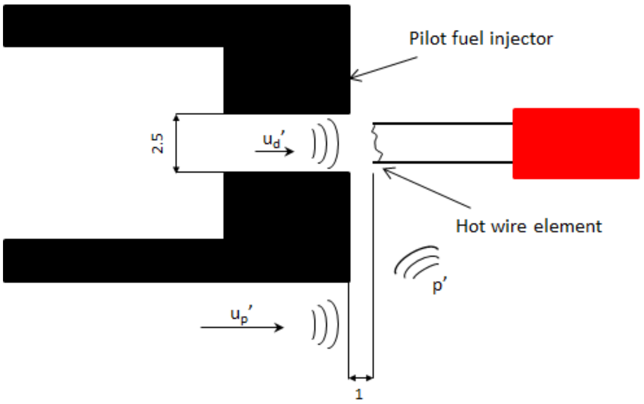

Fig. 5. Setup for hot wire measurements (dimensions in mm)

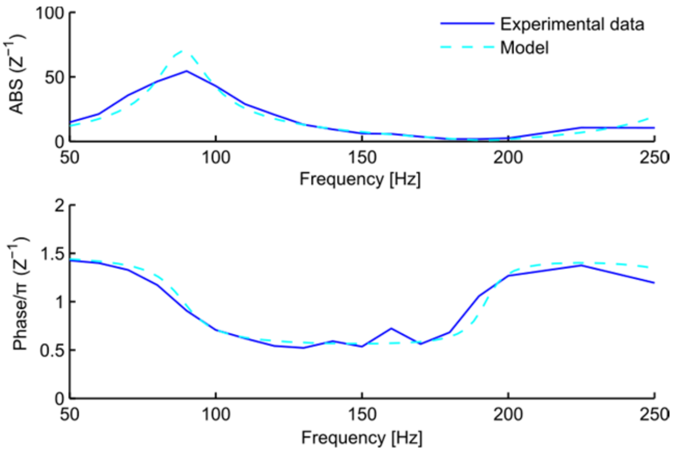

Fig. 6. Model validation

The combustion chamber of 1,250 mm presents a sustained limit cycle at a natural frequency around 110 Hz. So, Z^{-1} calculations were performed in the vicinity of this frequency for various values of L. The aim is to determine the range of injection line lengths that provide the desired range of Z^{-1} values, i.e, high magnitude and phases covering as much as possible of the theoretical 180º range.

Five lengths of the polyamide section were finally selected (1.30, 1.50, 1.65, 1.85 and 2.10 m), all of them yielding $|Z^{-1}|$>10 and a phase variation that covers 125º of the 180º physically possible. The calculations were again compared with measurements with hot wire anemometry for all these lengths (Fig. 7). The agreement between the experimental and predicted Z^{-1} is again very good, supporting the suitability of the model proposed also when the polyamide tube is installed.

In order to evaluate the effect of the PAIC strategy, the amplitude of the instability should be compared with the case without pilot fuel. However, this would not be a valid procedure, because the presence of diffusion flame, even without any modulation, alters the dynamic behavior with respect to the fully premixed operation [32]. The method adopted was to compare the results with cases in which the fluctuations in pilot fuel are low enough. With this purpose, additional tests were performed with configurations yielding very low absolute values of Z^{-1}, so that the u_d' amplitudes and, as a consequence, the magnitude of Q_d' are expected to be sufficiently small to serve as a reference. These conditions are expected to be achieved with shorter polyamide tubes, of L=0.85, 0.75 and 0.65 m. The module and phase of Z^{-1} at 110 Hz for the 8 cases tested are listed in Table 1, for the configurations intended to evaluate the effect of pilot fuel modulation (1-5) as well as for the shorter lengths providing low modulation amplitudes (6-8).

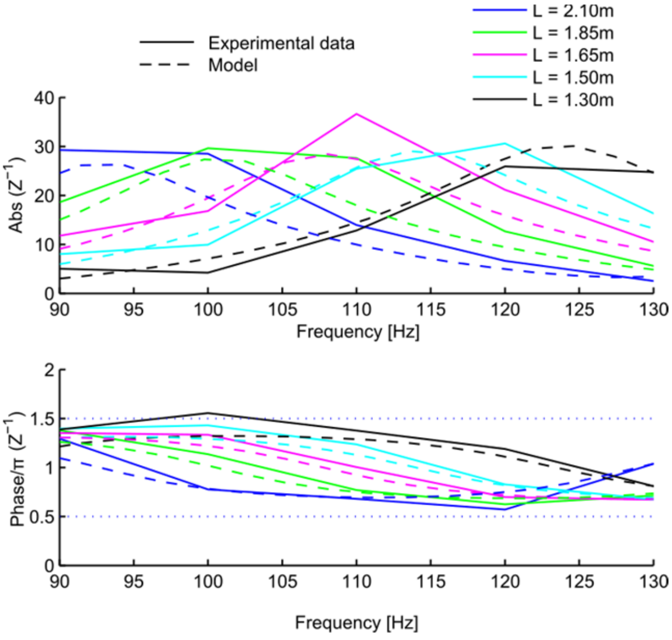

Fig. 7. Comparison between model predictions and experimental results for different lengths of the polyamide tube

Table 1. Lengths of the polyamide tubes and absolute values and phases of Z^{-1} at 110 Hz for cases 1-8

Case	1	2	3	4	5	6	7	8
L [m]	2.10	1.85	1.65	1.50	1.30	0.85	0.75	0.65
Abs (Z^{-1})	13.96	27.59	36.65	25.44	12.84	2.38	1.63	2.27
∠(Z^{-1}) [º]	110	126	168	210	235	218	175	132

EFFECT OF PAIC IN LIMIT CYCLE CONDITIONS

The eight configurations detailed above were tested for the same experimental conditions. The primary methane flow was

3 Nm^3/h in all cases, whereas the air flow rate was varied to achieve three different values of the equivalence ratio (Φ): 0.98, 0.86 and 0.72. The mean flow rate of pilot fuel was also fixed in all the experiments reported (0.05 Nm^3/h, 1.66% of the main fuel). This very low flow rate was selected on purpose, in order to evaluate the capabilities of the strategy without significantly increasing pollutants emissions due to the diffusion flame.

Each polyamide tube was tested for the three Φ values indicated, and the dynamic pressure in the combustion chamber was recorded at 4 kHz for 4 s. Each measurement was repeated twice. Figure 8 shows the results for all the cases, in terms of the amplitude of the pressure oscillations as a function the phase of the Z^{-1} associated to the various tube lengths, for the three Φ tested. Two data points are represented for each case, corresponding to the two repetitions. Apart from the (minor) deviations in p', there are also some small displacements in the phase values. These are a consequence of the differences in limit cycle frequencies between repeated tests, which have some effect on the acoustic impedance (see Fig. 7).

As it was previously noted, $|Z^{-1}|$ is very small for cases 6-8 (see Table 1), so that fluctuations in pilot fuel flow are expected to be very low and, hence, these tests can be taken as representatives of a steady pilot diffusion flame. In spite of the existence of this pilot flame, the combustor still exhibits a strong and well defined limit cycle with high pressure amplitudes for all equivalence ratios tested.

The results are very different for cases 1-5, characterized by a much higher module of Z^{-1} and, hence, larger modulation amplitudes of the pilot fuel flow for a given p'. The interaction between the unstable main flame and the fluctuating pilot flame results in an equilibrium p' inside the combustion chamber which is significantly smaller than the range of values recorded for cases 6-8. Since the only relevant difference between the tested configurations is the acoustic impedance of the pilot fuel tube, the large differences observed should be attributed to the modulation in secondary fuel flow rate induced by the pressure fluctuations inside the combustion chamber. This confirms that a strategy of the type of the 'pseudo-active control' analyzed here might yield significant reductions in the strength of combustion instabilities.

Also relevant are the differences observed among cases 1-5. Since the module of Z^{-1} is similar in all these tests, the changes in p' should be ascribed to the differences in the phase of the impedance which, for a given p', leads to different phase delays between the oscillations in the pilot fuel velocity and those of the main flame. This is considered a further confirmation that the rationale behind the PAIC strategy is consistent with the experimental results obtained.

A more precise analysis would require some knowledge about the dynamic response of the pilot flame. In the lack of detailed results, or even hints from the literature, in this regard, the results obtained in this parametric study may also be useful to extract some information about the dynamic behavior of the diffusion flame.

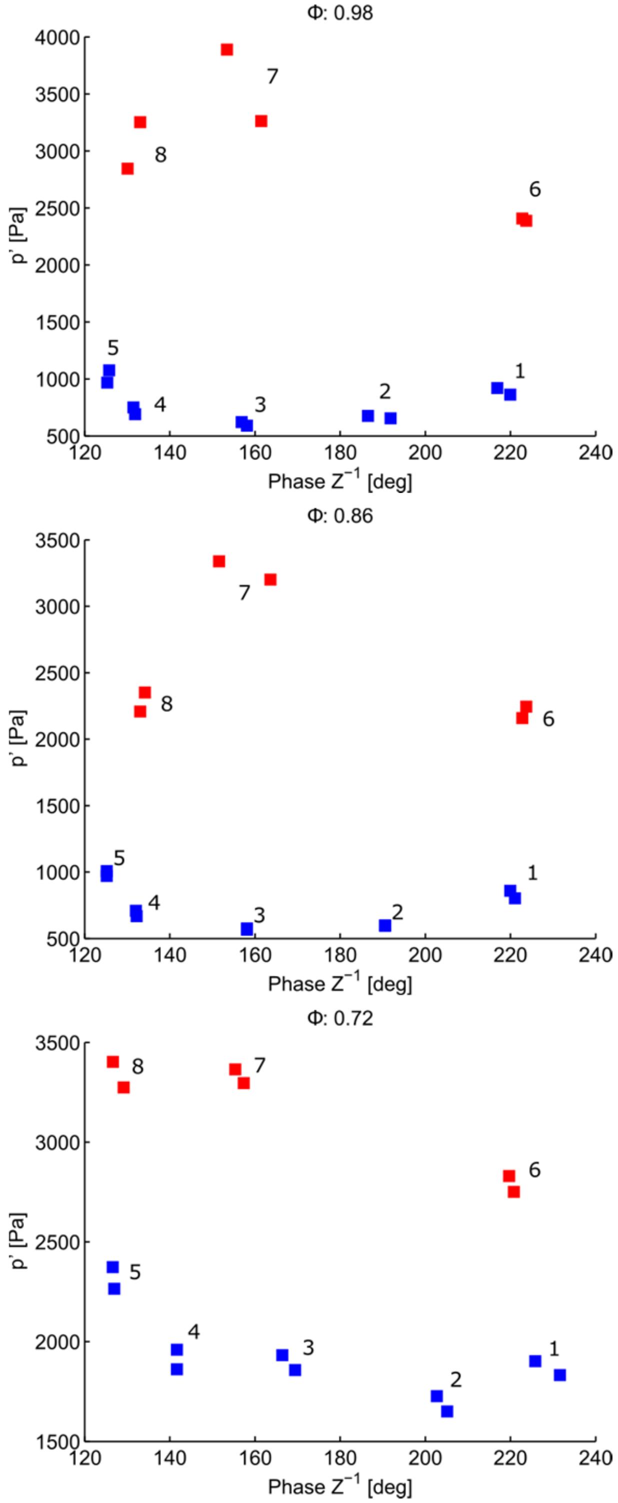

Fig. 8. p' amplitude versus Z^{-1} phase. Blue (cases 1-5) and red (cases 6-8) symbols denote, respectively, configurations with high and low Z^{-1} modules

In general, the significant reduction in p' achieved in cases 1-5 clearly points to Q_d' oscillations being out-of-phase with respect to p', so that the fluctuations acoustically induced in the pilot flame tend to damp the natural instability of the system. The relative variations among cases 1-5 allow identifying a minimum within the phase range covered by the impedances of the lines used in the tests.

This minimum must correspond approximately to the situation in which Q_d' is perfectly out-of-phase with respect to p' and, since the phase range covered is less than 180º and the minimum approximately falls in the middle of this range, it can be concluded that, in all cases, the modulation attained in Q_d' is expected to be out-of-phase with the dynamic pressure.

Based on this general idea, an attempt to estimate the FTF$_d$ phase for the various tested impedances can be carried out. Assuming that dynamic response of the pilot flame does not depend on the impedance of the fuel line, the minimum depicted by the p' values of cases 1 to 5 might be assumed to correspond to a situation in which Q_d' and p' are perfectly out-of-phase (180º). This reference point has been obtained with a second degree polynomic fit of the experimental values of cases 1 to 5. So the FTF$_d$ phase for each one of the tested cases can be estimated according to their relative phase difference with respect to the minimum obtained with the fitting. Figure 9 is a phasorial representation the phases estimated for the different cases tested.

The magnitudes of the u_d' phasors in Fig. 10 are proportional to the respective Z^{-1} amplitudes and, since the FTF$_d$ magnitude is unknown, the Q_d' phasors have been represented with the same length than the associated u_d'. The results obtained indicate that the response of the pilot flame is delayed by about 15-30° with respect to the velocity fluctuations at the injector. Also, the FFT$_d$ phase apparently increases for leaner flames. Obviously, this can only be taken as a qualitative and very preliminary analysis and should be studied more in depth, but it could serve to gain some insight into the dynamic behavior of pilot diffusion flames.

Cases 6-8 apparently depict an opposite trend to that observed for cases 1-5, despite the phase range is more or less the same. In particular, the maximum obtained (case 7) presents a similar value of Z^{-1} phase than that at which cases 1-5 display their minimum. So, these data might seem to invalidate the deductions presented before. However, cases 6-8 display some additional differences that make them not suitable to apply the same reasoning explained for cases 1-5. The polyamide lengths were selected to present low amplitudes of Z^{-1}, but they display significant differences between the cases (see Table 1). Case 7 has the lowest absolute value of Z^{-1}, while cases 6 and 8 give similar results (the exact quantification of them is difficult due to the high sensitivity of Z^{-1} with frequency when it presents low amplitudes). Therefore, this difference might cause that the projections on the p' direction of the Q_d' phasors for cases 6 and 8 are greater than the one for case 7; as a consequence, despite case 7 presents a more favorable phase to attenuate instability, cases 6 and 8 exhibit stronger damping than the case 7 because of their greater Z^{-1} magnitude. Therefore, the differences observed among the p' values recorded for cases 6-8 are thought to be due to additional causes and cannot be interpreted only in terms of the FFT$_d$ phase.

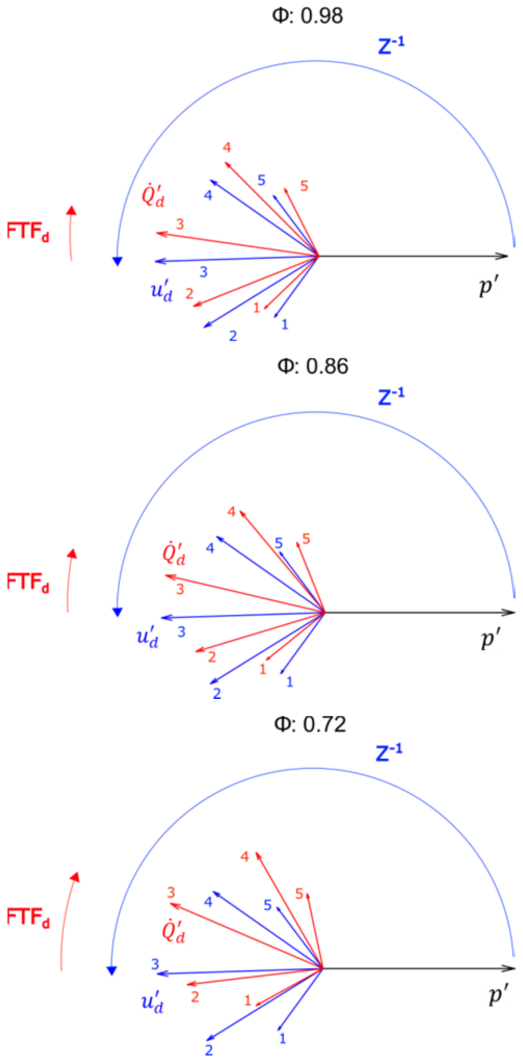

Fig. 9. Estimated phase of FTF$_d$ for different equivalence ratios

CONCLUSIONS

This article presents an exploratory study of the potential of acoustically-induced pilot fuel modulation for damping of thermo-acoustic instabilities. Due to the similarity with the principles of active instability control, this strategy has been denoted as ‘pseudo-active instability control’ (PAIC). The experiments were conducted in a laboratory swirl-stabilized premixed combustor, for a range of lengths of the pilot fuel line. This secondary injection generates a diffusion flame of very low power (1.6%), which can be naturally excited by the velocity modulation caused by the fluctuations of pressure in the combustion chamber. The tests were performed in limit cycle conditions.

The global dynamic behavior depends on the dynamics of the small diffusion flame, but its response (FFT) is unknown. So, the method applied consisted in evaluating the results for a range of configurations of the injection line, which are expected to lead to a wide range of phases between the modulated pilot flame and the natural instability of the premixed flame. A 1D acoustic model, verified by measurements using hot wire anemometry, was used to estimate the acoustic impedance of the pilot fuel line, so that the lengths of the tube were selected to obtain very different phases and amplitudes of velocity fluctuation at the pilot fuel injector. The results confirm a significant effect of the PAIC strategy, with significant reductions (by factors in the range 2-7) in dynamic pressure. Besides, the large variations observed due to changes in the acoustic impedance of the fuel line further confirm the general ideas behind the PAIC strategy. Further analysis of the results for different phases of the impedance may also provide some indication on the phase of the FTF of the diffusion flame, which is one of the parameters governing the global dynamics of the system.

ACKNOWLEDGMENTS

The financial support from the Spanish Ministry of Economy and Competitiveness through project RTC-2016-4845-3 is gratefully acknowledged.

NOMENCLATURE

FTF	flame transfer function
L	polyamide tube length
p	pressure
Q	heat flux
R	reflection coefficient
u	flow velocity
Z	acoustic impedance
Φ	equivalence ratio
$\overline{()}$	mean value
$()'$	fluctuation

Subscripts

d	refers to the secondary fuel (diffusion flame)
p	refers to the primary fuel (premixed flame)

REFERENCES

[1] Dowling, A. P. and Stow, S. R. "Acoustic Analysis of Gas Turbine Combustors." *J. Propul. Power* Vol. 19 No. 5 (2003): pp. 751-764

[2] Liewven, T. and Zinn, B. T. "Theoretical Investigation of Combustion Instability Mechanisms in Lean Premixed Gas Turbines." *Proceedings of the 36th AIAA Aerospace Sciences Meeting and Exhibit* AIAA-98-0641. Reno, NV, January 12-15, 1998.

[3] Sohn, C. H. and Park, J. H. "A Comparative Study on Acoustic Damping Induced by Half-Wave, Quarter-Wave, and Helmholtz Resonators." *Aerosp. Sci. Technol.* Vol. 15 No. 8 (2011): pp. 606-614

[4] Krebs, W., Bethke, S., Lepers, J., Flohr, P., Prade, B., Johnson, C. and Sattinger, S. "Thermoacoustic Design Tools and Passive Control: Siemens Power Generation Approaches." *Combustion Instabilities in Gas Turbine Engines, in Progress in Astronautics and Aeronautics.* AIAA, (2005): pp. 89-112.

[5] Dupère, I. D. J. and Dowling, A. P. "The Use of Helmholtz Resonators in a Practical Combustor." *J. Eng. Gas Turbine Power* Vol. 127 No. 2 (2005): pp. 268-275

[6] Zhao, D. and Morgans, A. S. "Tuned Passive Control of Combustion Instabilities Using Multiple Helmholtz Resonators." *J. Sound Vib.* Vol. 320 No. 4 (2009): pp. 744-757

[7] Li, S., Li, Q., Tang, L., Yang, B., Fu, J., Clarke, C. A., Jin, X., Ji, C. Z. and Zhao, H. "Theoretical and Experimental Demonstration of Minimizing Self-Excited Thermoacoustic Oscillations by Applying Anti-Sound Technique." *Appl. Energy* Vol. 181 No. (2016): pp. 399-407

[8] de Bedout, J. M., Franchek, M. A., Bernhard, R. J. and Mongeau, L. "Adaptive-Passive Noise Control with Self-Tuning Helmholtz Resonators." *J. Sound Vib.* Vol. 202 No. 1 (1997): pp. 109-123

[9] Estève, S. J. and Johnson, M. E. "Adaptive Helmholtz Resonators and Passive Vibration Absorbers for Cylinder Interior Noise Control." *J. Sound Vib.* Vol. 288 No. 4 (2005): pp. 1105-1130

[10] Dowling, A. P. and Morgans, A. S. "Feedback Control of Combustion Oscillations." *Annual Review of Fluid Mechanics* Vol. 37 No. 1 (2005): pp. 151-182

[11] McManus, K. R., Poinsot, T. and Candel, S. M. "A Review of Active Control of Combustion Instabilities." *Prog. Energy Combust. Sci.* Vol. 19 No. 1 (1993): pp. 1-29

[12] Sattinger, S. S., Neumeier, Y., Nabi, A., Zinn, B. T., Amos, D. J. and Darling, D. D. "Sub-Scale Demonstration of the Active Feedback Control of Gas-Turbine Combustion Instabilities." *J. Eng. Gas Turbine Power* Vol. 122 No. 2 (2000): pp. 262-268

[13] Neumeier, Y. and Zinn, B. T. "Experimental Demonstration of Active Control of Combustion Instabilities Using Real-Time Modes Observation and Secondary Fuel Injection." *Symp. (Int.) Combust.* Vol. 26 No. 2 (1996): pp. 2811-2818

[14] Guyot, D., Röbler, M., Bothien, M. R. and Paschereit, C. O. "Active Control of Combustion Instability Using Pilot and Premix Fuel Modulation." *Proceedings of the 14th International Congress on Sound and Vibration.* 235. Cairns, Australia, 9-12 July, 2007.

[15] Lee, J. G., Kim, K. and Santavicca, D. A. "Effect of Injection Location on the Effectiveness of an Active Control System Using Secondary Fuel Injection." *Proc. Combust. Inst.* Vol. 28 No. 1 (2000): pp. 739-746

[16] Moeck, J., Bothien, M., Guyot, D. and Paschereit, C. "Phase-Shift Control of Combustion Instability Using (Combined) Secondary Fuel Injection and Acoustic Forcing." *Active Flow Control.* Springer, (2007): pp. 408-421.

[17] Tachibana, S., Zimmer, L., Kurosawa, Y. and Suzuki, K. "Active Control of Combustion Oscillations in a Lean

Premixed Combustor by Secondary Fuel Injection Coupling with Chemiluminescence Imaging Technique." *Proc. Combust. Inst.* Vol. 31 No. 2 (2007): pp. 3225-3233

[18] Auer, M. P., Gebauer, C., Mösl, K. G., Hirsch, C. and Sattelmayer, T. "Active Instability Control: Feedback of Combustion Instabilities on the Injection of Gaseous Fuel." *J. Eng. Gas Turbine Power* Vol. 127 No. 4 (2004): pp. 748-754

[19] Richards, G. A. and Yip, J. M. "Oscillating Combustion &Om a Premix Fuel Nozzle." *Proceedings of the Combustion Institute/American Flame Research Committee Meeting.* DOE/METC/C-95/7189. San Antonio, TX, 23-26 April, 1995.

[20] Richards, G. A., Yip, J. M. and Gemmen, R. "Design Factors for Stable Lean Premix Combustion." *Proceedings of the Advanced Coal-Fired Power Systems 95 Review Meeting.* DOE/METC/C-96/7210. Morgantown, WV, 17-18 October, 1995.

[21] Richards, G. A., Straub, D. L. and Robey, E. H. "Dynamic Response of a Premix Fuel Injector." *Proceedings of the ASME Turbo Expo 2001: Power for Land, Sea, and Air.* 2001-GT-0036. New Orleans, LA, 4-7 June, 2001.

[22] Richards, G. A., Straub, D. L. and Robey, E. H. "Passive Control of Combustion Dynamics in Stationary Gas Turbines." *J. Propul. Power* Vol. 19 No. 5 (2003): pp. 795-810

[23] Huber, A. and Polifke, W. "Impact of Fuel Supply Impedance on Combustion Stability of Gas Turbines." *Proceedings of the ASME Turbo Expo 2008: Power for Land, Sea and Air.* GT2008-51193. Berlin, 11-13 June, 2008.

[24] Richards, G. A. and Robey, E. H. "Effect of Fuel System Impedance Mismatch on Combustion Dynamics." *J. Eng. Gas Turbine Power* Vol. 130 No. 1 (2008): pp. 1-7

[25] Noiray, N., Durox, D., Schuller, T. and Candel, S. "Dynamic Phase Converter for Passive Control of Combustion Instabilities." *Proc. Combust. Inst.* Vol. 32 No. 2 (2009): pp. 3163-3170

[26] Shinjo, J., Matsuyama, S., Mizobuchi, Y. and Ogawa, S. "Study on Flame Dynamics with Secondary Fuel Injection Control by Large Eddy Simulation." *Combust. Flame* Vol. 150 No. 4 (2007): pp. 277-291

[27] Paschereit, C. O., Flohr, P. and Gutmark, E. J. "Combustion Control by Vortex Breakdown Stabilization." *J. Turbomach.* Vol. 128 No. 4 (2002): pp. 679-688

[28] Li, C., Li, S., Cheng, X. and Zhu, M. "Measurements and Modeling of the Dynamic Response of a Pilot Stabilized Premixed Flame under Dual-Input Perturbation." *Proceedings of the ASME Turbo Expo 2017: Turbomachinery Technical Conference and Exposition.* GT2017-63843. Charlotte, NC, USA, 2017.

[29] Keller, J. J. "Thermoacoustic Oscillations in Combustion Chambers of Gas Turbines." *AIAA journal* Vol. 33 No. 12 (1995): pp. 2280-2287

[30] Alemela, P. R. "Measurement and Scaling of Acoustic Transfer Matrices of Premixed Swirl Flames." Ph.D. Thesis. Technischen Universität München. 2009

[31] Gentemann, A., Fischer, A., Evesque, S. and Polifke, W. "Acoustic Transfer Matrix Reconstruction and Analysis for Ducts with Sudden Change of Area." *Proceedings of the 9th AIAA/CEAS Aeroacoustics Conference.* AIAA 2003-3142. 2003.

[32] Li, J., Peluso, S., Quay, B. and Santavicca, D. A. "Effect of Pilot Flame on Flame Macrostructure and Combustion Instability." *Proceedings of the ASME Turbo Expo 2017: Turbomachinery Technical Conference and Exposition.* GT2017-64079. Charlotte, NC, 26-30 June, 2017.

COMBUSTION SCIENCE AND TECHNOLOGY
https://doi.org/10.1080/00102202.2020.1802588

Taylor & Francis
Taylor & Francis Group

Analysis of a Pseudo-active Approach for the Control of Thermoacoustic Instabilities

Ennio Luciano[a], Jesús Oliva[a], Álvaro Sobrino[a], and Javier Ballester[b]

[a]Laboratory of Research on Fluid Dynamics and Combustion Technologies (LIFTEC), CSIC, University of Zaragoza, Zaragoza, Spain; [b]Fluid Mechanics Group/LIFTEC, CSIC-University of Zaragoza, Zaragoza, Spain

ABSTRACT
This work describes a first characterization study of a novel approach, named 'pseudo-active' instability control (PAIC), which might afford the versatility of active control, but with much simpler hardware requirements. The objective is to spontaneously induce oscillations in pilot fuel injection due to the pressure fluctuations in the combustion chamber, in order to produce effects similar to those obtained with active instability control methods. For optimized designs, this interaction could be exploited to damp pressure fluctuations in gas-turbine combustors. The experimental study was performed for different PAIC configurations and under situations of strong, self-sustained pressure fluctuations. The results obtained show good potentialities of the system proposed, and also revealed purely acoustic interactions between the burner and the pilot line, which superimposed on the interaction between the pilot and main flames. Overall, this work provides novel results on the, previously unexplored, influence of the acoustic properties of the pilot fuel injection on the limit cycle as well as first evidence on the rationale and benefits that could be derived from the so-called PAIC strategy.

ARTICLE HISTORY
Received 29 August 2019
Revised 28 June 2020
Accepted 25 July 2020

KEYWORDS
Pseudo-active control; thermoacoustic instabilities; pilot flame; tunable acoustic impedance

Introduction

Lean-premixed combustion has become the most commonly adopted technology in gas turbines, due to its very low NO_x emissions, below the level required by most worldwide regulations (Dowling and Stow (2003b)). An important issue in lean-premixed technology is its susceptibility to the onset of combustion instabilities (Lieuwen and Zinn (1998), Dowling and Stow (2003a)), which has motivated great research and development efforts in this field, both at academic and at industrial level. This has led to significant progress in the understanding of the responsible physical phenomena as well as in the development of robust technological solutions. The problem, however, is far from being solved and the plants still must rely on continuous monitoring of combustion instability, which triggers palliative measures if the dynamic pressures exceed some predetermined thresholds. Overall, combustion instabilities can be considered one of the major issues in gas-turbine combustors and, even if correctly avoided, significantly restrict its operating range and flexibility (e.g., to fuel changes) and may cause important increases in NO_x emissions when the control imposes switching from fully premixed modes to avoid entering unstable

CONTACT Javier Ballester ✉ ballester@unizar.es 🖂 Fluid Mechanics Group, School of Engineering and Architecture, Zaragoza 50018, Spain

regimes. The demand for effective solutions has notably increased in recent years, due to the important changes in the role of gas-turbine plants, which are required to operate close to its minimum load and also to act as peaking and regulation plants as the penetration of renewable sources is continuously increasing. In this context, the requirements to reduce the minimum load and to enhance flexibility and robustness are fostering important efforts in this area.

The onset of combustion instabilities can lead to a sudden increase in dynamic pressure up to unbearable levels for the facility. The physical mechanism behind this instability is the constructive coupling of the dynamic pressure (p') and of the heat release rate fluctuation (Q') in the combustion chamber. This phenomenon was first described by Lord Rayleigh (1878), who stated that when p' and Q' are in-phase, the pulsation tends to grow, whereas it will be damped when both magnitudes oscillate out-of-phase. In case of a constructive interaction, flame oscillations continuously feed the instability and the dynamic pressure in the combustion chamber grows. This could result in damages to the facility hardware, both of minor (instrumentation failures, minor breaks), and major (partial or total failure of some component or of the entire facility) entity, and also in both technical problems and economical losses caused by a forced shut-down of the plant.

Due to these prejudicial effects, both the scientific community and, especially, the companies involved in the construction and operation of heavy-duty gas turbines have devoted great efforts for the development of solutions for the prevention and/or control of combustion instabilities. The technologies designed for this purpose can be classified into two groups: passive (Richards, Straub, and Robey (2003b)) and active (McManus, Poinsot, and Candel (1993)) methods. Passive systems consist of devices (e.g., quarter-wave tubes, Helmholtz resonators (Sohn and Park (2011)), perforated plates, or acoustic liners (Eldredge and Dowling (2003))) which act as dampers of the acoustic energy generated in the burner. These solutions have been analyzed in many works (e.g., Sohn and Park (2011), Krebs et al. (2005), Dupère and Dowling (2005), Zhao and Morgans (2009), Li et al. (2016)) which have highlighted their structural simplicity and high durability as well as their efficacy in weakening combustion instabilities. Nevertheless, acoustic dampers are generally designed to attenuate pressure fluctuations at a defined frequency, lacking the versatility that would be required for damping various unstable modes (to this end, tunable devices have been proposed by Zhao and Morgans (2009), de Bedout et al. (1997), Estève and Johnson (2005), which modify their natural frequency by varying their geometry). Also, optimizing their size and location on the facility is a difficult task to accomplish a priori, and this process results quite onerous if performed by “trial-and-error” (Kim et al. (2010)).

Active systems attenuate the instability by means of a dynamic element (a loudspeaker or a high-frequency valve), generally operating in closed-loop with a reference signal of the unstable condition (normally p'). The actuation of this element is intended for decoupling the constructive interaction between p' and Q' by modifying the thermoacoustic response of the system. This approach has been investigated in a number of works (e.g. Dowling and Morgans (2005), Sattinger et al. (2000), Neumeier and Zinn (1996), Hermann and Hoffmann (2005), to name a few) and presents a major advantage with respect to passive devices, that is, it is adaptable to variations of the unstable frequency of the facility. This is a very attractive feature, but the elevated cost of the equipment, the limited bandwidth of the pulsating valves, and their potential of making the system unstable (Kim et al. (2010)) have hindered the spread of this technology at industrial level (Hermann and Hoffmann (2005) is an example of application at full-scale).

Among the active control configurations, one often proposed is the modulation, through a pulsating valve, of the flow of a secondary injection of pure fuel into the core of the main flame. It has been observed that, in general, the presence of a diffusion flame in the combustion chamber of a premixed burner already represents a stability source for the system (Li et al. (2017b), Riazi et al. (2010), Choi, Tanahashi, and Miyauchi (2005), Shinjo et al. (2007), Tanahashi et al. (2004), García-Armingol et al. (2016)), although some works (Li et al. (2017b), Moeck et al. (2007)) have shown that there are cases in which a pilot fuel injection can support the instability. Moreover, a proper modulation of this injection can afford further reductions of the natural unstable mode by up to tens of decibels, through an out-of-phase oscillation of the heat released by the pilot flame (Guyot et al. (2007), Lee, Kim, and Santavicca (2000), Moeck et al. (2007), Tachibana et al. (2007), Lee and Santavicca (2003)).

In the implementation of this type of control, the acoustic impedance of the fuel feeding line between the pulsating valve and the combustion chamber plays a fundamental role (Auer et al. (2004)), since it determines the magnitude and phase of the flow velocity fluctuations at the combustion chamber inlet. Some authors have proposed to take advantage of this natural acoustic response of the fuel feeding line to replace the pulsating valve and using the dynamic pressure generated by the instability as the driving force to cause the final-desired effect, that is, the velocity fluctuations of the fuel flow. However, most of them applied this control to the main fuel line (Richards and Robey (2008), Richards, Straub, and Robey (2003a), Richards, Straub, and Robey (2001), Huber and Polifke (2008), Noiray et al. (2009)), whereas only Richards and coworkers (Richards and Yip (1995), Richards, Yip, and Gemmen (1995)) suggested the application of this control system to a secondary injection line. Still, in these works the secondary line is designed not to inject directly into the burner, but in the main, premixed air-fuel flow. Therefore, the mechanisms involved in the dynamics of the system are substantially different from the phenomena to consider for a pure-fuel flow directly injected into the combustion chamber. Auer et al. (2004), in their analysis of an active control modulating a pilot flame, characterized the response of the pilot line when the pulsating valve is not acting. The dynamic pressure obtained for two different impedances of the secondary line show considerable differences, demonstrating the importance of accounting for the acoustic properties of the pilot fuel line in order to properly design the control of the pulsating valve.

The purpose of the work is to explore a control system aimed at damping thermoacoustic instabilities in lean-premixed flames through the tuning of the acoustic impedance of a pure-fuel secondary line, which is directly injecting into the combustion chamber. This strategy has not been studied before in literature, at least to the authors' knowledge, so it can be considered as a substantially novel approach.

Since the whole control is composed of passive elements, systems like this have been generally classified by researchers in the passive group (Noiray et al. (2009)). Even if this classification is rigorously exact, in this case, the damping effect sought is identical to that achieved with active controls. Due to this connection, and despite its passive nature, this approach could be designated as "pseudo-active instability control" (PAIC). The rationale on which the PAIC approach and design are based is explained in the next section.

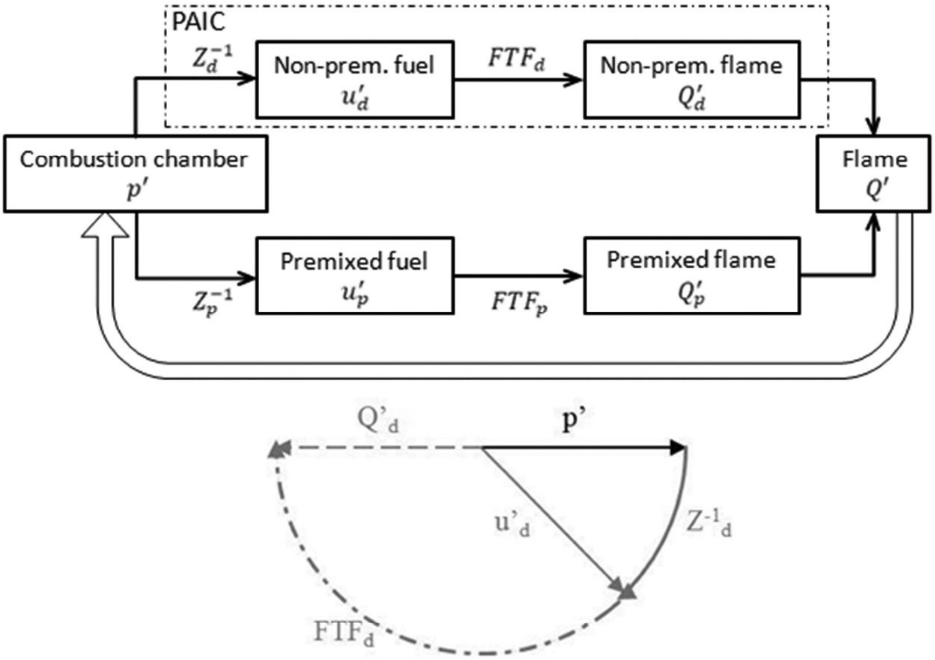

Figure 1. Conceptual diagram of PAIC (top) and ideal phase distribution (bottom).

Pseudo-active instability control

The logic of actuation of the PAIC system is sketched in Figure 1 (top), where FTF and Z^{-1} indicate, respectively, the flame transfer function and the inverse of the acoustic impedance (i.e., acoustic admittance) and the subscripts p and d refer to the main (premixed) and secondary (diffusion) fuel lines, respectively. The phasorial representation at the bottom of Figure 1 depicts the effect sought with PAIC: a heat release fluctuation from the diffusion flame Q'_d out-of-phase with respect to the dynamic pressure p'. This phase opposition will result, according to the Rayleigh criterion, in a reduction of the acoustic energy generated and, so, in a lower magnitude of the pressure fluctuation inside the combustion chamber. The Q'_d oscillation depends on the velocity fluctuation of the secondary fuel flow (u'_d) according to the dynamic response of the diffusion flame ($\mathrm{FTF_d}$). In PAIC, in contrast to active control, u'_d is not imposed by an external actuator but is spontaneously induced by the acoustic response of the pilot fuel line to the pressure fluctuation at the injection plane.

So, PAIC effectiveness strongly relies on a suitable combination of the acoustic response of both the secondary line and the diffusion flame. In particular, if the $\mathrm{FTF_d}$ characteristics (especially of the induced time delay) were known, an optimal value of Z_d^{-1} could be defined in order to induce a u'_d oscillation resulting in a secondary heat release out-of-phase with p'.

However, the determination of the dynamics of the secondary flame is not a trivial task. With the secondary injection located at the center of the burner, the final flame obtained is the combination of two, with a diffusion flame burning in the core of the main-premixed flame. No precedent or reliable experimental technique has been found that allows extracting the diffusion flame dynamics from the global one, and the interaction between the two flames makes their response completely different from the one observed if studied singularly. The problem becomes even more difficult for very small pilot flames. In this work, the pilot fuel accounts for only 1.7% or 2.7% of the total power, so that its dynamics is completely masked by the main flame. This problem has been tackled in some works using computational methods (e.g., Shinjo et al. (2007), Paschereit, Flohr, and Gutmark (2002)) and, recently, a model based on the G equation has been proposed by Li et al. (2017a) to predict the behavior of a flame similar to the one considered, with good results in the linear range, while predictions were not so precise for strong instabilities. It should be noted, however, that all these works focus on the global FTF and, hence, do not provide specific results for the $\mathrm{FTF_d}$. The knowledge available on the response of laminar non-premixed flames (see, e.g, Magina, Acharya, and Lieuwen (2019)) could also be useful to understand the dynamic behavior of pilot flames, although those results are not thought to be directly applicable for tiny pilot flames burning in the core of highly turbulent, swirl-stabilized premixed flames. In the authors' opinion, state-of-art CFD tools may allow extracting reliable data on the specific dynamics of small diffusion flames surrounded by a much larger premixed flame, but no precedent is known and it constitutes an objective well beyond the scope and possibilities of this investigation. As for this work, and given the lack of reliable methods to describe the dynamics of the pilot flame in limit cycle conditions, it was not possible to a priori design an optimal configuration of the PAIC system. Hence, an alternative strategy had to be devised, making use of all the experimental resources available for this study, to investigate the actual role of fluctuations in the pilot injection.

The effects achieved with a PAIC system will be analyzed in limit cycle conditions, with strong, self-sustained pressure fluctuations; the same operational condition will be tested without the pilot flame injection as a reference to compare the PAIC results. Due to the difficulties in describing the dynamic response of the diffusion flame, in this study the implementation of PAIC will be performed without *a priori* knowledge of $\mathrm{FTF_d}$. Apart from performing a parametric study to characterize the effects of PAIC on the strength of the limit cycle, further analyses will be attempted to identify the phenomena involved (which, as it will be discussed later, are not restricted to the mechanism described in Figure 1).

The next section describes the facility used to implement PAIC, the operational conditions selected to test the system and the instrumentation employed during the experiments. After that, the experimental results are presented and discussed. Finally, the main conclusions obtained are summarized.

Experimental method

Combustion rig and instrumentation

The PAIC system was implemented in an atmospheric, swirl-stabilized, premixed burner sketched in Figure 2. The primary fuel (pure methane) is supplied from a pressurized tank and online blended with the airflow conveyed by an air compressor; both mass flows are regulated by thermal mass flow controllers. The air-fuel mixture is injected into a plenum through two choked orifices which acoustically separate the feeding line from the rig; therefore, the main flame can be considered perfectly premixed, with constant equivalence ratio. The mixture flows into an annular duct where an axial swirler (theoretical swirl number, calculated from geometrical dimensions, S=0.48) is located 380 mm upstream of the dump plane. Combustion takes place in a cylindrical combustion chamber with its outlet open to the atmosphere. It is composed of a first, quartz-made section (220 mm in length), to allow optical access to the flame, followed by a second stainless steel section, for

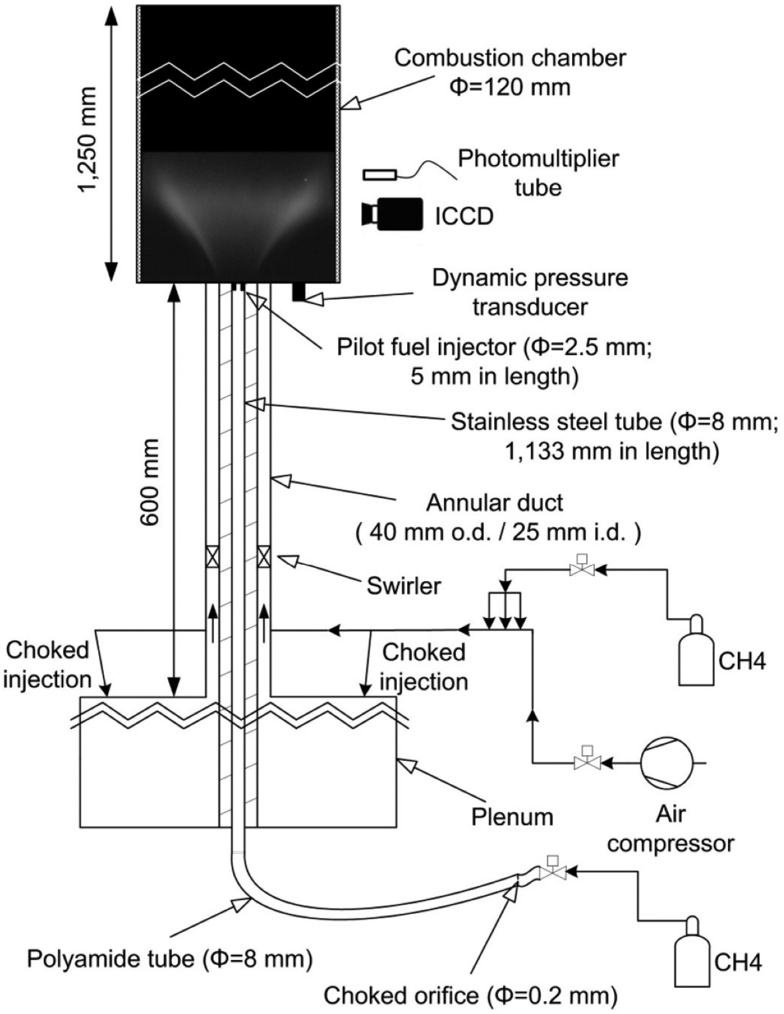

Figure 2. Combustion rig with PAIC implemented and the instrumentation used.

a total length of 1,250 mm. This length guarantees a strong limit cycle condition for premixed methane flames for a broad range of equivalence ratios.

A pressure transducer (PCB 103B02) is installed at the dump plane to record the dynamic pressure inside the combustion chamber of the rig. A photomultiplier tube (Hamamatsu H5784-03) fitted with a CH* filter (430 ± 5 nm) is positioned in front of the quartz section in such a way that its view angle included the whole flame; so the total instantaneous heat released by the flame can be measured. Also, an intensified CCD camera (Hamamatsu C8484-05) equipped with an OH* band-pass filter (310 ± 5 nm) is employed to record flame images. The time exposure is set at 80 μs, so that the flame images can be considered as instantaneous for the frequencies of interest. Chemiluminescence images were recorded with the ICCD camera for the OH* band and, in some cases, also with a band-pass filter centered at the CH* peak (431 nm), in order to explore if both methods provide different or complementary results. Since the OH*/CH* intensity ratio in diffusion flames is much lower than in premixed flames (Panoutsos, Hardalupas, and Taylor (2009)), CH* bandfiltered images could in principle contain more information on the diffusion flame. However, the patterns observed in both spectral bands were practically indistinguishable and did not reveal the presence of the diffusion flame at the root of the main, premixed flame. This is probably explained by the very low power of the secondary injection (1.7% for these tests). As usual in premixed flames, the intensity collected in the CH* band was lower than for OH*, resulting in a worse signal-to-noise ratio and, since CH* images did not provide additional information, the analysis will be based on OH* chemiluminescence maps. In fact, an important advantage of these is that they reliably reveal eventual changes in the main (premixed) flame, which is the driver of the thermo-acoustic oscillation (due to its low power, the contribution of the pilot flame to global heat release rate fluctuations is always much smaller than those due to the main flame).

The secondary fuel flow (V_d) was set to 0.05 and 0.08 Nm^3/h; this means only 1.7% and 2.7%, respectively, of the total thermal input in order to minimize eventual increments in NO_x emissions from the pilot (diffusion) flame. Experiments were carried out for three different equivalence ratios (Φ) of the primary flame: 0.98, 0.86, and 0.72, setting the primary fuel flow at 3 Nm^3/h (tests without pilot fuel, not shown here for brevity, confirmed that a change in the primary fuel flow does not affect sensibly the dynamics of the system). For each value of Φ, different lengths of the pilot fuel line were tested both with and without the secondary fuel flowing. For each condition, both instantaneous pressure and heat release rate were measured, respectively, by sampling the pressure transducer and the photomultiplier signals for 4 seconds at 4 kHz (16,000 data); each test was repeated twice, showing in all cases good repeatability (deviations always under 10%).

To analyze the flame shape and dynamics in some selected cases, 500 OH* bandfiltered images were recorded, at a frequency ~7 fps. Simultaneously to image acquisition, the $p\prime$ and Q' signals were registered at a higher sampling rate (20 kHz) and with a common time reference, in order to have the required time resolution to perform phase-conditioned analysis of the images along one oscillation cycle.

Design of the pilot fuel line

The secondary fuel line was designed with a geometry as simple as possible, in order to facilitate the study of its acoustic impedance. Its main elements are a chocked orifice, a duct of variable length, and an injector (see Figure 2), all with a circular cross-section. The pilot fuel is methane, supplied from a dedicated pressurized tank, and was automatically regulated with a mass flow controller. A small orifice (0.2 mm) was installed after the regulation valve. This orifice was designed to operate under choked conditions, on the one hand, to acoustically separate the feeding line from the facility and, on the other hand, to provide a well-defined acoustic boundary condition. Next, the fuel flows into the feeding line, which is composed of two pipes (both with 8 mm i.d.): a polyamide tube followed by a stainless steel one. In order to modify the acoustic properties of the pilot line, polyamide tubes with different lengths (1.3–2.1 m) were installed. The stainless steel pipe was an integral part of the central rod (see Figure 2) and had a fixed length of 1.133 m. Finally, an orifice of 5 mm in thickness and 2.5 mm in diameter discharges the fuel into the combustion chamber with a mean velocity of 3 and 4.8 m/s for 0.05 and 0.08 Nm3/h, respectively.

Since FTF_d is unknown, there is no possibility to a priori propose an optimized design of the geometry of the pilot line, according to Figure 1. In order to explore different situations, a range of geometries were defined with the following conditions for the acoustic admittance:

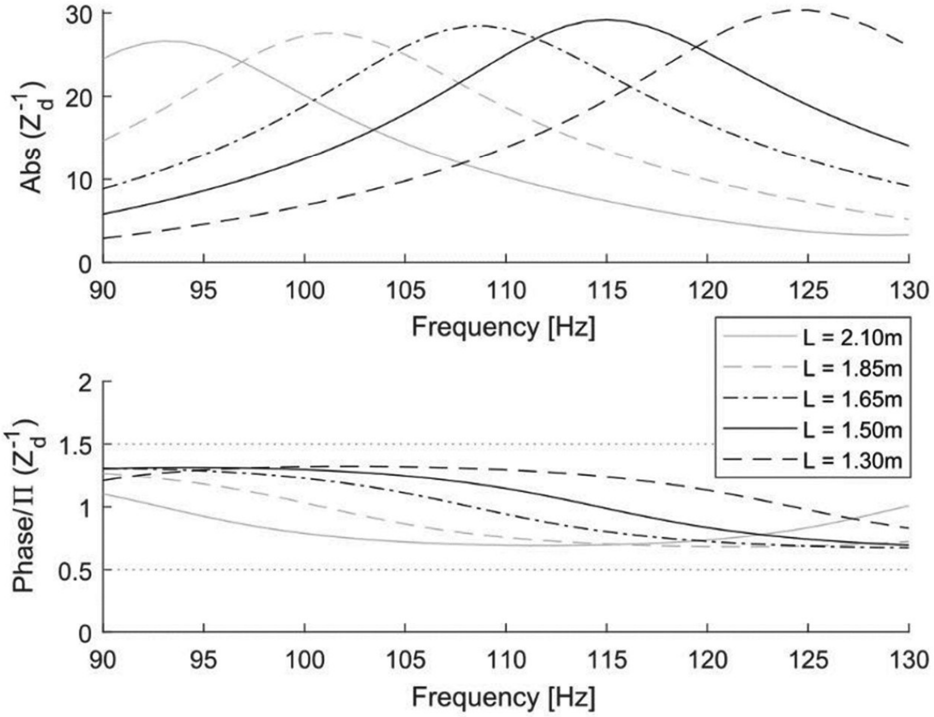

Figure 3. Z_d^{-1}curves for the five values of *L* in the neighborhood of 110 Hz.

The modulus of Z_d^{-1} should be high, to maximize the amplitude of the velocity fluctuations at the injector.

The Z_d^{-1} phase should cover most of the physically possible range (180°, as shown in the Appendix), to analyze the effect of the time delay between p' and u_d'.

The modifiable parameter was the length of the polyamide tube, *L*. The acoustic admittance of the whole pilot fuel line was calculated with the 1-D acoustic network model described in the Appendix, which was also experimentally validated by measuring fluctuations in injection velocity with hot wire anemometry. Even though similar measurements could not be performed during the combustion tests, the good match obtained between experimental data and predictions (see the Appendix) supports the reliability of the 1-D model to calculate pilot fuel fluctuations also in the presence of flame. The lengths of the polyamide tube selected to satisfy the two conditions indicated above were 1.30, 1.50, 1.65, 1.85, and 2.10 m. The corresponding calculated curves of Z_d^{-1} as a function of frequency are represented in Figure 3. The plot is centered at 110 Hz, which is very close to the unstable frequencies of the combustion rig (with slight variations as a function of the equivalence ratio). For this frequency, the chosen lengths satisfy the criteria defined above for Z_d^{-1}, i.e., high absolute value and large phase range covered. Table 1 lists the limit cycle frequencies experimentally obtained for each operational condition. All frequencies are very close to 110 Hz, so the range of impedances fulfills the criteria mentioned above. Due to the lack of information about $\mathrm{FTF_d}$, the methodology through which the set of lengths has been defined is thought to constitute a comprehensive test matrix that allows achieving solid conclusions about the dynamic effects induced by PAIC.

Table 1. Limit cycle frequency (in Hz) obtained for each experimental condition.

		V_d=0 Nm^3/h			V_d=0.05 Nm^3/h			V_d=0.08 Nm^3/h		
	Φ	0.98	0.86	0.72	0.98	0.86	0.72	0.98	0.86	0.72
L [m]	2.10	110.9	109.8	105.9	112.1	111.5	107.3	111.8	111.5	107.6
	1.85	112.4	111.0	105.8	113.0	112.4	108.0	113.1	112.1	108.8
	1.65	113.5	111.8	106.3	112.8	112.5	109.3	112.8	112.4	109.5
	1.50	113.6	112.5	106.8	112.5	112.3	109.1	112.9	112.1	109.9
	1.30	113.1	112.5	107.1	112.6	112.1	110.3	112.6	111.8	110.1

Results and discussion

Description of limit cycle conditions

Before analyzing the effects of PAIC on the instability, it is worth describing the general features of the limit cycle condition reached in the facility for the tests carried out. The spectra of both p' and Q' signals are shown in Figure 4 for Φ=0.72 without secondary injection. The p' spectrum shows a well-defined, strong peak at ~110 Hz, with an amplitude >2,200 Pa (i.e. >2.2% of the mean pressure). The Q' spectrum exhibits the same dominant mode and its harmonics, symptom of a non-linear response of the flame (mostly due to the

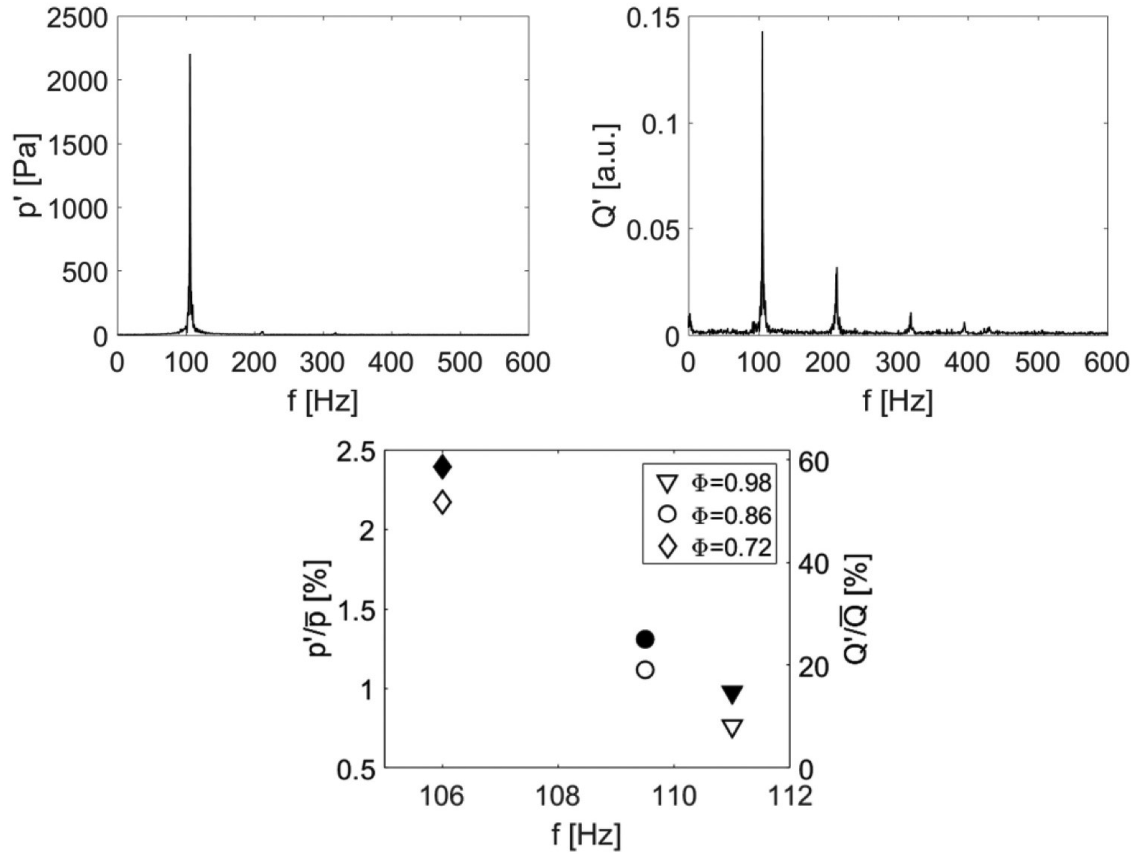

Figure 4. Top: Spectrum of p' (left) and Q' (right) signal for Φ=0.72 with no secondary fuel injection. Bottom: normalized values of the peak magnitudes and frequencies of both p' (hollow markers) and Q' (solid markers) with Φ.

saturation of the flame response (Dowling and Stow (2003a), Lieuwen (2003))), typical of limit cycle situations.

The variation of $p\prime$ amplitude and frequency with Φ, in absence of pilot flame, is represented in Figure 4c (normalized with respect to the ambient pressure). The plot evidences that leaner flames yield unstable modes with lower frequency and higher pressure amplitudes. In a first approximation, frequency variations can be directly linked with the combustion chamber temperature (Richecoeur et al. (2013), Lamraoui et al. (2011)), so the evolution obtained is coherent with the final temperature reached with a richer/leaner mixture (quantification is not easy though, due to the variation of the temperature along the chamber length). The frequency and magnitude of the dominant peak of the $Q\prime$ spectrum evolve consequently, as also shown in Figure 4c.

Richer information about the characteristics of the flames studied can be extracted from flame intensity maps, obtained by post-processing the 500 band-filtered OH* images recorded for each condition. Both the average and rms values of the local intensity (designated, respectively, as $\bar{I}_x$ and $\sigma(I_x)$) released at two different equivalence ratios (Φ=0.98 and 0.72) are shown in Figure 5. An increment of the airflow rate, from Φ=0.98 to 0.72, displaces the main reaction zone downstream, making the flame longer and slightly wider, with a long upstream zone characterized by a weak emission. As a result of this elongation, the average flame shape is altered and changes from a V-shaped flame into a trumpet one (Terhaar, Oberleithner, and Paschereit (2015), Terhaart, Krüger, and Oliver (2014)). Moreover, the peak intensity decreases with Φ, an effect already documented in

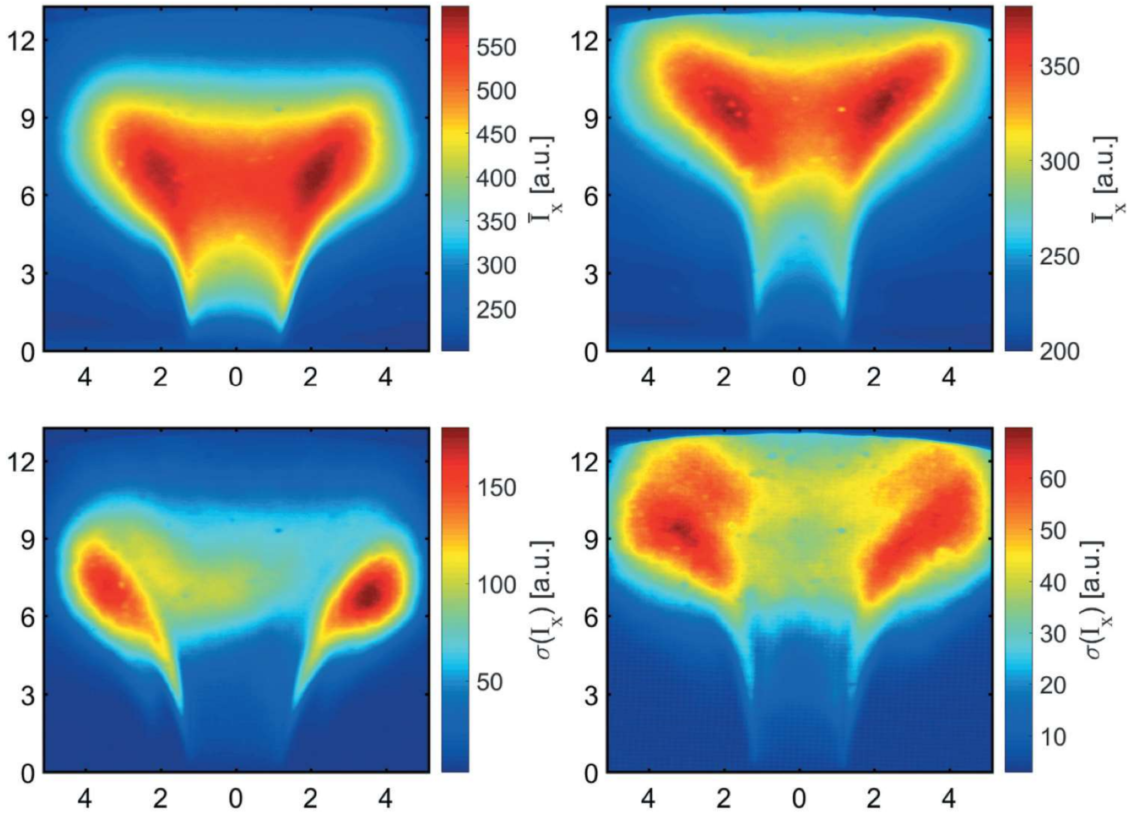

Figure 5. Mean intensity (top row) and standard deviation (bottom row) maps obtained for Φ=0.98 (left) and Φ=0.72 (right) without secondary fuel injection. Axes scale in cm.

various studies (García-Armingol, Ballester, and Smolarz (2013), Hardalupas and Orain (2004), Ballester et al. (2009)).

Fluctuation maps (bottom row of Figure 5) highlight that most of the heat release oscillation takes place at the tip of the flame, in the outer edge of the main reaction zone. For the richer flame (Φ=0.98), the peak areas are much smaller, whereas the amplitude of the fluctuations is greater than for the ones shown for leaner conditions (Φ=0.72). These behaviors were observed for changes in airflow rate and fixed fuel flow. The results could be somewhat different if Φ is changed for fixed airflow rate (i.e., constant injection velocity). In any case, this is not relevant here, since the purpose is simply to describe the baseline conditions before adding pilot fuel.

A better insight into the phenomena involved in the thermoacoustic coupling between the flame and the facility can be gained by studying the sequence along one oscillation cycle by means of phase conditional analysis of the images. The images were phase-locked taking $p\prime$ as the reference signal; the pressure cycle was divided into 34 slots (10.6^0 width), with a minimum of 12 images per phase interval. The average of these image subsets are presented in Figure 6 for the test at Φ=0.98 without secondary injection; for brevity, only multiples of 45^0 are shown.

Figure 6 clearly shows that the main fluctuation of the heat release rate is localized in the downstream region of the flame, which gives as a result the peak areas observed above in the fluctuation maps (Figure 5). This oscillation corresponds to a tip motion beginning at 45^0, where the flame starts to roll itself up toward the outer zone. This wrapped region moves downstream, increasing its intensity and size along the cycle, until 180^0. Here the structure gradually unwinds and the flame gets its original V shape back, up to 0^0, where the cycle starts over.

The flapping motion described is due to vortical structures shed at the dump plane and convected downstream, which disturb the V flame sheet along their convective travel. This vortex shedding phenomenon, and the consequent dynamics, has been observed also for the other Φ values tested and recognized in various works (e.g., Durox, Schuller, and Candel (2005), Candel (2002), Durox et al. (2009), Palies et al. (2010), Bellows et al. (2007), Palies et al. (2009), Balachandran et al. (2005)) as one of the main mechanisms responsible of generating combustion instabilities. So, vortex shedding is considered the primary cause of the limit cycle obtained for the cases analyzed.

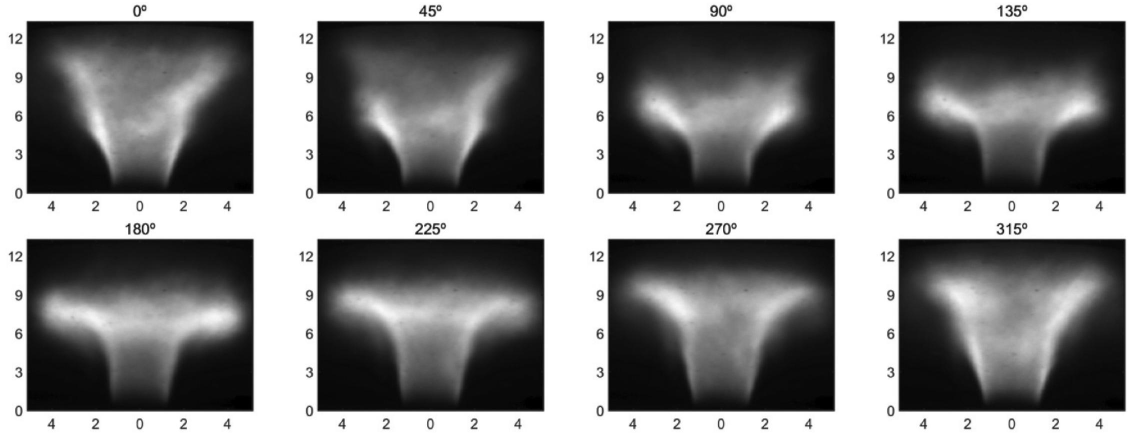

Figure 6. Average chemiluminescence maps along the pressure cycle every 45^0; Φ=0.98, no pilot flame.

Effects of PAIC implementation

In this section, the changes observed on both the amplitude of the dynamic pressure and on the flame structure and dynamics will be discussed. In order to assess the effect of the PAIC method, the test matrix includes different tube lengths (see Table 1), operating with and without pilot fuel injection. Figure 7 displays the ratio between the amplitude of p' with V_d=0.05 m^3/h, designated as $p'_{0.05}$ and the value obtained without any secondary fuel, p'_0, for different tube lengths and equivalence ratios and keeping constant all other conditions. Values of this ratio below 1 indicate that the addition of some pilot fuel through the central orifice effectively damps the oscillations, whereas ratios above 1 indicate that it further feeds the instability. According to the mechanisms initially postulated, this range of behaviors is consistent with the dynamic interaction between the pilot and main flames being either constructive or destructive.

Figure 7 clearly demonstrates that the secondary fuel can have significant effects on the amplitude of the limit cycle, even for the very small amount used (only 1.7% of the fuel fed to the main flame). The effect of the pilot fuel is very different for the various equivalence ratios tested and, hence, depending on the properties of the main flame: the variations are very small for Φ=0.72, significant reductions are achieved in most cases for Φ=0.86 and both positive and negative variations can be obtained for Φ=0.98, indicating that the addition of pilot fuel can either damp or amplify the limit cycle depending on the geometry of the injection line. These outcomes will be further analyzed below, but several clear and important conclusions can be derived from Figure 7:

The results shown in Figure 7 directly measure the stabilizing/destabilizing effect of the pilot fuel, independently of other possible mechanisms (e.g., purely acoustic damping, as discussed below), which are kept constant for each pair of cases involved in the ratios shown.

The fact that the pressure ratio significantly varies with L for a fixed fuel flow rate clearly demonstrates that the effects observed should not be ascribed to the well-known stabilizing

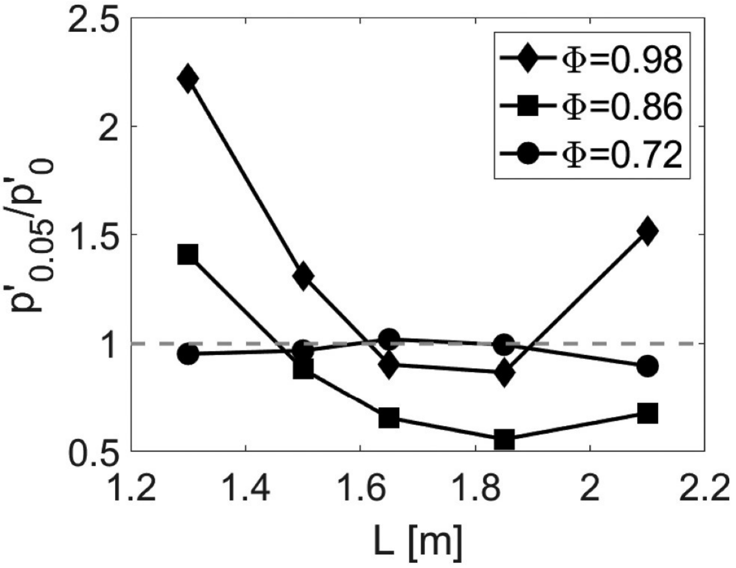

Figure 7. Ratio between p' amplitudes measured with V_d=0.05 and 0 m^3/h, for different equivalence ratios, as a function of the length of the pilot fuel injection.

effect of pilot flames. The variations due to changes in the tube length can only be due to the modifications of the acoustic properties of the injection line and the consequent dynamic response of the pilot flame.

The same applies for the cases in which an amplification of the dynamic pressure is observed. These variations cannot be ascribed to the simple presence of the pilot flame, but can only be the consequence of a dynamic interaction between the two flames.

All these conclusions are fully consistent with the rationale proposed for the 'pseudo-active' concept proposed here and confirm that this approach may be used to modify the dynamic behavior of premixed flames. Once the PAIC scheme has been verified to induce significant modifications in amplitude of the oscillations, different analyses were performed as an attempt to determine the roles of the different variables and mechanisms in the effects observed.

According to the block diagram proposed in Figure 1, the system behavior strongly depends on the flame transfer function of the pilot flame. Unfortunately, for this configuration, it was not possible to describe in detail the intrinsic dynamic response of the diffusion flame and it was necessary to devise some alternative approach to gain some insight on the role of the different parameters and mechanisms. In particular, the parametric study conducted for different lengths of the injection line proved to be an effective approach for investigating the performance of PAIC. The results are analyzed in terms of p' magnitudes versus the phase of Z_d^{-1} (which decreases with the polyamide tube length) in Figure 8, where the cases with pilot fuel (1.7% or 2.7% of total power) are compared with the same configuration without the secondary injection. The differences in the phase of Z_d^{-1} for the cases with and without pilot flame are due to slight variations of the limit cycle frequency, as it can be seen in Table 1.

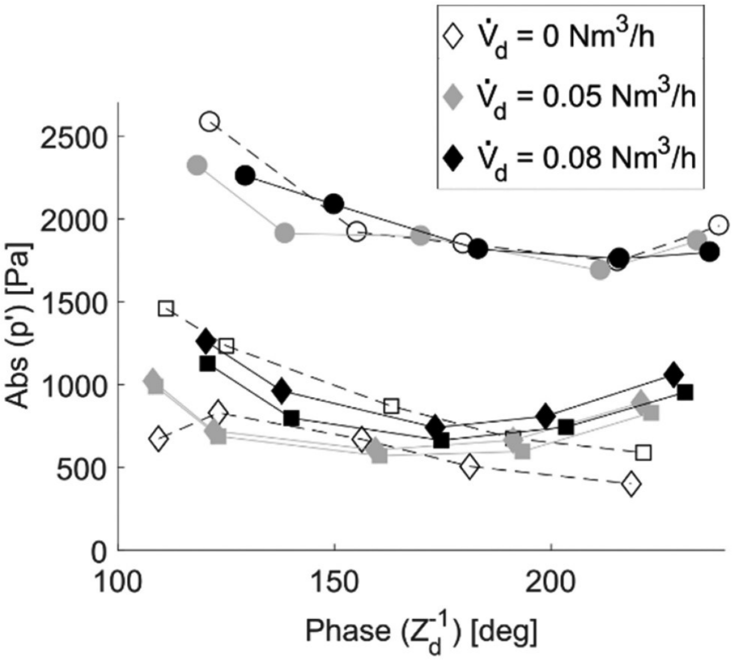

Figure 8. Peak value of p' vs. the phase of Z_d^{-1}. Test conditions identified by shape and color of the symbols: white/grey/black for 0/0.05/0.08 Nm^3/h; ○/□/◊ for Φ=0.72/0.86/0.98.

As it was noted for Figure 7, the results shown in Figure 8 clearly demonstrate that the pilot fuel does not act as a stabilizing agent for lean flames (Φ=0.72), which is the effect sought in some cases where the objective is to extend the lean static stability limit. However, this is not the primary objective of this work which, instead, is aimed at using the secondary injection to modify the characteristics of thermo-acoustic instabilities. As it has been observed above, significant variations in pressure amplitude are achieved over the range explored for the phase of Z_d^{-1}. The highest instability damping was observed for the cases with phases around the middle of this interval (corresponding to intermediate lengths in Figure 7). On the contrary, the fuel injection has a destabilizing effect for Φ=0.86 and, especially, for Φ=0.98 when the shortest tube, with the highest Z_d^{-1} phase, was installed. Wider differences in *p'* might have been obtained if it was feasible to cover a wider range of admittance phases (which, as it has been shown, is physically limited) or for different values of the FTF_d phase (for which no data are available).

The curves for Φ=0.72 display some peculiar behaviors. In the first place, the injection of pilot fuel has a negligible effect on the amplitude of the limit cycle (see Figure 7 and Figure 8). In the second place, the case without pilot fuel injection also displays some changes in p', with a difference of 32% between the peak value obtained for L=2.1 m and the lowest value recorded for L=1.6 m. These effects cannot be ascribed to the effect sought with the PAIC strategy. Repeated tests consistently confirmed the variations is p' observed in Figure 8 for cases without pilot fuel. Also, in order to discard other hidden interferences (e.g., in the feeding of main fuel due to the presence of the pilot line), the tests were repeated with the central orifice plugged. Those cases yielded negligible variations (well below the reported experimental repeatability of 10%) in p' for different tube lengths, which allowed to discard experimental artifacts, and further confirmed that the results shown in Figure 8 are meaningful and demonstrate that, besides the effect of the PAIC strategy, the presence of the orifice also has some effect on p'. This could be due to some kind of fluid-dynamic disturbance of the flow caused by the fluctuating velocity at the orifice or to passive acoustic interactions. Some further analyses were accomplished to assess the possible role of the different mechanisms.

In conclusion, the results clearly demonstrated that the dynamic interaction with the pilot fuel, which is the basis of the PAIC concept, has a significant effect on the amplitude of the pressure limit. As shown in Figure 7, a proper design can effectively damp the pressure fluctuations, whereas in other cases the instability might be amplified. Besides, the variations in p' observed with no pilot fuel revealed the presence of additional effects, which are thought to have a fluid-dynamic or a purely acoustic origin. In order to further investigate the role of the different phenomena involved, the cases with and without pilot fuel are separately analyzed in the following sections.

Analysis of the interaction with the pilot flame

The differences observed in Figure 8 between cases with and without pilot fuel for Φ=0.98 and 0.86 can only be ascribed to the interaction between the main and pilot flames. As an attempt to search for some evidence of that interaction, OH* chemiluminescence images are analyzed and compared for the same configuration, with secondary fuel switched on and off.

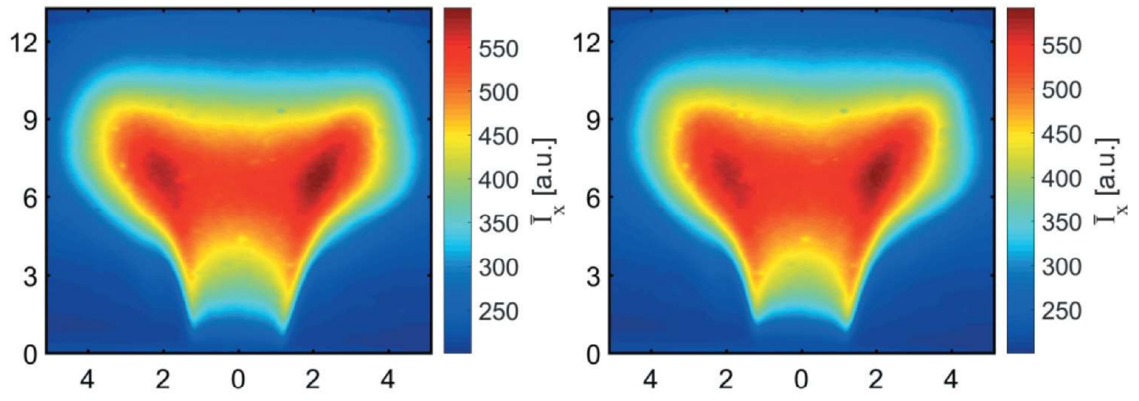

Figure 9. Average OH* intensity maps at Φ=0.98, without (left) and with (right) pilot fuel injection.

As it was mentioned before, the chemiluminescence of the pilot (diffusion) flame is not visible in the bandfiltered OH* images collected with the ICCD. This fact can be appreciated in the mean intensity maps of Figure 9, with negligible differences in flame shape and heat release distribution between both images. Therefore, the chemiluminescence images shown should be interpreted in terms of heat release rate and dynamics of the main premixed flame.

The images recorded were processed in several different ways, obtaining various flame maps each one highlighting different dynamic characteristics of the flames investigated. However, the final result was, for most of the maps, the same: no relevant differences could be spotted between the cases with and without pilot fuel in maps showing the standard deviation of intensity at each pixel or in the spatial distribution of the local Rayleigh index, calculated by synchronizing the images with p' (assumed constant over the flame volume), and, so, these maps are not included for brevity. Only the cross-correlation (CC) maps showed some difference worth of further analysis. The cross-correlation method has been recently proposed (Luciano and Ballester (2018)) as a simple yet effective procedure to study the dynamic response of flames. Cross-correlation maps represent the average cross-correlation function for zero time lag between the heat release rate measured the whole flame, Q', and that measured locally. Luciano and Ballester (2018) demonstrated that CC maps directly identify the flame parcels which contribute to the global fluctuation of the heat release rate (i.e. they fluctuate in-phase with Q') and those which tend to damp the main heat oscillation (i.e. with oscillation out-of-phase with Q'). Typically, CC maps contain regions with positive and negative values (i.e., with positive and negative contributions to Q'), as well as regions with negligible values which do not contribute to the global response of the flame. As for the maps reported here (Figure 10), it must be clarified that the absolute values are not meaningful but the spatial distribution reveals the relative contribution of the different flame regions to the global dynamic response. Due to length limitations, the interested reader is referred to the article by Luciano and Ballester (2018) for further details.

The CC maps obtained for the tests performed at Φ=0.98 are shown in Figure 10 for L=2.10, 1.50 and 1.30 m, since these three cases present some differences in p' values between tests with and without pilot fuel (in Figure 8, the leftmost point and the last two ones in the diamond-marked curves, respectively). The flame base displays almost null CC values in the cases without secondary injection, indicating negligible contributions of these

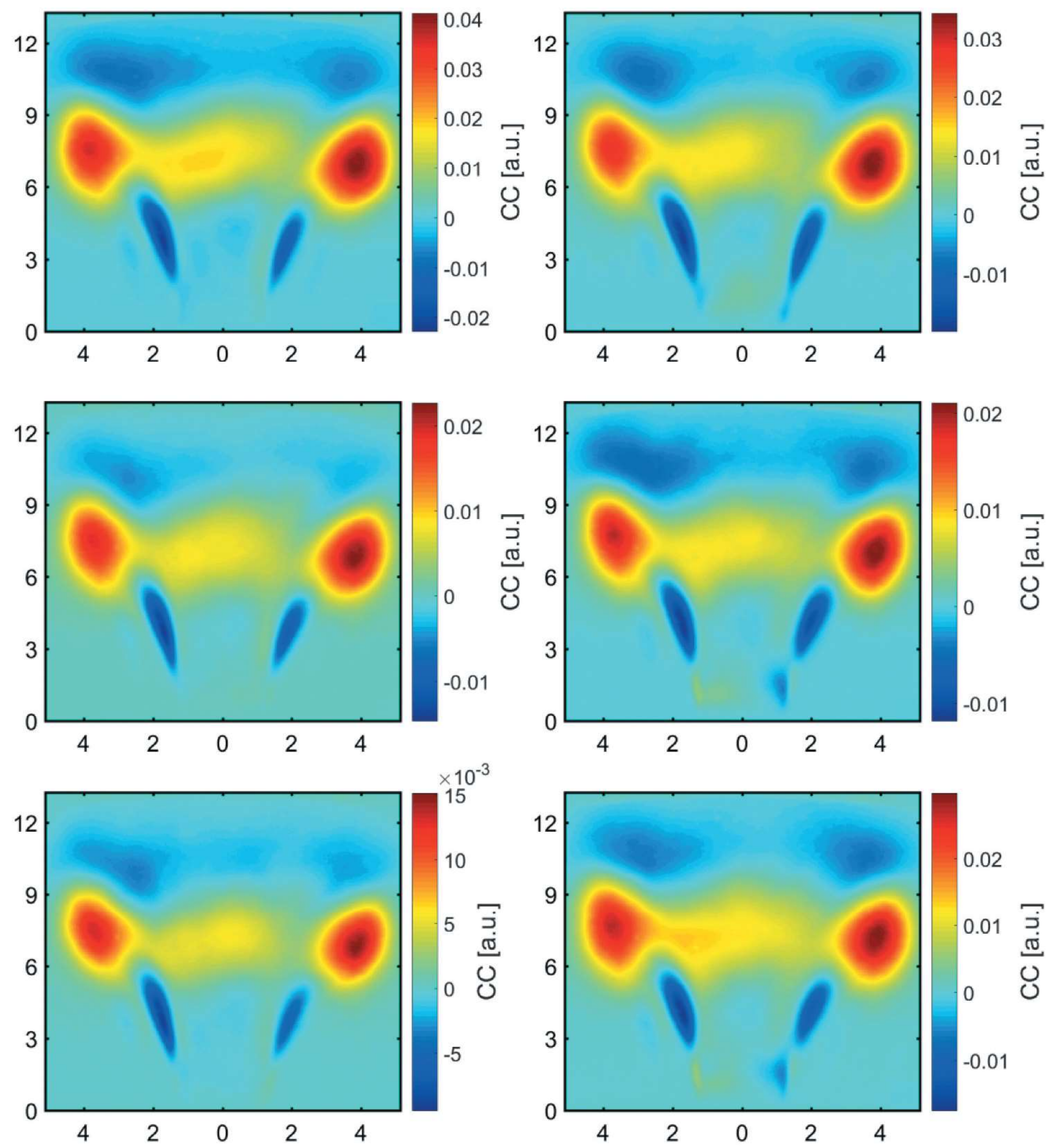

Figure 10. Cross-correlation maps at Φ=0.98 for different tube lengths, from top to bottom: L= 2.1, 1.85, 1.5 and 1.3 m. Left: no pilot flame; right: V_d=0.05 Nm^3/h.

areas to global Q'. On the contrary, non-zero values are observed at those regions in the images with pilot flame, so highlighting flame areas which are coupled (constructively or destructively, for positive or negative values, respectively) with the global heat release oscillation. Even though the differences are slight, they consistently appeared in those cases and can only be attributed to an oscillation induced by the presence of the diffusion flame in that zone. For the shortest lengths tested (L=1.50 and 1.30 m) the spots enhanced at the injection plane display opposite signs, which could reveal precession-related phenomena in that area. For L=2.10 m this antisymmetric pattern is not apparent; instead, compared to the case with no secondary fuel, the presence of the pilot flame seems to cause an elongation of the negative spots aligned with the V flame. For L=1.65 and 1.85 m (for 1.85 m see the second row of Figure 11), the maps with and without secondary fuel are

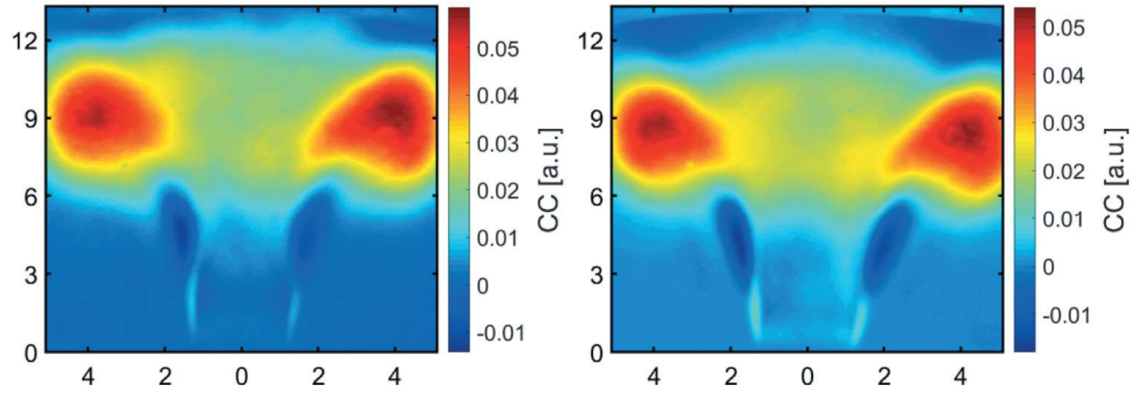

Figure 11. Cross-correlation maps for Φ=0.72 L=1.3 m. Left: no pilot flame; right: V_d=0.05 Nm^3/h.

practically identical. In these cases, the p' amplitudes obtained are almost the same irrespectively of the presence of the diffusion flame, evidencing a weak contribution of the pilot flame for these values of Z_d^{-1}. The same happens for Φ=0.72 (Figure 11), for which the dynamic influence of the pilot flame appears negligible (only results for one pipe length are reported for Φ=0.72, since CC maps for all other L are practically identical). In conclusion, there seems to be a clear correlation between the effect of the pilot fuel on the amplitude of the limit cycle and the changes, although modest, at the flame base, where the interaction between the pilot and main flames seems to be concentrated.

The vortex shedding phenomenon, whose effects govern the main flame dynamics, surely masks the fluctuations induced by the pilot flame, due to the very different magnitude of the heat release fluctuations involved. Nevertheless, as shown by Figure 8, the dynamic interaction between the tiny pilot flame (only 1.7% of the power) and the main premixed flame is able to considerably modify the thermoacoustic coupling, increasing the peak p' up to a factor of 2 in some cases (namely, for the shortest lengths at Φ=0.98, corresponding to highest Z_d^{-1} phases) or strongly reducing the limit cycle amplitude in some others (tests at Φ=0.86 for the lowest values of Z_d^{-1}, associated to the longest polyamide tubes). Moreover, the addition of pilot fuel should not be expected to induce the same variation in p' for all configurations of the pilot line, since the patterns obtained in Figure 8 varying Z_d^{-1} are quite different for the cases with and without a secondary fuel injection. Therefore, the passive modulation of a pilot flame shows the potential to attain the effect sought with PAIC, but a deeper analysis of the interaction between the system and the burner is needed, in order to reliably conduct the p' amplitude toward the desired state (i.e. lower limit cycle amplitudes or even stable conditions). An important difficulty in this regard is the lack of information on the transfer function of the pilot flame, in particular its phase. The selection of lengths successfully led to a wide range of Z_d^{-1} phases (close to 180°, which as demonstrated in the Appendix is the theoretical broadest interval), leading to variations of different sign in p' for the different cases. According to the PAIC scheme explained in a previous section, the different behaviors should be ascribed to the occurrence of either constructive or destructive interaction between the pilot and premixed flames, depending on the phase between $p\prime$ and Q' (see Figure 1).

As mentioned before, the curves shown in Figure 8 suggest that changes in limit cycle strength are the outcome of several effects of different origin. For the curves at Φ=0.98 and

0.86, with no pilot fuel injected, the observed monotonic decrease of p' with the Z_d^{-1} phase can only be ascribed to either fluid dynamic or acoustic interactions between the flame and the pilot line. The additional effects induced by the presence of the pilot flame cannot be isolated but are superimposed when the secondary fuel is injected, leading to a different evolution of p' with the phase of Z_d^{-1}. If the global effect can be assumed to correspond to the superposition of different mechanisms, the comparison between both test series (with and without pilot fuel) could provide some hints on the part of p' variations which are caused by the flame. For example, for Φ=0.98, the fluctuations in heat release from the pilot flame seem to amplify the oscillations at both ends of the interval tested, whereas reduction in the Z_d^{-1} phases leads to a significant damping for Φ=0.98. Nevertheless, this is only a tentative deduction and further work is needed to confirm these conclusions as well as if the superposition principle is actually applicable in these situations. In other cases like Φ=0.72, however, the injection of pilot fuel does not seem to entail any appreciable effect. This might be due to an enhanced dispersion of the pilot fuel before burning. In fact, the luminosity of the flame near the injection was reduced as the flame becomes leaner, which also causes a delayed ignition of the non-premixed fuel, so that it can be entrained into the main jet and its combustion is thought to take place, at least partially, in premixed mode. Some attempts were made to determine the magnitude and location of fluctuations in heat release rate due to the pilot fuel from chemiluminescence signals. However, the results were not conclusive, due to the very small amount of pilot fuel, which makes it difficult to identify distinct local increase in radiation, which could be ascribed to the pilot fuel, from the much stronger signal due to the main premixed fuel. Nevertheless, although only of qualitative value, the visual observations clearly point to an enhanced dispersion of the pilot fuel as Φ decreased. It is then reasonable propose that the mode in which this fuel is burnt (diffusion or premixed flame) can explain the much weaker effect of PAIC for leaner conditions. Quantifying this difference and, in general, characterizing the specific dynamic response of the pilot flame (in terms of FTF_d) appears as a challenging and relevant objective, not only for research related to PAIC but also for a better understanding of the interaction between the main flame and the pilot fuel in the more general case. However, this would require specific diagnostic methods and a more focused investigation on this particular matter, which is clearly beyond the scope and possibilities of this work.

The possibility of a fluid-dynamic interaction between the pilot fuel jet and the main flame has been also mentioned above. However, this is not supported by the data obtained. In fact, no variation in the flame pattern is observed among the maps in the left column of Figure 10, when no pilot fuel is injected.

Effects due to the variation of L with no diffusion flame

The results shown in the previous section, especially those without pilot fuel, suggest that other effects not involving combustion are superimposed on the PAIC scheme initially proposed (as outlined in Figure 1). The observed variations in p'in absence of secondary fuel injection clearly point to a purely acoustic interaction with the pilot fuel injector. A first hypothesis is that the secondary injection line acts as a tunable resonator, causing losses in acoustic energy which depend on its geometry (pipe length). Some calculations were attempted to verify the plausibility of this interpretation.

The acoustic losses caused by the pilot injection line, Σ can be calculated as the acoustic energy flux across the orifice:

$$\Sigma = \frac{1}{T}\int_T\int_{S_d} p'(t)u_d'(t).dSdt \approx -\frac{p'u_d'}{2}\cos\left(\angle p'u_d'\right)S_d = -\frac{1}{2}\frac{p'^2}{\bar{\rho}\bar{c}}\Re\left(Z_d^{-1}\right)S_d \qquad (1)$$

where p' and u_d' are, respectively, the pressure oscillation at the dump plane (assumed constant over the cross-section of the combustion chamber) and the velocity fluctuation at the orifice (both supposed as harmonic oscillations), S_d is the cross-sectional area of the injector and $\angle p'u_d'$is the phase between both variables. From the definition of the acoustic admittance, it can be easily deduced that the cosine can be expressed as its real part, $\mathrm{Re}\left(Z_d^{-1}\right)$. Therefore, the acoustic losses can be estimated for each geometry (with known Z_d^{-1}, see Appendix) from the pressure fluctuation measured at the dump plane, p'.

For the experiments carried out (both with and without diffusion flame), Eq. (1) has been applied considering the whole injection line full of pure methane at ambient temperature. Although some gas from the combustion chamber could be ingested into the injection line, this is a suitable approximation, since the possible deviations caused by the variation in chemical properties are negligible. Some uncertainties must be admitted in the estimated values of u_d', due, for example, to the assumption of a constant velocity at the injection orifice, so neglecting effects of the boundary layer which may be important for small orifices. However, an exact estimation of Σ is not necessary for the aim of this study, which is just to assess whether the order of magnitude of these losses could sensibly affect the p' amplitude.

The estimated Σ values range between almost zero losses and values around 1 W, depending on the operational condition and, of course, on the value of Z_d^{-1}. Therefore, some fraction of the acoustic energy generated in the combustion chamber is expected to dissipate in the pilot line. However, given the large difference in the cross-sectional area of both cavities (diameter 2.5 mm vs. 120 mm), it is not obvious whether this acoustic interaction could be strong enough to cause measurable variations in p'. In order to determine if these acoustic losses can be significant and affect the amplitude of the limit cycle, its magnitude is compared to the generation of acoustic energy from the flame. The acoustic source term, E, can be calculated as (Dowling and Morgans (2005)):

$$E = \frac{1}{T}\int_T\int_V \frac{(\gamma-1)p'(t)q'(t)}{\bar{\rho}\bar{c}^2}.dVdt \approx \frac{P'Q'}{2}\cos(\angle p'Q')\frac{\gamma-1}{\bar{\rho}\bar{c}^2} \qquad (2)$$

where q' represents the heat fluctuation released per unit of volume (also considered harmonic in time), V the flame volume and γ the specific heat capacities ratio. Assuming that the flame is acoustically compact, p'can be considered constant over the flame volume and the integral can be approximated as shown in the right hand side of Eq. (2). The source term can be estimated for the different tests from the values of p' and Q' measured with the microphones and photomultiplier. The thermodynamic parameters are calculated for the combustion products at the adiabatic flame temperature. Equation (2) was applied with the values measured for the different tests, yielding estimated values of E below 10 W. Since these values are of the order of magnitude of the acoustic losses at the orifice (Σ could reach 10% of E) and the existence of other energy sinks (dissipation, loss through the boundaries), the effect of the injector is not negligible but may play a significant role in the acoustic balance in the combustion chamber, so modifying the limit cycle amplitude.

As an additional verification, the relationship between limit cycle amplitudes reached and the estimated acoustic losses has been explored for a wide range of cases. The results are analyzed in terms of the acoustic losses normalized byp'^2. The acoustic dissipation tends to reduce the acoustic energy and, at the same time, is proportional to p'^2 (see Eq. (1)). So, the actual dissipative performance of the pilot line is not correctly quantified by the absolute dissipation, but is better expressed by the normalized value, which is independent of the equilibrium pressure reached inside the combustion chamber. According to Eq. (1), the normalized dissipation, (Σ/p'^2), is proportional to $-\mathrm{Re}\left(Z_d^{-1}\right)$, with a proportionality factor constant for all cases. Figure 12 represents the pressure fluctuation reached for different tests as a function of $-\mathrm{Re}\left(Z_d^{-1}\right)$ (this is a positive magnitude, since $\mathrm{Re}\left(Z_d^{-1}\right)$ is negative for a passive system, as shown in the Appendix), indicative of the magnitude of the normalized dissipation for the various tube lengths. The set of data includes the different acoustic admittances tested, with different amounts of pilot fuel (0, 0.05, 0.08 Nm^3/h of methane). The graphs clearly show an inverse relationship, i.e. the amplitude of the limit cycle is consistently reduced as the normalized acoustic losses at the pilot line increase. This correlation is more apparent for Φ=0.72, which agrees with the discussion of the previous section, concluding that the pilot flame seemed to be not so relevant in this case, while the pilot fuel acquires more importance for richer flames. The data appear more scattered for Φ=0.86 (the R^2 coefficient from a polynomial fitting was 0.54, significantly lower than the value of 0.82 obtained for Φ=0.72), since the limit cycle is thought to be more affected by the presence of the pilot flame, making the acoustic interaction less evident; nevertheless, the results still show a clear negative correlation also in this case. The data obtained for Φ=0.98 present a similar pattern to that displayed for Φ=0.86 (and, so, they are not shown for brevity), since, also in this case, the dynamic interaction between the pilot and the main flame is not negligible and superposed to the pure acoustic interaction.

In order to exclude that some thermal and/or fluid-dynamic effects could be the actual responsible for the p' variation in absence of the secondary flame, some additional experiments were carried out in cold conditions. In these tests, the length of the combustion chamber was 750 mm, with a resonant frequency at an ambient temperature of 100 Hz, very close to the frequency obtained in limit cycle conditions as well as to the range for which the pilot line impedances were designed. External excitation was provided with two loudspeakers (10”,

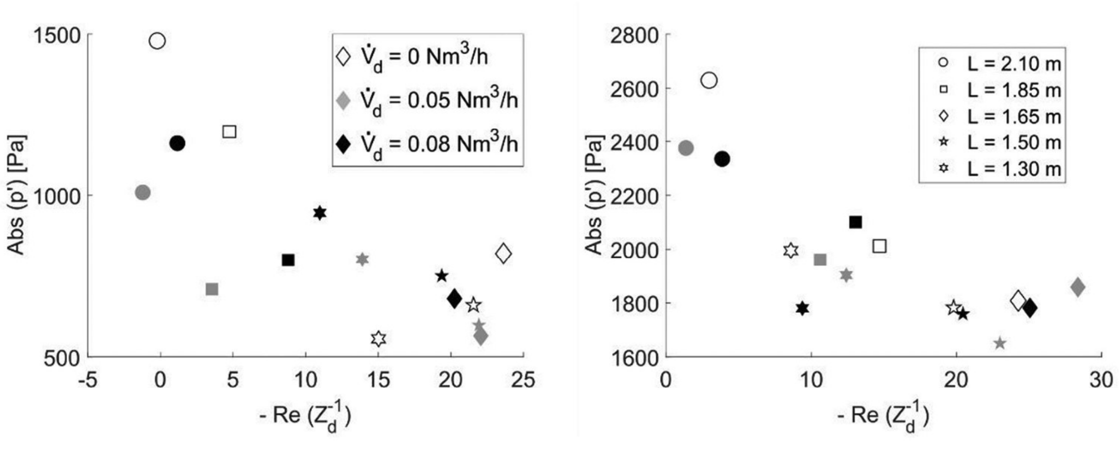

Figure 12. Amplitude of the limit cycle with normalized acoustic losses, as a function of the flow rate of pilot fuel and tube lengths (denoted, respectively, by the different colors and symbols). Left:Φ=0.86, Right: Φ=0.72.

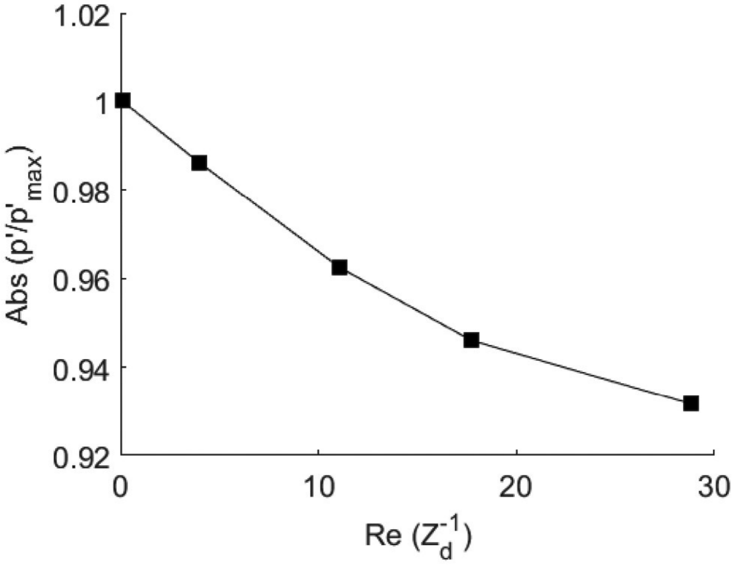

Figure 13. p′ amplitude vs acoustic losses, both normalized, for tests performed in cold conditions.

350 W, Eminence DELTA 10A) located in the plenum and in-phase powered by the same amplifier. The results are summarized in Figure 13, for a constant power of the external excitation and only changing the length of the secondary line. The curve reveals a strong correlation between the pressure reached in the combustion chamber and the acoustic admittance of the pilot fuel injection. These results can only be ascribed to an acoustic interaction between the orifice and the combustion chamber, so confirming the interpretations proposed above.

Even though the evidence discussed above are somewhat indirect or based on rough estimates and should be considered with caution, all of them are thought to demonstrate that acoustic dissipation in the pilot line may explain the variations in p' observed in Figure 8 due to changes in the tube length without pilot fuel injection. Therefore, for the PAIC implementation explored in this work, this purely acoustic effect is expected to induce some additional damping of pressure fluctuations, besides that exclusively due to the dynamic interaction with the pilot flame, which has been clearly demonstrated (see Figure 7) and is the basis of the PAIC concept explored here.

Conclusions and final remarks

A preliminary study about a novel approach to damp thermoacoustic instabilities in gas-turbine combustors has been carried out. The system is purely passive, since it takes advantage of the acoustic response of the secondary injection line (characterized by its acoustic admittance, Z_d^{-1}) to modulate the heat released by a tiny pilot flame in the core of the main, premixed one; however, the effects sought are similar to those of active systems, and so it has been named as ‘pseudo-active instability control’ (PAIC).

The configuration of the pilot line was designed to explore the influence of its acoustic properties on the amplitude of the limit cycle. The results are expected to also depend on the (unknown) flame transfer function of the pilot flame (FTF_d) and, in order to identify different behaviors, the tests were designed to cover a range of Z_d^{-1} values as wide as physically possible.

The experiments performed demonstrated that the injection of pilot fuel, even in very small amounts (1.7% or 2.7% of the total), substantially modified the amplitude of the limit cycle with respect to the same configuration without secondary injection. As it was anticipated, the results strongly depend on the acoustic properties of the injection line, so that for the range explored the limit cycle could be either damped by a factor of 2 or amplified in the same proportion; this provides a wide range of variation, exclusively attributable to the dynamic interaction between the main flame and a very small pilot fuel injection (only 1.7% of the total power). Cross-correlation chemiluminescence maps demonstrate, for those cases, the appearance of localized fluctuations at the flame root. These results support the dynamic interaction between the main flame and the small diffusion flame, as it was initially postulated, leading to either amplification or damping of the oscillation, depending on the acoustic characteristics of the pilot fuel injection.

The tests also revealed that, in some cases, the limit cycle amplitude (p') in the burner varies considerably with the values of Z_d^{-1} also when no pilot fuel is injected in the combustion chamber. Two main hypotheses of possible interactions not related to the oscillations in heat release rate induced by the pilot flame were considered:

The secondary line may act as a tunable resonator, dissipating more or less acoustic energy according to the value of Z_d^{-1}

The fluctuating velocity induced at the central injector may cause a fluid-dynamic perturbation at the base of the main flame.

Flame images do not show any effect on the flame when pilot fuel is shut off and so, the possibility of a purely fluid-dynamic interaction has been discarded. On the contrary, all the analysis performed to evaluate the potential relevance of acoustic dissipation at the orifice apparently confirm that this mechanism may explain the variations observed when the pilot line is modified, without secondary fuel injection. Of course, there is an opportunity to further reduce pressure amplitude by applying the abundant knowledge available on the use of resonators (e.g., one-fourth wave tubes), but this was not the primary objective of the study and was not attempted.

In summary, significant reductions in limit cycle amplitude were confirmed for very small amounts of pilot fuel with the passive approach proposed. The dynamic interaction between the small pilot and the main flames, initially postulated as the basis of the PAIC concept, has been clearly demonstrated throughout this study. It was verified that, for a given configuration, very small amounts of non-premixed pilot fuel (1.7% of the total power) are enough to significantly damp or amplify the limit cycle, depending on the acoustic characteristics of the pilot injection line (in this case, through changes in its length). Furthermore, flame imaging revealed that the addition of pilot fuel induces dynamics at the flame root consistent with the observed variations in p’. Other effects are superimposed on this primary effect of PAIC, leading to the variations in p’ observed in tests without pilot fuel. It was concluded that these effects can be explained by acoustic dissipation at the orifice, which can still lead to additional reductions in pressure fluctuations with respect to those achieved due to the fluctuations induced in the pilot fuel flow.

This study is thought to constitute a novel exploration on the effect of pilot line impedance on the limit cycle as well as to provide a first evidence of the benefits that could be derived from the so-called PAIC strategy. From a practical viewpoint, this method also offers some important advantages. Besides avoiding the need for high-frequency actuators, the response of the system can be widely varied by suitably adjusting the acoustic properties of the secondary injection as well as the pilot fuel flow rate. All these variables can be regulated by relatively inexpensive, conventional means and could be adapted to the requirements of different situations. Nevertheless, the results reported here should be considered as a first 'proof of concept' on the, previously unexplored, effect of the acoustics of the pilot injection on the limit cycle as a purely passive approach; further work is needed to gain a better understanding on the phenomena involved and how to control them in a suitable way to maximize the damping of the limit cycle amplitude. In particular, this objective would be facilitated if the dynamic response of the pilot flame (FTF_d) was known, which requires the development of methods (experimental or CFD-based) suitable for small diffusion flames burning inside a much larger (by up to 2 orders of magnitude) premixed flame, in limit cycle conditions.

Acknowledgments

The support of the Spanish Ministry of Economy and Competitiveness and by the European Union (FEDER), through Project RTC-2016-4845-3 (Program Retos-Colaboración) is gratefully acknowledged.

References

Alemela, P. R. 2009. Measurement and scaling of acoustic transfer matrices of premixed swirl flames. Ph.D. Thesis. Technischen Universität München

Auer, M. P., C. Gebauer, K. G. Mösl, C. Hirsch, and T. Sattelmayer. 2004. Active instability control: Feedback of combustion instabilities on the injection of gaseous fuel. *J. Eng. Gas Turb. Power* 127:4.

Balachandran, R., B. O. Ayoola, C. F. Kaminski, A. P. Dowling, and E. Mastorakos. 2005. Experimental investigation of the nonlinear response of turbulent premixed flames to imposed inlet velocity oscillations. *Combust. Flame* 143 (1–2):1–2. doi:10.1016/j.combustflame.2005.04.009.

Ballester, J., R. Hernández, A. Sanz, A. Smolarz, J. Barroso, and A. Pina. 2009. Chemiluminescence monitoring in premixed flames of natural gas and its blends with hydrogen. *Proc. Combust. Inst.* 32 (2):2. doi:10.1016/j.proci.2008.07.029.

Bellows, B. D., M. K. Bobba, A. Forte, J. M. Seitzman, and T. Lieuwen. 2007. Flame transfer function saturation mechanisms in a swirl-stabilized combustor. *Proc. Combust. Inst.* 31 (2):2. doi:10.1016/j.proci.2006.07.138.

Candel, S. 2002. Combustion dynamics and control: Progress and challenges. *Proc. Combust. Inst.* 29 (1):1. doi:10.1016/S1540-7489(02)80007-4.

Choi, G.-M., M. Tanahashi, and T. Miyauchi. 2005. Control of oscillating combustion and noise based on local flame structure. *Proc. Combust. Inst.* 30 (2):2. doi:10.1016/j.proci.2004.08.249.

de Bedout, J. M., M. A. Franchek, R. J. Bernhard, and L. Mongeau. 1997. Adaptive-passive noise control with self-tuning Helmholtz Resonators. *J. Sound Vib.* 143 (1):1. doi:10.1006/jsvi.1996.0796.

Dowling, A., and S. R. Stow. 2003a. Acoustic analysis of gas turbine combustors. *J. Propul. Power* 19 (5):5. doi:10.2514/2.6192.

Dowling, A. P., and A. S. Morgans. 2005. Feedback control of combustion oscillations. *Annu. Rev. Fluid Mech.* 37 (1):151–82. doi:10.1146/annurev.fluid.36.050802.122038.

Dowling, A. P., and S. R. Stow. 2003b. Acoustic analysis of gas turbine combustors. *J. Propul. Power* 19 (5):5. doi:10.2514/2.6192.

Dupère, I. D. J., and A. P. Dowling. 2005. The use of helmholtz resonators in a practical combustor. *J. Eng. Gas Turb. Power* 127:2.

Durox, D., T. Schuller, and S. Candel. 2005. Combustion dynamics of inverted conical flames. *Proc. Combust. Inst.* 30 (2):2. doi:10.1016/j.proci.2004.08.067.

Durox, D., T. Schuller, N. Noiray, and S. Candel. 2009. Experimental analysis of nonlinear flame transfer functions for different flame geometries. *Proc. Combust. Inst.* 32 (1):1. doi:10.1016/j.proci.2008.06.204.

Eldredge, J. D., and A. P. Dowling. 2003. The absorption of axial acoustic waves by a perforated liner with bias flow. *J. Fluid Mech.* 485:307–35. doi:10.1017/S0022112003004518.

Estève, S. J., and M. E. Johnson. 2005. Adaptive Helmholtz resonators and passive vibration absorbers for cylinder interior noise control. *J. Sound Vib.* 288 (4–5):4. doi:10.1016/j.jsv.2005.01.017.

García-Armingol, T., J. Ballester, and A. Smolarz. 2013. Chemiluminescence-based sensing of flame stoichiometry: Influence of the measurement method. *Measurement* 46 (9):9. doi:10.1016/j.measurement.2013.06.008.

García-Armingol, T., Á. Sobrino, E. Luciano, and J. Ballester. 2016. Impact of fuel staging on stability and pollutant emissions of premixed syngas flames. *Fuel* 185:122–32. doi:10.1016/j.fuel.2016.07.086.

Guyot, D., M. Röbler, M. R. Bothien, and C. O. Paschereit 2007. Active control of combustion instability using pilot and premix fuel modulation. 14th International Congress on Sound and Vibration, Cairns, Australia, paper 235

Hardalupas, Y., and M. Orain. 2004. Local measurements of the time-dependent heat release rate and equivalence ratio using chemiluminescent emission from a flame. *Combust. Flame* 139 (3):3. doi:10.1016/j.combustflame.2004.08.003.

Hermann, J., and S. Hoffmann. 2005. Implementation of active control in a full-scale gas-turbine combustor. *Combustion instabilities in gas turbine engines, in progress in astronautics and aeronautics AIAA*, T. Lieuwen and V. Yang. ed.., Vol. 210. Whashington: American Institute of Aeronautics and Astronautics, Inc., 611–34

Huber, A., and W. Polifke 2008. Impact of fuel supply impedance on combustion stability of gas turbines. ASME Turbo Expo 2008: Power for Land, Sea and Air, paper GT2008-51193, Berlin, Germany.

Keller, J. J. 1995. Thermoacoustic oscillations in combustion chambers of gas turbines. *Aiaa J.* 33 (12):12. doi:10.2514/3.12980.

Kim, H. J., J. P. Cha, J. K. Song, and Y. S. Ko. 2010. Geometric and number effect on damping capacity of Helmholtz resonators in a model chamber. *J. Sound Vib.* 329 (16):16. doi:10.1016/j.jsv.2010.02.018.

Krebs, W., S. Bethke, J. Lepers, P. Flohr, B. Prade, C. Johnson, and S. Sattinger. 2005. Thermoacoustic design tools and passive control: Siemens power generation approaches. In *combustion instabilities in gas turbine engines, in progress in astronautics and aeronautics AIAA*, ed. T. C. Lieuwen and V. Yang, Vol. 210, 89–112. Washington DC: American Institute of Aeronautics and Astronautics, Inc.

Lamraoui, A., F. Richecoeur, S. Ducruix, and T. Schuller 2011. Experimental analysis of simultaneous non-harmonically related unstable modes in a swirled combustor ASME Turbo Expo 2011: Turbine Technical Conference and Exposition, paper GT 2011-46701, Vancouver, British Columbia, Canada.

Lee, J. G., K. Kim, and D. A. Santavicca. 2000. Effect of injection location on the effectiveness of an active control system using secondary fuel injection. *Proc. Combust. Inst.* 28 (1):1. doi:10.1016/S0082-0784(00)80276-3.

Lee, J. G., and D. A. Santavicca. 2003. Experimental diagnostics for the study of combustion instabilities in lean premixed combustors. *J. Propul. Power* 19 (5):5. doi:10.2514/2.6191.

Li, C., S. Li, X. Cheng, and M. Zhu 2017a. Measurements and modeling of the dynamic response of a pilot stabilized premixed flame under dual-input perturbation. ASME Turbo Expo 2017: Turbomachinery Technical Conference and Exposition, paper GT2017-63843, Charlotte, North Carolina, USA.

Li, J., S. Peluso, B. Quay, and D. A. Santavicca 2017b. Effect of pilot flame on flame macrostructure and combustion instability. ASME Turbo Expo 2017: Turbomachinery Technical Conference and Exposition, paper GT2017-64079, Charlotte, North Carolina, USA.

Li, S., Q. Li, L. Tang, B. Yang, J. Fu, C. A. Clarke, X. Jin, C. Z. Ji, and H. Zhao. 2016. Theoretical and experimental demonstration of minimizing self-excited thermoacoustic oscillations by applying anti-sound technique. *Appl. Energy* 181:399–407. doi:10.1016/j.apenergy.2016.08.069.

Lieuwen, T. 2003. Modeling premixed combustion–acoustic wave interactions: A review. *J. Propul. Power* 19 (5):5. doi:10.2514/2.6193.

Lieuwen, T., and B. T. Zinn 1998. Theoretical investigation of combustion instability mechanisms in lean premixed gas turbines. 36th AIAA Aerospace Sciences Meeting and Exhibit paper AIAA-98-0641, Reno, Nevada, USA.

Luciano, E., and J. Ballester. 2018. Analysis of the dynamic response of premixed flames through chemiluminescence cross-correlation maps. *Combust. Flame* 194:296–308. doi:10.1016/j.combustflame.2018.05.005.

Magina, N., V. Acharya, and T. Lieuwen. 2019. Forced response of laminar non-premixed jet flames. *Prog. Energy Combust. Sci.* 70:89–118. doi:10.1016/j.pecs.2018.08.001.

McManus, K. R., T. Poinsot, and S. M. Candel. 1993. A review of active control of combustion instabilities. *Prog. Energy Combust. Sci.* 19 (1):1. doi:10.1016/0360-1285(93)90020-F.

Moeck, J., M. Bothien, D. Guyot, and C. Paschereit. 2007. Phase-shift control of combustion instability using (combined) secondary fuel injection and acoustic forcing. *Active flow control*, R. King. ed.., Vol. 95. 408–21. Berlin, Germany: Springer.

Neumeier, Y., and B. T. Zinn. 1996. Experimental demonstration of active control of combustion instabilities using real-time modes observation and secondary fuel injection. *Symp. (Int.) Combust* 26 (2):2. doi:10.1016/S0082-0784(96)80120-2.

Noiray, N., D. Durox, T. Schuller, and S. Candel. 2009. Dynamic phase converter for passive control of combustion instabilities. *Proc. Combust. Inst.* 32 (2):2. doi:10.1016/j.proci.2008.05.051.

Palies, P., D. Durox, T. Schuller, and S. Candel. 2010. The combined dynamics of swirler and turbulent premixed swirling flames. *Combust. Flame* 157 (9):9. doi:10.1016/j.combustflame.2010.02.011.

Palies, P., D. Durox, T. Schuller, P. Morenton, and S. Candel. 2009. Dynamics of premixed confined swirling flames. *C. R. Mecanique* 337 (6–7):6–7. doi:10.1016/j.crme.2009.06.001.

Panoutsos, C. S., Y. Hardalupas, and A. M. K. P. Taylor. 2009. Numerical evaluation of equivalence ratio measurement using OH* and CH* chemiluminescence in premixed and non-premixed methane–air flames. *Combust. Flame* 156 (2):2. doi:10.1016/j.combustflame.2008.11.008.

Paschereit, C. O., P. Flohr, and E. J. Gutmark. 2002. Combustion control by vortex breakdown stabilization. *J. Turbomach.* 128:4.

Peters, M., A. Hirschberg, A. Reijnen, and A. Wijnands. 1993. Damping and reflection coefficient measurements for an open pipe at low mach and low helmholtz numbers. *J. Fluid Mech.* 256:499–534. doi:10.1017/S0022112093002861.

Rayleigh, J. W. S. 1878. THE EXPLANATION OF CERTAIN ACOUSTICAL PHENOMENA1. *Nature* 18 (455):455. doi:10.1038/018319a0.

Riazi, R., M. Farshchi, M. Shimura, M. Tanahashi, and T. Miyauchi. 2010. An experimental study on combustion dynamics and NOx emission of a swirl stabilized combustor with secondary fuel injection. *J. Therm. Sci. Tech* 5 (2):2. doi:10.1299/jtst.5.266.

Richards, G., D. Straub, and E. Robey 2003a. Control of Combustion Dynamics Using Fuel System Impedance. ASME Turbo Expo 2003: International Joint Power Generation Conference, paper GT2003-38521, Atlanta, Georgia, USA.

Richards, G. A., and E. H. Robey. 2008. Effect of fuel system impedance mismatch on combustion dynamics. *J. Eng. Gas Turb. Power* 130 (1):1. doi:10.1115/1.2771249.

Richards, G. A., D. L. Straub, and E. H. Robey 2001. Dynamic response of a premix fuel injector. ASME Turbo Expo 2001: Power for Land, Sea, and Air, paper GT2001-0036, New Orleans, Louisiana, USA.

Richards, G. A., D. L. Straub, and E. H. Robey. 2003b. Passive control of combustion dynamics in stationary gas turbines. *J. Propul. Power* 19 (5):5. doi:10.2514/2.6195.

Richards, G. A., and J. M. Yip 1995. Oscillating combustion &om a premix fuel nozzle. Combustion Institute/American Flame Research Committee Meeting, paper DOE/METC/C-95/7189, San Antonio, Texas, USA.

Richards, G. A., J. M. Yip, and R. Gemmen 1995. Design factors for stable lean premix combustion. Advanced Coal-Fired Power Systems 95 Review Meeting, paper DOE/METC/C-96/7210, Morgantown, West Virginia, USA.

Richecoeur, F., T. Schuller, A. Lamraoui, and S. Ducruix. 2013. Analytical and experimental investigations of gas turbine model combustor acoustics operated at atmospheric pressure. *C. R. Mecanique* 341 (1–2):1. doi:10.1016/j.crme.2012.11.011.

Sattinger, S. S., Y. Neumeier, A. Nabi, B. T. Zinn, D. J. Amos, and D. D. Darling. 2000. Sub-scale demonstration of the active feedback control of gas-turbine combustion instabilities. *J. Eng. Gas Turb. Power* 122 (2):2. doi:10.1115/1.483204.

Shinjo, J., S. Matsuyama, Y. Mizobuchi, and S. Ogawa. 2007. Study on flame dynamics with secondary fuel injection control by large eddy simulation. *Combust. Flame* 150 (4):4. doi:10.1016/j.combustflame.2007.01.011.

Sohn, C. H., and J. H. Park. 2011. A comparative study on acoustic damping induced by half-wave, quarter-wave, and Helmholtz resonators. *Aerosp. Sci. Technol.* 15 (8):8. doi:10.1016/j.ast.2010.12.004.

Tachibana, S., L. Zimmer, Y. Kurosawa, and K. Suzuki. 2007. Active control of combustion oscillations in a lean premixed combustor by secondary fuel injection coupling with chemiluminescence imaging technique. *Proc. Combust. Inst.* 31 (2):2. doi:10.1016/j.proci.2006.08.037.

Tanahashi, M., S. Murakami, T. Miyauchi, and G.-M. Choi 2004. Control of oscillating combustion and measurements of turbulent flames. Proceedings of 5th Symposium on Smart Control of Turbulence, Tokyo, Japan, paper 3.2

Terhaar, S., K. Oberleithner, and C. O. Paschereit. 2015. Key parameters governing the precessing vortex core in reacting flows: An experimental and analytical study. *Proc. Combust. Inst.* 35 (3):3. doi:10.1016/j.proci.2014.07.035.

Terhaart, S., O. Krüger, and P. C. Oliver. 2014. Flow field and flame dynamics of swirling methane and hydrogen flames at dry and steam diluted conditions. *J. Eng. Gas Turb. Power* 137:4.

Zhao, D., and A. S. Morgans. 2009. Tuned passive control of combustion instabilities using multiple Helmholtz resonators. *J. Sound Vib.* 320 (4–5):4. doi:10.1016/j.jsv.2008.09.006.

Appendix. A modeling of the acoustic impedance of the pilot fuel line

The acoustic response the pilot fuel line can be quantified in terms of its acoustic impedance Z,

$$Z(\omega) = \frac{\hat{p}(\omega)/\overline{\rho c}}{\hat{u}(\omega)} \tag{A.1}$$

In Eq. (A. 1), $\hat{p}$ and $\hat{u}$ represent, respectively, the complex amplitudes of pressure and velocity fluctuations at the considered frequency ω, whereas $\bar{\rho}$ and $\bar{c}$ stand for the mean value of the density and the speed of sound. Since the physical effect concerning PAIC is the velocity fluctuation induced for a given oscillation of the dynamic pressure, it is more practical to work with its inverse, i.e. the acoustic admittance Z^{-1}.

Alternatively, the response can be described in terms of the reflection coefficient R,

$$R(\omega) = \frac{f(\omega)}{g(\omega)} \tag{A.2}$$

where f and g are the Riemann invariants, representing the plane waves traveling, respectively, forward and backward with respect to the flow direction. Z^{-1} can be calculated from $R = |R|\angle\alpha$ as

$$Z^{-1} = \frac{|R|\angle\alpha - 1}{|R|\angle\alpha + 1} = \frac{|R|^2 - 1 + i2|R|\sin\alpha}{(|R| - 1)^2 + 2|R|(1 + \cos\alpha)} \tag{A.3}$$

This expression is useful to derive some important conclusions on the possible values of Z^{-1}. For passive elements, as it is the case for the pilot line, the amplitude of the reflected wave $|f|$ at its boundary cannot be greater than the incident one $|g|$, so that $|R| \leq 1$, while its phase presents no particular constraint. Therefore, the real part of Z^{-1} is always negative; this implies that all the possible values of Z^{-1} are confined to the left half-plane of the complex domain. Also, it can be demonstrated (not shown here for brevity) that, for a given $|R|$ (so, a circumference in the complex domain), the values of Z^{-1} also describe a circumference whose radius diverges for $|R|$ tending to 1 (see Figure A1).

This has important implications for the design of a tunable PAIC system. On the one hand, in theory, there is no limit for $|Z^{-1}|$ and, hence, for the amplitude of velocity fluctuations at the injector for a given $p\prime$ (there are limits, however, due to real flow effects). On the other hand, the real part of Z^{-1} is always negative and, hence, the phase of the acoustic admittance is limited to the range [90^0, 270^0]. So, the phase between $u_d^{'}$ and p' can only be adjusted in this range (i.e., only one half of the possible values). This imposes an important restriction for the tuning of a PAIC system, which should be tuned so that the heat released in the pilot flame, $Q_d^{'}$, fluctuates out-of-phase with p'. Since the flame transfer function of the pilot flame cannot be measured, the actual phase between $Q_d^{'}$ and p' cannot be known a priori.

The acoustic admittance of the pilot line, Z_d^{-1}, determines the phase between $u_d^{'}$ and p' hence, has a direct influence on the phase between $Q_d^{'}$ and p'. The strategy followed consists in testing a wide range of pilot tube lengths, in order to identify the ranges for which the main (premixed) and pilot (diffusion) flames interact in a constructive or destructive manner. A 1-D acoustic model was used to assist in the design of the pilot line and, in particular, to select the most convenient tube lengths.

The pilot fuel line is modeled as an acoustic network, including the orifice and the tube. The upstream boundary is a choked orifice, located downstream of the fuel flowmeter which, as proposed by Keller (1995), can be modeled with good approximation as a closed end ($R = 1$). The fuel pipe consists of two parts (both with 8 mm i.d.): a polyamide pipe of variable length, followed by a stainless steel one (fixed length), at the end of which is installed the injector orifice. The model proposed in Peters et al. (1993) for straight tubes with damping was applied. It takes into account thermal and viscous damping effects, through the shear and the Prandtl numbers (Sh and Pr), as well as the roughness of the inner surface of the duct, through an empirical coefficient C_d (set as 1 and 2 for the stainless steel and the polyamide tube, respectively). All these phenomena are modeled through the wavenumber, calculated as:

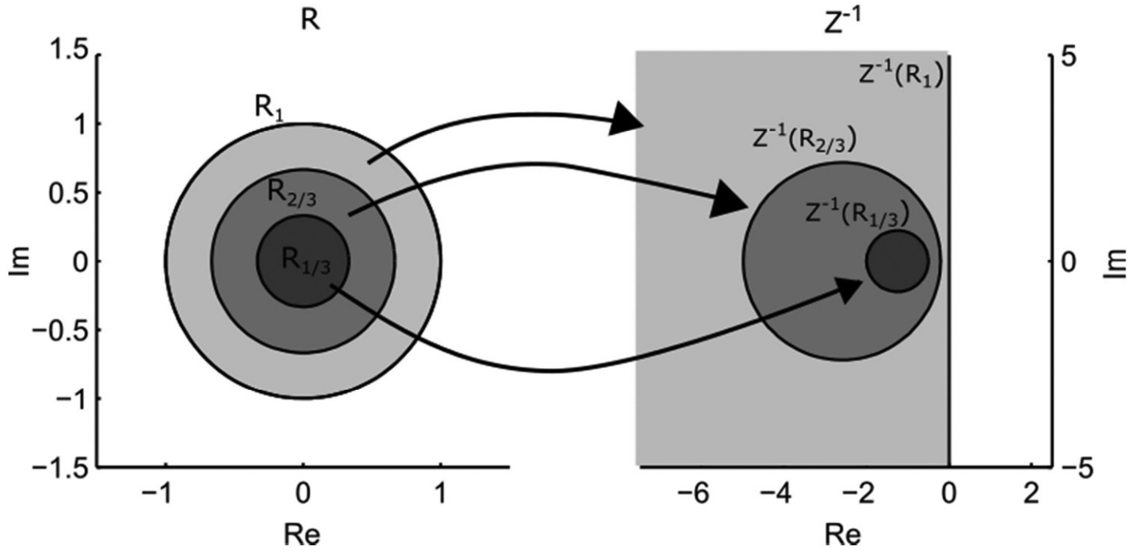

Figure A1. Possible values of Z^{-1} for a given module of R, with the constraint $|R| \leq 1$. The transformation of the curves for $|R|$=1, 1/3 and 2/3 are shown.

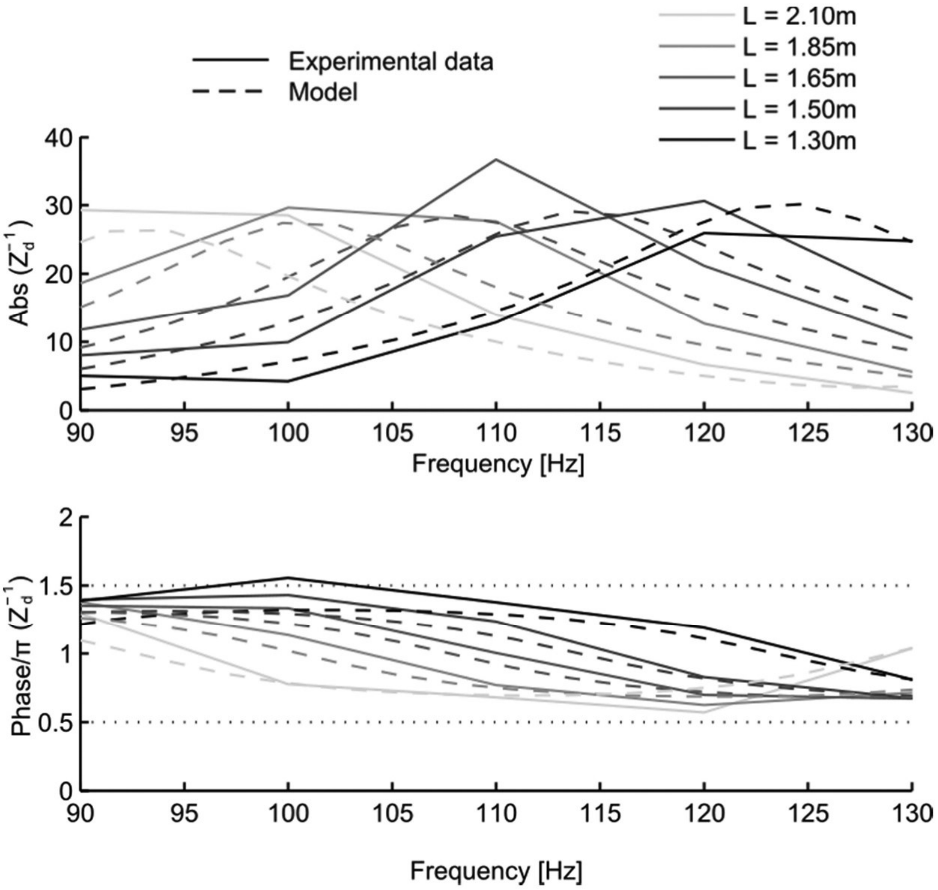

Figure A2. Theoretical and experimental values of Z_d^{-1} for the five values of L in the neighborhood of 110 Hz.

$$k_{\pm} = \frac{\omega}{c \pm \bar{u}} \left[1 + C_d \frac{1-i}{\sqrt{2}S_h} \left(1 + \frac{\gamma - 1}{\sqrt{Pr}} \right) \right] \tag{A.4}$$

Finally, the injection orifice was modeled as a combination of a sudden area change (from 8 to 2.5 mm in diameter) and a straight tube of 2.5 mm in diameter and 5 mm in length. The acoustic model for a sudden area change is described in Alemela (2009), which can be summed up in the transfer matrix before and after the area change (subscripts 1 and 2, respectively):

$$\begin{pmatrix} \frac{p\prime}{\rho c} \\ u\prime \end{pmatrix}_2 = \begin{pmatrix} 1 & (1 - \zeta - \alpha^2)M_1 - i\frac{\omega}{c} l_{ef} \\ -i\frac{\omega}{c} l_{red} + \alpha M_1 - M_2 & \alpha \end{pmatrix} \begin{pmatrix} \frac{p\prime}{\rho c} \\ u\prime \end{pmatrix}_1 \tag{A.5}$$

being α the area ratio, ζ the acoustic loss coefficient, l_{ef} the effective length, and l_{red} the reduced length. Actually, the core of the model of Alemela (2009) lies in the calculation of these three latter parameters.

The reliability of the developed model was verified by comparing the predictions obtained with experimental measurements. The acoustic response of the secondary line was analyzed by measuring the dynamic pressure in the combustion chamber and the velocity fluctuations at the injector by means of a hot wire anemometer. The acoustic excitation was provided by two loudspeakers (see Figure 1), for a forcing frequency between 50 and 250 Hz with 10 Hz steps. The signals of both the pressure transducer and the hot wire anemometer was sampled at 4 kHz and recorded for 4 s. The validation of the model was performed by testing the lengths then used to implement PAIC in the burner (L = 1.30, 1.50, 1.65, 1.85, and 2.10 m) in the neighborhood of 110 Hz, covering the range of the experimental frequencies produced in limit cycle conditions. The results are shown in Figure A2. The match between the model and the experimental results is quite good, confirming the reliability of the developed model in simulating the acoustic response of the secondary line.

Appendix

Paper 1: E. Luciano, J. Ballester, Analysis of the Dynamic Response of Premixed Flames through Chemiluminescence Cross-Correlation Maps, *Combust. Flame* 194 (2018) 296-308.

- DOI: https://doi.org/10.1016/j.combustflame.2018.05.005
- Thematic areas: Thermoacoustics, Combustion, Chemical and Mechanical Engineering
- Impact factor of the Journal: 4.57

Paper 2: E. Luciano, J. Ballester, Analysis of the Dynamics of Premixed Methane and Biogas Flames Based on Cross-correlation Maps, *Combust. Sci. Technol.* 191 (2019) 1-26

- DOI: https://doi.org/10.1080/00102202.2019.1662407
- Thematic areas: Thermoacoustics, Combustion, Chemical and Mechanical Engineering
- Impact factor of the Journal: 1.73

Paper 3: E. Luciano, E. Tizné, J. Ballester, Use of Flame Transfer Function to Predict Combustor Unstable Modes, *24th International Congress on Sound and Vibration* (2017), paper 905

- Congress website: https://iiav.org/icsv24/index.php?va=viewpage&vaid=175
- Thematic areas: Thermoacoustics, Combustion, Chemical and Mechanical Engineering

Paper 4: J. Oliva, E. Luciano, J. Ballester, Damping of Combustion Instabilities Through Pseudo-Active Control, *ASME Turbo Expo 2018: Turbomachinery Technical Conference and Exposition* (2018), paper 51067

- DOI: https://doi.org/10.1115/GT2018-77102
- Thematic areas: Thermoacoustics, Combustion, Chemical and Mechanical Engineering

Paper 5: E. Luciano, J. Oliva, Á. Sobrino, J. Ballester, Analysis of a Pseudo-active Approach for the Control of Thermoacoustic Instabilities, *Combust. Sci. Technol.* 192 (2020) 1-28

- DOI: https://doi.org/10.1080/00102202.2020.1802588
- Thematic areas: Thermoacoustics, Combustion, Chemical and Mechanical Engineering
- Impact factor of the Journal: 1.73

Área de Mecánica de Fluidos / LIFTEC
Dpto Ciencia y Tecnología de Materiales y Fluidos
Universidad de Zaragoza
Escuela de Ingeniería y Arquitectura
María de Luna 3
50018-Zaragoza

Javier Ballester
Tf: +34-976 762153, 761881
Fax: +34-976 761882
ballester@unizar.es

Zaragoza, 28 de Septiembre de 2020

A quien corresponda,

Como director de tesis de D. Ennio Giovanni Luciano, hago constar que su contribución a los artículos incluidos en la tesis ha sido la siguiente:

- *E. Luciano, J. Ballester, Analysis of the dynamic response of premixed flames through chemiluminescence cross-correlation maps, Combust. Flame 194 (2018) 296-308*
- *E. Luciano, J. Ballester, Analysis of the Dynamics of Premixed Methane and Biogas Flames Based on Cross-correlation Maps, Combustion Science and Technology (2019)* DOI: 10.1080/00102202.2019.1662407
    - En estos dos artículos, el candidato, con mi supervisión, diseñó y llevó a cabo la campaña experimental, analizó los resultados obtenidos y redactó los artículos publicados.
- *E. Luciano, E. Tizné, J. Ballester, Use of Flame Transfer Function to Predict Combustor Unstable Modes, 24th International Congress on Sound and Vibration (2017), paper 905*
    - Este artículo está basado en los resultados obtenidos en el marco del Trabajo Fin de Grado de Eduardo Tizné, del cual fue co-director Ennio G. Luciano, quien supervisó y participó muy activamente en el diseño y desarrollo de la campaña experimental, guió la elaboración del modelo, y supervisó el análisis de resultados y redactó el artículo presentado al congreso ICSV24.
- *J. Oliva, E. Luciano, J. Ballester, Damping of Combustion Instabilities Through Pseudo-Active Control, ASME Turbo Expo 2018: Turbomachinery Technical Conference and Exposition (2018), paper 51067*
- *E. Luciano, J. Oliva, A. Sobrino, J. Analysis of a pseudo-active approach for the control of thermoacoustic instabilities, Combustion Science and Technology (2020) DOI: 10.1080/00102202.2020.1802588*
    - Respecto a lose studios publicados en estos dos artículos, Ennio Luciano supervisó y participó muy activamente en el diseño y desarrollo de la campaña experimental, guió la elaboración del modelo, supervisó el análisis de resultados, realizó íntegramente el análisis de las imágenes de quimioluminiscencia y escribió ambos artículos. En esta parte del trabajo también participó Jesús Oliva durante la realización de su Trabajo Fin de Máster, que fue codirigido por Ennio.

Firmado,

BALLESTER
CASTAÑER JAVIER
MANUEL - DNI
73255625G

Firmado digitalmente por
BALLESTER CASTAÑER JAVIER
MANUEL - DNI 73255625G
Fecha: 2020.09.28 11:29:28
+02'00'

Javier Ballester